



**HAL**  
open science

# Luminance-Chrominance linear prediction models for color textures: An application to satellite image segmentation

Imtnan-Ul-Haque Qazi

► **To cite this version:**

Imtnan-Ul-Haque Qazi. Luminance-Chrominance linear prediction models for color textures: An application to satellite image segmentation. Signal and Image processing. Université de Poitiers, 2010. English. NNT: . tel-00574090

**HAL Id: tel-00574090**

**<https://theses.hal.science/tel-00574090>**

Submitted on 7 Mar 2011

**HAL** is a multi-disciplinary open access archive for the deposit and dissemination of scientific research documents, whether they are published or not. The documents may come from teaching and research institutions in France or abroad, or from public or private research centers.

L'archive ouverte pluridisciplinaire **HAL**, est destinée au dépôt et à la diffusion de documents scientifiques de niveau recherche, publiés ou non, émanant des établissements d'enseignement et de recherche français ou étrangers, des laboratoires publics ou privés.

# THÈSE

pour l'obtention du Grade de  
DOCTEUR DE L'UNIVERSITÉ DE POITIERS  
(Faculté des Sciences Fondamentales et Appliquées)  
(Diplôme National - Arrêté du 7 Août 2006)

*École Doctorale* : **Sciences et Ingénierie pour l'Information**  
*Secteur de Recherche* : **Traitement du signal et des images**

Présentée par :  
Imtnan-Ul-Haque QAZI

## **Luminance-Chrominance linear prediction models for color textures: An application to satellite image segmentation**

Directrice de Thèse : Mme Christine FERNANDEZ-MALOIGNE  
Co-directeur de Thèse : Mr Olivier ALATA  
Co-directeur de Thèse : Mr Jean-Christophe BURIE

Soutenue le 01 Juillet, 2010 devant la Commission d'Examen composée de :

Mr Yannick Berthoumieu, Prof., IMS-ESI, Uni. Bordeaux, France ..... Rapporteur  
Mr Zoltan Kato, Prof., Institute of Informatics, Uni. Szeged, Hungary ..... Rapporteur  
Mr Paul F. Whelan, Prof., CIPA, Uni. Dublin, Ireland ..... Examineur  
Mr André Smolarz, MCF HDR, ICD/LM2S, Uni. Troyes, France ..... Examineur  
Mr Olivier Alata, MCF, XLIM-SIC, Uni. Poitiers, France ..... Co-directeur de Thèse  
Mr Jean-Christophe Burie, MCF, L3I, Uni. La Rochelle, France ..... Co-directeur de Thèse  
Mme Christine Fernandez-Maloigne, Prof., XLIM-SIC, Uni. Poitiers, France Directrice de Thèse



Proclaim! And thy Lord is Most Bountiful,-  
He Who taught (the use of) the pen,-  
Taught man which he knew not.  
*(Quran 96:3-5)*

To  
*Ammi & Abbu.*

## Acknowledgments

Foremost, I would like to thank, Dr. Olivier ALATA, who shared with me a lot of his expertise and research insight. He quickly became for me, the role model of a successful researcher in the field. I also like to express my gratitude to Dr. Jean-Christophe BURIE, whose thoughtful advise often served to give me a sense of direction during my PhD studies.

It is difficult to overstate my appreciation to Prof. Christine FERNANDEZ-MALOIGNE, who has always been there for all my professional problems. Not only a great mentor and colleague, she has also been a cornerstone in my professional development.

I wish to thank everybody whom I have shared my life with. From the people who first persuaded and got me interested into the study of image processing, to those, the gift of whose company made my days enjoyable and worth living when I was down and out.

I am tempted to individually thank all of my friends which, from my childhood untill graduate school, have joined me in the discovery of what is life about and how to make the best of it. However, because the list might be too long and by fear of leaving someone out, I will simply say thank you very much to you all. Some of you are away, I am quite lucky ;-): thank you JOJIANS... you rock!!! for being my very best friends and giving me the first ever dream of doing a PhD, as I still remember Dr. NNC Qazi.

I cannot finish without saying how grateful I am to my family members who have given me a loving environment to develop. Particular thanks, of course, to my siblings: my best mates. Lastly, and most importantly, I wish to thank my parents, who have always supported and encouraged me to do my best in all matters of life.

## Abstract

This thesis details the conception, development and analysis of a novel color texture descriptor based on the luminance-chrominance complex linear prediction models for perceptual color spaces. In this approach, two dimensional complex multichannel versions of both causal and non-causal models are developed and used to perform the simultaneous parametric power spectrum estimation of the luminance and the *combined chrominance* channels of the proposed two channel complex color image. The accuracy and precision of these spectral estimates along with the spectral distance measures ensure the robustness and pertinence of the approach for color texture classification. A luminance-chrominance spectral interference based quantitative measure for the color space comparison is also introduced. The experimental results for different test data sets, in IHLS and L\*a\*b\* color spaces are presented and discussed. These results have shown that the chrominance structure information of the color textured images could get better characterized in L\*a\*b\* color space and hence could provide the better color texture classification results.

A Bayesian framework based on the multichannel linear prediction error is also developed for the segmentation of textured color images. The main contribution of this segmentation methodology resides in the robust parametric approximations proposed for the multichannel linear prediction error distribution. These comprised of a unimodal approximation based on the Wishart distribution and a multimodal approximation based on the multivariate Gaussian mixture models. Another novelty of this approach is the fusion of a region size energy term with the conventional Potts model energy to develop a Gibbs random field model of the class label field. This improved label field model is used for the spatial regularization of the initial class label estimates computed through the proposed parametric priors. Experimental results for the segmentation of synthetic color textures as well as high resolution QuickBird and IKONOS satellite images validate the application of this approach for highly textured images. Advantages of using these priors instead of classical Gaussian approximation and improved label field model are evident from these results. They also verify that the L\*a\*b\* color space exhibits better performance among the used color spaces, indicating its significance for the characterization of complex textures through this approach.

### Keywords:

Multichannel complex linear prediction models, Parametric spectrum estimation, Color texture classification, Color texture segmentation, High resolution satellite images, IKONOS, QuickBird.

## Résumé

Cette thèse détaille la conception, le développement et l'analyse d'un nouvel outil de caractérisation des textures exploitant les modèles de prédiction linéaire complexe sur les espaces couleur perceptuels séparant l'intensité lumineuse de la partie chromatique. Des modèles multicanaux 2-d causaux et non-causaux ont été utilisés pour l'estimation simultanée des densités spectrales de puissance d'une image "bi-canal", le premier contenant les valeurs réelles de l'intensité et le deuxième les valeurs complexes de la partie chromatique. Les bonnes performances en terme de biais et de variance de ces estimations ainsi que l'usage d'une distance appropriée entre deux spectres assurent la robustesse et la pertinence de l'approche pour la classification de textures. Une mesure de l'interférence existante entre l'intensité et la partie chromatique à partir de l'analyse spectrale est introduite afin de comparer les transformations associées aux espaces couleur. Des résultats expérimentaux en classification de textures sur différents ensembles de tests, dans différents espaces couleur (RGB, IHLS et  $L^*a^*b^*$ ) sont présentés et discutés. Ces résultats montrent que la structure spatiale associée à la partie chromatique d'une texture couleur est mieux caractérisée à l'aide de l'espace  $L^*a^*b^*$  et de ce fait, cet espace permet d'obtenir les meilleurs résultats pour classifier les textures à l'aide de leur structure spatiale et des modèles de prédiction linéaire.

Une méthode bayésienne de segmentation d'images texturées couleur a aussi été développée à partir de l'erreur de prédiction linéaire multicanale. La contribution principale de la méthode réside dans la proposition d'approximations paramétriques robustes pour la distribution de l'erreur de prédiction linéaire multicanale : la distribution de Wishart et une approximation multimodale exploitant les lois de mélanges gaussiennes multivariées. Un autre aspect original de l'approche consiste en la fusion d'un terme d'énergie sur la taille des régions avec l'énergie du modèle de Potts afin de modéliser le champ des labels de classe à l'aide d'un modèle de champ aléatoire possédant une distribution de Gibbs. Ce modèle de champ aléatoire est ainsi utilisé pour régulariser spatialement un champ de labels initial obtenu à partir des différentes approximations de la distribution de l'erreur de prédiction. Des résultats expérimentaux en segmentation d'images texturées couleur synthétiques et d'images satellites hautes résolutions QuickBird et IKONOS ont permis de valider l'application de la méthode aux images fortement texturées. De plus les résultats montrent l'intérêt d'utiliser les approximations de la distribution de l'erreur de prédiction proposées ainsi que le modèle de champ de labels amélioré par le terme d'énergie qui pénalise les petites régions. Les segmentations réalisées dans l'espace  $L^*a^*b^*$  sont meilleures que celles obtenues dans les autres espaces couleur (RGB et IHLS) montrant à nouveau la pertinence de caractériser les textures couleur par la prédiction linéaire multicanale complexe à l'aide de cet espace couleur.

### Mots clés:

Modèles de prédiction linéaire 2-d multicanale complexe, Estimation paramétrique de spectres, Classification de textures couleur, Segmentation d'images texturées couleur, Images satellites hautes résolutions, IKONOS, QuickBird.



---



---

## LIST OF FIGURES

---

3.1	RGB color space. . . . .	36
3.2	IHLS color space. . . . .	37
3.3	L*a*b* color space. . . . .	37
3.4	NSHP neighborhood support region for model order $(M_1, M_2)$ with $M_1 = 2$ and $M_2 = 2$ . . . . .	41
3.5	$QP_1$ and $QP_2$ neighborhood support regions for model order $(M_1, M_2)$ with $M_1 = 2$ and $M_2 = 2$ . . . . .	42
3.6	GMRF neighborhood support region for model order $M$ with $M = 3$ . . . . .	45
3.7	RGB converted noisy Sinusoidal images and their respective chroma sinusoids supposedly generated in IHLS and L*a*b* color spaces. For 3.7a and 3.7b, $(A_r = 0.5$ and $A_c = 0.5)$ , $(\phi_r = 30^\circ$ and $\phi_c = 30^\circ)$ and $(\nu_r = (0.3, -0.1)$ and $\nu_c = (0.01, -0.03))$ . . . . .	47
3.8	The sinusoidal test image (3.8a) in IHLS color space and the magnitude spectrum of the luminance 3.8b and the chrominance 3.8c channels computed through 2D FFT are shown. Also, auto spectra estimates of these two channels using GMRF model of order 14 (3.8d and 3.8e respectively), NSHP AR model of order $(4, 4)$ (3.8f and 3.8g respectively), QP AR model via HM method of order $(4, 4)$ (3.8h and 3.8i respectively) are presented. . . . .	49
3.9	The sinusoidal test image (3.9a) in L*a*b* color space and the magnitude spectrum of the luminance 3.9b and the chrominance 3.9c channels computed through 2D FFT are shown. Also, auto spectra estimates of these two channels using GMRF model of order 14 (3.9d and 3.9e respectively), NSHP AR model of order $(4, 4)$ (3.9f and 3.9g respectively), QP AR model via HM method of order $(4, 4)$ (3.9h and 3.9i respectively) are presented. . . . .	50
3.10	Mean Error plots of horizontal and vertical frequency estimates against the varying image size $n$ , for luminance channel in IHLS color space, for different values of SNR. . . . .	52

3.11	Mean Error plots of horizontal and vertical frequency estimates against the varying image size $n$ , for chrominance channel in IHLS color space, for different values of SNR. . . . .	53
3.12	Mean Error plots of horizontal and vertical frequency estimates against the varying image size $n$ , for luminance channel in $L^*a^*b^*$ color space, for different values of SNR. . . . .	54
3.13	Mean Error plots of horizontal and vertical frequency estimates against the varying image size $n$ , for chrominance channel in $L^*a^*b^*$ color space, for different values of SNR. . . . .	55
3.14	Log variance of estimation error of horizontal and vertical frequency estimates against the varying image size $n$ , for luminance channel in IHLS color space, for different values of SNR. . . . .	56
3.15	Log variance of estimation error of horizontal and vertical frequency estimates against the varying image size $n$ , for chrominance channel in IHLS color space, for different values of SNR. . . . .	57
3.16	Log variance of estimation error of horizontal and vertical frequency estimates against the varying image size $n$ , for luminance channel in $L^*a^*b^*$ color space, for different values of SNR. . . . .	58
3.17	Log variance of estimation error of horizontal and vertical frequency estimates against the varying image size $n$ , for chrominance channel in $L^*a^*b^*$ color space, for different values of SNR. . . . .	59
3.18	Estimated PSD of the luminance and the chrominance channels in IHLS (a,b) and $L^*a^*b^*$ (c,d) with 2D multichannel complex QP AR model via HM method with a model order (5, 5). . . . .	60
3.19	Estimated PSD of the Red, Green and Blue channels in RGB color space, with 2D multichannel real QP AR model via HM method. . . . .	61
3.20	Comparison of the interference between luminance and chrominance information <i>i.e.</i> $IR_{CL}$ (left) and $IR_{LC}$ ( <i>right</i> ) in the two color spaces. . . . .	63
4.1	The 24 textures of dimensions $512 \times 512$ forming $DS_1$ . From top left to bottom right, in raster scan order: Bark0; Bark12; Brick0; Clouds0; Fabric0; Fabric4; Fabric7; Fabric8; Fabric11; Fabric13; Fabric15; Fabric17; Fabric19; Flowers0; Food0; Grass1; Leaves12; Metal0; Misc2; Sand0; Stone4; Tile7; Water0; Wood2. . . . .	67
4.2	Sample textures from Outex color texture data base. . . . .	68
4.3	Sample texture from the Vistex database. . . . .	69
4.4	Spectral estimates of the image shown in Figure 4.3 in IHLS color space. . . . .	70
4.5	Spectral estimates of the image shown in Figure 4.3 in $L^*a^*b^*$ color space. . . . .	71
4.6	Sample texture from the Outex database. . . . .	72
4.7	Spectral estimates of the image shown in Figure 4.6 in IHLS color space. . . . .	73
4.8	Spectral estimates of the image shown in Figure 4.6 in $L^*a^*b^*$ color space. . . . .	74

4.9	Test color textured images and their pixel classification results in the three discussed color spaces. . . . .	89
5.1	A generalized block diagram of the image observation model parameter estimation from the training sub image. . . . .	99
5.2	Data base of ten color images used for simulations. . . . .	105
5.3	Comparison of the average percentage error of the segmentation results obtained using three different parametric models of the LPE in RGB, IHLS and L*a*b* color spaces (from left to right respectively). The observation model used is 2D multichannel QP AR model. . . . .	106
5.4	Comparison of the standard deviation of the average segmentation error in three different color spaces using 2D multichannel GMRF, NSHP AR and QP AR models (from left to right respectively). The parametric model used for LPE approximation is MGMM. . . . .	107
5.5	Comparison of the average percentage error of the segmentation results obtained with region penalty term, using three different parametric models of the LPE in RGB, IHLS and L*a*b* color spaces (from left to right respectively). The observation model used is 2D multichannel QP AR model. . . . .	109
5.6	Comparison of the standard deviation of the average segmentation error in three different color spaces with region penalty term, using 2D multichannel multivariate Gaussian, MGMM and Wishart distribution models (from left to right respectively). The observation model used is 2D multichannel QP AR model. . . . .	110
5.7	Segmentation results without spatial regularization (column $\beta = 0$ ), with spatial regularization using only Potts model (column <b>Potts</b> ) and with spatial regularization using Potts model with varying $\beta$ and region size penalty (column <b>Potts + Region</b> ) for the color texture 3 using single Gaussian (row 2), MGMM (row 3) and Wishart approximation (row 4) in RGB color space. . . . .	112
5.8	Segmentation results without spatial regularization (column $\beta = 0$ ), with spatial regularization using only Potts model (column <b>Potts</b> ) and with spatial regularization using Potts model with varying $\beta$ and region size penalty (column <b>Potts + Region</b> ) for the color texture 3 using single Gaussian (row 2), MGMM (row 3) and Wishart approximation (row 4) in L*a*b* color space. . . . .	113
5.9	Segmentation results without spatial regularization (column $\beta = 0$ ), with spatial regularization using only Potts model (column <b>Potts</b> ) and with spatial regularization using Potts model with varying $\beta$ and region size penalty (column <b>Potts + Region</b> ) for the color texture 10 using single Gaussian (row 2), MGMM (row 3) and Wishart approximation (row 4) in RGB color space. . . . .	114

5.10	Segmentation results without spatial regularization (column $\beta = 0$ ), with spatial regularization using only Potts model (column <b>Potts</b> ) and with spatial regularization using Potts model with varying $\beta$ and region size penalty (column <b>Potts + Region</b> ) for the color texture 10 using single Gaussian (row 2), MGMM (row 3) and Wishart approximation (row 4) in $L^*a^*b^*$ color space. . .	115
5.11	The original images (row 1) and the final segmentation results using our method in RGB (row 2) and ( $L^*a^*b^*$ ) color spaces for a comparative analysis with [KP06]. . . . .	116
5.12	The relative spectral response of IKONOS imagery [web]. . . . .	118
5.13	Four multichannel Satellite images used for initial simulations. . . . .	120
5.14	Segmentation results of the four used satellite images in RGB color space. . .	122
5.15	Segmentation results of the four used satellite images in $L^*a^*b^*$ color space. .	123
5.16	Average percentage pixel classification of four satellite images in RGB (row 1) and $L^*a^*b^*$ (row 2) color space using classical Gaussian (left) and MGMM (right) approximations for the distribution of multichannel LPE. . . . .	124
5.17	Average percentage sensitivity of four satellite images in RGB (row 1) and $L^*a^*b^*$ (row 2) color space using classical Gaussian (left) and MGMM (right) approximations for the distribution of multichannel LPE. . . . .	125
5.18	Average percentage global error of four satellite images in RGB (row 1) and $L^*a^*b^*$ (row 2) color space using classical Gaussian (left) and MGMM (right) approximations for the distribution of multichannel LPE. . . . .	126
5.19	Segmentation results of the four used satellite images in RGB color space. . .	128
5.20	Segmentation results of the four used satellite images in $L^*a^*b^*$ color space. .	129
5.21	High resolution IKONOS satellite images (Sat image $IK_5$ (row 1) and Sat image $IK_6$ (row 2)) used in the second set of experiments. . . . .	130
5.22	High resolution QuickBird satellite images (Sat image $QB_7$ to Sat image $QB_{20}$ in raster scan manner) used in the second set of experiments. . . . .	131
5.23	Segmentation results of the images Sat image $IK_5$ in RGB color space using classical Gaussian (row 2) and MGMM (row 2) approximations for the multichannel LPE. . . . .	133
5.24	Segmentation results of the images Sat image $IK_5$ in $L^*a^*b^*$ color space using classical Gaussian (row 2) and MGMM (row 2) approximations for the multichannel LPE. . . . .	134
5.25	Segmentation results of the images Sat image $IK_6$ in RGB color space using classical Gaussian (row 2) and MGMM (row 2) approximations for the multichannel LPE. . . . .	135
5.26	Segmentation results of the images Sat image $IK_6$ in $L^*a^*b^*$ color space using classical Gaussian (row 2) and MGMM (row 2) approximations for the multichannel LPE. . . . .	136

C.1	Segmentation results of the satellite images Sat image $QB_7$ to Sat image $QB_{10}$ (rows 1 to 4 respectively) in RGB color space. . . . .	150
C.2	Segmentation results of the satellite images Sat image $QB_7$ to Sat image $QB_{10}$ (rows 1 to 4 respectively) in $L^*a^*b^*$ color space. . . . .	151
C.3	Segmentation results of the satellite images Sat image $QB_{11}$ to Sat image $QB_{14}$ (rows 1 to 4 respectively) in RGB color space. . . . .	152
C.4	Segmentation results of the satellite images Sat image $QB_{11}$ to Sat image $QB_{14}$ (rows 1 to 4 respectively) in $L^*a^*b^*$ color space. . . . .	153
C.5	Segmentation results of the satellite images Sat image $QB_{15}$ to Sat image $QB_{18}$ (rows 1 to 4 respectively) RGB color space. . . . .	154
C.6	Segmentation results of the satellite images Sat image $QB_{15}$ to Sat image $QB_{18}$ (rows 1 to 4 respectively) in $L^*a^*b^*$ color space. . . . .	155
C.7	Segmentation results of the satellite images Sat image $QB_{19}$ and Sat image $QB_{20}$ (rows 1 and 2 respectively) in RGB color space. . . . .	156
C.8	Segmentation results of the satellite images Sat image $QB_{19}$ and Sat image $QB_{20}$ (rows 1 and 2 respectively) in $L^*a^*b^*$ color space. . . . .	156



---

# LIST OF TABLES

---

4.1	Optimal values of combination coefficient $\eta$ , calculated individually for each model and for all values of $k$ in the $k$ -nearest neighbor algorithm, where $k \in \{1,3,5,7\}$ . . . . .	77
4.2	Average percentage classification results of 24 color textures using 2D multichannel complex NSHP AR, 2D multichannel complex QP AR model via HM method and 2D multichannel complex GMRF for all values of $k$ in the $k$ -nearest neighbor algorithm, where $k \in \{1,3,5,7\}$ . . . . .	78
4.3	Average positive predicted values of 24 color textures using 2D multichannel complex NSHP AR, 2D multichannel complex QP AR via HM method and 2D multichannel complex GMRF for all values of $k$ in the $k$ -nearest neighbor algorithm, where $k \in \{1,3,5,7\}$ . . . . .	79
4.4	Average percentage classification of 24 color textures of $DS_1$ in all the three color spaces, using 3D color histograms for all values of bin cubes $B$ , where $B \in \{4, 6, 9, 10\}$ . . . . .	80
4.5	Average percentage classification of 54 color textures of $DS_2$ in all the three color spaces, using 3D color histograms for all values of bin cubes $B$ , where $B \in \{8, 12, 16\}$ . . . . .	81
4.6	Average percentage classification of 68 color textures of $DS_3$ in all the three color spaces, using 3D color histograms for all values of bin cubes $B$ , where $B \in \{8, 12, 16\}$ . . . . .	81
4.7	Average percentage classification of $DS_1$ , $DS_2$ and $DS_3$ in the IHLS color space. . . . .	82
4.8	Average percentage classification of $DS_1$ , $DS_2$ and $DS_3$ in the L*a*b* color space. . . . .	83
4.9	Average percentage classification of $DS_1$ , $DS_2$ and $DS_3$ in the RGB color space.	84

4.10	Average percentage classification of $DS_1$ . Structure feature cues are computed through 2D multichannel QP AR model via HM method with model order (2, 2). Columns RGB, IHLS and L*a*b* show results of structure feature cues being computed in respective color spaces combined with pure color feature cues in each color space. For $\mathcal{H}_{lab}$ , $B = 9$ whereas $B = 10$ for $\mathcal{H}_{ihls}$ and $\mathcal{H}_{rgb}$ .	85
4.11	Average percentage classification of $DS_2$ . Structure feature cues are computed through 2D multichannel QP AR model via HM method with model order (2, 2). Columns RGB, IHLS and L*a*b* show results of structure feature cues being computed in respective color spaces combined with pure color feature cues in each color space. For $\mathcal{H}_{lab}$ , $\mathcal{H}_{ihls}$ and $\mathcal{H}_{rgb}$ , $B = 16$ .	85
4.12	Average percentage classification of $DS_3$ . Structure feature cues are computed through 2D multichannel QP AR model via HM method with model order (2, 2). Columns RGB, IHLS and L*a*b* show results of structure feature cues being computed in respective color spaces combined with pure color feature cues in each color space. For $\mathcal{H}_{lab}$ , $\mathcal{H}_{ihls}$ and $\mathcal{H}_{rgb}$ , $B = 16$ .	86
4.13	Comparison of best average percentage classification results for $DS_1$ with state of the art results presented in [PFJ06]. Best results are indicated in bold faces.	86
4.14	Comparison of best average percentage classification results for $DS_2$ with state of the art results presented in [MP04].	87
4.15	Comparison of best average percentage classification results for $DS_3$ with state of the art results presented in [MP04].	87
4.16	Percentage classification error for pixel classification experiments, for each class in each test color image. Average percentage error value for the 4 color textures in each color space is given in the bold faces.	90
4.17	Average PPV for pixel classification experiments, for each class in each test color image. Average percentage PPV value for the 4 color textures in each color space is given in the bold faces.	91
5.1	Average percentage pixel classification error of 10 color textures with corresponding values of $\beta$ . The parametric model of the LPE used is the classical multivariate Gaussian distribution. The best result is indicated in bold faces.	107
5.2	Average percentage pixel classification error of 10 color textures with corresponding values of $\beta$ . The parametric model of the LPE distribution used is MGMM. The best result is indicated in bold faces.	107
5.3	Average percentage pixel classification error of 10 color textures with corresponding values of $\beta$ . The parametric model of the LPE distribution used is the Wishart distribution. The best result is indicated in bold faces.	107
5.4	Average percentage pixel classification error of 10 color textures. The image observation model is 2D multichannel QP AR model. The best results are indicated in bold faces.	110

5.5	Comparative analysis of the approach with the results presented in [KP06] with respect to the percentage error. . . . .	116
5.6	Brief description of the twenty high resolution satellite images. . . . .	119
5.7	Land cover classification results in terms of classification, sensitivity and global error in RGB color space. . . . .	119
5.8	Land cover classification results in terms of classification, sensitivity and global error in L*a*b* color space. . . . .	121
5.9	Land cover classification results in terms of percentage values of pixel classification and sensitivity along with global error in RGB color space. . . . .	126
5.10	Land cover classification results in terms of classification, sensitivity and global error in L*a*b* color space. . . . .	127
5.11	Land cover classification results in terms of classification, sensitivity and global error in the RGB color space. . . . .	127
5.12	Land cover classification results in terms of classification, sensitivity and global error in the L*a*b* color space. . . . .	132



---

## LIST OF SYMBOLS

---

$\hat{S}_x^P(\nu_1, \nu_2)$	Generalized power spectral density .....	30
$\nu_1$	Normalized horizontal frequency .....	30
$\nu_2$	Normalized vertical frequency .....	30
$x$	2D image sequence .....	30
$x(n_1, n_2)$	Single observation of $x$ .....	30
$n_1$	Horizontal location of $x(n_1, n_2)$ .....	30
$n_2$	Vertical location of $x(n_1, n_2)$ .....	30
$\Lambda$	Finite 2D image lattice region .....	30
$\mathbb{Z}$	Set of integers .....	30
$N_1$	Horizontal dimension of $x$ .....	30
$N_2$	Vertical dimension of $x$ .....	30
$w(n_1, n_2)$	Window function .....	30
$\hat{\gamma}_x(f_1, f_2)$	Autocorrelation of $x(n_1, n_2)$ .....	30
$\hat{S}_x^C(\nu_1, \nu_2)$	2D correlogram of $x(n_1, n_2)$ .....	30
$m_1$	Horizontal model order for $x$ .....	31
$m_2$	Vertical model order for $x$ .....	31
$D$	Neighborhood support region .....	31
$\{a_m\}_{m \in D}$	Model coefficient vector .....	31
$e$	2D linear prediction error .....	31
$\sigma_e^2$	Variance of $e$ .....	31
$S_{e,\nu}$	Power spectral density of $e$ .....	31
$\hat{S}(\nu)$	Parametric PSD estimate of $x$ .....	31
$H(z_1, z_2)$	Transfer function of an LTI system .....	32
$\hat{S}^{AR-HM}(\nu)$	Harmonic mean of PSD estimate of $x$ .....	33
$\hat{S}^{QP_1}(\nu)$	PSD estimate of $x$ with the 1st quarter plane support .....	33
$\hat{S}^{QP_2}(\nu)$	PSD estimate of $x$ with the 2nd quarter plane support .....	33
$l_n$	Single outcome of real valued luminance channel .....	38
$c_n$	Single outcome of complex valued chrominance channel .....	38

$\mathbb{R}$	Set of real numbers	38
$\mathbb{C}$	Set of complex numbers	38
$X$	2D multichannel complex valued image sequence	38
$X_n$	Single outcome of $X$	38
$P$	Number of channels in $X$	39
$\mu$	Mean value of $X$	39
$A_m$	Complex model coefficient matrix	39
$E$	2D multichannel complex valued linear prediction error	39
$\Sigma_e$	$P \times P$ complex valued covariance matrix of $E$	39
$S_\nu$	PSD matrix of $X$	39
$S_{LL}(\nu)$	Autospectrum of luminance channel	40
$S_{CC}(\nu)$	Autospectrum of chrominance channel	40
$S_{LC}(\nu)$	Cross spectrum of luminance channel	40
$S_{CL}(\nu)$	Cross spectrum of chrominance channel	40
$S_{RR}(\nu)$	Autospectrum of red channel	40
$S_{GG}(\nu)$	Autospectrum of green channel	40
$S_{BB}(\nu)$	Autospectrum of blue channel	40
$D_{M_1, M_2}^{NSHP}$	NSHP neighborhood support region	40
$M_1$	Horizontal model order for $X$	40
$M_2$	Vertical model order for $X$	40
$\hat{S}_\nu^{NSHP}$	Estimate of PSD matrix of $X$ with NSHP support	41
$A_m^{NSHP}$	Complex matrix of NSHP AR model coefficients	41
$D_{M_1, M_2}^{QP_1}$	First quarter plane neighborhood support region	42
$D_{M_1, M_2}^{QP_2}$	Second quarter plane neighborhood support region	42
$A_m^{QP_1}$	Complex matrix of $QP_1$ AR model coefficients	42
$A_m^{QP_2}$	Complex matrix of $QP_2$ AR model coefficients	42
$\hat{S}_\nu^{QP_1}$	Estimate of PSD matrix of $X$ with $QP_1$ support	43
$\hat{S}_\nu^{QP_2}$	Estimate of PSD matrix of $X$ with $QP_2$ support	43
$\hat{S}_\nu^{QPHM}$	Estimate of PSD matrix of $X$ via HM method	43
$D_M^{GMRF}$	GMRF neighborhood support region	44
$M$	Model order for GMRF model	44
$A_m^{GMRF}$	Complex matrix of GMRF model coefficients	44
$\hat{S}_\nu^{GMRF}$	Estimate of PSD matrix of $X$ with GMRF support	44
$A_r$	Amplitude of the 2D real valued sinusoid	46
$\nu_r$	Normalized frequency set of the 2D real valued sinusoid	46
$\phi_r$	Phase angle of the 2D real valued sinusoid	46
$A_c$	Amplitude of the 2D complex valued sinusoid	46
$\nu_c$	Normalized frequency set of the 2D complex valued sinusoid	46
$\phi_c$	Phase angle of the 2D complex valued sinusoid	46
$A_{cr}$	Mean amplitude of chrominance sinusoid in luminance spectrum	62

$IR_{LC}$	Spectral interference ratio of chrominance in luminance channel	62
$A_{rc}$	Mean amplitude of luminance sinusoid in chrominance spectrum	62
$IR_{CL}$	Spectral interference ratio of luminance in chrominance channel	62
$DS_1$	Color texture data set 1	66
$DS_2$	Color texture data set 2	67
$DS_3$	Color texture data set 3	67
$B$	Number of bins in color histograms	71
$N_{ijk}$	Number of pixels in a cubical bin	71
$K_\beta(S_{1,\beta}, S_{2,\beta})$	KL divergence between two spectra	73
$\mathcal{H}$	3D color histogram	75
$KL(\mathcal{H}_1, \mathcal{H}_2)$	KL divergence between two histograms	75
$K_{LL}$	Spectral distance between two luminance spectra	75
$K_{CC}$	Spectral distance between two chrominance spectra	75
$\eta$	The combination coefficient	75
$K_{LL}$	Combined Spectral distance	75
$\hat{\omega}$	Estimated class label for a test texture sample	75
$P_k(w_i x)$	Posterior conditional probability of a class label	76
$d_k(x, x_i)$	Distance between test and training textures	76
$E_x$	Observation space containing $x$	97
$\omega$	Class label field of $x$	97
$\omega_n$	Estimated class label for the pixel at location $n$	97
$p(\omega x)$	Conditional probability of label field $\omega$ given $x$	97
$p(x \omega)$	Probability distribution defining the likelihood of $x$	97
$p(\omega)$	Prior probability of label field $\omega$	97
$p(x)$	Probability distribution of observation $x$	97
$E_c$	set of all possible class labels	97
$C$	Total number of texture classes in the image	97
$c$	Class label set for a given texture class	97
$\theta_c^{(X)}$	Model parameter set for the texture class $c$	97
$\theta^{(X)}$	Model parameter set for all the texture classes	97
$\hat{\omega}_{MAP}$	Maximum <i>a posteriori</i> estimate of $\omega$	98
$F_c$	Set of possible configurations of the label set $\omega$	98
$p(e_n \theta_c^{(X)})$	Conditional likelihood probability of the vector $e_n$	100
$\theta_M$	Texture observation model parameter set	99
$J$	$\epsilon \times d$ matrix of LPE vectors	100
$\epsilon$	Number of LPE vectors used to define the Wishart distribution	100
$d$	Size of a multichannel LPE vector	100
$G$	$d \times d$ positive semidefinite matrix	100
$\alpha_k$	Prior probability of $k^{th}$ Gaussian in an MGMM	101
$K$	Number of Gaussian components in an MGMM	101

$\mu_{k,e}$	Mean value of $k$ th component of the MGMM .....	101
$\Sigma_{k,e}$	The covariance matrix of $k$ th component of the MGMM .....	101
$\theta_k$	Model parameter set of $k$ th component of the MGMM .....	101
$\theta_K$	Complete model parameter set of the MGMM .....	101
$U_D(x, \omega)$	Energy function of the observation and label field .....	103
$U_i(\omega)$	Energy function of the label field .....	103
$U_x(\omega)$	Sum of the two energy functions .....	103
$U_{i,1}(\omega)$	Energy function related to Gibbs energy .....	103
$U_{i,2}(\omega)$	Energy function related to the region size .....	103
$\beta$	Hyperparameter of the Potts model .....	104
$R$	Single connected region with same class label .....	104
$A$	Size of the connected region $R$ .....	104
$p(A)$	Probability for region $R$ to form .....	104
$\gamma$	Segmentation scale control parameter .....	104
$\phi$	Region size control parameter .....	104
$n_R$	Total number of regions .....	104

---

## LIST OF ABBREVIATIONS

---

NSHP AR	Non-symmetric half plane autoregressive	4
QP AR	Quarter plane autoregressive	4
GMRF	Gauss Markov random field	4
LBP	Local binary patterns	9
PDF	Probability distribution function	11
DFT	Discrete Fourier transform	14
DCT	Discrete cosine transform	14
STFT	Short-Term Fourier transform	14
CBIR	content based image retrieval	16
QPCA	Quaternion principal component analysis	17
QS	Quaternion S transform	17
QFT	Quaternion Fourier transform	17
AR	Autoregressive	18
MRF	Markov random field	18
MMRF	Multispectral Markov random field	18
PMRF	Pseudo-Markov random field	18
LS	Least squares	18
MSAR	Multispectral simultaneous autoregressive	18
GMM	Gaussian mixture model	20
SAR	Simultaneous autoregressive	20
CMM	Conditional Markov model	20
ML	Maximum likelihood	20
CAR	3D simultaneous causal autoregressive	20
EM	Expectation maximization	22
TFR	Texture fragmentation and reconstruction	22
SVM	Support vector machine	24
CCM	Color isotropic co-occurrence matrix	24
MLDT	Multi-spectral local differences texem	25
PSD	Power spectral density	30

FFT	Fast Fourier transform	30
ACF	Autocorrelation function	30
MLE	Maximum likelihood estimation	32
HM	Harmonic mean	33
SNR	Signal to noise ratio	46
LSE	Least squares estimation	49
KL	Kullback-Leibler	72
PPV	Positive predictive value	77
LPE	Linear prediction error	97
MAP	Maximum <i>a posteriori</i>	103
ICM	Iterative condition mode	106
MGMM	Multivariate Gaussian mixture model	111

---

---

# CONTENTS

---

<b>1</b>	<b>Introduction</b>	<b>1</b>
1.1	Problem Statement and Motivation . . . . .	1
1.2	Research Objectives . . . . .	2
1.3	Contributions and Overview of the Thesis . . . . .	3
1.4	Thesis Organization . . . . .	4
<b>2</b>	<b>Literature Survey</b>	<b>7</b>
2.1	Color Texture Descriptors . . . . .	7
2.1.1	Structural Descriptors . . . . .	8
2.1.2	Statistical Descriptors . . . . .	9
2.1.3	Transform based Descriptors . . . . .	14
2.1.4	Model based Descriptors . . . . .	17
2.2	Color Space Comparison . . . . .	22
2.3	Texture in Satellite Images . . . . .	25
2.4	Conclusion . . . . .	26
<b>3</b>	<b>Color Spectral Analysis</b>	<b>29</b>
3.1	2D Spectral Analysis . . . . .	29
3.1.1	Non-Parametric Spectral Estimates . . . . .	30
3.1.2	Parametric Spectral Estimates . . . . .	31
3.2	Two Channel Complex Color Image . . . . .	34
3.2.1	The Candidate Color Spaces . . . . .	34
3.2.2	Complex Color Image . . . . .	38
3.3	Complex Vectorial Color Spectral Analysis . . . . .	38
3.3.1	Causal Models . . . . .	40
3.3.2	Non-Causal Models . . . . .	44
3.4	Experiments and Results . . . . .	45
3.4.1	Sinusoidal Data - The Chroma Sinusoids . . . . .	45

3.4.2	Spectral Estimator Performance Analysis . . . . .	48
3.4.3	Color Space Comparison . . . . .	59
3.5	Conclusion . . . . .	64
<b>4</b>	<b>Color Texture Classification</b>	<b>65</b>
4.1	Color Texture Databases . . . . .	66
4.1.1	Data Set 1 . . . . .	66
4.1.2	Data Set 2 . . . . .	67
4.1.3	Data Set 3 . . . . .	67
4.2	Image Feature Cues . . . . .	68
4.2.1	Spatial Structure Cues . . . . .	68
4.2.2	Color Feature Cue . . . . .	69
4.3	Similarity Measures and Cue Fusion . . . . .	72
4.3.1	Distance Measures . . . . .	72
4.3.2	Multiple Cue Fusion . . . . .	75
4.4	Experiments and Results . . . . .	76
4.4.1	Choice of a Pertinent Model . . . . .	76
4.4.2	Choice of a Pertinent Color Space . . . . .	79
4.4.3	Comparative Analysis . . . . .	86
4.4.4	Pixel Classification . . . . .	88
4.5	Conclusion . . . . .	91
<b>5</b>	<b>Color Texture Segmentation</b>	<b>95</b>
5.1	Model Based Texture Segmentation . . . . .	96
5.2	Multichannel Texture Segmentation Model . . . . .	98
5.2.1	Image Observation Model . . . . .	98
5.2.2	Multivariate Gaussian probability distribution . . . . .	99
5.2.3	Wishart distribution . . . . .	100
5.2.4	Multivariate Gaussian Mixture Model . . . . .	101
5.2.5	Label Field Estimation . . . . .	103
5.3	Synthetic Color Textures . . . . .	104
5.3.1	Classical Potts Model . . . . .	106
5.3.2	Region Size Penalty . . . . .	109
5.3.3	Comparative Analysis . . . . .	111
5.4	High Resolution Satellite Images . . . . .	115
5.4.1	The Fusion Approach . . . . .	117
5.4.2	Effects of Varying Region Parameters . . . . .	123
5.5	Conclusion . . . . .	129

<b>6 Discussion</b>	<b>137</b>
6.1 Conclusion . . . . .	137
6.2 Perspectives . . . . .	140
<b>A Color space Transformations</b>	<b>145</b>
<b>B Performance Measures</b>	<b>147</b>
<b>C Segmentation Results</b>	<b>149</b>
<b>Bibliography</b>	<b>157</b>



---

# CHAPTER 1

---

## INTRODUCTION

---

The main objective of this chapter is to introduce the motivation for the investigation of a new color texture descriptor that can be used for the color texture characterization tasks, including color texture classification and/or segmentation. The major objective of this thesis along with the main contributions that emerged from this research study will be discussed. Finally a brief outline of the thesis organization will be presented.

### **1.1 Problem Statement and Motivation**

Color texture characterization is one of the most important areas of research in the fields of image processing and pattern analysis and/or recognition. This is motivated by the fact that the texture is an attribute of a color image that is commonly exploited in the high-level image analysis tasks such as scene understanding, image or video retrieval and image segmentation. The approximation and estimation accuracy of the texture descriptor has a decisive impact on the overall performance of the developed vision system. Over the past few decades the field of color texture analysis has developed extensively. Due to the improvements and advances in the computer and photographic technologies, the research community is capable of addressing real life problems including natural image understanding, video and satellite image processing.

The pertinence of texture attribute for natural as well as satellite image analysis is evident. In the former case, they are required to discern between objects or the regions appearing in the image whereas in the later case, it is of importance to discriminate between cultivated regions, barren lands, forests or man-made struc-

tures. Researchers have proposed, presented and validated a large spectrum of mathematical models and algorithms to exploit the local and global properties of this essential image attribute.

A widely acceptable mathematical definition of the texture of a given color image is still not known to the researchers worldwide. However, it can be referred to as, a function of the spatial structure variation of the pixel values *i.e.* color or intensity values of the image. Therefore some rough categorization can be defined for the texture content of the image including, coarse, fine, smooth, granulated etc. For the texture content of an image, it is generally perceived that small texture pattern units are periodic in a given image *i.e.* they appear in the image periodically. Therefore, the aim of understanding the color texture of a given image is to comprehend and develop the capability to model and estimate the spatial structure variations of the image.

Although texture analysis in color images is one of the fundamental areas of the research for many years now, it still represents a challenging topic for the image processing and computer vision community. This difficulty arises from the fact that the real world images often exhibit a high degree of complexity, randomness and irregularity.

It is evident that the comprehensive mathematical understanding and model based description of the texture content for the classification or segmentation of color images leads to an improved and robust performance of computer vision systems as compared to the algorithms and methods which are developed for particular applications. Exploitation of the pure color information of the image is also very important while developing and proposing a robust, comprehensive and composite color texture descriptor for natural as well as high resolution satellite images, given the complex nature of the problem as stated before. Thus, the development of a comprehensive and non-application specific texture descriptor for color images and its utilization in the complex applications of texture classification and segmentation for both color and high resolution satellite images is addressed in this research study.

## 1.2 Research Objectives

The core aim of this research study is to propose and develop a practical framework based on theoretical basis for the computation of a model based comprehensive and robust color texture descriptor that can be used for the color texture characterization in both color and multispectral aerial images. As indicated earlier color texture analysis is an active topic of research and many existing approaches, methods and algorithms have addressed this problem in a simplistic manner, most of which consider and process color and texture as independent attributes (cf.

Chapter 2). Often, these approaches consider the texture of a color image to be limited to the luminance plane only and hence lack the characterization of the spatial structure information of the chromatic plane of the image, which certainly limits their performance.

Comprehensive description of the texture content of a given color image is a complicated task which has to take into account the luminance as well as the chrominance spatial structural variations along with the pure color distribution information of the said image. Choice of a particular color space for color image representation also affects the performance of the application. These challenges lead us to the definition of the following major objectives of this research study:

- To develop a model based generic color texture descriptor capable of describing the spatial structure of color and high resolution satellite images.
- To develop a new color texture classification framework based on this color texture descriptor.
- To develop a novel color texture segmentation algorithm based on the Bayesian segmentation exploiting the same color texture descriptor for color as well as satellite images.
- To study and compare different color spaces and their performance for the proposed color texture classification and segmentation frameworks and for the choice of the most pertinent color space for the task.
- To conduct a large number of experiments to produce quantitative and qualitative results when these algorithms are applied to the standard databases of color textures. Also the proposed algorithms will have to be benchmarked against state of the art approaches for color texture characterization.

### 1.3 Contributions and Overview of the Thesis

The major objectives stated in the previous section generated the major and minor contributions of this research study. One of the major contribution of this thesis is the development of a composite two dimensional multichannel complex image observation model. This generic color image observation model is based on the proposed luminance and combined chrominance channel complex color image for perceptual color spaces.

Main novelty and another originality of this work resides in the exploitation of this image observation model to develop a concurrent parametric spectral estimation framework for both luminance and combined chrominance channels of the above stated two channel complex color image. The auto and cross spectra

of these two channels characterize the spatial structure information of both these channels. This 2D multichannel spectrum estimation through 2D multichannel complex random fields lead us to the development of a model based approach for color texture characterization and classification in perceptual color spaces. For this, multichannel complex versions of linear prediction models including two dimensional (2D) Non-Symmetric Half Plane Autoregressive (*NSHP AR*) model, 2D Quarter Plane Autoregressive (*QP AR*) model and Gauss Markov Random Field (*GMRF*) model are derived and used to model the multichannel complex image.

A quantitative criterion for the comparison and performance evaluation of different color spaces is also an important contribution of this thesis. This criterion exploits inter-plane decorrelation of the color images to choose the best performing color space. For perceptual color spaces, this comparison is based on the degree of decorrelation between luminance and chrominance information provided by different color space transformations.

During the course of this thesis, a novel Bayesian framework of color texture segmentation has also been developed. This framework exploits the various parametric approximations for multichannel complex linear prediction error. These parametric approximations are used to improve the performance of the color texture segmentation algorithms. The linear prediction error of the proposed texture models is classically approximated with Multivariate Gaussian probability distribution. We present two other parametric models using multivariate Gaussian mixture models and Wishart distribution.

## 1.4 Thesis Organization

The organization of this thesis is a systematic and logical extension of the previous section.

Chapter 2 reviews the existing approaches related to the color texture analysis. It gives a brief overview of the main descriptors proposed in the recent years to characterize color textures. In this chapter we would emphasize on model based descriptors. A review of the research works done on color space comparison for color texture description along with the texture segmentation in the high resolution satellite images is also discussed.

Then in the chapter 3, the mathematical basis of the parametric color spectral analysis approach developed is detailed. The proposed two channel complex color image representation and the derived multichannel complex and/or real valued linear prediction models employed for the parametric color spectral estimation are also discussed. Performance analysis of this color spectral analysis is presented at the end of the chapter.

Chapter 4 discusses the color texture classification framework developed on the basis of the parametric color spectral analysis developed and presented in the chapter 3. Spatial structure and pure color feature cues computation along with their probabilistic fusion for color texture classification is illustrated. The framework is analyzed in detail on various standard color texture databases. Experimental results and comparison to state of the art color texture classification methods is presented.

In chapter 5, the multichannel linear prediction models developed in chapter 3 are used to sketch a model based color texture segmentation scheme for synthetic as well as high resolution textured satellite images. This scheme involves different parametric approximations for the distribution of multichannel linear prediction error including MGMM and the Wishart distribution. The experimental results are presented, analyzed and discussed. A comparative analysis with a state of the art model based approach is also presented. Results on different high resolution multispectral satellite images show the pertinence of the scheme for the land cover classification through satellite image segmentation.

Finally, chapter 6 discusses the main conclusions drawn at the end of this thesis. It also highlights a few perspectives for the follow up of this research work.



---

## CHAPTER 2

---

# LITERATURE SURVEY

---

The core objective of this chapter is to present the research background of color texture analysis. An overview of the concerned state of the art approaches in the domain will be presented. Pros and cons of using different proposed color texture descriptors for classification and/or segmentation will be overviewed along with a detailed discussion on the model based parametric approaches presented so far for this purpose. A brief discussion on the different research works presented on the color space comparison for color texture analysis is also a part of this chapter. Finally, various existing approaches for the classification and segmentation of multispectral satellite images are overviewed.

### 2.1 Color Texture Descriptors

Robust identification of texture content and primitives in both gray level and colored digital images plays a very key role in various image processing applications. This applications spread over the various domains of computer vision and pattern recognition including, object recognition, scene classification, segmentation, remote sensing and biomedical image analysis. This pertinence of the texture descriptors has motivated the development of numerous color texture descriptors in recent years. Each of these descriptors exploit any one or different mathematical properties of spatial variations in an image and hence proposes a more or less different working framework from the other.

These color texture descriptors can be roughly divided into two categories [MP04]:

- Methods which process color and texture information separately. These methods assume that the spatial structure variations and color distribution of the image are independent feature cues. Either of these two feature cues independently or their fusion can better characterize color textures for a specific application. Examples of such methods are presented in [PFJ06] and [KP06].
- Methods which consider color and texture a joint phenomenon. These methods mostly use the multichannel versions of gray level texture descriptors. In these methods, normally no separate color feature is used. Example of such methods is presented in [Pas98].

Various literature surveys have presented the categorization of these texture attributes [CPW98, MS98]. The four main categories of texture characterization methods presented in these reviews are :

- Structural
- Statistical
- Transform based
- Model based

It is to note that the boundaries of the categories are not very distinct and a given method can lie in more than one of these categories. Most of the descriptors and methods address the gray level texture analysis. However, logical extensions of these methods for color images are either developed or can be conceived. We will discuss each of these four categories one by one with a focal interest on color texture description.

### **2.1.1 Structural Descriptors**

Structural approaches like [Har79] represent textures as microtextures and macrotextures. Microtextures are the well defined primitives and macrotextures are the hierarchy of spatial arrangements of those primitives. According to [Har79], the choice of a microtexture and the probability of the chosen microtexture to be placed at a particular location can be a function of location or the microtextures near the location. A good symbolic description of the image is a considerable advantage of this approach which is useful for the analysis of synthetic textures. Another approach based on the same idea for mathematical morphology in images is presented in [Ser83]. The main disadvantage of the approach lies in the

poor discrimination of the microtextures and macrotextures in the case of the natural textures. This concept of the texture description is more useful for texture synthesis rather than texture characterization.

In [JCR05], the authors proposed an image segmentation algorithm that is based on spatially-adaptive texture features. The authors developed two types of features: one describes the local color composition and the second exploits the spatial characteristics of the gray scale component of the texture. The algorithm first develops these features independently and then separates the image into smooth and textured areas using the spatial texture features. It then combines the color composition and spatial texture features to consolidate textured areas into regions. The color texture features are combined using a region growing algorithm which results in a coarse label set of the segmented image. This image is then post-processed using a border refinement procedure.

In [dLGDAL08], the authors worked out a novel segmentation scheme for textured gray-level and color images based on the combined use of the local structure tensor and the original image components. A combined segmentation approach has been proposed that combines both elements within a common energy minimization framework. Afterwards, a method is proposed to dynamically adapt the relative weight of these two distinct information.

Another family of such texture descriptors, is based on the analysis of spatial variations in spatial domain of the images. The descriptors based on the spatial variation information, exploit the transitions per unit surface area in the given image to characterize the texture content of the image [CPW98]. Fine textures tend to have a strong density of the transitions per unit surface area as compared to the coarse textures. These descriptors are best suited and have been used for the color texture segmentation problem. One such method is suggested in [DZ86]. The author has presented the use of tensor gradient of multichannel images regarded as vector fields. In this work author explains the method for characterizing the edge information of the multichannel images which is another indirect method to study the spatial variations *i.e.* textural content of the image.

### 2.1.2 Statistical Descriptors

Statistical approaches are the ones which exploit the image statistics of any order to represent the textures. These attributes are based on the relation between the pixel intensity and/or color values and their distributions. Hence they base the description of the texture content of the image on a non-deterministic description. The histograms, autocorrelation function, local binary patterns (*LBP*), energy features and different statistical features computed from chromatic co-occurrence matrices are the salient texture descriptors from this category.

The approaches based on the statistics of different order are the ones which use mean, variance, skewness, kurtosis and histograms of the image to characterize the underlying textures in the image. One of such approach is presented in [LMVMPF08]. In this work, authors have presented *soft color texture descriptors* method. The authors have used several statistical measures of the color images to characterize the color texture content of the images. The set of factors includes the number of neighbors in the k-NN classifier (several values of k parameter), color space representation schemes (CIE Lab, CIE Luv, RGB, and gray scale), and color texture features. The utility of different combinations of all of these factors is evaluated in this work.

The histogram of an image gives an estimation of the probability distribution of the image pixels values. Therefore, as a mathematical model it does not characterize the spatial structure information of the image yet it can be useful as a pure color descriptor, to discriminate a texture sample from another based on its specific global probability distribution of pixel color values. For color images, two different types of histograms can be computed. These include a combination of three mono dimensional histograms for three color planes and three dimensional (*3D*) color histograms in which bins are formed in a cubical shape in the 3D color space gamut. In [MTJ02] and [MP04] the authors showed the pertinence of using both these attributes as pure color feature cues for the problem of color texture classification. Another work based on these attributes for color texture classification is given in [VMP03]. In this work authors used median, mode and the dispersion characteristics of these histograms as the feature attributes. Histograms are also used as a color feature attribute for color texture classification in [PP03]. He proposed to concatenate the mono dimensional color histograms and then these bins are combined on one to one basis and resulting ratios are used for the color texture classification.

As stated earlier, histograms are just a descriptor of the probability distribution of the image pixel intensity and/or color values and does not give information about the underlying spatial structure information of the texture. Therefore, certain statistical attributes based on the higher order statistics are used to complement this short coming of the histogram attributes.

One of these attributes is the auto correlation function [CPW98]. The texture characterization techniques based on this attribute estimate the rate of decay of the auto correlation function with increasing spatial shift with respect to origin of the image to be analyzed. It is evident from the stated methodology that the coarse textures *i.e.* the textures with high degree of complexity would show a slow variational increase in the said function [CPW98]. The technique performs much better than other techniques in terms of computational cost. However there

is a risk of its inability to model the detailed local spatial structures of the image as the technique exploits the global structural characteristics of the image.

In [AZ07], the authors have proposed an approach which combines the region and boundary information. This approach uses active contours to build a partition of the image. The region information is based on mixture modeling of the combined color and texture features, while the boundary information is modeled using the polarity information. They use a combination of color and texture features to calculate a mixture of the probability distribution functions (*PDF*), that models the distribution of these features. For texture, they use features calculated from the correlogram of the pixel neighborhood. They compute four typical features, including energy, entropy, inverse-difference-moment and correlation. Then they average each feature over the number of orientations and displacements. To model the distribution of these features, they use a mixture of generalized Gaussian distributions.

Another important statistical texture descriptor is co-occurrence matrices. The basic idea was introduced by Haralick in [HSD73], to use these matrices for texture characterization for the gray level images. The work described some easily computable textural features based on gray-tone spatial dependencies, and illustrated their application in category-identification tasks of three different kinds of image data. The results from this study and later related works indicated that these textural features have a general applicability for a wide variety of image-classification applications.

The concept of co-occurrence matrices for color texture classification was first introduced in [Pal04]. In this work, integrative co-occurrence matrices are introduced as novel features for color texture characterization. The extended co-occurrence notation allows the comparison between integrative and parallel color texture concepts to be carried out. The parallel concept for color texture analysis separates the processing of both color and texture while in integrative concept, the information dependency between both image features is taken into account. The method is applied to the RGB and the LUV color spaces in which the combined color and intensity textures are studied and the existence of intensity independent pure color patterns is demonstrated.

In recent years, several works based on co-occurrence matrices for color texture characterization have been proposed. One such work is presented in [FAA00]. The authors have used these matrices for the classification of weed species. This work used the color co-occurrence matrices to determine whether traditional statistical discriminant analysis can be used to discriminate between different classes of weed.

In another work [AML08], the authors used these matrices for characterizing the color textures in industrial products. A new extension of gray level co-

occurrence matrix to color images is proposed in this work. The authors proposed a methodology in which statistical features are computed from an isotropic color co-occurrence matrix for classification.

In [ADB04], three different approaches to color texture analysis are tested on the classification of images from the different color texture databases. The authors present a multispectral extension since co-occurrence matrices are computed both between and within the color bands. They also present a joint color-texture feature, in which color features are added to gray scale texture features in the entry of the classifier.

Another recent color texture analysis work based on color co-occurrence matrices is presented in [MALDTB05]. The method presented in this work, used for the recognition of textures is based on the sum and difference histograms and is a faster version of the co-occurrence matrices. This work uses an LVQ neural network for the clustering and classification of marble slabs according to their texture information characterized by the co-occurrence matrices. An LVQ network is a method for training competitive layers in a supervised manner. It consists of two weight layers. The first layer is a competitive layer, which learns to classify input vectors forming subclasses, and the second layer transforms the competitive layer's subclasses into target classifications defined by the user. Another work based on the sum and difference histograms is presented in [MVK<sup>+</sup>02]. In this work authors compute intra- and inter-plane second order features to capture the co-occurrences between the color bands. A powerful set of features is obtained by non-linear color space conversion to HSV color space and thresholding operation to eliminate the influence of sensor noise on color information.

These co-occurrence matrices perform better than the autocorrelation function in general. This is motivated by the fact that co-occurrence matrices exploit the local relationship between the pixels whereas, autocorrelation function tends to estimate the global structure of the image. There are a number of approaches for color texture analysis which use several Haralick features [HSD73] calculated from these matrices instead of directly using these matrices. Authors in [PVM08b] have presented the same idea. They propose to study the influence of the neighborhood used to process the color co-occurrence matrices on the quality of texture analysis. They measure the discriminating power of each Haralick feature computed with one of the color co-occurrence matrices of the color images. They compare the 28 considered color spaces and select the most discriminating ones on the basis of this discriminating power.

The texture analysis related to the co-occurrence matrices is proved to be an effective technique, especially for discriminating various data sets of natural and synthetic textures. However, there are two main disadvantages of this approach. First, the idea is based on an assumption that the textural patterns are repetitive

and are uniformly distributed in the image. Secondly, these are computationally expensive and require higher memory and computational resources than other statistical texture features.

Another important texture descriptor frequently used to characterize the spatial variations of images in recent research works is LBP. Initially LBP were proposed for scalar *i.e.* gray level images in [OPH96]. Logical extensions of these attributes for color texture characterization were developed and used in [MP04] and [PMV02]. LBP are highly discriminative texture descriptors. Their main advantage is the invariance to any monotonic change in the gray level or color and their computational simplicity [OPM02b].

The LBP are gray scale invariant texture primitive statistic. For each pixel in an image, a binary code is produced by thresholding a circularly symmetric neighborhood with the value of the center pixel. A histogram is created to collect up the occurrences of different binary patterns. The basic version of the LBP operator considers only the eight-neighbors of a pixel, but the definition can be extended to include all circular neighborhoods with any number of pixels. By extending the neighborhood one can collect larger-scale texture primitives but the computational complexity increases significantly. However, the spatial support of the LBP operator is much smaller than that of the Gabor filters (cf. section 2.1.3). The variations of the LBP operator are denoted by  $LBP_{P,R}$ , where  $P$  is the number of the neighboring pixels and  $R$  is the radius of the circular neighborhood region.

In [PMV02], the authors used histograms of LBP patterns for texture description. For classification with LBP distributions, a log-likelihood dissimilarity measure was chosen in this work. Simple variations of the basic LBP operator were also used. Instead of the traditional  $3 \times 3$  rectangular neighborhood, the authors sampled the neighborhood circularly with two different radii (1 and 3), produced a histogram out of the result of both of these operators, and concatenated the histograms. The resulting operators are denoted by  $LBP_{(8,1)}$  and  $LBP_{(8,1+8,3)}$ , where the subscripts tell the number of samples and the neighborhood radii [PMV02] and [OPH96].

In [PVM08a], the authors have presented an approach for color texture classification by use of Haralick features extracted from co-occurrence matrices computed from LBP images. They again used 28 different color spaces and computed the most discriminating ones through an iterative procedure.

In this work authors also proposed a simple joint color texture LBP operator. In the case of an RGB image, the local threshold (neighborhood center) is taken from three different color channels. The neighborhood to be thresholded is also taken from three channels, which makes up a total of nine different combinations. The histograms were concatenated into a single distribution containing  $256 \times$

9 = 2304 bins. This joint operator contains unichrome features computed within spectral bands and opponent color features combining information across bands [PMV02].

### 2.1.3 Transform based Descriptors

Texture information of an image can also be analyzed in the frequency domain. Frequency domain texture attributes are often based on two very important transforms i.e. Discrete Fourier Transform (*DFT*) and Discrete Cosine Transform (*DCT*). Different filter banks (multiple filters) tuned to particular frequencies are used to characterize the color textures. To interpret the intra-component information, all of these filters are applied to each component of a multi-component image. Once we have filtered the image, different statistical measures can be computed over these filtered images to characterize the color textures. Therefore we obtain several attributes for each of these filters. In [DW01] a similar method based on DCT to characterize color textures is presented. In this work different filter masks, each tuned to extract different information from the image are applied. The authors used DCT on gray level images and its extension on color images to characterize the color textures. They have also compared the performance of these attributes to the other gray level and color texture attributes.

Another important work based on these transforms to analyze color textures for the problem of color texture classification is presented in [PFJ06]. For the structure features the authors used different kind of features in this work including energies of DCT regions. They computed the energies of DCT coefficients in regions of frequency space corresponding to a wavelet decomposition.

DFT and DCT are well adapted and suited to characterize the coarse textures which show continuities between the pixel values of color images. For low frequency variations of the color images, these transforms are efficient whereas for high frequency variations these transforms do not give us much information. The color texture descriptors computed from these transforms perform better than the ones computed on the gray level information of the color images and the computational complexity required to compute these descriptors is moderate.

Besides the methods exploiting spatial characteristics in either one of the spatial or spectral domain, there exist certain approaches which combine both these information to characterize the color textures. The descriptors of this group which are mostly used are the ones computed from Gabor transform and Wavelet transform.

Fourier transform translates the information about the regular and periodic variations of the spatial domain in spectral domain very well, yet it suffers from a significant problem. It is incapable of providing the information about the spatial location of these variations. The problem can be addressed using different variants

of the Fourier transform like Short-Term Fourier transform (*STFT*), a Fourier-related transform used to determine the sinusoidal frequency and phase content of local sections of an image along the spatial axis. In this case, the choice of the windowing functions and their size can create problems. This analysis also has the tendency to suffer from the artifacts at the boundaries of the windows. In order to avoid these artifacts, overlapping window functions are used. Different windowing functions are used to analyze the image spectrum including Hamming, Hanning and Gaussian window functions. The Gabor transform is a special case of the STFT when the windowing function used is a Gaussian function.

In [PKLS00], an idea for the characterization of color textures using these Gabor filters is proposed. The authors proposed that the interpretation of hue and saturation as polar coordinates allows direct use of the HSV color space for Gabor feature extraction of color textures. An extension to this work using the basic concept of complex chromatic Fourier transforms was presented when Gabor filters are again used for the color texture characterization in [PL02]. The authors proposed a Gabor texture descriptor for the gray scale as well as the color domain. This descriptor relies on local phase changes characterizing the homogeneity of a texture in the spatial frequency domain. The authors presented two Gabor filter bank variants, Gabor wavelet and Gabor log-polar filter banks in this work. According to the comparison of these variants, statistically, the differences do not establish a trend towards one of the filter banks.

Another work based on the Gabor wavelets for the color texture characterization is presented in [LTR99]. The method comprises of a low-level Gabor wavelets-based feature extraction algorithm and a high-level neural network-based pattern recognition algorithm. In [HGS05], the authors proposed a framework for the local measurement of texture in wavelength-Fourier space. They propose to measure the spatial frequency by sampling the image with a shifted Gaussian window function in the spatial frequency domain, and measure color by sampling the signal with a Gaussian approximation in the wavelength domain. Therefore, color texture measurement implies the sampling with a 3D Gaussian window in a wavelength-Fourier space. This provides the basis for the integration of the Gabor texture measurement with opponent color measurement.

Gabor filters and their variants are the most widely used color texture descriptors specially for the color texture classification problems. This acceptance of the method is because of its efficiency and near optimal results in the description of the spatial variations. The main disadvantage of using this technique is the choice of different filter parameters. This makes the descriptor less robust and hence needs to be regulated before each experiment. For optimal results through these descriptors one needs to have a larger window size which can increase the computational complexity significantly.

Gabor filter descriptors are based on fixed sized window functions which proves to be a disadvantage in the case of color textures which present themselves on different scales. To resolve this problem, Wavelet transform is used which characterizes the image with an analysis on different scales. This analysis is carried out with the window functions of varying sizes.

Wavelet color texture descriptors compute different classical color texture descriptors in the transform domain. These descriptors include features like wavelet statistical features and wavelet co-occurrence features. In [WSLD99], authors presented an extension of gray level wavelet techniques to color images. They introduced wavelet energy-correlation signatures and derived the transformation of these signatures upon linear color space transformations. Experiments reported in [WSLD99] are conducted on a set of 30 natural colored texture images in which color and gray level texture classification performances are compared. The authors prove that the wavelet correlation features contain more information than the intensity or the energy features of each color plane separately. Another work based on a similar approach is presented in [Sen08]. This work investigates the usage of wavelet transform and adaptive neuro-fuzzy inference system for color texture classification problem. The proposed scheme composed of a wavelet domain feature extractor and an adaptive neuro-fuzzy inference system classifier. The color texture descriptors consist of entropy and energy features computed in wavelet domain.

Content based image retrieval (*CBIR*) is another major area of application for color texture descriptors. In [PP06], the authors have studied wavelet based color texture features for the same problem. The authors in this work, describe an algorithm for texture feature extraction using wavelet decomposed coefficients of an image and its complement. Different approaches to color texture analysis are presented. The first one is a multispectral approach, in which texture features are extracted from each channel of the RGB color space. The second method uses HSV and YCbCr color spaces in which texture features are extracted from the luminance channel and color features from the chromaticity channels. The last one uses gray scale texture features computed for a color image. Another important work of this family is presented in [IMK<sup>+</sup>04]. The authors proposed to exploit the spectral information of the three color channels forming the endoscopic frames for the description of the colonic mucosa. The suitability of different color models for this application is also investigated in this work. The textural properties of the colonic mucosal surface are measured using second order statistical descriptors on the wavelet transform of the multichannel video signals.

Like in the case of other transform based color texture descriptors, the color texture descriptors based on wavelet transform are also well adapted and suited to characterize the coarse textures. The main advantage of these descriptors lie

in the successful description of color textures on different scales. However, the results obtained for different applications for example color texture classification [IMK<sup>+</sup>04], through these descriptors are not optimal.

An emerging domain of research is the representation of color images through hypercomplex numbers or Quaternions [ES00], [SE01], [ES07]. In one of these works [DCFM07], authors discuss the various theoretical and practical conditions on the spectrum coefficients needed to reconstruct a color image without loss of information through the inverse quaternionic Fourier transform process. The result is used to interpret the quaternionic spectrum coefficients of this specific color Fourier transform. The authors used these results to apply for the spatial filtering problem in color images, yet this color spectral analysis form the basis to study the spatial variations *i.e.* the texture in an image.

In recent years some interesting works over the color texture characterization problem, based on this approach are presented. In [SF07], the problem of color texture segmentation is addressed with quaternionic point of view. the authors propose a quaternion principal component analysis (*QPCA*) framework. A low dimensional basis for the color textures found in a given image is derived via *QPCA* of a training color texture. This color texture sample is then projected onto this basis to obtain a concise description of the texture.

In another work [AMT<sup>+</sup>09], the authors propose a joint space-wavenumber localized quaternion S transform (*QS*) for a simultaneous determination of the local color image spectra. This transform is expressed as a convolution of the circularly symmetric Gaussian window and the product of the image with the kernel of the quaternion Fourier transform (*QFT*) . The invertible and rotation invariant *QS* transform allows local analysis of all color components simultaneously, as compared to separate analysis of color components.

#### 2.1.4 Model based Descriptors

Model based texture and/or color texture descriptors are the ones which tend to model the probability distributions of the spatial information of the intensity or color values [HS80]. For gray level images, spatial interaction models characterize statistical dependence by representing the intensity at each pixel as a combination of neighboring intensities and additive noise. For a given pixel, neighboring pixels are defined by a finite neighbor set. If this finite neighborhood is defined in such a manner that it only consists of the previous pixel values following a particular order of the pixels (e.g. lexicographical order), the model obtained will be causal. Non-causal models which allow more general neighbor sets are supposed to be more powerful for the modeling of images [PH95].

A model used for representing color textures should take into account not only the spatial interaction within each of the three color planes, but also the interac-

tion between different color planes. Thus, for color images each component of the color vector at a given pixel location will be represented as a linear combination of the color components of the neighbors and additive noise. This can be achieved by selecting a neighborhood structure that models both within-plane and across-plane interactions. For example, the neighbor set defining spatial interaction of a red measurement can be approximated with the red color components of the neighborhood while another set defining its interaction with the green color components of its neighbors could also be defined [PH95].

In the family of random field models, Markov Random Field (*MRF*) models and Autoregressive (*AR*) models are often employed for texture analysis, both for texture classification and segmentation problems. In the following we will discuss the salient works presented on color texture analysis based on these two types of models.

MRF models have been extensively used for characterizing the textures in gray level images in the past years [CJ83], [CC85], [CFP91]. In these and many other such works, these models have been successfully used to model the texture content of the single channel intensity images for classification, segmentation and retrieval problems.

In [PH95], the authors used MRF models for the problem of unsupervised color texture segmentation. They illustrated an unsupervised segmentation algorithm which uses Gaussian MRF models for color texture description. These models are defined in each color plane with interactions between different color planes. The model parameters are estimated through ML estimation and the segmentation algorithm consists of two steps. The first step of the algorithm splits the image into the square regions until a uniformity criterion is upheld. This step is followed by a step of agglomerative hierarchical clustering which merges the regions with similar characteristics in order to form the texture boundaries. At each step of merging phase, the conditional likelihood of the image is maximized.

In [KBH06] the authors have also used two multispectral versions of MRF models to characterize the color textures in RGB color space which were initially proposed in [BK98] and [BK99]. These include Multispectral Markov random field (*MMRF*) model, Pseudo-Markov random field (*PMRF*) model and multispectral AR models *i.e.* Multispectral simultaneous autoregressive (*MSAR*) model. A multispectral image may be considered Markovian with respect to its neighbor set if the conditional probability of an observation (pixel) given all other observations is equal to the conditional probability of that observation given the probability of a finite neighborhood observations. Model parameters for MMRF are computed through a non-linear iterative approach of least squares (*LS*) estimate. The last model discussed in this work is PMRF, which is same in structure as MMRF. However, the parameters in the case of MSAR and PMRF models are

estimated through a linear solution of LS estimate by restricting the correlation structure of the stationary noise sequences in the case of PMRF model.

After the estimation of model parameters, the authors have defined the features for color textures on the estimated parameters of the considered multispectral model. The estimated parameters on each individual channel are used directly whereas ratios of the inter-channel parameters of different color planes are utilized to make the features robust to illumination changes. The experimental results presented in [KBH06] demonstrate clearly the interest of using these models for the problem of supervised color texture classification. These models capture both inter-plane and intra-plane interactions of image pixels resulting in richer characterization of the image compared to their gray level counterparts [KC83] and [MJ92].

In [KPQ03], the authors have proposed a multi-layer MRF model to characterize and segment the color texture information in the color images. They propose a new approach to texture characterization which aims at combining color and texture features. They use different features at different layers which allows the parameters of different models to be estimated and later on choosing the one model which best describes the given feature data at a given layer. In addition, they propose a special layer, called combined layer, which does not correspond to any feature but provides a way to combine different features. Herein, to describe texture content of the color texture images, on the texture layer, the observation consists of a set of Gabor and multispectral versions of AR image features.

In [HM04], an unsupervised multispectral texture segmentation method is presented. Single decorrelated texture factors in each color plane are assumed to be represented by a set of local GMRF models evaluated for each pixel centered image window and for each color plane. The approach presented herein is an earlier and somewhat similar version of the one presented in [HM06]. The visible difference is of the utilization of GMRF with a non-causal neighborhood support region instead of CAR model with four causal neighborhood supports. In this work also, the authors have based the segmentation framework on the parameter space describing the multichannel textures. This method on the other hand requires a contextual neighborhood selection and two additional thresholds.

In the case of AR models which are a special case of MRF models, the texture attributes are computed through the model parameters for different textures. 2D AR models have been used for gray level texture classification over the recent years. Often these models are used for parametric spectrum estimation and hence for the characterization of the texture content in the images [ABN97], [ACRN98], [CHK83], [TES99]. In [AR05], segmentation of gray level images using 2D QP AR model is discussed.

The same idea of the spatial variation characterization in a color image through 2D AR models was used in [PFJ06]. In this work the authors have defined Gaussian mixture models (*GMM*) of color textures on several feature spaces and compared the performance of these models in various classification tasks. They constructed GMM over a variety of different color and texture feature spaces, with a view to the retrieval of textured color images from databases. Here along with other texture parameters, the authors analyzed the texture information of color images with 2D single channel AR models. The structure features related to AR model in this work are the coefficients estimated by a least squares LS estimator of NSHP, directly from the image data. In addition to the AR coefficients the authors also added the mean and the variance of the image block to these features. The authors compared supervised classification results for different choices of color and texture features and proposed the best set of features and the best GMM configuration for this task. To our knowledge these classification results are the best percentage color texture classification results for small image sizes i.e.  $32 \times 32$ . Yet two main issues are not considered in this work. First, the chrominance structure information of the color images is not considered at all. Second, for AR model, the AR coefficients have been modeled along with the mean of luminance information. In this joint model, AR coefficients do not contain the pure structure information but they are also somewhat influenced by the pure color information. The DC component for DCT coefficients also carries the mean information of the image. Therefore, the structure descriptor presented in the paper is *contaminated* with the pure color information of the image.

A detailed overview and application of different variants of AR models to the characterization of textures was first introduced in [KC83], [KCK82]. These variants included simultaneous autoregressive (*SAR*) models and conditional Markov models (*CMM*). In this early proposal of these models, the authors limited their investigation to the estimation of the unknown parameters in both SAR and CM models and the choice of an appropriate model from a class of such competing models. They proposed a maximum likelihood (*ML*) parameter estimation method and avoided the heavy computation problems of nonlinear optimization problem through an iterative scheme for SAR models, which gave approximate ML estimates in the Gaussian case and reasonably good estimates in some non-Gaussian situations as well. In [KCK82], a new feature extraction method for classifying a texture image and the textured images were modeled through SAR models. The introduction of these models for the characterization of textures in intensity images provided the opportunity to the researchers for a detailed investigation of these models.

The MSAR models were explored along with the neural networks to address the problem of color texture classification in [HCG<sup>+</sup>05] in RGB color space. In

this work, the authors presented a neural network based classification framework of color textures for a large heterogeneous database. All of these three multispectral random field models are used to characterize the textures. The classifying features are based on the estimated parameters of these models and functions defined on them. The authors used two different types of neighborhood sets for these models, a non-causal (8-connected) and a causal (4-connected) neighborhood. The full neighborhood set consisted of the eight elements that surround the pixel being observed, and the half neighborhood consisted of the four elements of the surrounding eight in the vertical and horizontal directions. Promising color texture classification results are presented in this work.

The same models are used for color texture segmentation and content based image retrieval problems in [HCG<sup>+</sup>04] and [KH03] respectively. In [HCG<sup>+</sup>04], the authors use ratios of sample color means to characterize the general color content of the image. Then, the image is segmented into regions of homogeneous color textures through an unsupervised histogram clustering approach based on the combination of MSAR parameters and color features. These feature vectors are computed through a sliding window operation. The image regions are obtained by mapping back to the spatial domain of the image the significant clusters obtained in the 22-dimensional feature space during the clustering process.

In [KH03], utility of these models for a color texture based color image retrieval problem is discussed. This retrieval process involves segmentation of the image into regions of uniform color texture using the same approach as in [HCG<sup>+</sup>04]. The color-texture content, location, area and shape of the segmented regions are used to develop similarity measures describing the closeness of a query image to database images. These attributes are derived from the maximum fitting square and best fitting ellipse to each of the segmented regions. The authors discussed the effectiveness of the approach using two different databases containing synthetic mosaics of natural textures and natural scenes.

Although in these works related to MSAR color texture features, the authors have shown the advantages of using multispectral random field models for various problems of color texture analysis, yet these models suffer from a disadvantage. These models are proposed and estimated only in RGB color space which possess high inter-channel correlation. If not exploited accordingly, this high correlation could create a redundant information representation problem for these models. The adaptation of these models for perceptual color spaces (which are considered better for color texture characterization cf. section 2.2) having lower degree of inter-channel correlation is still an open problem. Hence, these models in RGB color space, produce a better characterization of color textures than the gray level models yet they can not be declared as optimal and robust descriptors.

In [HM06], a multispectral modeling approach for the unsupervised segmentation of color textures is discussed. In this framework, color textures are locally represented by four causal multispectral random field models recursively evaluated for each pixel. Each of these four models is a 3D simultaneous causal autoregressive random field model (*CAR*). These models have identical contextual neighborhood with different movement directions i.e. top-down, bottom-up, rightward and leftward. The authors have expressed this model as a stationary causal uncorrelated noise driven 3D AR process. A recursive Bayesian approach has been used for the estimation of the parameters of these models. Once this parametric space is formed, the authors propose to model this space through a GMM with diagonal covariance matrices due to the previous *CAR* parametric space decorrelation. The parameters of this GMM are estimated through expectation maximization (*EM*) algorithm. As this model uses recursive parameter estimation, it risks to suffer from heavy computational costs.

In another work on model based segmentation of color texture images [HMP09], the authors have proposed a multispectral, multi-resolution, multi-segmenter for unsupervised color texture segmentation. This framework named as *MW3AR*, is based on the weighted combination of segmented results computed at different resolutions. In essence, the approach is a multi-resolution version of the approach discussed and presented in [HM06]. In this approach, the segmentation results from the framework proposed in [HM06] are computed at different resolutions and then are combined through the modified sum rule.

For unsupervised image segmentation, the authors in [SHZ07], have presented a hierarchical, discrete and region based probabilistic model for multichannel texture representation. The image to be segmented is first discretized and then a hierarchical finite-state region-based model is automatically coupled with the data by means of a sequential optimization scheme, namely the Texture Fragmentation and Reconstruction (*TFR*) algorithm. *TFR* first estimates the states of the finest level (fragmentation), and then relates them hierarchically (reconstruction) as to provide the desired hierarchical segmentation.

Here we have discussed salient model based color texture descriptors used in different applications including classification and segmentation. Besides these descriptors, several model based algorithms and approaches for color texture segmentation also exist which may not use model based descriptors. Some of these approaches will be discussed in the chapter 5.

## 2.2 Color Space Comparison

Choice of the best performing color space for the color texture characterization (classification and/or segmentation) has been an open question in recent years

as using one space instead of another can bring considerable improvements in certain applications of image processing.

The pertinence of carrying out the color texture analysis in different color spaces is discussed in [CSF05]. The authors herein, propose the use of color texture classifier combination schemes which utilize information from different color spaces. They subsequently use suitable measures to investigate the diversity of the information infused by the different color spaces. In this work they have used other color spaces in addition to the RGB and its derivative, the normalized RGB (nrgb), and explored their contribution to the classification of 2 sets of different color texture classes, from two different databases. They also used the CIEL\*a\*b and CIEL\*u\*v\* developed to overcome the problem of non-perceptual uniformity of the RGB color space. Experiments in this work are also carried out using the HSV color model and two other color spaces, YIQ and YUV.

The results of this diversity based predictive model for color texture analysis are interesting. The authors supported the use of different color spaces as a diversity inducement method based on the investigated diversity measures. The authors have also reported a strong correlation between the accuracy and the diversity measures in the majority of the ensemble cases investigated in this study.

Once the fact that the choice of a color space can affect the performance of a given color texture descriptor to a certain degree (depending upon the underlying methodology of the descriptor), it becomes more important to search for a pertinent and suitable color space for color texture analysis.

While comparing two color spaces one can state his particular choice based on final results for a particular application of color texture analysis *i.e.* classification, segmentation or retrieval, for example in [PFJ06], [OMTM02] and [VMP03]. Based on this principle, an empirical evaluation of perceptually uniform color spaces for color texture classification is presented in [Pas01]. In this work the author has compared perceptually uniform spaces, such as L\*a\*b\*, as well as approximately-uniform color spaces, such as HSV, in which measured color differences are proportional to the human perception of such differences along with RGB, a nonuniform color space, universally accepted by the image processing community. These experimental results state a clear advantage of using perceptually uniform color spaces over the RGB color space for color texture classification.

The presented color texture classification framework incorporates a family of Gabor filters specially tuned to measure specific orientations and sizes within each color texture. Effectiveness of a particular color space is measured by the classification performance, as well as by classifier-independent measures. Experimental results, obtained with a variety of color texture images have shown that incorporating color into a texture analysis and recognition scheme can be very important

and beneficial. Overall, perceptually uniform spaces are shown to outperform RGB in many cases.

A comparison of three perceptual color spaces including HLS, LCH and  $L^*a^*b^*$  for optic disc localization in retinal images is presented in [OMTM02]. An automatic initialization of the snake and the application of morphology in all color spaces is proposed in this work. The authors demonstrate that their proposed Lab color morphology method is particularly suitable for the characteristics of the used optic disc images.

In [DW01], three gray level texture descriptors including local linear transforms, Gabor filters and co-occurrence matrices are extended for the color texture analysis. In this work, authors used RGB, HSI, CIE XYZ, CIE Lab and YIQ color spaces. The reported results state no significant difference in the color space performance. However, comparing only the color texture classification accuracy, YIQ produces the better results. It is important to note that authors considered only the classification accuracy as the comparison criterion in this work.

Similarly in [WSLD99], four color spaces including RGB, CIE UVW, YIQ and K-L color space (based on Karhunen-Loeve transform) are used for wavelet correlation signature based color texture classification. Here also, only on the basis of the classification accuracy, it is stated that K-L color space performs better than other color spaces. In [IMK<sup>+</sup>04] too, authors have compared six different color spaces for the identification of colon cancer precursors using color video endoscopy measurements and Support Vector Machine (SVM). They also prove a slight improvement in classification measures in the case of K-L color space which they attribute to the orthogonality of the space.

The experiments conducted and demonstrated by the researchers on the performance analysis of soft color texture descriptors for surface grading in [LMVMPF08] indicate the pertinence of using  $L^*a^*b^*$  color space for this application using this particular method. Contrarily authors in [AML08] propose that the color isotropic co-occurrence matrix (CCM) performed the best for color texture discrimination in RGB and HSL color spaces and in the  $La^*b^*$  color space, the method could not effectively discriminate between close color texture samples. However, the authors in [AML08] do not produce any statistical evidence of this observation.

In this section, we have reported the findings of different researchers with various color texture analysis methods for diverse applications in numerous color spaces. It is evident from these illustrations that perceptual color spaces perform better than nonuniform and highly correlated RGB color space [Pas01], [PFJ06], [LMVMPF08], [WSLD99] and [DW01]. Another important observation made is that most of these comparisons are made only on the color texture discrimination performance of different methods for specific applications. Not much of these works exploit the *a priori* known mathematical characteristics of the color space

transformations to state a hypothesis about the comparison criterion in advance and to prove it through experimental results afterwards.

## 2.3 Texture in Satellite Images

Characterization and discrimination of regions and/or objects in satellite images are the basis for many real world environmental and socioeconomic applications. This motivation has long attracted the attention of the remote-sensing community to carry out the research focusing on satellite image analysis. Scientists and practitioners have made great efforts in developing advanced classification approaches and techniques for improving classification accuracy in these images based on various features including statistical parameters [Aba08], Fourier transform [CCF07], multifractal models [GTYH07], combination of different classifiers [GW07], pixel block based techniques [LM98], co-occurrence matrices [MKC88] and model based approaches [SZ06]. A detailed survey of such approaches and techniques is presented in [LW07].

The different features which have been used in these methods include spectral signatures, vegetation indices, transformed images, textural or contextual information, multitemporal images, multisensor images, and ancillary data. Textural and contextual information become significant in high spatial resolution data [SD98]. Hence, the feature of spectral response is the most important information used for land-cover classification [LW07]. Several works presented in past years have used gray level texture descriptors including first-, second-, and third-order statistics in the spatial domain [NTA02], gray level co-occurrence matrices [RSS<sup>+</sup>02] and Gabor filtering [AH03].

Random field models have also been used for the analysis of satellite and aerial images [SRSD98]. Herein, the authors emphasize the success of the application of GMRF models for the spatial information extraction from remote-sensing images. The authors first extract information at one fixed scale. Then to analyze the possibly present structures in remote-sensing images, such as agricultural fields, valleys, and geological structures, they apply several Gibbs models at multiple scales of the image. The authors proposed to use the maximum pseudo-likelihood and the conditional least squares estimator for the GMRF parameter estimation. These estimation methods are chosen for being computationally efficient and faster than the conventional parameter estimation methods.

A multi-spectral texture characterization model, the Multi-spectral local differences texem (*MLDT*), based on Texem model is proposed in [PGGS<sup>+</sup>09]. This model is an efficient approach to be used in multi-spectral images that may contain large number of bands. It models the image as a generative process where a set of image primitives generate the image by superposition of image patches

from a number of texture exemplars, Texems [XM07]. These texems are computed through a Gaussian mixture. In this case study this Gaussian mixture is considered to be an MGMM. The MLDT characterization represents the integrated spatial and spectral information in a single representation through the difference patterns within a multispectral image.

Another important work presented in [DJG00], discusses the fusion of color and texture features for aerial image segmentation application. In this approach, ML segmentation is applied to the image in each feature space (color and gray level texture) separately. A final segmentation is obtained by combining the likelihoods in the two spaces using a certainty function. For texture feature computation in the intensity information of the image, the authors have made use of the SAR model discussed in [MJ92]. The texture parameters at each pixel are computed using LS estimation in a finite sized window centered around that pixel. Then authors propose to compute the multiple resolution SAR models by fitting these SAR models to down-sampled versions of the image. The color features computed in this work consist of pixel values in RGB, Yuv, RGBuv, and C5 color spaces. The C5 color space is a 5 dimensional space defined using the color components from RGB color space. Maximum likelihood pixel classification is used in this approach which is a common supervised image segmentation technique in the remote sensing domain. In this work authors have assumed a multivariate Gaussian probability distribution for the data and gave a hypothesis that the reported results could be improved using multimodal probability distributions.

An overview of the methods presented in this section highlights the importance of spatial and spectral information utilization in the aerial image classification and segmentation. Most of the methods proposed in these works are based on the descriptors and algorithms developed for normal gray level and color images.

## 2.4 Conclusion

Certain important conclusions can be drawn from the literature survey presented in this chapter. Comprehensive interpretation of the chromatic texture information present in the color images is very important for color texture analysis. Although, a lot of attempts have been made towards the development of the algorithms and methods for the characterization of color texture images, yet a very few have succeeded in exploring this information with an efficient and robust manner.

Thus this study of the state of art approaches reinforces the research objectives stated in the previous chapter. Most of the research works discussed in this survey rely either on the gray level texture information or on weakly established color texture descriptors. Therefore, one of the main goals of this research study was to define and develop a multichannel, comprehensive, robust and applica-

tion independent color texture descriptor which can produce decent results on different applications of color texture analysis and multispectral satellite image segmentation. In the following chapters of this thesis report, the development and computation of our parametric modeling based color texture descriptor is detailed and then the results for different applications are analyzed and discussed.



---

## CHAPTER 3

---

# COLOR SPECTRAL ANALYSIS

---

In color image analysis, frequency domain measures are considered to be less sensitive to noise processes as typical noise processes tend to affect local spatial variation of the luminance levels but they present uniform distribution in spatial frequency. The power spectrum information of the color images can be used to obtain very useful knowledge regarding spatial feature variations as discussed in [KTB04]. Given this reason, we base our approach for color texture description on parametric 2D spectral analysis.

This chapter presents the mathematical basis of the parametric color spectral analysis approach developed for the color texture analysis detailed later in this thesis. Section 3.1 focuses on the research background of the spectral analysis method developed during our research. Then, section 3.2 describes the various color spaces used in this analysis along with the novel two channel complex color image representation. The derived multichannel linear prediction models employed for the parametric color spectral estimation are detailed in the section 3.3. Performance analysis of the color spectral analysis approach is done in the section 3.4. Finally, the section 3.5 concludes the chapter.

### 3.1 2D Spectral Analysis

In this section, we briefly overview the existing techniques for the spectral content estimation of 2D signal or image data. In its very core 2D spectral analysis methods are the extension of classical 1-D methods developed in last three decades. Classically, there exist two major types of spectral analysis algorithms which we will overview in the following subsections.

### 3.1.1 Non-Parametric Spectral Estimates

The *traditional* or *non-parametric methods* are called so because they do not represent any modeling of the underlying 2D process. These are the ones which are derived from the definition of the Power Spectral Density (*PSD*) of a 2D process. Two important methods belonging to this category are the periodogram and correlogram.

The reason of the general acceptance and wide usage of periodogram as a spectrum estimator is the simplicity of its implementation. This simplicity relies on the algorithm resources of 2D Fast Fourier Transform (*FFT*). In this technique, the generalized form PSD  $\hat{S}_X^P(\nu_1, \nu_2)$  estimated over a grid of discrete, normalized frequency set  $(\nu_1, \nu_2)$ , of the 2D sequence  $x = \{x(n_1, n_2)\}_{(n_1, n_2) \in \Lambda \subset \mathbb{Z}^2}$  where  $\Lambda$  is the finite 2-D image lattice region of size  $|\Lambda|$ , is given as:

$$\begin{aligned} \hat{S}_x^P(\nu_1, \nu_2) &= \frac{1}{N_1 N_2} \left| \sum_{n_1=0}^{N_1-1} \sum_{n_2=0}^{N_2-1} w(n_1, n_2) x(n_1, n_2) \exp(-j2\pi(\nu_1 n_1 + \nu_2 n_2)) \right|^2 \\ &= \frac{1}{N_1 N_2} |FT(w, x)|^2 \end{aligned} \quad (3.1)$$

Here, the signal  $w(n_1, n_2)$ , also defined on the same grid as of  $x(n_1, n_2)$  is a deterministic function with respect to a rectangular window and is hence called *window function*. Utilization of this signal reduces power of the side lobes but often widens the main lobe itself, consequently reducing the resolution of the PSD estimate considerably. These window functions are separable *i.e.* obtained from their equivalent functions in 1-D. Some important window functions include Hamming, Hanning, Bartlett and Parzen windows. In [Gar08], it is demonstrated that this estimator is not consistent.

The second method in the family of non-parametric spectral estimators is the correlogram technique which is also known as Blackman-Tukey spectral estimator [BT59]. The 2D correlogram can be computed if we take the definition of the PSD of a process and replace the autocorrelation function (*ACF*) theory by one of the estimates observed by a window function. This estimate can be given as:

$$\hat{S}_x^C(\nu_1, \nu_2) = \sum_{f_1=-F_1}^{F_1} \sum_{f_2=-F_2}^{F_2} w(f_1, f_2) \hat{\gamma}_x(f_1, f_2) \exp(-j2\pi(\nu_1 f_1 + \nu_2 f_2)) \quad (3.2)$$

where  $\hat{\gamma}_x(f_1, f_2)$  is an ACF estimation resulting from an outcome of the process  $x(n_1, n_2)$ . A detailed overview on this estimation and the selection of window function can be found in [Gar08].

Although these two are the classically used spectral estimation methods yet they suffer from the same drawback. Same as due to FT in the 1-D domain, the

spectral resolution of these methods is inversely proportional to the duration of the signal. Thus, the use of traditional or non-parametric methods is justified only in the cases where we have sufficient size of the observed wide sense stationary (WSS) process [Gar08]. In fact, in most of the real world applications, this condition is not met and hence the use of these methods as precise spectral analysis methods is limited.

### 3.1.2 Parametric Spectral Estimates

In the case of parametric spectral analysis methods, the PSD is parametrized and is generally a deterministic function of reduced, unknown parameters of the underlying 2D single or multichannel data (gray level or color image in our case) observation model. This comes through the fact that these parametric spectral estimation methods are based on the PSD modeling of the random fields.

A 2D centered, random process represented by a sequence  $x = \{x_n\}_{n \in \Lambda \subset \mathbb{Z}^2}$  where  $n = (n_1, n_2) \in \Lambda \subset \mathbb{Z}^2$  in which  $\Lambda$  is the finite 2D lattice region of size  $|\Lambda|$ , following a linear prediction model can be defined through the prediction sequence:

$$\hat{x}_n = - \sum_{m \in D} a_m x_{n-m}. \quad (3.3)$$

as

$$x_n = \hat{x}_n + e_n. \quad (3.4)$$

where  $m = (m_1, m_2) \in D \subset \mathbb{Z}^{*2}$  is a point inside the neighbor support region defined by  $D$ , the prediction support.  $a_m, m \in D$ , are coefficient vectors and  $e = \{e_n\}_{n \in \mathbb{Z}^2}$  is the prediction error sequence which is supposed to be a 2D stationary process having a variance denoted by  $\sigma_e^2$  and PSD denoted by  $S_{e,\nu}$ . Prediction neighborhood support  $D$  may be of QP, NSHP, symmetric half plane or non-causal type. In the case of GMRF i.e. non-causal neighborhood support and  $e$  a Gaussian process, the hypothesis over the noise sequence is changed and it is considered as a correlated noise sequence.

The PSD of  $x$  is computed using 2D linear prediction model coefficient vectors  $a_m, m \in D$ , and may be given as:

$$\hat{S}(\nu) = \frac{\sigma_e^2}{1 + \sum_{(m_1, m_2) \in D} a_{m_1, m_2} \exp(-j2\pi(\nu_1 m_1 + \nu_2 m_2))} \quad (3.5)$$

where  $\nu = (\nu_1, \nu_2)$  is the normalized frequency. The error  $e_n$  is an outcome of a centered 2D white noise  $e$  in a linear time invariant system with transfer function given as:

$$\begin{aligned}
H(z_1, z_2) &= \frac{\sigma_e^2}{1 + \sum_{(m_1, m_2) \in D} a_{m_1, m_2} z_1^{-m_1} z_2^{-m_2}} \\
&= \frac{1}{A(z_1, z_2)}
\end{aligned} \tag{3.6}$$

It is to note that this is the frequency response of the filter defined by the Equation (3.4). It is evident here that the PSD can be estimated as a deterministic function of model parameters  $\{a_m\}_{m \in D}$  and variance  $\sigma_e^2$  of the error sequence.

Hence the problem of spectral estimation of 2D signals *i.e.* gray level images in this case, by AR modeling has reduced to find an estimate  $\{\hat{a}_m\}_{m \in D}$  of parameters with a finite neighborhood support region  $D$  and an estimate of the input noise variance  $\hat{\sigma}_e^2$ .

Contrary to the 1-D processes, where the number of the model parameters is the same as the number of ACF coefficients [Cas06], there is no corresponding correlation matching property for 2D AR processes. As, estimation of parameters requires more ACF coefficients than the parameters themselves [Gar08]. Therefore, simpler and efficient parameter estimation techniques like partial correlation or reflection coefficients have been developed for these models in 2D case instead of developing the 2D extension of ACF estimation based 1-D Yule-Walker equations. Some of these are extensions of their 1-D versions as well, yet are computationally effective. The most frequently used techniques among these include the maximum likelihood estimation (*MLE*), LS solution of the linear system of equations, Levinson algorithm [Jus77], and the calculation of reflection coefficients [Mar80].

Several research works presented in the literature have used these methods for different applications for gray level images. In [CHK83], model based Spectrum estimation of a 2D single channel real valued sequence *i.e.* gray level image is proposed through 2D GMRF model has been discussed. This work gave a basic idea to the domain but the method is not able to deal with 2D multichannel data, neither real nor complex. Again in [ZL88], the authors analyzed the approach and provided a synthesis of the performance of these methods for 2D single channel complex valued data. In [TES99], the authors presented a 2D multichannel autoregressive model based method for the spectrum estimation of the real valued multichannel data. The authors calculated the autospectra and the cross spectra of the 2D multichannel data using forward and backward AR models. Since the method is discussed for the real valued multichannel case, therefore the method is not very well suited for the polar representations of color images (cf. section 3.2).

Thus, the main advantages of 2D spectral estimation by the means of 2D AR models are:

- Complexity of the problem is reduced as the problem of PSD estimation is now reduced to the model parameter estimation which includes the AR coefficients  $\{\hat{a}_m\}_{m \in D}$  and the variance  $\hat{\sigma}_e^2$ .
- The spectral estimates computed through these methods are stable and less noisy.
- These belong to a family of methods known as high *resolution methods* as the resolution of these estimates is much better than those of the non-parametric methods [Gar08]. This is one of the most important advantage of these methods which makes them widely acceptable for the application where high resolution spectral estimates are required *e.g.* radar signal processing and radioastronomy.

Besides these advantages, these methods based on NSHP AR and QP AR models inherit some undesired properties also. One of which is the dissymmetry of the energy around the spectral peaks *i.e.* shape of the estimated frequency lobes becomes dependent on the type of neighborhood  $D$ , used for the estimation of model parameters [Gar08]. The phenomenon of spurious peaks also exhibit in the case where the model order *i.e.* the size of the neighborhood  $D$ , is over estimated [Cas06].

To resolve all these problems a parametric spectral estimator was proposed in [JC79, KT81]. The authors named this estimator as the harmonic mean (*HM*) estimator and is defined by the following relation [Gar08]:

$$\frac{1}{\hat{S}_{AR-HM}(\nu)} = \frac{1}{2} \left( \frac{1}{\hat{S}^{QP_1}(\nu)} + \frac{1}{\hat{S}^{QP_2}(\nu)} \right) \quad (3.7)$$

where  $\hat{S}^{QP_1}(\nu)$  and  $\hat{S}^{QP_2}(\nu)$  are the PSD values estimated using AR modeling with respective neighborhood supports in the first and second QPs. As it is clear that a stochastic AR model can not be computed over two mutually exclusive neighborhood support regions, therefore this estimate rests as an empirical spectral estimate. The advantageous properties of this estimator and its variants have been used frequently in different research works [ZL88, ACRN98, Law85].

In this section we have very briefly discussed some of the salient and frequently used approaches and methods for parametric and non-parametric spectral analysis of the 2D data either signal or gray level image. A more detailed study and analysis on all the existing methods can be found in [Gar08].

## 3.2 Two Channel Complex Color Image

Since the spectral content of an image can be a very useful tool (if rightfully exploited) for characterizing the spatial variations in an image, hence we base our proposed approach for the comprehensive and robust color texture description on the multichannel real and complex valued extensions of random field theory based precise 2D parametric spectral estimates of the color images. In order to develop the approach we adopt the given real valued color image into a two channel complex valued color image in perceptual color spaces. The details of the choice of candidate color spaces for this study, the two channel complex color image formation and the approach for parametric color spectral analysis will be presented in this section.

### 3.2.1 The Candidate Color Spaces

A *color space* is a mathematical model which provides the data representation of a digital color image as color components. As it provides the very preliminary mathematical interpretation of the underlying information in an image, hence plays a very important role in all the domains of color image processing. Since the advent of color images, large number of color spaces have been proposed by the researchers based on the different mathematical characteristics of the information representation, whether or not related to the perception of color in human vision.<sup>1</sup> The two important objective functions around which these different color spaces have revolved are device independence and uniformity in perception (in the case of perceptual color spaces). Device independence means that the mathematical representation of the color information offered by a color space should be independent of the device used. Perceptual uniformity determines that the two colors should have as much distance between them in a color space as they are distinct in the human perception.

Similar to other color image processing application areas, for color texture analysis too, the selection of a proper color space is of high importance and should be given proper attention. Selection of the *most suitable* color space is highly subjective to categorization of all the available color spaces. In [VMP03], authors propose to group the most classical color spaces into four main families, namely:

- The primary color spaces, which are based on the trichromatic theory, assuming that it is possible to match any color by mixing appropriate amounts of three primary colors. These include  $(R_C, G_C, B_C)$ ,  $(R_E, G_E, B_E)$ ,  $(R_F, G_F, B_F)$  and  $(X, Y, Z)$  etc.

---

<sup>1</sup>[www.couleur.org](http://www.couleur.org)

- The Luminance-Chrominance color spaces  $(L^*, a^*, b^*)$ ,  $(L^*u^*v^*)$ , where one component represents the luminance and the two others the chrominance including  $(Y, U, V)$ ,  $(Y, I, Q)$  etc.
- The perceptual color spaces, which try to quantify the subjective human color perception using the intensity, the hue and the saturation *e.g.*  $(H, S, I)$ ,  $(L, C, H)$ ,  $(H, L, S)$  etc.
- The independent axis color spaces resulting from different statistical methods which provide as less correlated components as possible like  $(I_1, I_2, I_3)$  and K-L color space.

In [VMP03], the authors have also discussed the concept of an adapted hybrid color space which is built by the means of a sequential feature selection scheme. In another work [Pas01], the author discussed the role of perceptually uniform color spaces for the characterization of color textures. In this evaluation, the author indicated on the basis of his experimental results that the perceptually uniform color spaces perform better than the classical RGB color space for color texture classification problem.

The categorization of the available color spaces discussed in [VMP03] and the results of the study presented in [Pas01] have influenced our choice of the color spaces. As discussed in [VMP03], the first three families of the color spaces *i.e.* the primary, the Luminance-Chrominance and the perceptual color spaces are the most widely used color space families in color image processing applications. We have chosen one representative color space from each of these three families for the color spectral analysis presented in this chapter and subsequently for the color texture analysis detailed in this thesis. Other representatives of these families might also be considered.

### Red Green Blue Color Space

The RGB color space and its different variants belong to the first family and are the most widely used color spaces in computer applications and image processing. In this study we have used the standard RGB color space [SBS99]. It is defined by the three chromaticities of the red, green, and blue additive primaries, and can produce any chromaticity that is the triangle defined by those primary colors. The RGB color space can be represented by a cube as shown in Figure 3.1<sup>2</sup>. This space is easier to use for color image analysis but all possible colors can not be represented in this color space. Also, this color space is non-uniform as the color distances computed in it are not correlated to the human perception. In

---

<sup>2</sup><http://www.couleur.org/>

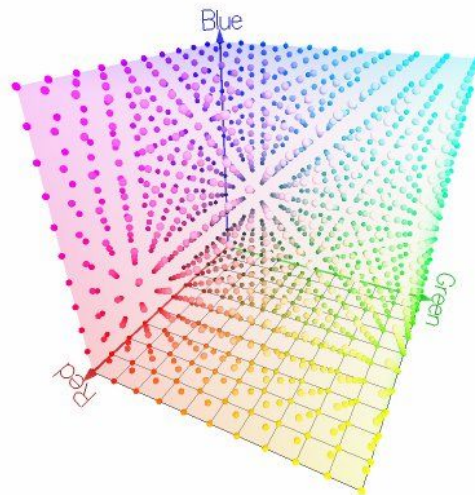


Figure 3.1: RGB color space.

an RGB image whose colors are defined as vectors  $[R, G, B]^T$ , each term  $R$ ,  $G$  and  $B$  of the vectors belongs to the interval  $[0, 255]$ . However the normalised values of these color vectors belong to  $[0, 1]$ . Thereby all colors are included in a cube  $[0, 1] \times [0, 1] \times [0, 1]$ . In this representation, luminance and chrominance components are not explicitly defined and all the three color variables *i.e.*  $R$ ,  $G$  and  $B$  contain the combined information of luminance and chrominance.

### Improved Hue Luminance and Saturation Color Space

Many color space conversion systems define a saturation coordinate which is dependent on the brightness coordinate of the image and hence are not very suitable for image analysis applications. To overcome this shortcoming of conversion systems, an improved saturation measurement is presented in [HS03]. This improved saturation measurement has following two advantages :

1. It always has small values for achromatic colors.
2. It is independent of brightness values.

The 3D representation of RGB cube in IHLS color space is shown in Figure 3.2. Let us consider an RGB color image defined by the RGB vector (cf. 3.2.1). For this RGB image, Luminance, Saturation and Hue values in IHLS color space can be computed as given in the appendix A.

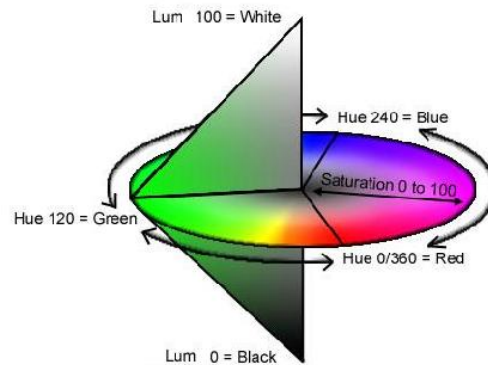


Figure 3.2: IHLS color space.

### L\*a\*b\* Color Space

L\*a\*b\* is a uniform color space based on human perceptual system. It is defined by CIE in [CIE86]. L\*a\*b\* color gamut is shown in Figure 3.3<sup>3</sup>. The transforma-

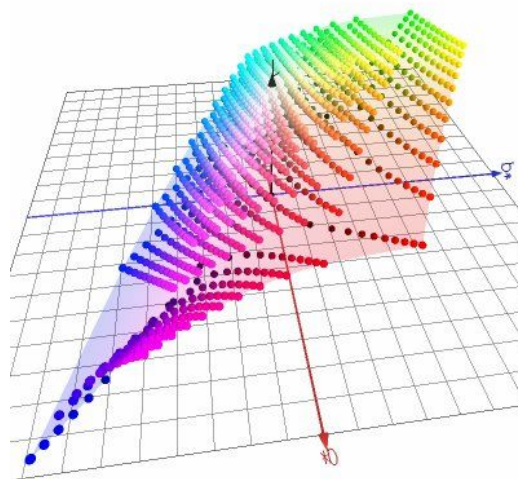


Figure 3.3: L\*a\*b\* color space.

tion from the RGB color space to the L\*a\*b\* color space is performed by the set of equations given in appendix A.

The degree of decorrelation of luminance and overall chrominance information offered by a given color space plays a very important role in the characterization of color textures. Therefore, we are interested in the individual analysis of chrominance as well as luminance spatial structure information in color images.

<sup>3</sup><http://www.couleur.org/>

We use an adapted complex two channel color image representation. Details of this image representation are given in the next section.

### 3.2.2 Complex Color Image

We use the color information obtained through RGB to IHLS and RGB to L\*a\*b\* transformations to build a two channel image that contains pure luminance values in one channel and complex chrominance values in the other channel. We define this chrominance value as a complex function depending upon two chrominance variables  $H$  and  $S$  in the case of IHLS while  $a^*$  and  $b^*$  in case of L\*a\*b\*. The combined chrominance exponential for IHLS color space is defined as:

$$C = S \times \exp\left(j \times \left(\frac{\pi}{180}\right) \times H\right) \quad (3.8)$$

where  $H$  is the hue and  $S$  is the saturation value obtained after the RGB to IHLS transformation (cf. section 3.2.1). While in the case of L\*a\*b\* this combined chrominance function can be computed as:

$$C = a^* + j \times b^* \quad (3.9)$$

where  $a^*$  and  $b^*$  are two chroma variables obtained from RGB to L\*a\*b\* transformation (cf. section 3.2.1). We obtain a complex representation of chrominance content of the image whose spectrum is interesting to analyze in order to characterize the spatial variations of the chromatic part of the image. Now the image to be analyzed consists of two 2D channels in which first channel contains the luminance information and second is complex valued channel containing combined chrominance information and is expressed as:

$$x_n = \begin{bmatrix} l_n \\ c_n \end{bmatrix} \quad (3.10)$$

where  $l_n \in \mathbb{R}$  and  $c_n \in \mathbb{C}$  and  $n$  is a pixel location  $n = [n_1, n_2]^T \in \Lambda \subset \mathbb{Z}^2$  in which  $\Lambda$  is the finite 2D image lattice region of size  $|\Lambda|$ .

As it is evident that the methods discussed in the section 3.1 are unable to model this vectorial complex valued image, therefore we develop the complex vectorial extensions of the parametric models discussed in the section 3.1.2.

## 3.3 Complex Vectorial Color Spectral Analysis

Given a 2D multichannel complex, stationary (each channel is assumed jointly stationary) random process represented by a vector sequence  $X = \{X_n\}_{n \in \mathbb{Z}^2}$

with dimension  $P$  representing the number of channels, following a linear prediction model can be defined through the prediction sequence:

$$\hat{X}_n = - \sum_{m \in D} A_m (X_{n-m} - \mu). \quad (3.11)$$

as

$$X_n = \hat{X}_n + E_n + \mu. \quad (3.12)$$

where  $\mu$  is the mean, and  $m = (m_1, m_2) \in D \subset \mathbb{Z}^{*2}$  is a point inside the neighborhood support region defined by  $D$ . In this complex vectorial case,  $A_m$ ,  $m \in D$ , are  $P \times P$  complex coefficient matrices and  $E = \{E_n\}_{n \in \mathbb{Z}^2}$  is 2D complex  $P$  channel prediction error sequence which is supposed to be a 2D  $P$  channel stationary process having a  $P \times P$  complex covariance matrix denoted by  $\Sigma_e$  and PSD matrix denoted by  $S_{e,\nu}$  where  $\nu = (\nu_1, \nu_2)$  is the normalized frequency,  $\nu \in [-0.5, 0.5]^2$ .

The transfer function of the filter defined by the Equation 3.11 can be written as:

$$H_\nu = (A_\nu)^{-1} \quad (3.13)$$

where  $A_\nu$  are  $P \times P$  matrices computed using 2D multichannel complex linear prediction model coefficient matrices  $A_m$ ,  $m \in D$  given by:

$$A_\nu = I + \sum_{m \in D} A_m \exp(-j2\pi \langle \nu, m \rangle) \quad (3.14)$$

In Equation (3.14),  $I$  is an identity matrix of dimensions  $P \times P$  which represents the coefficients at origin  $(0, 0)$  and  $\langle ., . \rangle$  represents scalar product. The PSD matrix  $X$  is computed through these  $P \times P$  dimensional matrices  $A_\nu$  in the normalized frequency domain, and may be given as:

$$S_\nu = A_\nu^{-1} S_{e,\nu} (A_\nu^H)^{-1} \quad (3.15)$$

In Equation (3.15),  $S_\nu$  denotes the PSD matrix of the 2D vectorial random process  $X$  at normalized frequency  $\nu$ .  $A_\nu^H$  represents the hermitian transpose of the matrix  $A_\nu$ .

For the color images defined by Equation (3.10),  $P = 2$ . The PSD for a 2D  $P$  channel random process defined by Equations (3.11) and (3.12) is computed using Equation (3.15) and Equation (3.14). The PSD matrix gives us the auto spectra and the cross spectra of the luminance and the combined chrominance channels. The structure of this PSD matrix is given as:

$$S_\nu = \begin{bmatrix} S_{LL}(\nu) & S_{LC}(\nu) \\ S_{CL}(\nu) & S_{CC}(\nu) \end{bmatrix} \quad (3.16)$$

where  $S_{LL}(\nu)$  denotes the auto spectrum of real valued luminance channel and  $S_{CC}(\nu)$  denotes the autospectrum of the complex valued chrominance channel, while  $S_{CL}(\nu) = S_{LC}^*(\nu)$  are the cross spectra of the luminance and chrominance channels respectively.

For RGB color space, basic approach remains the same. Since the model is a 2D multichannel real linear prediction model with  $P = 3$ , therefore the PSD matrix structure in this case is given as:

$$S_\nu = \begin{bmatrix} S_{RR}(\nu) & S_{RG}(\nu) & S_{RB}(\nu) \\ S_{GR}(\nu) & S_{GG}(\nu) & S_{GB}(\nu) \\ S_{BR}(\nu) & S_{BG}(\nu) & S_{BB}(\nu) \end{bmatrix} \quad (3.17)$$

where  $S_{RR}(\nu)$ ,  $S_{GG}(\nu)$  and  $S_{BB}(\nu)$ , denote the auto spectra of real valued red, green and blue channels respectively while rest are the cross spectra of these three real valued channels.

In the following, the power spectrum estimation of two channel complex color images is done using 2D multichannel complex versions of both causal and non-causal prediction models. These include NSHP AR, 2D multichannel complex QP AR via HM method and 2D multichannel complex GMRP prediction models. Details of these models are given in the following subsections.

### 3.3.1 Causal Models

The notion of causality is defined very clearly for 1-D systems as: *A system is said to be causal if its output does not precede its input.* However for dimensions higher than 1-D i.e.  $\mathbb{Z}^n$  with  $n \geq 2$ , it becomes very difficult to establish the strict concept of causality as time (the support dimension of 1-D signals) which makes it possible in 1-D case disappears. This past and future notion of 2D data is established by making a hypothesis that there exist non-trivial relations of finite partial order between data points. This hypothesis allows us to consider different causal neighborhood supports for 2D multichannel linear prediction. Here we consider the NSHP and QP neighborhood support based 2D multichannel linear prediction models.

#### 2D Multichannel Complex NSHP AR Model

A multichannel 2D NSHP AR process is defined by Equation (3.11) and Equation (3.12) with a neighborhood support region  $D = D_{M_1, M_2}^{NSHP}$  such that:

$$D_{M_1, M_2}^{NSHP} = \{(m_1, m_2) / 1 \leq m_1 \leq M_1 \text{ for } m_2 = 0, \\ -M_1 \leq m_1 \leq M_1 \text{ for } 1 \leq m_2 \leq M_2\} \quad (3.18)$$

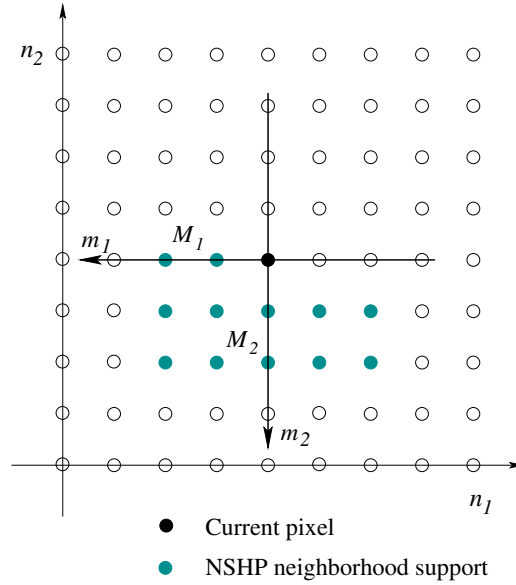


Figure 3.4: NSHP neighborhood support region for model order  $(M_1, M_2)$  with  $M_1 = 2$  and  $M_2 = 2$ .

where  $(M_1, M_2) \in \mathbb{N}^2$  is the model order and in the case of 2D NSHP AR model,  $E = \{E_n\}_{n \in \mathbb{Z}^2}$  is supposed to be a multichannel white noise stationary process having  $S_{e,\nu} = \Sigma_e$  which in the case of IHLS and L\*a\*b\* color spaces is a  $2 \times 2$  complex matrix as  $P = 2$  and a  $3 \times 3$  real matrix in the case of RGB color space, as  $P = 3$ . An example of such neighborhood support region is shown in Figure 3.4.

We use least squares estimation method to estimate the model parameters by a matrix solution of a system of normal equations using Moore-Penrose pseudoinverse matrix.

Then these multichannel 2D NSHP AR model coefficients denoted by  $A_m^{NSHP}$  are used to estimate the PSD matrix of the real valued luminance and the complex valued chrominance channel. As  $E$  is supposed to be a multichannel white noise therefore the estimate of PSD matrix for 2D multichannel complex NSHP AR model takes the form:

$$\hat{S}_\nu^{NSHP} = \hat{A}_\nu^{NSHP^{-1}} \hat{\Sigma}_e \left( \hat{A}_\nu^{NSHP^H} \right)^{-1} \quad (3.19)$$

where the matrix  $\hat{A}_\nu^{NSHP}$  can be estimated using  $A_m^{NSHP}$  through the Equation (3.14). The structure of this PSD matrix is the same as given in Equation (3.16).

### 2D Multichannel Complex QP AR Model

2D multichannel complex QP AR model is defined by Equation (3.11) and (3.12) for which the causal  $QP_1$  and  $QP_2$  neighborhood support regions are defined as follows:

$$D_{M_1, M_2}^{QP_1} = \{(m_1, m_2) / 0 \leq m_1 \leq M_1, \quad (3.20)$$

$$0 \leq m_2 \leq M_2, (m_1, m_2) \neq (0, 0)\}$$

$$D_{M_1, M_2}^{QP_2} = \{(m_1, m_2) / 0 \geq m_1 \geq -M_1, \quad (3.21)$$

$$0 \leq m_2 \leq M_2, (m_1, m_2) \neq (0, 0)\}$$

An example of  $QP_1$  and  $QP_2$  neighborhood support regions is shown in Figure 3.5. These 2D  $QP_1$  AR and 2D  $QP_2$  AR complex parameter matrices denoted by  $A_m^{QP_1}$  and  $A_m^{QP_2}$  are again estimated by a matrix solution of a system of normal equations through Moore-Penrose pseudoinverse matrix.

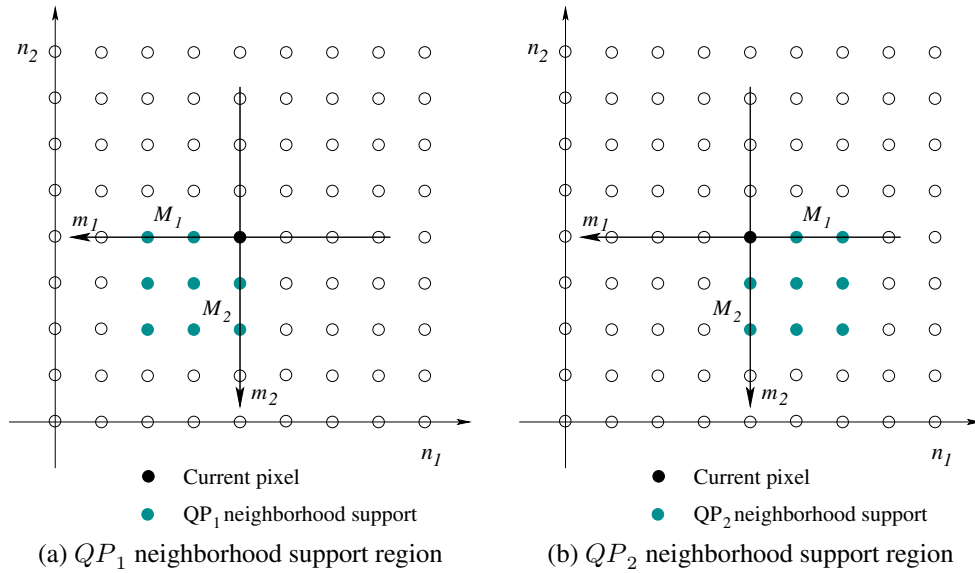


Figure 3.5:  $QP_1$  and  $QP_2$  neighborhood support regions for model order  $(M_1, M_2)$  with  $M_1 = 2$  and  $M_2 = 2$ .

For 2D multichannel complex QP AR model also, we have  $S_{e,\nu} = \Sigma_e$  which consequently gives us two  $2 \times 2$  complex matrices  $\Sigma_{e,1}$  and  $\Sigma_{e,2}$  for each of the quarter planes as  $P = 2$  for IHLS and L\*a\*b\* color spaces and two  $3 \times 3$  real matrices in the case of RGB color space. The 2D PSD matrices estimated with 2D  $A_m^{QP_1}$  and  $A_m^{QP_2}$  parameters have a general form same as expressed in Equation (3.19) and can be written as:

$$\hat{S}_\nu^{QP_1} = \hat{A}_\nu^{QP_1^{-1}} \hat{\Sigma}_{e,1} \left( \hat{A}_\nu^{QP_1^H} \right)^{-1} \quad (3.22)$$

and

$$\hat{S}_\nu^{QP_2} = \hat{A}_\nu^{QP_2^{-1}} \hat{\Sigma}_{e,2} \left( \hat{A}_\nu^{QP_2^H} \right)^{-1} \quad (3.23)$$

where the matrices  $\hat{A}_\nu^{QP_1^{-1}}$  and  $\hat{A}_\nu^{QP_2^{-1}}$  can be estimated using the complex coefficient matrices  $A_m^{QP_1}$  and  $A_m^{QP_2}$  through the Equation (3.14) with  $D = D_{M_1, M_2}^{QP_1}$  and  $D = D_{M_1, M_2}^{QP_2}$  respectively.

Besides the desired inherited characteristics presented by the parametric spectral estimates computed through these multichannel complex causal models *i.e.* both NSHP AR and QP AR, they also inherit the problems of their 2D scalar versions. These include:

- Highly conditioned estimate of PSD, even at higher model orders.
- Optimal frequency localization is compromised.
- Dissymmetry of energy due to the particular form of the neighborhood support region.

To resolve all these problems we propose the matrix version of the idea proposed in [JC79, KT81, ACRN98]. We propose to use the HM estimate being computed through the two causal neighborhood support regions. Mathematically this HM, over the two estimated PSD matrices is calculated as:

$$\hat{S}_\nu^{QPHM} = \left[ \frac{1}{2} \times \left( \hat{S}_\nu^{QP_1^{-1}} + \hat{S}_\nu^{QP_2^{-1}} \right) \right]^{-1} \quad (3.24)$$

where  $\hat{S}_\nu^{QP_1}$  and  $\hat{S}_\nu^{QP_2}$  are the 2D PSD matrices estimated using Equations (3.22) and (3.23) respectively. As stated in [Gar08] for 2D scalar version of this estimate, the matrix version also is an empirical estimation yet it exhibits following advantages (cf. section 3.4):

- PSD anisotropy shown by causal models is significantly reduced.
- Spurious lobes disappear.
- Spectral resolution of the estimate is increased.

### 3.3.2 Non-Causal Models

It is possible that an observation in a 2D random field may depend on its neighboring observations in all directions unlike the case in NSHP or QP AR model and thus making the model non-causal. There exist the possibilities for AR models to have a non-causal supports, examples of which are 2D AR with non-causal neighborhood support region [Gar08] and 2D SAR models [MJ92]. Here we consider a special case of linear prediction models with non-causal neighborhood support region *i.e.* 2D GMRF model [Gar08].

#### 2D Multichannel Complex GMRF Model

A multichannel 2D GMRF process is defined by the Equations (3.11) and (3.12). For a model order  $M$ ,  $D = D_M^{GMRF}$  is a non-causal, symmetric neighborhood excluding the origin  $(0, 0)$  such that if  $\{m \in D_M^{GMRF}\}$  then  $\{-m \in D_M^{GMRF}\}$ . Such a support is defined as:

$$\Omega_1 = \left\{ m, \underset{m \neq (0,0)}{\operatorname{argmin}} \|m\|_2 \right\} \quad (3.25a)$$

$$\Omega_k = \left\{ m, \underset{m \notin \bigcup_{1 \leq p \leq k-1} \Omega_p}{\operatorname{argmin}} \|m\|_2, m \neq (0, 0) \right\}, k > 1 \quad (3.25b)$$

$$D_M^{GMRF} = \bigcup_{1 \leq k \leq M} \Omega_k \quad (3.25c)$$

where  $\|m\|_2 = \sqrt{m_1^2 + m_2^2}$ . An example for such neighborhood support region is shown in Figure 3.6. In the case of 2D multichannel complex GMRF  $E = \{E_n\}_{n \in \mathbb{Z}^2}$  is a 2D multichannel complex Gaussian correlated noise sequence which has a  $P \times P$  covariance matrix denoted by  $\Sigma_e$ . GMRF model parameter matrices  $A_m^{GMRF}$  are estimated again by solving a system of normal equations using the least squares method. These GMRF model parameters are then used to estimate the PSD matrix of the process  $X$ . It can be verified that the PSD matrix for the 2D multichannel complex valued GMRF is given as:

$$\hat{S}_\nu^{GMRF} = \Sigma_e \times (A_\nu^H)^{-1} \quad (3.26)$$

where  $A_\nu$  is given by Equation (3.14), leading to:

$$S_{e,\nu} = A_\nu \Sigma_e \quad (3.27)$$

This shows that  $E$  is a correlated noise sequence. As in the case of 2D NSHP AR spectrum estimation, the PSD matrix contains both the auto and cross spectra of the luminance and chrominance channels as given in Equation (3.16).

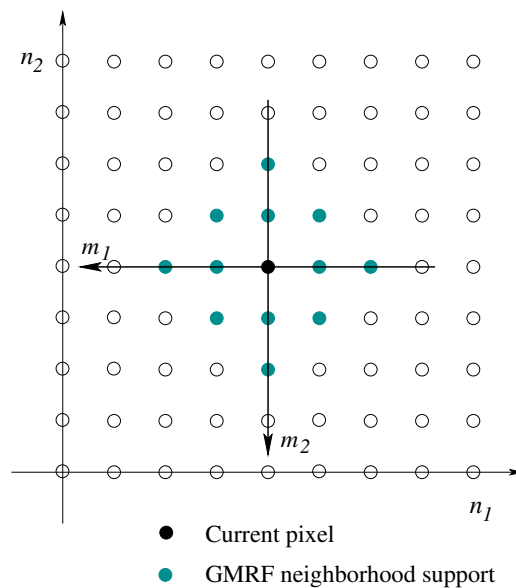


Figure 3.6: GMRF neighborhood support region for model order  $M$  with  $M = 3$ .

## 3.4 Experiments and Results

To validate experimentally, the conceived theoretical approach of using two dimensional multichannel complex random field models as precise spectrum estimators, large number of experiments were performed. These included simulations for the estimation of model parameters and consequently the estimation of power spectrum using multichannel complex versions (proposed in the section 3.3) of 2D NSHP AR, 2D QP AR model via HM method and 2D GMRF models. Experimental procedures for these simulations and the obtained results are presented in the next subsections. The approach is evaluated on the two notions of spectral estimator comparison and the used color space comparison.

### 3.4.1 Sinusoidal Data - The Chroma Sinusoids

To have a preliminary evaluation of the color spectral estimation approach on the proposed two channel complex color image (cf. section 3.2), two such images were simulated through 2D two channel sinusoidal image data. These sinusoidal images were generated supposedly being in the perceptual color space under consideration *i.e.* IHLS or  $L^*a^*b^*$  in the following manner:

A 2D real sinusoid  $x_1 = \{x_{1,n}\}_{n \in \Lambda}$  was generated to simulate the real valued luminance channel of the two channel image expressed by the Equation 3.10:

$$x_{1,n} = A_r \cos(2\pi\langle n, \nu_r \rangle + \phi_r) \quad (3.28)$$

where  $A_r$ ,  $\nu_r$  and  $\phi_r$  are the amplitude, frequency and phase angle of the real sinusoid respectively. Another complex sinusoid  $x_2 = \{x_{2,n}\}_{n \in \Lambda}$  was generated to simulate the complex valued chrominance channel as :

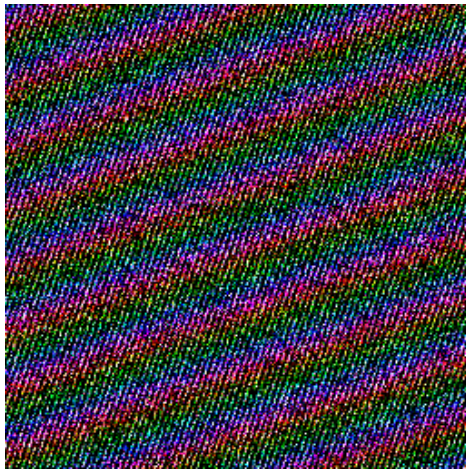
$$x_{2,n} = A_c \exp(j\phi_c) \times \exp(j2\pi\langle n, \nu_c \rangle) \quad (3.29)$$

where  $A_c$ ,  $\nu_c$  and  $\phi_c$  are the amplitude, frequency and phase angle of the complex sinusoid respectively. We term this complex 2D sinusoid as the **Chroma Sinusoid**. It contains the pure color information and forms the complex *combined* chrominance channel of the two channel sinusoidal test images. These real and complex 2D sinusoids are stacked together to simulate the two channel complex color image.

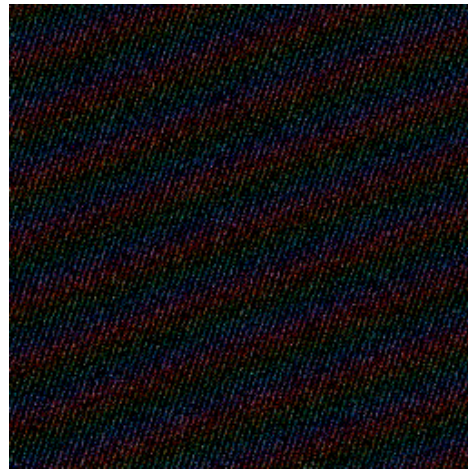
One way for spectral analysis of such images could be to analyze these images directly, but this would give us negligible information about the characteristics of the color transformations. To avoid this we proceed in the following way:

1. Generate the two channel complex color image supposedly in one of the perceptual color spaces *i.e.* IHLS or L\*a\*b\* by generating 2D sinusoids using Equations (3.28) and (3.29) and stacking them together.
2. Convert the two channel image to RGB color space using IHLS to RGB or L\*a\*b\* to RGB (whichever applicable) transformation.
3. Add RGB Gaussian noise to this RGB image in such a way that the final noisy RGB image has a controlled signal to noise ratio (*SNR*).
4. Convert this noisy RGB image to the perceptual color space in which it was generated in step 1 using RGB to IHLS or RGB to L\*a\*b transformation.
5. Use the Equations (3.8) or (3.9) with the Equation (3.10) to form the final two channel complex noisy sinusoidal color image.

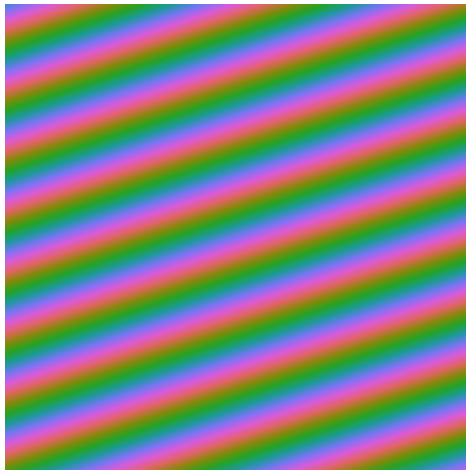
Examples of such noisy sinusoidal images in RGB color space *i.e.* the ones computed after the step 3 in IHLS and L\*a\*b\* color spaces are shown in Figures 3.7a and 3.7b for which ( $A_r = 0.5$  and  $A_c = 0.5$ ), ( $\phi_r = 30^\circ$  and  $\phi_c = 30^\circ$ ) and ( $\nu_r = (0.3, -0.1)$  and  $\nu_c = (0.1, -0.3)$ ). The RGB converted *chroma sinusoids* associated to these images in respective color spaces are shown in Figures 3.7c and 3.7d for which luminance is kept constant. These images in Figure 3.7, *i.e.* for both noisy sinusoids and *chroma sinusoids*,  $\nu_c$  is reduced by a factor of 10



(a) Noisy sinusoid in IHLS color space



(b) Noisy sinusoid in L\*a\*b\* color space



(c) Chroma sinusoid in IHLS color space



(d) Chroma sinusoid in L\*a\*b\* color space

**Figure 3.7:** RGB converted noisy Sinusoidal images and their respective chroma sinusoids supposedly generated in IHLS and L\*a\*b\* color spaces. For 3.7a and 3.7b, ( $A_r = 0.5$  and  $A_c = 0.5$ ), ( $\phi_r = 30^\circ$  and  $\phi_c = 30^\circ$ ) and ( $\nu_r = (0.3, -0.1)$  and  $\nu_c = (0.01, -0.03)$ ).

for better visualization of the chromatic spatial variations characterized by this sinusoid.

In the next subsection we present the performance comparison and analysis of the different parametric color spectral estimators proposed in the section 3.3.

### 3.4.2 Spectral Estimator Performance Analysis

The comparison and performance analysis of the different 2D complex multichannel parametric models for color spectral analysis can be carried out based on two criteria:

- Visual analysis *i.e.* To analyze the symmetry of the energy in the estimated spectra around the sinusoidal frequency peak, presence of spurious peaks etc.
- Statistical analysis *i.e.* To generate sufficient number of sinusoidal image samples and analyze the estimation accuracy by comparing different parameters for these estimates. These spectra are continuous in nature. Therefore one has to use a method for multidimensional constrained/unconstrained minimization to evaluate the accuracy of the spectral estimates in terms of estimated amplitude as well as frequency localization. Here, we used a widely known direct search method, named as the Nelder-Mead simplex algorithm, stated in [LRWW98].

#### Visual Comparison

For the visual analysis, PSD estimates for the sinusoidal image generated through the procedure stated in the section 3.4.1 are generated. The PSD estimates for this image computed using different models discussed in the section 3.3, in IHLS and  $L^*a^*b^*$  color spaces are shown in Figures 3.8 and 3.9 respectively.

In Figures 3.8 and 3.9, the first row (3.8a and 3.9a) shows the sinusoidal test image in IHLS and  $L^*a^*b^*$  color spaces respectively. The second rows of both these figures show the magnitude spectrum of the luminance (3.8b and 3.9b) and the chrominance (3.8c and 3.9c) channels of the respective sinusoidal images. These magnitude spectra are computed through 2D FFT applied on the luminance and the chrominance channels of each image separately. Third rows show the auto spectra estimates of the luminance (3.8d and 3.9d) and chrominance (3.8e and 3.9e) channels using 2D multichannel GMRF model of order 14 in the two color spaces. Luminance (3.8f and 3.9f) and chrominance (3.8f and 3.9f) autospectra estimated using 2D multichannel NSHP AR model of order (4, 4) are shown in the row four of these figures. Row five shows the estimates for luminance (3.8h and 3.9h) and chrominance (3.8i and 3.9i) channels using 2D multichannel QP AR model via HM method of order (4, 4). The model orders for these models are chosen in such a way that the number of free parameters remain the same and hence to facilitate the comparison between the different models.

Analyzing the different spectral estimates certain observations regarding the nature of the model used can be made. It is to note that, the parameters of both

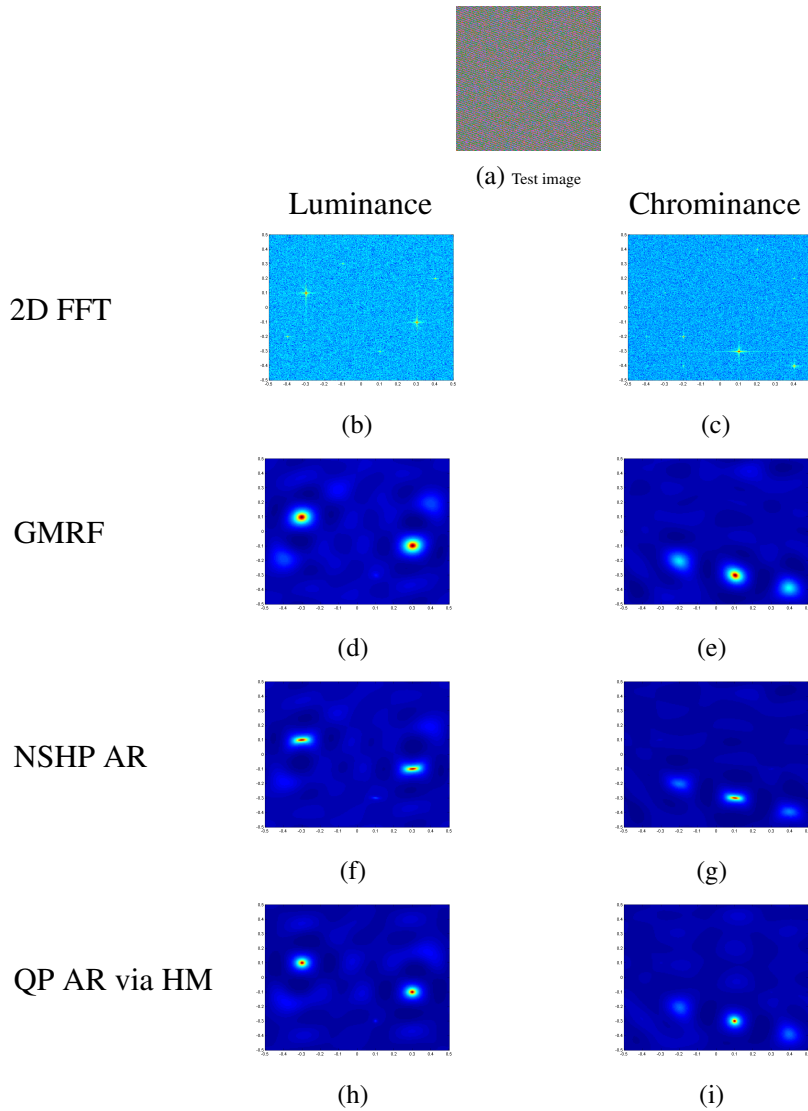


Figure 3.8: The sinusoidal test image (3.8a) in IHLS color space and the magnitude spectrum of the luminance 3.8b and the chrominance 3.8c channels computed through 2D FFT are shown. Also, auto spectra estimates of these two channels using GMRF model of order 14 (3.8d and 3.8e respectively), NSHP AR model of order (4, 4) (3.8f and 3.8g respectively), QP AR model via HM method of order (4, 4) (3.8h and 3.8i respectively) are presented.

the causal models are estimated using the Least Squares Estimation ( $LSE$ ). For these causal models we assume the process to be Gaussian, therefore the LSE of model parameters is the same as the MLE. In the case of NSHP the estimates of sinusoidal frequency peaks have elongated shape (Figures 3.8f, 3.8g, 3.9f and 3.9g). For QP AR model via HM method, the effect of harmonic mean being

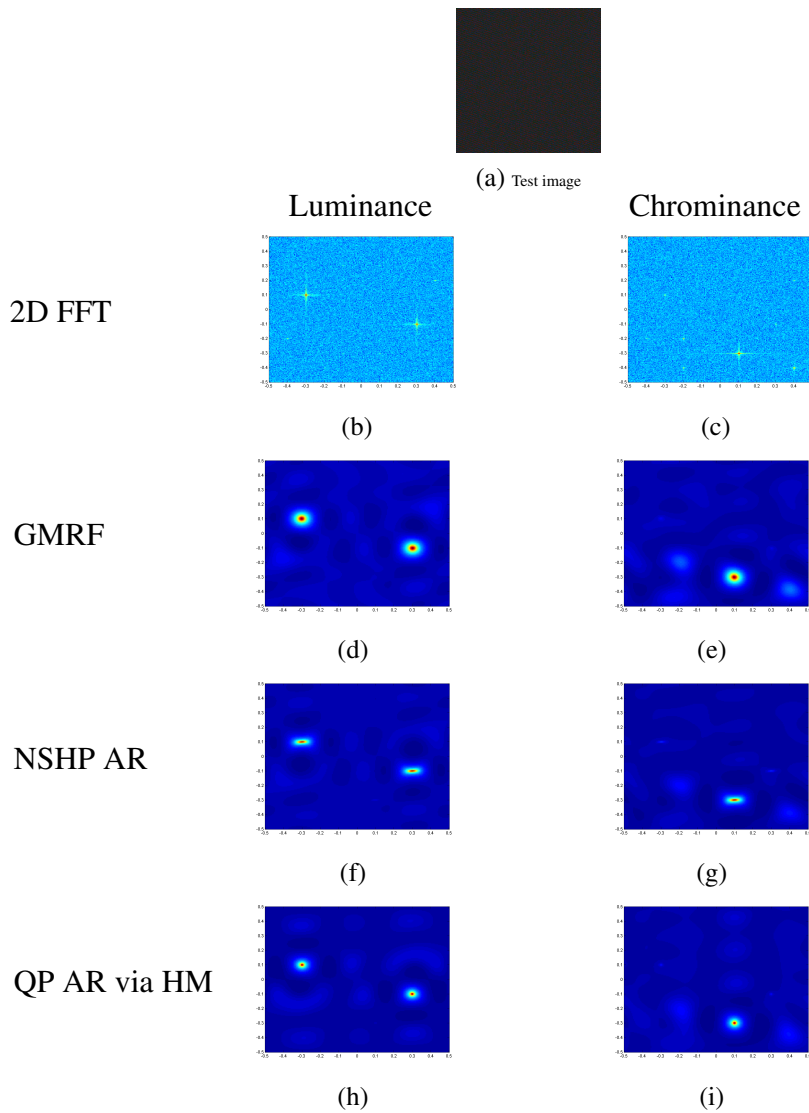


Figure 3.9: The sinusoidal test image (3.9a) in  $L^*a^*b^*$  color space and the magnitude spectrum of the luminance 3.9b and the chrominance 3.9c channels computed through 2D FFT are shown. Also, auto spectra estimates of these two channels using GMRF model of order 14 (3.9d and 3.9e respectively), NSHP AR model of order (4, 4) (3.9f and 3.9g respectively), QP AR model via HM method of order (4, 4) (3.9h and 3.9i respectively) are presented.

computed on two opposite quadrants of neighborhood support region gives us a much precise frequency estimate of the frequency peak with a good circular shape (Figures 3.8h, 3.8i, 3.9h and 3.9i). These behaviors of 2D multichannel complex versions of these models are same as of their 2D scalar versions [Gar08].

In the case of the GMRF model, symmetry of the neighborhood support region around a pixel gives us a well circular shape but rather in the form of a larger lobe (Figures 3.8d, 3.8e, 3.9d and 3.9e). This larger lobe represents a less precisely estimated location of the frequency peak despite of a symmetric, non-causal neighborhood support region having same number of free model parameters used to predict each observation as compared to the causal AR models. This larger lobe also depicts the low *frequency resolution* of the estimated spectra using the LSE for GMRF model parameter estimation.

### Statistical Comparison

To compare statistically, spectrum estimation given by the three models presented above, a number of tests were carried out on multichannel sinusoidal images of size  $n \times n$ , where  $n \in \{24, 32, 40, 48, 56, 64\}$ . Use of different image sizes for spectral analysis permits to study the effects of the total number of observations on spectral estimates. The image size  $n$ , is limited to  $64 \times 64$  to counter the heavy computational loads of spectral estimates, yet these sizes give us a precise idea about spectral estimates of the different image sizes. For each value of  $n$ , twenty images of the same amplitude ( $A_r = 0.5$  and  $A_c = 0.5$ ), ( $\phi_r = 30^\circ$  and  $\phi_c = 30^\circ$ ) and ( $\nu_r = (0.3, -0.1)$  and  $\nu_c = (0.1, -0.3)$ ) were generated to serve as a test set, using twenty different multichannel noise sequences. The spectral estimates were computed for three different levels of the SNR *i.e.*  $\text{SNR} \in \{-3, 0, 3\}$  dB. This configuration of parameters provided us a total of 720 images for the two considered color spaces, for each model. These image sizes and test parameters are the same as the ones used in [Gar08] for parametric spectral analysis through 2D single channel real linear prediction models.

The mean error plots for horizontal and vertical frequency estimates of both luminance and chrominance channels of the generated sinusoidal images in IHLS and L\*a\*b\* color spaces are shown the Figures 3.10, 3.11, 3.12 and 3.13 respectively. While the log variance of the estimation error for horizontal and vertical frequency estimates of both luminance and chrominance channels of the generated sinusoidal images in IHLS and L\*a\*b\* color spaces are shown in Figures 3.14, 3.15, 3.16 and 3.17 respectively.

It is important to note that the results obtained for both log variance and mean error over such a large database of 2D complex multichannel sinusoidal images correspond very well to the results obtained from the 2D single channel real linear prediction models applied in [Gar08]. This coherence of both the results provides an experimental validation to the theoretical basis of the approach being adopted for multichannel complex versions of the discussed models.

We can see that for all of the models, as the number of observations *i.e.* image size in our case, increases, the mean error of the spectral estimate decreases.

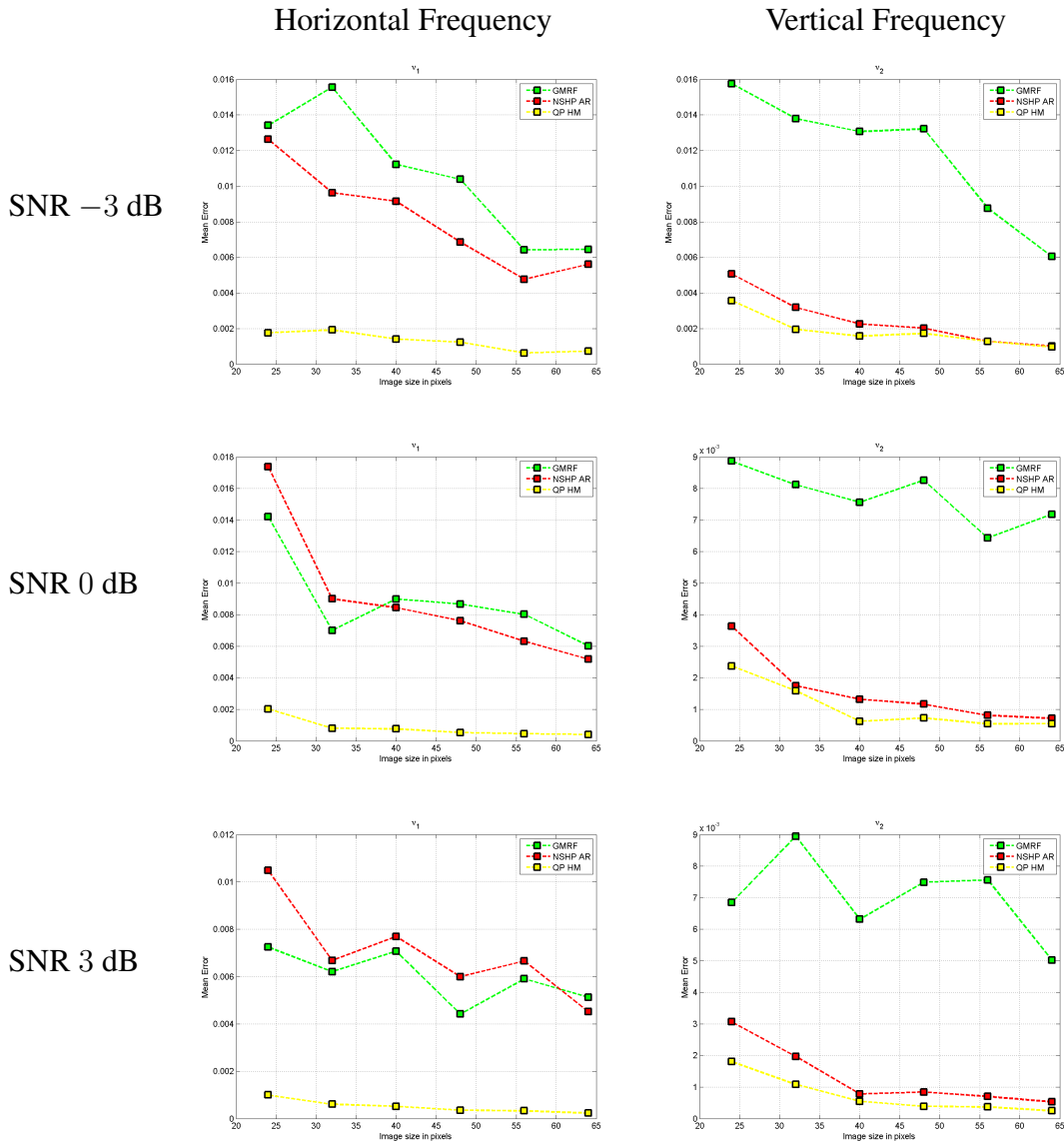


Figure 3.10: Mean Error plots of horizontal and vertical frequency estimates against the varying image size  $n$ , for luminance channel in IHLS color space, for different values of SNR.

This proves the estimation method to be correct. This statistical comparison indicates that QP AR model via HM method gives us the best results in terms of the mean error of both horizontal and vertical frequency estimates. In the case of 2D complex multichannel NSHP model, non-symmetric neighborhood support region along horizontal and vertical axis of the image gives us a scale shift in the curve although the basic tendency of curve is preserved in both type of plots. For

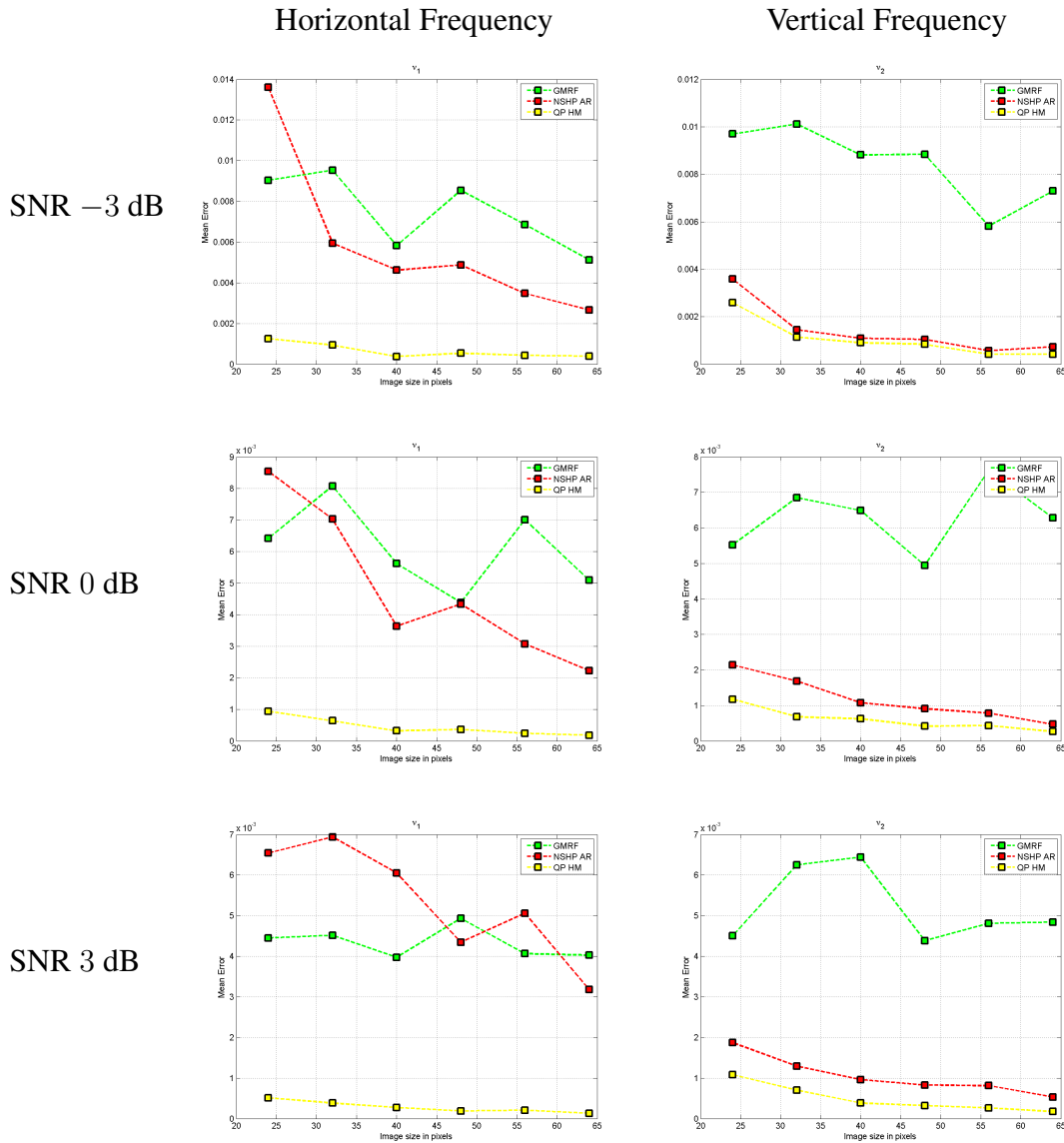


Figure 3.11: Mean Error plots of horizontal and vertical frequency estimates against the varying image size  $n$ , for chrominance channel in IHLs color space, for different values of SNR.

increasing values of SNR, the mean error decreases which shows another mathematical conformance of the approach to the 2D scalar version of the same.

Same trends are observed for the log variance plots for horizontal and vertical frequency estimates, computed through the three models against test images of different sizes and different values of SNR in both IHLs and  $L^*a^*b^*$  color spaces.

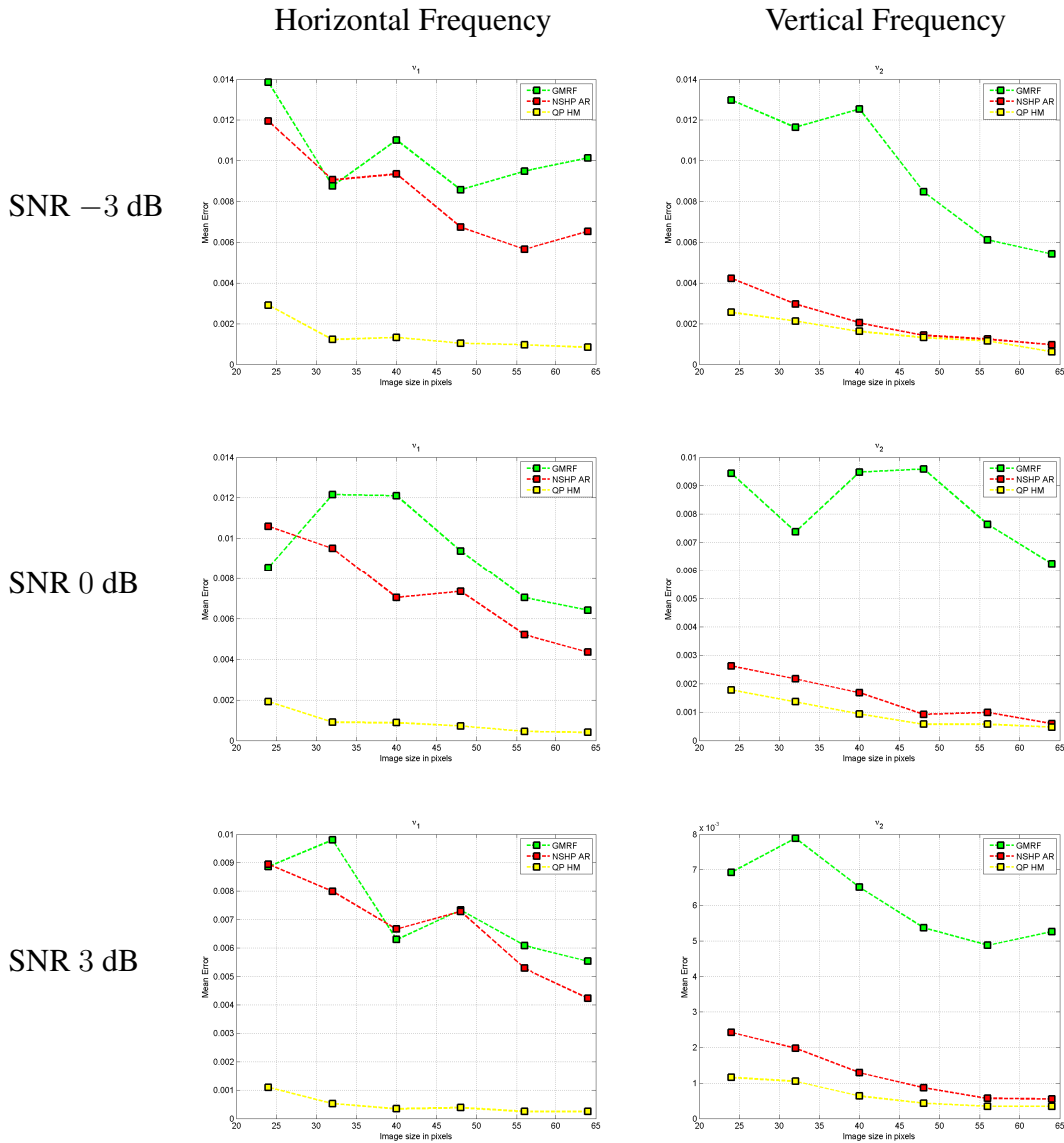


Figure 3.12: Mean Error plots of horizontal and vertical frequency estimates against the varying image size  $n$ , for luminance channel in  $L^*a^*b^*$  color space, for different values of SNR.

In these curves we again see an overall better performance of the QP AR model via the HM method.

The performance shown by 2D multichannel complex GMRF model clearly depicts the nature of the parameter estimation method used. The parameter estimation method in our approach is the same for all the models *i.e.* the LSE by solving a system of normal equations (see Section 3.3.2). This is done so to facil-

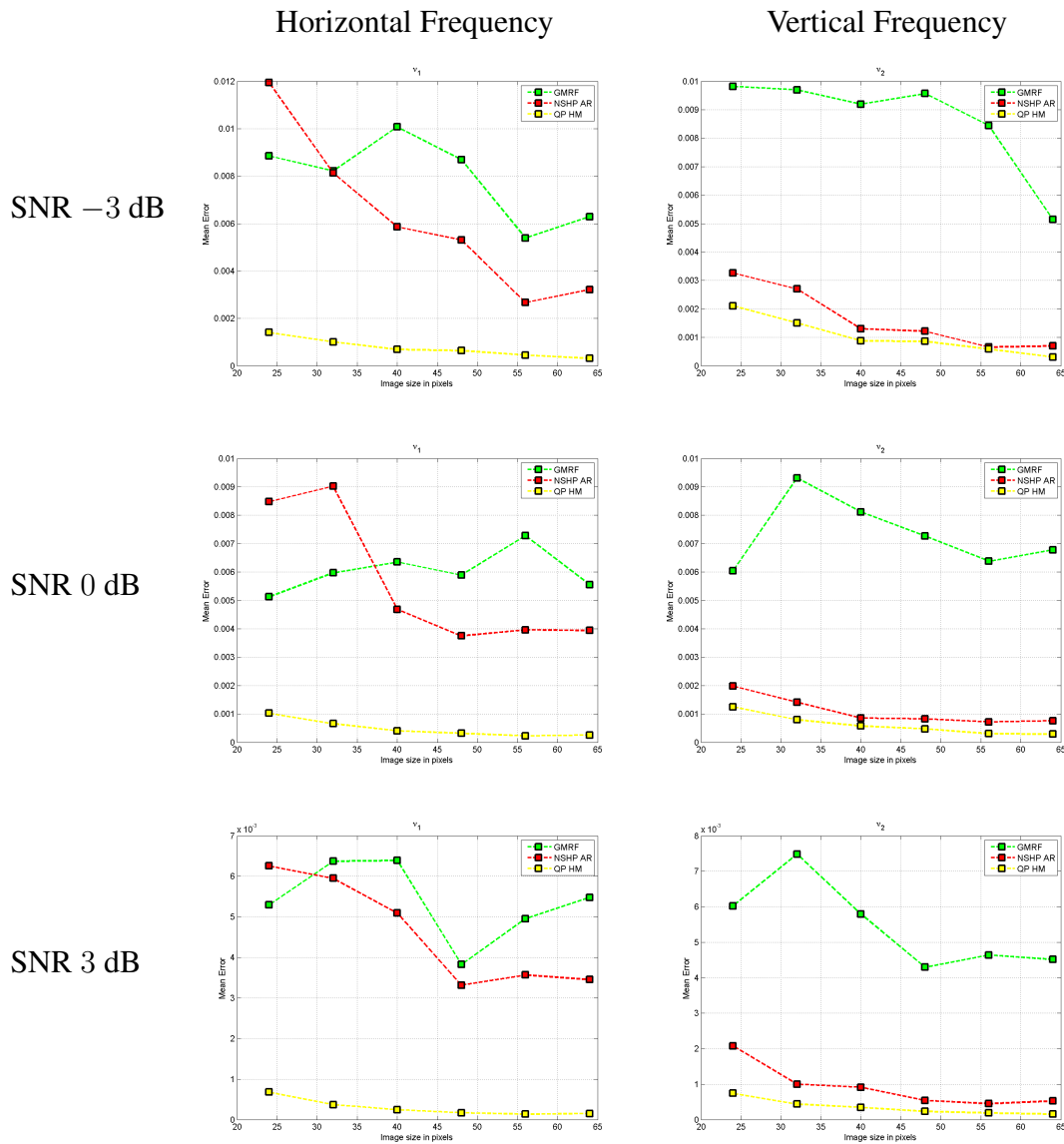


Figure 3.13: Mean Error plots of horizontal and vertical frequency estimates against the varying image size  $n$ , for chrominance channel in  $L^*a^*b^*$  color space, for different values of SNR.

iterate the comparison of the different models for this type of spectral estimation. Unlike in causal AR models, in the case of GMRF with a Gaussian assumption, the LSE method does not give the same parameter estimates as the MLE. In the case of 2D multichannel complex GMRF model, the MLE of model parameters may improve the results [BJC95]. We do not present the spectral analysis results

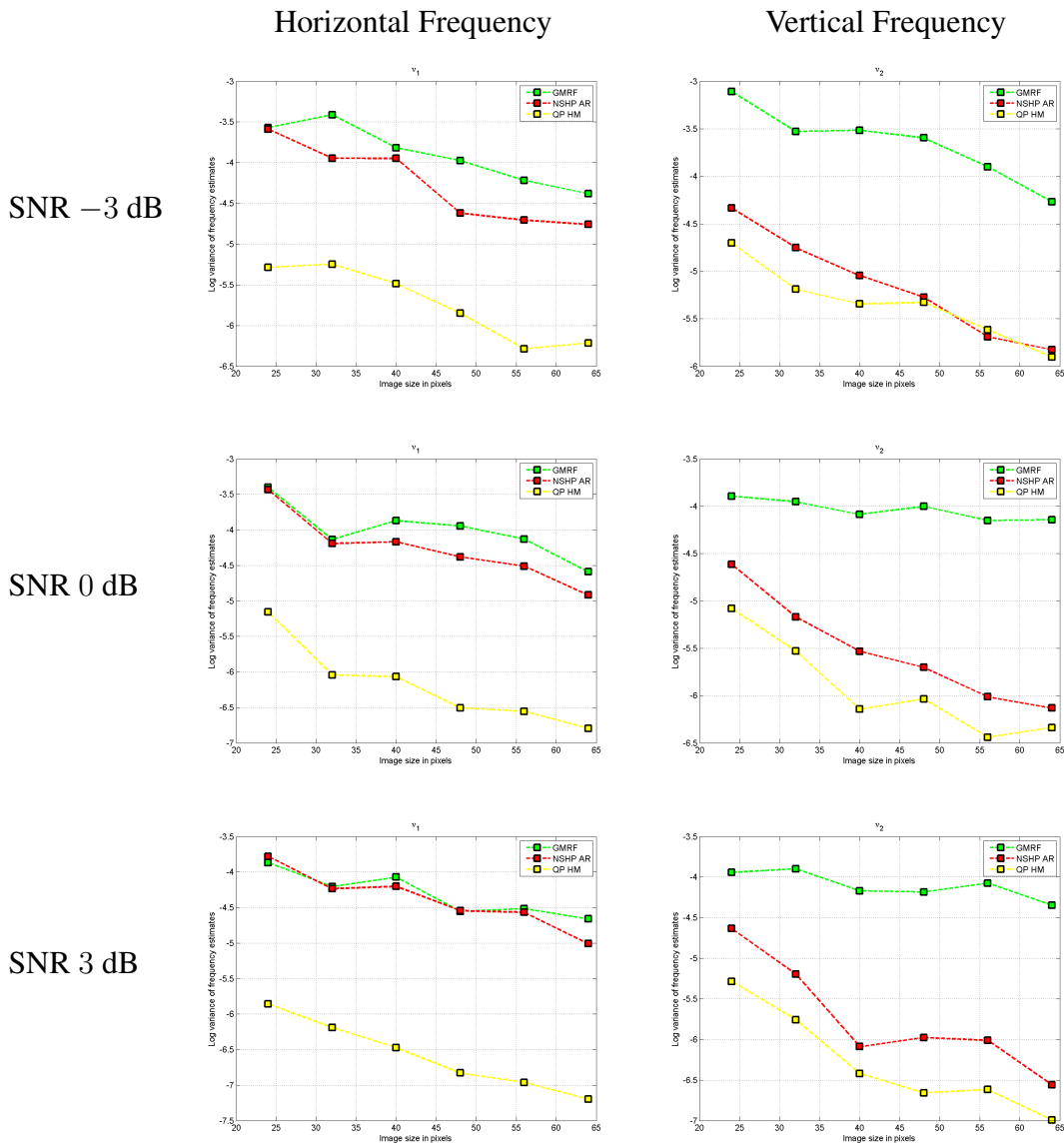


Figure 3.14: Log variance of estimation error of horizontal and vertical frequency estimates against the varying image size  $n$ , for luminance channel in IHLS color space, for different values of SNR.

of GMRF using MLE method to avoid heavy computational loads of the method in the case of the 2D multichannel complex GMRF model.

If we compare these results obtained in the two color spaces, we observe that there is a slight improvement in the spectral estimates computed in the  $L^*a^*b$  as compared to the ones in the IHLS color space. This difference can be observed in

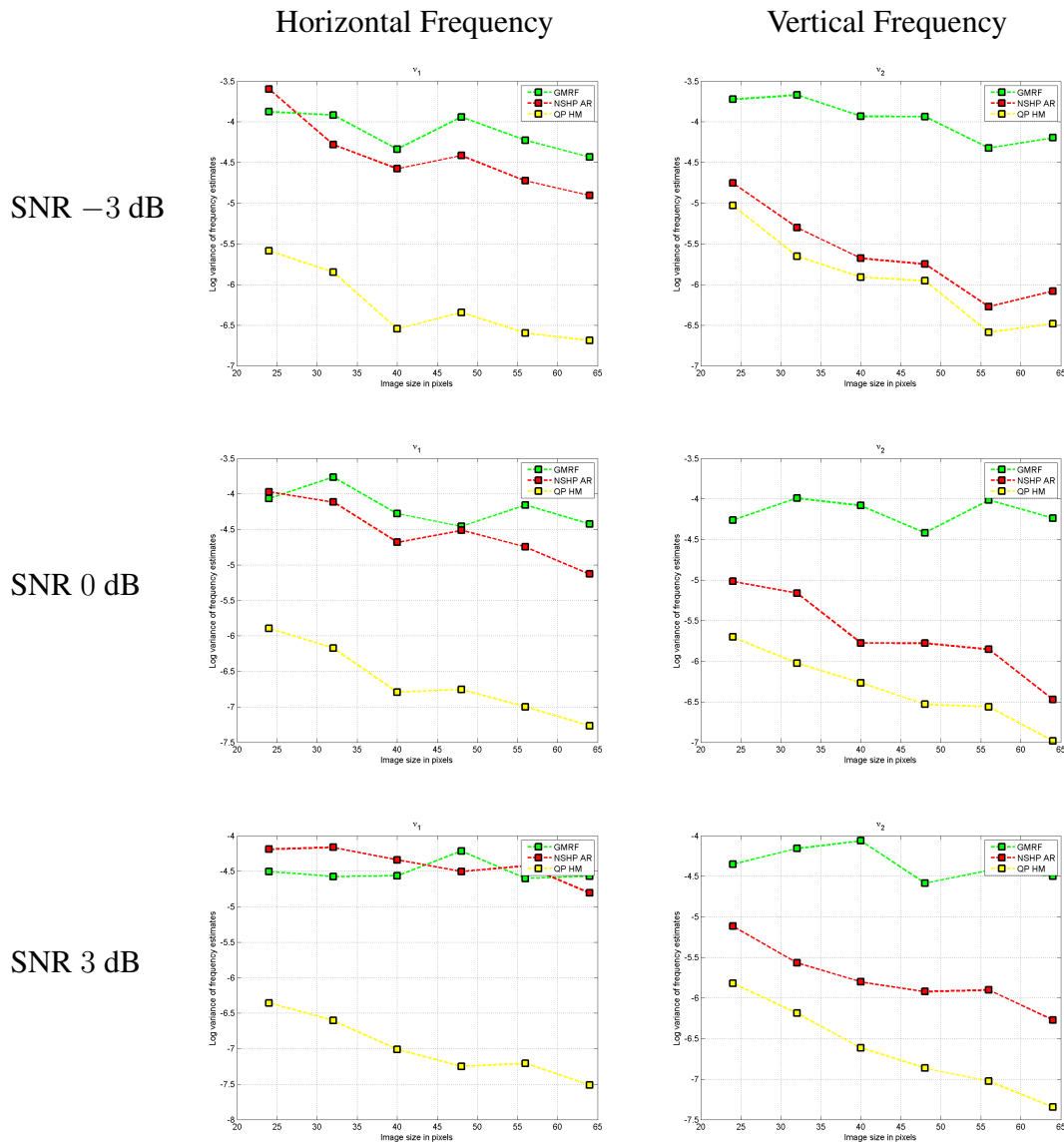


Figure 3.15: Log variance of estimation error of horizontal and vertical frequency estimates against the varying image size  $n$ , for chrominance channel in IHLS color space, for different values of SNR.

the plots of both the parameters *i.e.* mean error and the log variance for horizontal as well as vertical frequencies.

In this section we have analyzed the performance of the different spectral estimators used for the parametric spectral estimation of the generated two channel

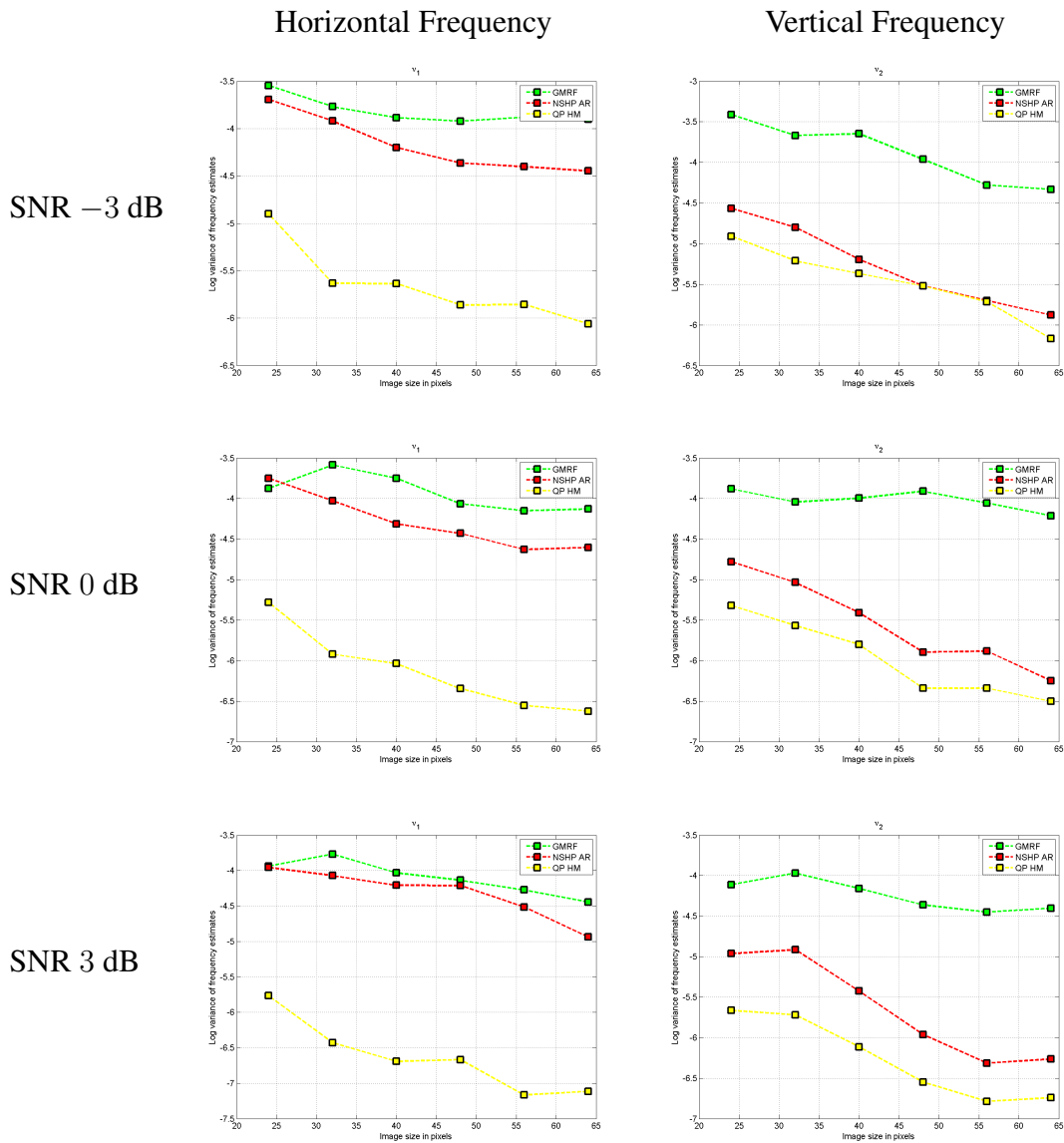


Figure 3.16: Log variance of estimation error of horizontal and vertical frequency estimates against the varying image size  $n$ , for luminance channel in  $L^*a^*b^*$  color space, for different values of SNR.

sinusoidal images. Another important aspect is to compare the spectral estimation achieved in the two used color spaces. This, we will discuss in the next section.

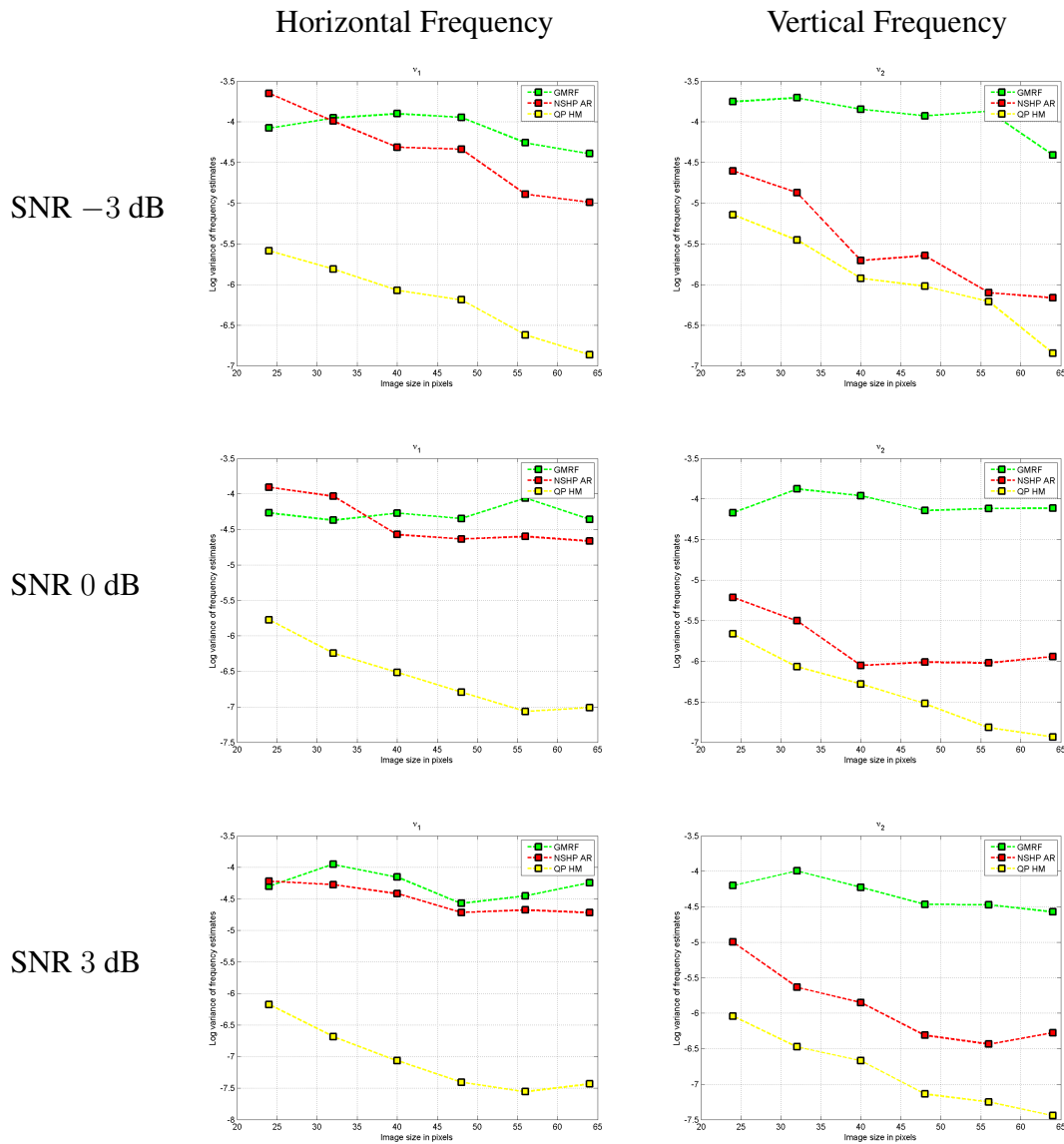


Figure 3.17: Log variance of estimation error of horizontal and vertical frequency estimates against the varying image size  $n$ , for chrominance channel in L\*a\*b\* color space, for different values of SNR.

### 3.4.3 Color Space Comparison

If we observe closely, the images shown in Figures 3.8 and 3.9, it is clear from the figures that we observe an extra frequency peak in the luminance channel auto spectrum in the case of IHLS color space. This frequency peak is localized at the normalized frequency position of the chrominance channel. However the spectral

estimate of the image generated with same parameters in  $L^*a^*b^*$  color space shows negligible interference of this chrominance in the luminance channel.

Similarly we see extra peaks in the power spectrum of the chrominance channel in the case of  $L^*a^*b^*$  color space. These peaks are localized at the normalized frequency location of the luminance frequency *i.e.*  $\nu_r$ . However, the same phenomenon is not significantly visible in the case of the image generated in the IHLS color space.

To observe these phenomenon clearly, spectral estimates for the luminance and chrominance channels of the sinusoidal test image in Figures 3.8 and 3.9 are computed again through 2D multichannel complex QP AR model via HM method with a model order (5, 5) and are presented in Figure 3.18. The two channel com-

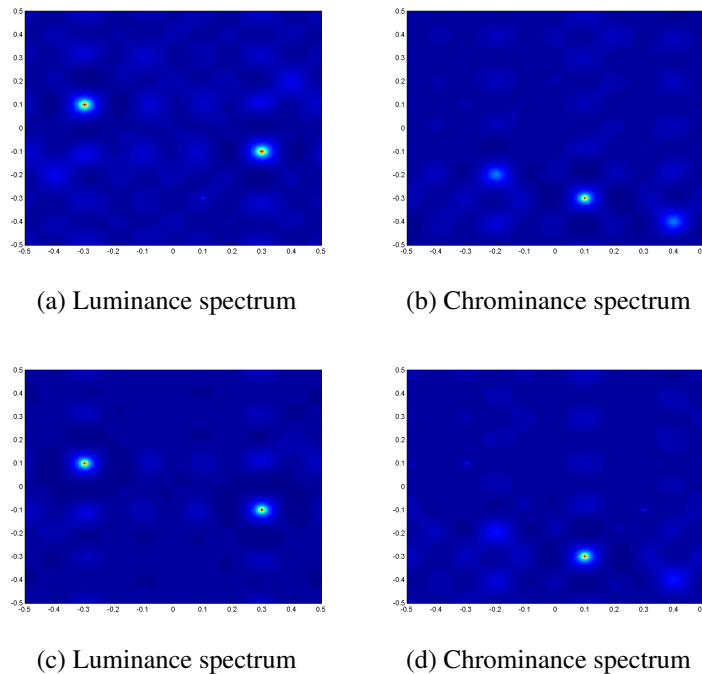


Figure 3.18: Estimated PSD of the luminance and the chrominance channels in IHLS (a,b) and  $L^*a^*b^*$  (c,d) with 2D multichannel complex QP AR model via HM method with a model order (5, 5).

plex sinusoidal images used in these tests are generated in perceptual color spaces *i.e.* IHLS or  $L^*a^*b^*$ , transformed to RGB and again re-transformed to the perceptual color spaces before spectrum estimation (cf. section 3.4.1). To observe the inter-channel interference in the RGB color space, the image with the same parameters are generated in the perceptual color spaces and transformed to the

RGB color space. Then noise is added to this RGB image. The spectral estimates of this noisy image (in RGB color space) computed through 2D multichannel real QP AR model via HM method with a model order (5, 5) are presented in Figure 3.19. As in the case of RGB color space the model is real, therefore we observe the spectral symmetry for both the sinusoidal frequencies which appear in all the three planes. As we base our approach of color texture characterization

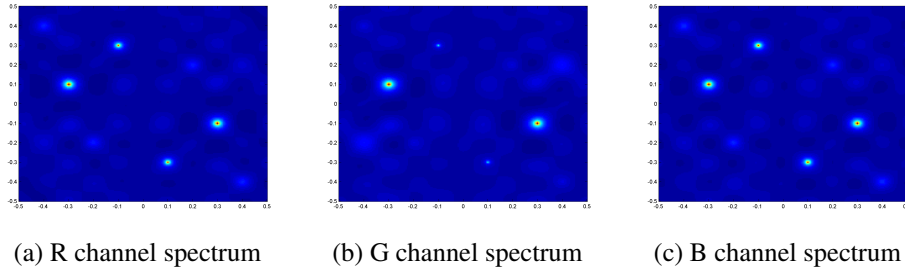


Figure 3.19: Estimated PSD of the Red, Green and Blue channels in RGB color space, with 2D multichannel real QP AR model via HM method.

on the degree of decorrelation of the luminance and chrominance information of a color image, therefore RGB having a significantly high degree of correlation between all the three channels, is not the best candidate for such an approach. However, this *luminance-chrominance spectral interference*, in the case of perceptual color spaces needs to be analyzed and quantified as we present in the next section.

### Luminance-Chrominance Spectral Interference

To have a quantitative overview of this interference we generated twenty (20) images, of size  $n \times n$  where  $n \in \{64, 96, 128, 160, 192, 224, 256\}$ , and each color space, of same amplitude ( $A_r = 0.25$  and  $A_c = 0.25$ ) and phase angle ( $\phi_r = 30^\circ$  and  $\phi_c = 30^\circ$ ), and with three different frequency sets. In these three frequency sets,  $\nu_r$  was kept the same *i.e.* (0.3, 0.3), whereas for complex channel of these two channel sinusoidal images,  $\nu_c \in \{(-0.3, 0.3), (0.3, -0.3), (-0.3, -0.3)\}$ .

It is to note that for all images, mean value for each channel is forced to zero. The spectral estimates were computed for three different levels of the SNR *i.e.*  $\text{SNR} \in \{-3, 0, 3\}$  dB. Then for these two perceptual color spaces, we quantify the level of the interference of the chrominance channel information in the luminance channel spectra through an interference ratio  $IR_{CL}$  defined as:

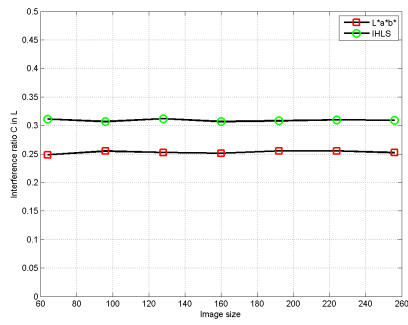
$$IR_{CL} = \frac{A_{cr}}{A_r} \quad (3.30)$$

where  $A_{cr}$  is the mean value of estimated chrominance peak found in luminance channel spectra of 20 image samples for a given image size  $n$ , a given frequency set  $(\nu_r, \nu_c)$  and a given SNR. We also define a quantitative measure in the same manner, to measure the interference of the luminance channel in the chrominance channel through an interference ratio  $IR_{LC}$  defined as:

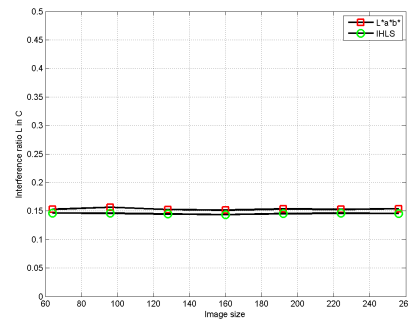
$$IR_{LC} = \frac{A_{rc}}{A_c} \quad (3.31)$$

where  $A_{rc}$  is the mean value of estimated luminance peaks found in chrominance channel spectra of 20 image samples for a given image size  $n$ , a given frequency set  $(\nu_r, \nu_c)$  and a given SNR. The spectra are estimated using only 2D multichannel complex QP AR model via HM method with a model order  $(2, 2)$ . Graphical representations of this ratio for different values of image size  $n$ , in both the color spaces are shown in Figure 3.20. In this figure, the results for the frequency set  $\{(0.3, 0.3), (0.3, -0.3)\}$  are presented. The Figures 3.20a, 3.20c and 3.20e represent the comparison of the interference levels of the chrominance peak in the autospectrum of the luminance channel for the two color spaces with SNR = -3 dB, SNR= 0 dB and SNR = 3 dB respectively. Similarly, the Figures 3.20b, 3.20d and 3.20f represent the comparison of the interference levels of the luminance peaks in the autospectrum of the chrominance channel for the two color spaces with SNR = -3 dB, SNR= 0 dB and SNR = 3 dB respectively. These plots are presented on a fixed scale for a better visual comparison and interpretation. Following important observations can be made over the results shown in Figure 3.20:

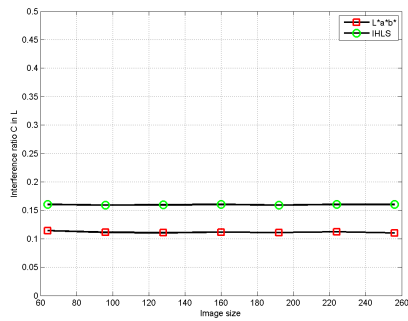
- Overall values of the interference ratio of the luminance spectral information in the chrominance autospectrum i.e.  $IR_{LC}$  are approximately one half of the overall values of the interference ratio of the chrominance spectral information in the luminance autospectrum i.e.  $IR_{CL}$ .
- For all the three values of SNR, if we analyze the plots of  $IR_{LC}$  values against varying image sizes, it becomes clear that the difference between the two color spaces is very marginal. Therefore, we can say that both the color spaces show approximately the same interference of luminance information in the chrominance channel.
- The interference ratio of chrominance in the auto spectrum of luminance channel i.e.  $IR_{CL}$  is more significant in the IHLS color space than that of L\*a\*b\* color space for all values of SNR.
- It is also clear that the value of the  $IR_{CL}$  reduces by approximately 50% with each 3dB increase in the SNR level. However, comparing the inter-



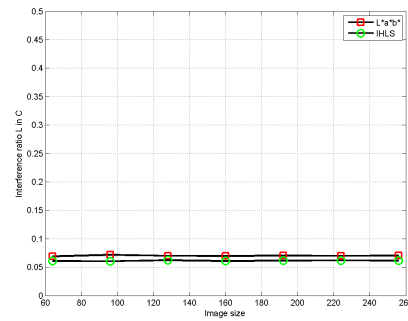
(a) SNR -3 dB



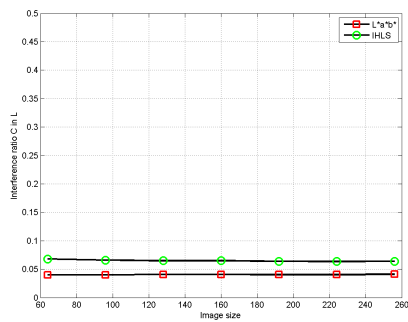
(b) SNR -3 dB



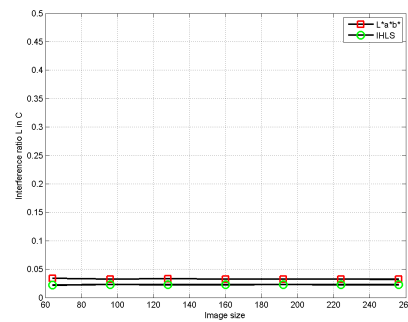
(c) SNR 0 dB



(d) SNR 0 dB



(e) SNR 3 dB



(f) SNR 3 dB

Figure 3.20: Comparison of the interference between luminance and chrominance information *i.e.*  $IR_{CL}$  (left) and  $IR_{LC}$  (right) in the two color spaces.

ference levels in the two color spaces,  $L^*a^*b^*$  continues to show lower interference than IHLS for different SNR levels.

- Interestingly at lower SNR values *i.e.* 0 and  $-3$  dB, the difference between the  $IR_{CL}$  values in the two color spaces increases at IHLS shows a higher interference than the  $L^*a^*b^*$  color space.

### 3.5 Conclusion

The main observations made and conclusions drawn from this chapter are:

- We presented a new luminance and combined chrominance based complex valued representation for color images in perceptual color spaces.
- In this chapter we have also theoretically adapted and successfully used the 2D multichannel complex linear prediction models for modeling of such two channel complex color images in perceptual color space like IHLS and  $L^*a^*b^*$  which has not been reported so far.
- We have presented a new parametric approach for model based combined power spectrum estimation for both luminance and combined chrominance channels in IHLS and  $L^*a^*b^*$  color spaces. Detailed analysis and performance comparison of these models have shown that all of these models exhibit satisfactory results for parametric color spectral estimation.
- A comparative analysis of luminance and chrominance information decorrelation in both the considered perceptual color spaces is done. The analysis, under varying test conditions *i.e.* different image sizes, varied noise levels and different frequency sets proved IHLS to exhibit more correlation of luminance and chrominance information than that of  $L^*a^*b^*$ .

This comparative analysis of perceptual color spaces is very important as we base our color texture descriptor on the luminance as well as chrominance spectral information characterization to an optimal level as well as the maximum decorrelation of the two information. Thus, we establish the hypothesis that higher the decorrelation of the channels, higher would be the performance of color texture characterization scheme, provided this scheme exploits this independence in an optimal way.

---

## CHAPTER 4

---

# COLOR TEXTURE CLASSIFICATION

---

The general methodology of the solution of the color texture classification or more specifically supervised color texture classification problem is to assign a certain class to a test color texture sample based on some *a priori* knowledge about that class of the color texture. This process, in practice can be divided in two steps: Training and Test. The first step training, is an off line process in which a certain number of color texture samples with known class affiliations are acquired, and various feature descriptors on these samples are computed and stored. The second step test, is an online process in which, for each new test image, a set of same type of features (as in the training step) are computed. Then, a decision on the class label assignment for this image, based on some similarity measure computed between the training and test features is made.

As the final decision is based on them, these feature descriptors computed from the training and test images, are of the critical importance in any color texture classification method. In chapter 2, we have presented the state of the art approaches of color texture description, for both classification and segmentation problems. Since most of these approaches do not exhibit optimal results, hence we propose to characterize the color texture content of both luminance and chrominance channels in an image, through the spectral estimates computed using the 2D multichannel complex linear prediction models (cf. chapter 3).

In this chapter we discuss the different color texture databases (section 4.1) used for the experiments along with the spatial structure and pure color feature cues (section 4.2) used for the description of color texture images. In section 4.3,

we represent the similarity measures and a probabilistic method for the fusion of these feature cues. Experiments for the comparison of different models and the color spaces used are presented in the section 4.4. Finally, section 4.5 concludes the chapter.

## 4.1 Color Texture Databases

We chose the test images for our experiments, from the two well known and widely used color texture databases Vistex [PGM<sup>+</sup>] and Outex [OMP<sup>+</sup>02]. Various research works addressing the color texture classification problem have used both Vistex [HCG<sup>+</sup>05, KBH06, CSF05, Pal04, ADB04] and Outex [MP04, PMV02, Sen08, ADB04].

In Vistex, unlike other texture collections, the images do not conform to rigid frontal plane perspectives and studio lighting conditions. Vistex color texture images are representative of real world conditions. Images in Vistex are available in different categories and sizes and contain both frontal and oblique type structures [PGM<sup>+</sup>].

The Outex database contains a large collection of surface textures captured under different specific and known conditions, which facilitates construction of a wide range of texture analysis problems. Different test suites are prepared for different texture analysis problems including classification, segmentation and retrieval. The images in Outex are taken with a fixed imaging geometry and with specified illumination source (a 2856 K incandescent CIE A light source). So differences between images are due only to a difference in medium.

We used three different data sets containing the images taken from these two databases for experimental validation of the color texture classification approach which we discuss in next sections.

### 4.1.1 Data Set 1

For the first data set which we denote as  $DS_1$  24,  $512 \times 512$  color texture images from the Vistex database, shown in Figure 4.1 were chosen. In  $DS_1$ , each  $512 \times 512$  image was considered as an individual class. For each textured color image *i.e.* for each class, the image feature cues were computed on the sub image blocks of size  $32 \times 32$ , hence forming 256 sub images for each image. Training data set for each color texture consisted of 96 sub images, while the remaining 160 sub images were used as the test data set, for each textured color image. By this configuration we had a total of 2304 training and 3840 test sub images in total. To be able to have a comparative look on the results, color textures chosen as  $DS_1$ , sub image size *i.e.*  $32 \times 32$  and number of sub images taken as training and test

data sets correspond to the ones presented in [PFJ06]. With smaller test image size and higher number of test sub images in  $DS_1$  we evaluated the ability of the approach to recognize and classify the textures even in the cases when very little spatial structure information is available.



Figure 4.1: The 24 textures of dimensions  $512 \times 512$  forming  $DS_1$ . From top left to bottom right, in raster scan order: Bark0; Bark12; Brick0; Clouds0; Fabric0; Fabric4; Fabric7; Fabric8; Fabric11; Fabric13; Fabric15; Fabric17; Fabric19; Flowers0; Food0; Grass1; Leaves12; Metal0; Misc2; Sand0; Stone4; Tile7; Water0; Wood2.

### 4.1.2 Data Set 2

In the second data set  $DS_2$ , 54 images from Vistex database are used. The 54 original Vistex images of dimensions  $512 \times 512$  were split into 16 samples of  $128 \times 128$ .  $DS_2$  is available on the Outex web site [Out] as test suite *Contrib\_TC\_00006*. For each texture, half of the samples were used in the training set and the other half served as testing data. The samples of the training set were the white squares of a draughtboard (beginning in the upper left corner) in order to consider a possible non uniformity of the original images.

### 4.1.3 Data Set 3

The third data set  $DS_3$  included 68 images of the Outex database [OMP<sup>+</sup>02]. From the 68 Outex images of size  $746 \times 538$  originally, 20 samples of size  $128 \times$

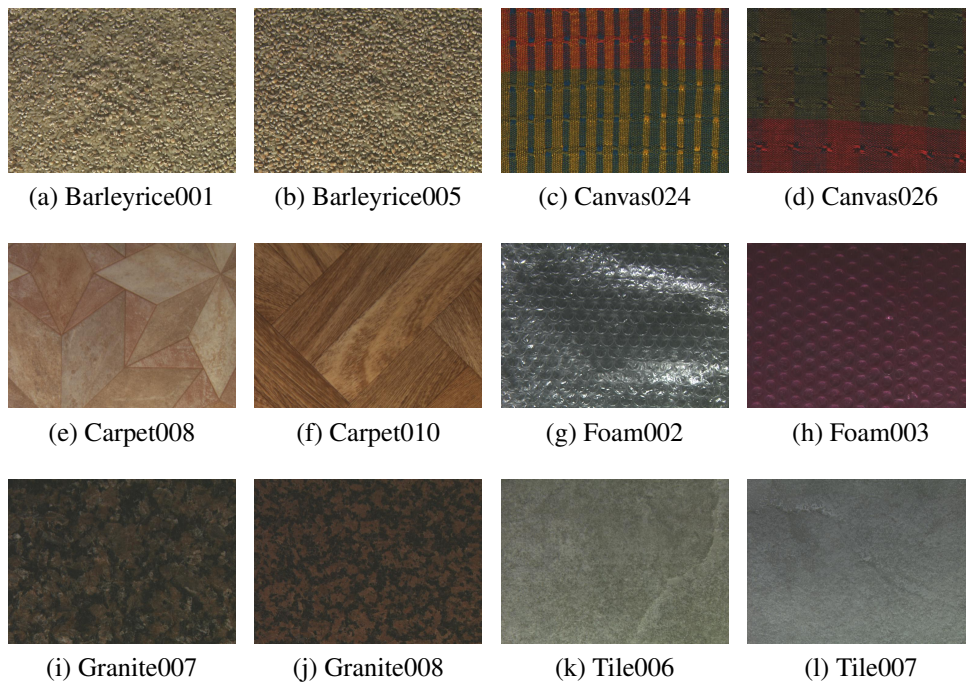


Figure 4.2: Sample textures from Outex color texture data base.

128 were obtained. The training and test sets were chosen in the same way as in  $DS_2$ , thus giving a total of 680 samples in each of training and test set. At the Outex site, this is the test suite *Outex\_TC\_00013*. Some sample textures from Outex database are shown in Figure 4.2.

## 4.2 Image Feature Cues

The spatial and spectral content of an image can be characterized and analyzed using different image feature cues including color, texture, shape, edge etc. In this thesis we have used color and spatial structure information of the image to characterize the color textures. These feature cues are discussed in the following sections.

### 4.2.1 Spatial Structure Cues

Comprehensive spatial structure information of a color image is an ensemble of the spatial variations measured in the luminance as well as in the chrominance channels of the image. Among large number of works on color texture analysis

presented in recent years, there are a few which take into account the chromatic spatial variations *i.e.* the texture content in the chrominance channels of the image efficiently (cf. chapter 2). Herein, we use the PSD estimates computed through the 2D multichannel complex linear prediction models (cf. chapter 3) for the two channel complex color image as the spatial structure features of a color texture image. These PSD estimates depict the global spatial variation information of the luminance as well as the combined chrominance channels.

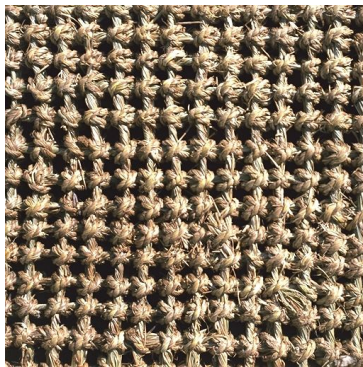


Figure 4.3: Sample texture from the Vistex database.

One of the color textures from Vistex database is shown in Figure 4.3. PSD estimates for the color texture shown in Figure 4.3, using different models in IHLS and  $L^*a^*b^*$  color spaces are shown in Figures 4.4 and 4.5 respectively.

Another color texture, this time chosen from the Outex database is shown in Figure 4.6. PSD estimates for this color texture, using different models in IHLS and  $L^*a^*b^*$  color spaces are shown in Figures 4.7 and 4.8 respectively. These spectra for both of these sample textures, are computed in Cartesian coordinates for normalized frequency range  $\nu = (\nu_1, \nu_2) \in [-0.5, 0.5]^2$  and are computed using 2D multichannel complex valued versions of QP AR and NSHP AR models of order (4, 4) and GMRF model of order 14.

A comparison of the estimated PSD images of luminance and chrominance channels with the magnitude spectra of the same channels using 2D FFT clearly indicates that these models give a decent approximation of the channel spectrum.

### 4.2.2 Color Feature Cue

A color histogram is a standard statistical description of the color distribution in terms of occurrence frequencies of different regions in color space. For 2D image, a pixel location is  $n = (n_1, n_2) \in \Lambda \subset \mathbb{Z}^2$  in which  $\Lambda$  is the finite 2D image lattice region of size  $|\Lambda|$ . In this work, 3D histogram cubes are used as pure color feature

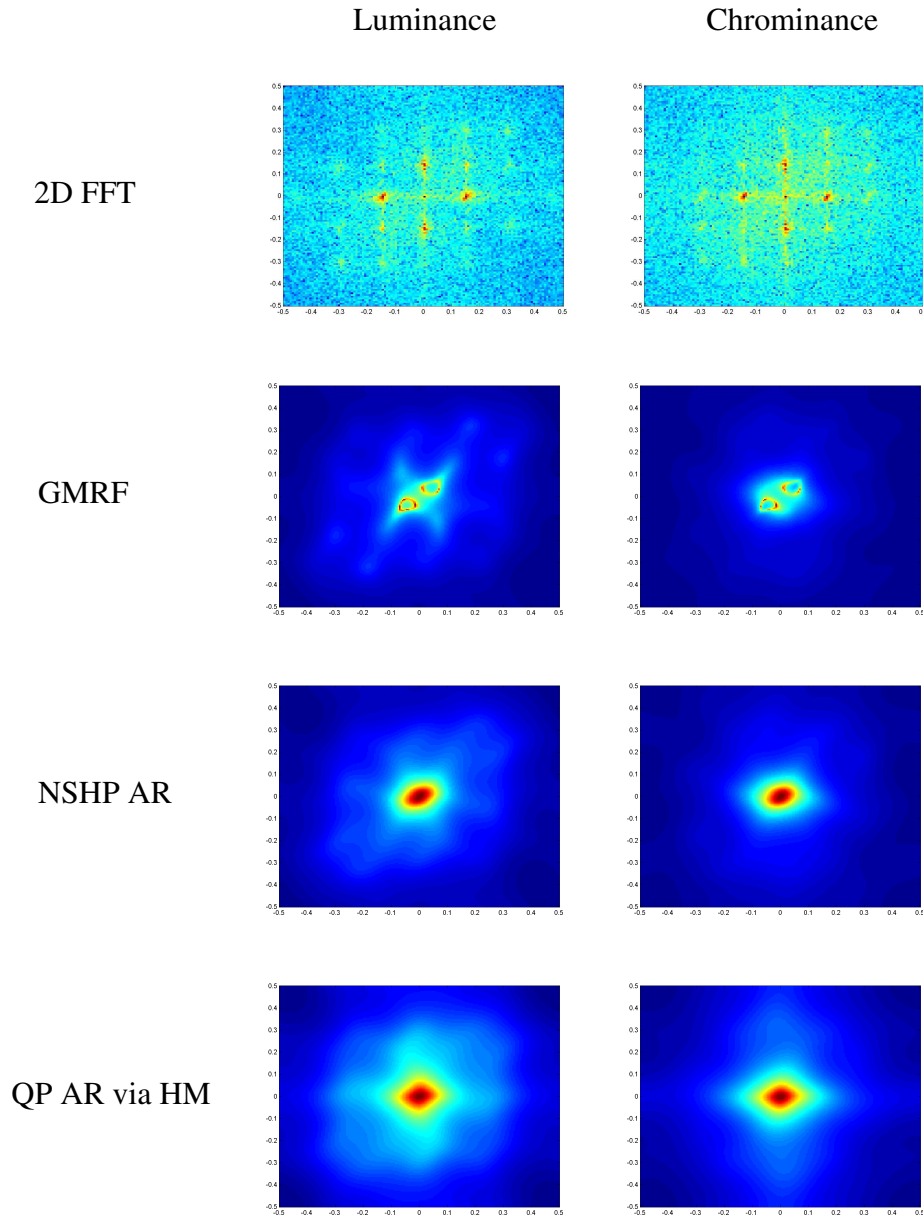


Figure 4.4: Spectral estimates of the image shown in Figure 4.3 in IHLS color space.

cues, for all color spaces. We define a 3D histogram in the form of a 3D step function as:

$$h(c_1, c_2, c_3) = \sum_{i,j,k=(1,1,1)}^{B,B,B} \frac{N_{ijk}}{|\Lambda| \times \gamma^3} 1_{B_{ijk}}(c_1, c_2, c_3) \quad (4.1)$$

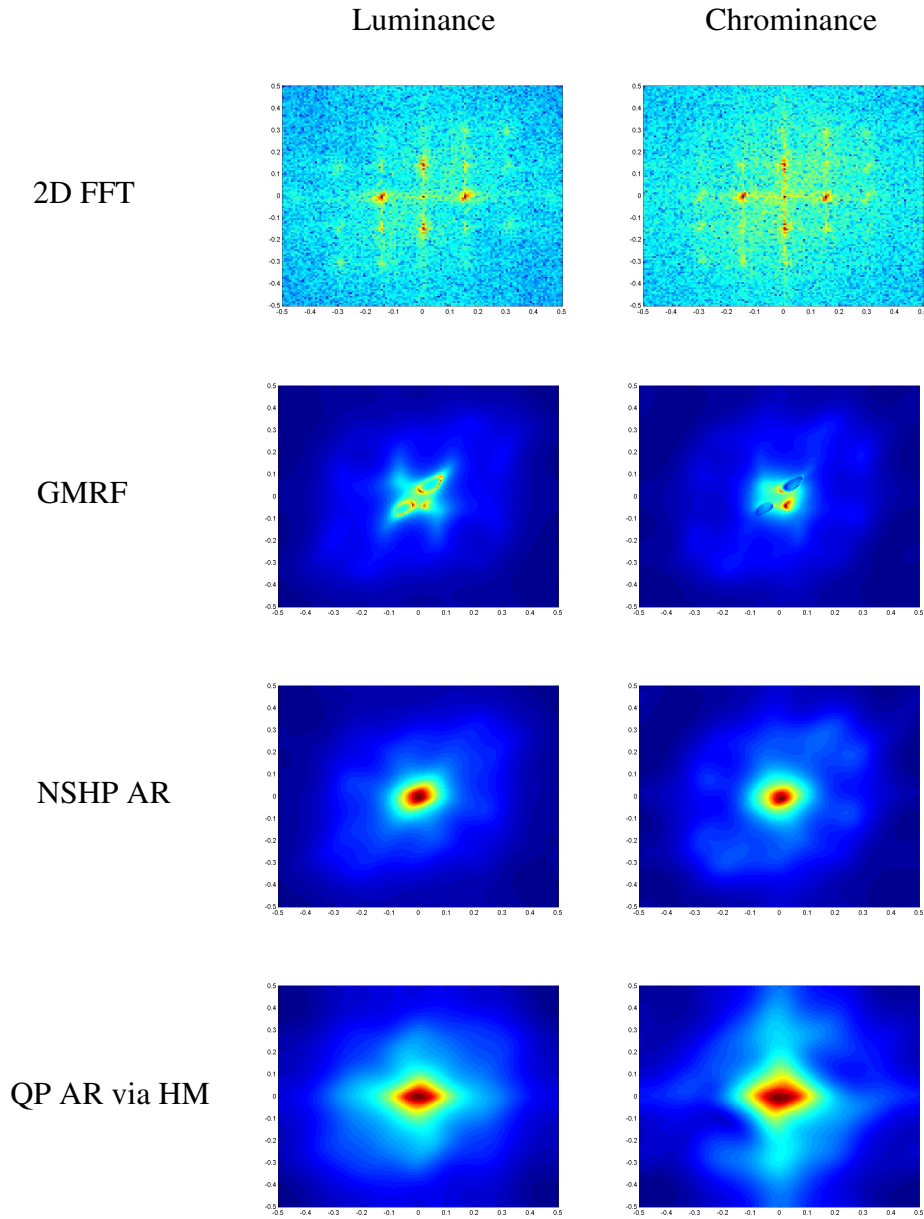


Figure 4.5: Spectral estimates of the image shown in Figure 4.3 in L\*a\*b\* color space.

where  $(c_1, c_2, c_3) \in \mathbb{R}^3$ .  $B$  is the number of bins which is kept same for each color channel.  $N_{ijk}$  is the total number of pixels whose color values are included in the cube  $B_{ijk} = B_i \times B_j \times B_k$ ,  $(i, j, k) \in \llbracket 1, B \rrbracket^3$  which are the regular intervals of

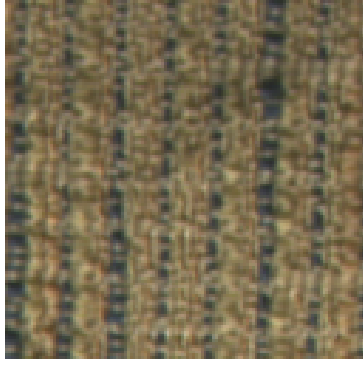


Figure 4.6: Sample texture from the Outex database.

length  $\gamma$  for each color channel. For each color channel,  $\bigcup_{i=1}^B B_i = I$ , the definition interval of the values where  $B_{i_1} \cap B_{i_2} = \emptyset, \forall (i_1, i_2) \in \llbracket 1, B \rrbracket^2$ . The step function  $1_{B_{ijk}}$  is defined as:

$$1_{B_{ijk}} = \begin{cases} 1, & \text{if } (c_1, c_2, c_3) \in B_{ijk} \subset \mathbb{R}^3 \\ 0, & \text{elsewhere} \end{cases} \quad (4.2)$$

### 4.3 Similarity Measures and Cue Fusion

In this section we discuss the distance measures used to measure the similarity between the test and training data sets using the information of each individual feature cue. Afterwards a probabilistic framework of combining this information is presented.

#### 4.3.1 Distance Measures

To measure overall closeness of luminance and chrominance spectra at all frequencies, spectral distance measures are used. In [Bas89], the author has presented a discretized symmetric extension of Kullback-Leibler (*KL*) divergence for spectral distance between two spectra. We use the same distance to measure the closeness of luminance and chrominance spectra. The spectral distance measure is given as:

$$K_\beta(S_{1,\beta}, S_{2,\beta}) = \frac{1}{2} \times \sum_{\nu_1, \nu_2} \left| \sqrt{\frac{S_{1,\beta}(\nu_1, \nu_2)}{S_{2,\beta}(\nu_1, \nu_2)}} - \sqrt{\frac{S_{2,\beta}(\nu_1, \nu_2)}{S_{1,\beta}(\nu_1, \nu_2)}} \right|^2 \quad (4.3)$$

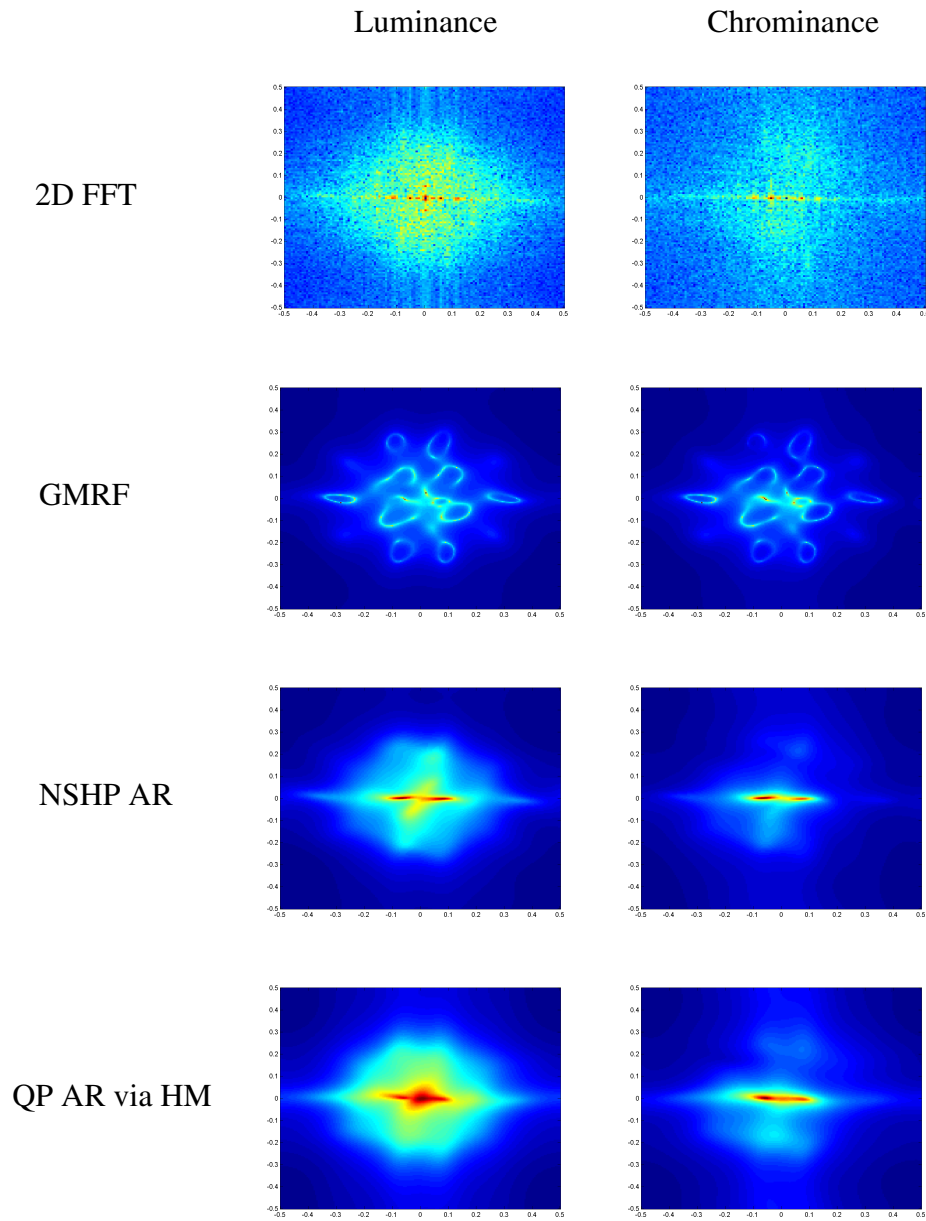


Figure 4.7: Spectral estimates of the image shown in Figure 4.6 in IHLS color space.

where  $\beta \in \{LL, CC\}$  (cf. equation 3.16). The spectral distance measure given in Equation 4.3 gives the closeness of each channel individually.

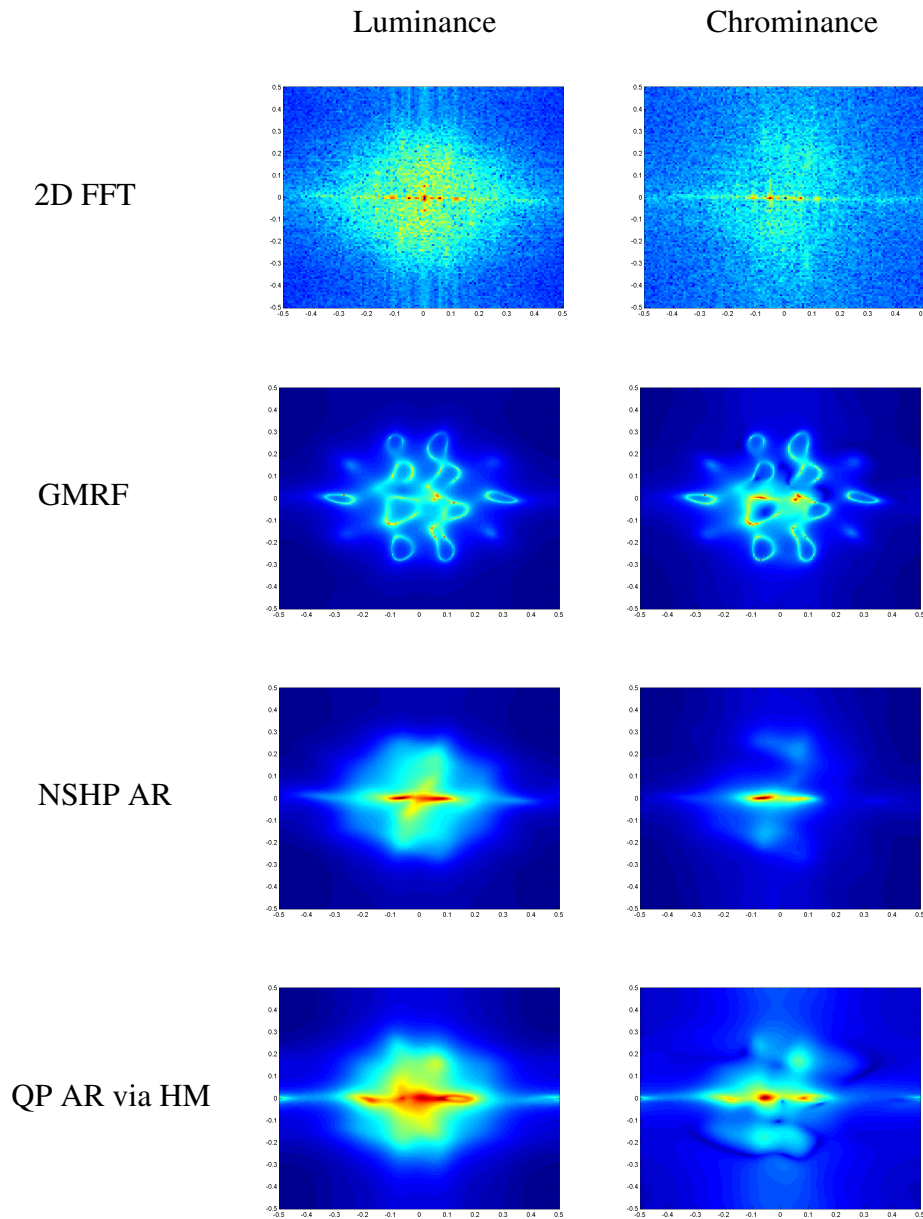


Figure 4.8: Spectral estimates of the image shown in Figure 4.6 in L\*a\*b\* color space.

In order to measure the closeness of 3D color histogram cubes, symmetrized KL divergence, given in [JJS01] is used:

$$K_{\mathcal{H}}(\mathcal{H}_1, \mathcal{H}_2) = \frac{KL(\mathcal{H}_1, \mathcal{H}_2) + KL(\mathcal{H}_2, \mathcal{H}_1)}{2} \quad (4.4)$$

where  $KL(\mathcal{H}_1, \mathcal{H}_2)$  is KL divergence between two histograms  $\mathcal{H}_1$  and  $\mathcal{H}_2$ , given as:

$$KL(\mathcal{H}_1, \mathcal{H}_2) = \sum_{i,j,k=(1,1,1)}^{B,B,B} \frac{N_{1,ijk}}{|\Lambda| \times \gamma^3} \times \log \frac{N_{1,ijk}}{N_{2,ijk}} \quad (4.5)$$

where probabilities  $\mathcal{H}_1$  and  $\mathcal{H}_2$  represent the probability distribution of the pure color information of the image computed through 3D color histograms (cf. section 4.2.2).

### 4.3.2 Multiple Cue Fusion

The information coming from each of these three cues is combined in order to get their combined effect on percentage classification of color textures. For this purpose we developed two different approaches:

#### The Combination Coefficient

This is a basic and simple approach presented to combine the two spectral information. In order to combine the luminance and the chrominance channel spectral information and make it useful for improvement of color texture classification results we define the following combined spectral distance measure:

$$K_{LC}(\nu_1, \nu_2) = \eta K_{LL}(\nu_1, \nu_2) + (1 - \eta) K_{CC}(\nu_1, \nu_2) \quad (4.6)$$

This distance combines the information from both spectra using a combination coefficient  $\eta$ , where  $0 \leq \eta \leq 1$ . The choice of optimal value for this combination coefficient  $\eta$  is discussed in detail in the section 4.4. Although this approach is simple and easy to use when the number of feature cues is less than 3, it becomes significantly difficult to use if the number of feature cues increases.

#### The Probabilistic Cue Fusion

This approach is more robust, reliable cue fusion approach based on the probabilistic fusion of the luminance structure, chrominance structure and pure color feature cue fusion. In this approach, *a posteriori* class probabilities are computed using each of these three feature cues independently. The different *a posteriori* class probabilities obtained through each of these three cues are combined by multiplying these individual *a posteriori* class probabilities. A pattern  $x$  is assigned the label  $\hat{\omega}$  which maximizes the product of the *a posteriori* probabilities provided by each of the independent feature cues (in our case,  $K = 3$ ):

$$\hat{\omega} = \arg \max_{\omega_i, i \in \{1, \dots, n\}} \left( \prod_{k=1}^K P_k(w_i|x) \right) \quad (4.7)$$

where  $n$  is the number of texture classes. In order to quantify these probabilities we used a distance based normalized similarity measure which is given as:

$$P_k(w_i|x) = \frac{\frac{1}{1+d_k(x, x_i)}}{\sum_{j=1}^n \frac{1}{1+d_k(x, x_j)}} \quad (4.8)$$

where  $d_k(x, x_i)$  is the Kullback-Leibler distance measure for respective feature cue. In Equation (4.7) we utilize the degree of independence between the different feature cues to obtain a better result when the cues are fused together. More the individual feature cues are decorrelated, better will be the results computed after their fusion through Equation (4.7). This would eventually result in a better model for spatial variations of the color images.

Now in the next section, we present the procedures and methodology for different experiments carried out for the validation of the approach, search of the best performing model for spectral estimate and comparison of color spaces.

## 4.4 Experiments and Results

For the experimental validation of the color texture classification, we conducted two main experiments. These experiments are presented in the next subsections.

### 4.4.1 Choice of a Pertinent Model

The main objective of this set of experiments was to validate the method along with the performance analysis of the different parametric models discussed in this thesis, for the problem of color texture classification. In this set of experiments we used the  $DS_1$ . The spatial structure cues were computed for both luminance and chrominance channels using 2D multichannel complex versions of the linear prediction models using GMRF, NSHP AR and QP AR via HM method (cf. section 3.3). In this initial set of experiments, the goal was to have an initial evaluation and comparison of these models. In these initial experiments, we used only IHLS color space (cf. section 3.2.1) and did not use the pure color feature cues in these experiments. We used the *combination coefficient* approach for the fusion of luminance and chrominance feature cues along with the k-nearest neighbor algorithm (cf. next subsection) for the class label decision. The results of these experiments were published in [QABFM09, QABFM10].

	GMRF	NSHP	QP AR
$k = 1$	0.53	0.75	0.76
$k = 3$	0.72	0.82	0.83
$k = 5$	0.55	0.65	0.73
$k = 7$	0.55	0.53	0.66

Table 4.1: Optimal values of combination coefficient  $\eta$ , calculated individually for each model and for all values of  $k$  in the  $k$ -nearest neighbor algorithm, where  $k \in \{1, 3, 5, 7\}$ .

In this approach one of the points of interest is to find an optimal value for the combination coefficient  $\eta$  (cf. section 4.3.2). This value was learned through the classification of the training subimages using kNN. For this, the training database was used as the test database. The combination coefficient  $\eta$  was calculated individually for each model and for all values of  $k$  in the  $k$ -nearest neighbor algorithm, where  $k \in \{1, 3, 5, 7\}$ . For each case, the value of  $\eta$ , which gave the maximum classification percentage for these training subimages, was used during the classification of test subimages. These values are shown in the Table 4.1. From the Table 4.1, it is observed clearly that the optimal values of  $\eta$  generally appear to be in the range of 0.5 to 0.8, depending upon the specific model and number of nearest neighbors considered for the color texture classification.

#### k-nearest Neighbor Algorithm

The  $k$ -nearest neighbor algorithm is amongst the most fundamental machine learning algorithms. An object is classified by a majority vote of its neighbors, with the object being assigned to the class most common amongst its  $k$ -nearest neighbors.  $k$  is a positive integer, typically small. If  $k = 1$ , then the object is simply assigned to the class of its nearest neighbor.

Once the individual and combined spectral distances of both luminance and chrominance channels are calculated, the  $k$ -nearest neighbor algorithm was used to classify the color textures of the test database. Experiments were carried out for  $k \in \{1, 3, 5, 7\}$ .

#### Classifier Performance Measures

Two criteria were employed to assess the performance of color texture classification carried out by the proposed approach: percentage color texture classification and positive predictivity or Positive Predictive Value (*PPV*) [RVAB06]. These criteria are stated in the appendix B.

Experimental results indicating the best average percentage color texture classification and PPV using the three models for 24 color textures were obtained for the case where  $k = 3$ . These results are shown in Table 4.2 and Table 4.3 respectively.

	GMRF			NSHP			QP AR		
	L	C	LC	L	C	LC	L	C	LC
$k = 1$	72.47	66.98	86.93	82.11	83.18	93.18	87.37	85.76	94.74
$k = 3$	74.45	68.39	89.71	82.89	83.70	94.38	87.32	86.67	95.29
$k = 5$	73.75	67.94	89.22	82.16	83.26	93.65	86.20	85.44	94.48
$k = 7$	72.63	66.61	89.43	81.28	82.73	92.66	85.05	85.03	94.61

Table 4.2: Average percentage classification results of 24 color textures using 2D multichannel complex NSHP AR, 2D multichannel complex QP AR model via HM method and 2D multichannel complex GMRF for all values of  $k$  in the  $k$ -nearest neighbor algorithm, where  $k \in \{1,3,5,7\}$ .

In both these tables *i.e.* Table 4.2 and Table 4.3, for each of the three models, there are three sub columns. First sub column **L** shows the percentage classification of the respective color texture taking into account only the luminance information of the image *i.e.* spectral distance based on the luminance power spectrum information. Similarly second sub column **C** shows the percentage classification of the color texture using only chrominance information *i.e.* the chrominance auto spectra information of the respective texture. The third sub column **LC** indicates the results obtained by using both luminance and chrominance informations *i.e.* the power spectrum information obtained from both luminance and chrominance auto spectra, combined through Equation (4.6) using the combination coefficient  $\eta$ .

Analysis of the results presented in these tables depicts that all the three models have shown reliable results for the color texture classification of  $DS_1$  in the IHLS color space. Moreover two very important observations could be made over these results.

Firstly it is clear that the percentage classification of color textures increases significantly if we use pure chrominance structure information as an additional information with standard luminance structure information and which was the primary purpose of this study. This fact can be seen for approximately all 24 color textures. Secondly, it is to note that increasing the number of considered nearest-neighbors does not disturb the percentage classification results on a large scale. This observation indicates the robustness of the approach.

Comparing the results obtained through the various models used in this approach, we clearly see that the 2D multichannel complex QP AR model via HM

	GMRF			NSHP			QP AR		
	L	C	LC	L	C	LC	L	C	LC
$k = 1$	0.73	0.70	0.87	0.82	0.84	0.93	0.87	0.86	0.94
$k = 3$	0.75	0.72	0.90	0.84	0.84	0.94	0.88	0.87	0.95
$k = 5$	0.73	0.71	0.90	0.83	0.84	0.93	0.86	0.85	0.94
$k = 7$	0.72	0.70	0.90	0.82	0.83	0.92	0.85	0.85	0.94

Table 4.3: Average positive predicted values of 24 color textures using 2D multichannel complex NSHP AR, 2D multichannel complex QP AR via HM method and 2D multichannel complex GMRF for all values of  $k$  in the  $k$ -nearest neighbor algorithm, where  $k \in \{1,3,5,7\}$ .

method performs best in terms of the color texture classification. This is as expected, keeping in view the better accuracy and precision of the model in parametric spectral analysis (cf. chapter 3). Results obtained from the 2D multichannel complex NSHP AR model are also competitive. However, the percentage classification values obtained for 2D multichannel complex GMRF model are not that high. The main reason for this is again the low resolution of the estimated spectra using LSE for GMRF parameter estimation. It is clear from the PSD estimates of the sample color textures (cf. Figures 4.4 to 4.8) that for the same number of free model parameters, GMRF gives us a larger lobe like estimation of the frequency content of both the channels. This consequently produces low color texture classification percentage. These results for GMRF may be improved using the MLE method for model parameter estimation as is considered to be better than LSE method. Again for the color texture classification also, the MLE method is not presented for GMRF to overcome the computational complexity in this particular application. The results in terms of percentage classification presented in this section and [QABFM10] are better than the state of the art results presented for same problem [PFJ06]. A detailed comparative analysis of our approach with state of the art methods is presented later in the section 4.4.3.

The statistical comparison on the spectral estimates (cf. chapter 3) and the experiments stated in this section gave us 2D multichannel complex QP AR model via HM method as the better performing model than the other two models considered. Thus, we now will use this model to find the most pertinent color space for such type of color texture analysis methodology.

#### 4.4.2 Choice of a Pertinent Color Space

While comparing color spaces for color texture classification, it is necessary to compare the performance of these for the characterization of spatial structure in-

formation as well as for the description of the pure color information. Hence, we base our comparison of the color spaces on both these criteria. In the experiment set designed for this purpose, we used 2D multichannel complex QP AR model via HM method (cf. section 3.3) for the characterization of the luminance and chrominance spatial variations while 3D color histograms are used as pure color feature cues (cf. section 4.2.2). As the decorrelation of the feature cues offered by a color space is also a focal criteria, therefore we used the probabilistic cue fusion for combining the information coming through different feature cues along with the nearest neighbor algorithm (cf. sections 4.4.1 and 4.3.2). In these experiments we used all the three test data sets *i.e.*  $DS_1$ ,  $DS_2$  and  $DS_3$ .

In the following we will discuss the individual as well as the combined results computed using these feature cues for color texture classification, in all the three color space.

### Color Feature Cue

We conducted experiments to evaluate the color texture characterization based on the pure color distribution using 3D histogram information (cf. section 4.2.2). For the three data sets, these 3D histograms were computed for different number of bin cubes  $B \times B \times B$ . For  $DS_1$ ,  $B \in \{4, 6, 9, 10\}$  and for  $DS_2$  and  $DS_3$   $B \in \{8, 12, 16\}$ . The choice of the number of bin cubes for the 3D color his-

	L*a*b*	IHLS	RGB
$B = 4$	75.3	87.5	82.8
$B = 6$	89.3	93.4	95.1
$B = 9$	92.5	95.8	96.4
$B = 10$	91.8	96.4	96.6

Table 4.4: Average percentage classification of 24 color textures of  $DS_1$  in all the three color spaces, using 3D color histograms for all values of bin cubes  $B$ , where  $B \in \{4, 6, 9, 10\}$ .

tograms was made keeping in view, the sizes of the test and training sub images in each data set. For the small sub image sizes *i.e.* the color textures in  $DS_1$ , small bin sizes are chosen. Whereas, for the large sub image sizes *i.e.* the color textures in  $DS_2$  and  $DS_3$ , larger bin sizes are chosen. For all the three color spaces *i.e.* RGB, IHLS and L\*a\*b\* the tests were performed on the three data sets. The training and test data sets were taken as explained in Section 4.1. For each test texture sub image, 3D histogram was computed. Then symmetrized Kullback-Leibler divergence was computed using Equation (4.4). Finally a class label was assigned to the test texture sub image using nearest neighbor method (cf. section

4.4.1). Average percentage classification results obtained for  $DS_1$ ,  $DS_2$  and  $DS_3$

	L*a*b*	IHLS	RGB
$B = 8$	97.0	98.1	99.3
$B = 12$	98.8	99.5	99.5
$B = 16$	99.1	100.0	99.5

Table 4.5: Average percentage classification of 54 color textures of  $DS_2$  in all the three color spaces, using 3D color histograms for all values of bin cubes  $B$ , where  $B \in \{8, 12, 16\}$ .

are shown in Table 4.4, 4.5 and 4.6 respectively. For the data set  $DS_1$ , maximum percentage classification is achieved in the RGB color space with  $B = 10$ . While for the data sets  $DS_2$  and  $DS_3$ , maximum percentage classification achieved is in IHLS color space with  $B = 16$ . As we have larger sub image sizes in  $DS_2$  and  $DS_3$ , therefore we have higher percentage classification values in these data sets than that of the values obtained for the  $DS_1$  data set. For a given data set and fixed number of 3D histogram bins, percentage classification obtained in different color spaces varies significantly. This indicates that all the color spaces does not estimate the global distribution of the color content in the same manner and this estimate depend upon the shape of the color space gamut. The bins considered for 3D histograms are of regular cubical shape. The color spaces with regular shaped color gamut *i.e.* RGB and IHLS are more appropriate for this kind of bin shape and therefore show slightly better results than those of the L\*a\*b\* color space. It is of significance important to note that L\*a\*b\* color space has proven to give

	L*a*b*	IHLS	RGB
$B = 8$	74.7	93.5	92.5
$B = 12$	90.0	93.1	94.4
$B = 16$	92.2	94.5	94.0

Table 4.6: Average percentage classification of 68 color textures of  $DS_3$  in all the three color spaces, using 3D color histograms for all values of bin cubes  $B$ , where  $B \in \{8, 12, 16\}$ .

better results for the estimation of global distribution of pure color content of an image when used with a parametric approximation with MGMM [AQ09]. This parametric approximation is *well suited* to irregular gamut shape of the L\*a\*b\* color space and hence authors in [AQ09] have indicated L\*a\*b\* as the better performing color space for parametric multimodal color distribution approximation.

Here we do not use such a parametric approximation for the spatial distribution of color content in textured images as:

- Image size in the  $DS_1$  is  $32 \times 32$ . For such small image size, it is probable that one will have to face a significant problem of numerical instabilities while calculating the model parameters for MGMM.
- Similarity metrics used for the distance measures between two MGMM distributions are not very well suited to the problem and have a tendency to produce suboptimal results.

### Structure Feature Cues in the Perceptual Color Spaces

To compute luminance and chrominance spatial structure feature cues, auto spectra were estimated using the approach given in the chapter 3. The auto spectra are computed in Cartesian coordinates for normalized frequency range  $\nu = (\nu_1, \nu_2) \in [-0.5, 0.5]^2$ . Then in order to compute the overall closeness of luminance ( $L$ ) and chrominance ( $C$ ) spectra at all frequencies, spectral distance measure, given in Equation (4.3) is used. Again, a class label was assigned to the test texture sub

	L	C	LC
$DS_1$	87.4	85.8	95.4
$DS_2$	91.4	87.5	97.4
$DS_3$	75.1	73.2	84.1
<b>Average</b>	<b>84.6</b>	<b>82.1</b>	<b>91.3</b>

Table 4.7: Average percentage classification of  $DS_1$ ,  $DS_2$  and  $DS_3$  in the IHLS color space.

image using the nearest neighbor method, based on the information from both luminance and chrominance structure feature cues individually. The individual and independent information obtained through these two spatial structure cues is then combined using Equations (4.7) and (4.8). This gives us the class label assignment based on both the luminance and chrominance structure information. These results for the two color spaces i.e. IHLS and  $L^*a^*b^*$  are shown in Table 4.7 and Table 4.8 respectively. In each of these two tables, for each of the three data sets, there are three columns. First column L shows the percentage classification of the respective color texture taking into account only the luminance information of the image i.e. spectral distance based on the luminance power spectrum information. Similarly second column C shows the percentage classification of the color texture using only chrominance information i.e. chrominance auto spectra

	L	C	LC
$DS_1$	87.7	92.1	97.2
$DS_2$	90.3	91.2	96.5
$DS_3$	79.4	78.5	88.0
<b>Average</b>	<b>85.8</b>	<b>87.3</b>	<b>93.9</b>

Table 4.8: Average percentage classification of  $DS_1$ ,  $DS_2$  and  $DS_3$  in the L\*a\*b\* color space.

information of the respective texture. The third column LC indicates the results obtained by using both luminance and chrominance information i.e. the power spectrum information obtained from both luminance and chrominance auto spectra, combined using the Equations (4.7) and (4.8).

Analysis of these results shows a clear difference in the average percentage classification results obtained in both the color spaces. While comparing the results, we see that for  $DS_1$ , results obtained with L\*a\*b\* color space are better than the ones computed in IHLS color space for real world textures. The reason for these improved results is a better decorrelation of luminance and chrominance channel of  $DS_1$  in L\*a\*b\* color space as is already stated in Section 3.4.3. This better decorrelation of the two information leads to improved percentage classification results in the case of L\*a\*b\* color space when only chrominance channel spatial structure information is used (compare column C of the Tables 4.7 and 4.8). Subsequently this better decorrelation results in an improved average percentage classification of color textures in the case of L\*a\*b\* color space as compared to IHLS color space, when luminance and chrominance spatial structure information are combined using the Equations (4.7) and (4.8). For the other two data sets  $DS_2$  and  $DS_3$ , better characterization of chrominance channel exists and it continues to give us better results than that of the luminance channel spatial structure information.

### Structure Feature Cues in the RGB Color Space

We validated the argument made over the choice of perceptual color spaces (see Section 3.5) through experiment by comparing the results with RGB color space. We used the same test data sets  $DS_1$ ,  $DS_2$  and  $DS_3$  under same test conditions i.e. sub image sizes, number of training and test sub images as stated for the perceptual color spaces.

For the RGB color space, simulations were carried out using the 2D multi-channel QP AR model via HM method. Results for this method in RGB color space are presented in Table 4.9. The first column R shows the average percent-

	R	G	B	RGB
$DS_1$	78.3	80.0	83.1	85.9
$DS_2$	89.6	88.4	90.3	92.1
$DS_3$	75.3	76.6	72.2	82.8
<b>Average</b>	<b>81.1</b>	<b>81.7</b>	<b>81.9</b>	<b>86.9</b>

Table 4.9: Average percentage classification of  $DS_1$ ,  $DS_2$  and  $DS_3$  in the RGB color space.

age classification of the three chosen data sets ( $DS_1$ ,  $DS_2$  and  $DS_3$ ) taking into account only the information in the red channel of the RGB image *i.e.* spectral distance based on the red channel power spectrum information. Similarly the second column G and the third column B show the average percentage classification of the three data sets using only the information from the green and the blue channels respectively. The fourth column RGB indicates the results obtained by using the combined information of all the three channels *i.e.* the red, the green and the blue channels. The three auto spectra information are combined using Equations (4.7) and (4.8). It is clear from these results that the percentage classification results obtained by individual channels in RGB color space are inferior than those obtained by the luminance and chrominance spectra using our approach in both the perceptual color spaces. One can also see that for the same test conditions and same information fusion approach with proposed method, combined overall results in IHLS and L\*a\*b\* color spaces are approximately 6% to 7% higher (for the used data sets) than those computed in the RGB color space. This provides an experimental evidence to the hypothesis given in the Section 3.5 over the choice of a perceptual color space for color texture classification instead of the standard RGB color space.

### Structure-Color Cue Fusion

The three computed feature cues *i.e.* two structure (L and C) and a pure color feature cue (3D histograms denoted by  $\mathcal{H}$ ) are then combined to have a better color texture characterization. This multiple cue fusion is carried out again using *a posteriori* probability fusion as in Equations (4.7) and (4.8). The structure feature cues computed through the discussed 2D multichannel QP AR model via HM method in the three color spaces could be fused with color feature cues computed through all color spaces. For  $DS_1$ , as it is clear from the Table 4.4 that for IHLS and RGB color spaces we obtain the best results when  $B = 10$ , while for L\*a\*b\* color space we obtain the best percentage classification with  $B = 9$ . For  $DS_2$  and  $DS_3$ , we obtain the best classification results in the RGB color space when

	RGB	IHLS	L*a*b*
	R G B	L C	L C
$\mathcal{H}_{lab}$	95.2	98.4	98.9
$\mathcal{H}_{ihls}$	96.8	98.9	99.3
$\mathcal{H}_{rgb}$	96.1	98.9	99.3

Table 4.10: Average percentage classification of  $DS_1$ . Structure feature cues are computed through 2D multichannel QP AR model via HM method with model order (2, 2). Columns RGB, IHLS and L\*a\*b\* show results of structure feature cues being computed in respective color spaces combined with pure color feature cues in each color space. For  $\mathcal{H}_{lab}$ ,  $B = 9$  whereas  $B = 10$  for  $\mathcal{H}_{ihls}$  and  $\mathcal{H}_{rgb}$ .

$B = 16$  and  $B = 12$  respectively. Whereas, L\*a\*b\* and IHLS color spaces give the best classification results for both these data sets when  $B = 16$ . We combine these best classification results for each data set in each color space using only color feature cue results with the best achieved structure feature cue results in each color space. For  $DS_1$ ,  $DS_2$  and  $DS_3$ , the best classification results using

	RGB	IHLS	L*a*b*
	R G B	L C	L C
$\mathcal{H}_{lab}$	94.9	98.4	98.8
$\mathcal{H}_{ihls}$	95.8	98.8	99.1
$\mathcal{H}_{rgb}$	95.6	98.6	99.1

Table 4.11: Average percentage classification of  $DS_2$ . Structure feature cues are computed through 2D multichannel QP AR model via HM method with model order (2, 2). Columns RGB, IHLS and L\*a\*b\* show results of structure feature cues being computed in respective color spaces combined with pure color feature cues in each color space. For  $\mathcal{H}_{lab}$ ,  $\mathcal{H}_{ihls}$  and  $\mathcal{H}_{rgb}$ ,  $B = 16$ .

only spatial structure feature cues combined with the best results obtained by using only color feature cues in each color space, are presented in the Tables 4.10, 4.11 and 4.12 respectively. From the results presented in these tables, it is clear that perceptually uniform color spaces perform better than RGB color space for all three test data sets. Also, the two considered perceptual color spaces perform

very close to each other when all the three feature cues are combined. However the best value of average percentage classification of  $DS_1$  is 99.3%. This value is achieved when structure feature cues are computed in  $L^*a^*b^*$  color space while pure color feature cue is computed in IHLS color space.

	RGB	IHLS	$L^*a^*b^*$
	R G B	L C	L C
$\mathcal{H}_{lab}$	86.2	87.5	86.3
$\mathcal{H}_{ihls}$	87.2	88.9	87.8
$\mathcal{H}_{rgb}$	86.8	88.9	87.2

Table 4.12: Average percentage classification of  $DS_3$ . Structure feature cues are computed through 2D multichannel QP AR model via HM method with model order (2, 2). Columns RGB, IHLS and  $L^*a^*b^*$  show results of structure feature cues being computed in respective color spaces combined with pure color feature cues in each color space. For  $\mathcal{H}_{lab}$ ,  $\mathcal{H}_{ihls}$  and  $\mathcal{H}_{rgb}$ ,  $B = 16$ .

#### 4.4.3 Comparative Analysis

Average percentage classification of color textures obtained in different color spaces can easily be compared to the average percentage classification results of color textures computed through other existing approaches. In the case of  $DS_1$ , best known results are presented in [PFJ06]. Comparison of the results achieved

	Best results in [PFJ06]	Our method
Only structure cue	91.2	<b>97.2</b>
Only pure color cue	90.8	<b>96.6</b>
Structure + Pure color	96.6	<b>99.3</b>

Table 4.13: Comparison of best average percentage classification results for  $DS_1$  with state of the art results presented in [PFJ06]. Best results are indicated in bold faces.

by our approach with the results presented in [PFJ06] is given in Table 4.13. Best value for average percentage classification achieved using only the structure information in [PFJ06], is 91.2% which is obtained using wavelet like DCT coefficients as structure descriptors. Compared to this value of average percentage classification, we observe a significant increase in average percentage classification value

of 24 color textures with our method. In our work, the best average percentage classification achieved using only structure feature cues is 97.24%. In the case

	Best results in [MP04]	Our method
Only structure cue	100.0 (with $LBP_{16,2}$ in $L^*a^*b^*$ )	96.5
Only pure color cue	100.0 (with 3D histograms in $I_1I_2I_3$ , $B = 32$ )	100.0
Structure + Pure color	99.8 (with $LBP_{16,2}^{u2}$ and 3D histograms in RGB, $B = 16$ )	99.1

Table 4.14: Comparison of best average percentage classification results for  $DS_2$  with state of the art results presented in [MP04].

of  $DS_2$  and  $DS_3$  test data sets, best average percentage classification results are presented in [MP04]. The authors have compared the results of a large number of existing texture descriptors for both  $DS_2$  and  $DS_3$  without concentrating on the performance of a given algorithm. Comparison of results with our approach for these two test data sets with best results presented in [MP04] are given in Table 4.14 and 4.15 respectively. In [MP04], the best reported results using different feature cues for each case, are not obtained using the same descriptors.

For example, for  $DS_2$ , the best results presented using only color feature cues are obtained using 3D histograms in  $I_1I_2I_3$  with  $B = 32$  and the best results presented for structure information are computed using LBP [OPM02a] *i.e.*  $LBP_{16,2}$  in  $L^*a^*b^*$ . Then the best results by fusing both the feature cues are presented for 3D histograms in RGB with  $B = 16$  used as color feature cue and  $LBP_{16,2}^{u2}$  as structure feature cues. The decision rule used for fusion is the Borda count. In [MP04], for  $DS_3$ , the best results presented using only color feature cues are

	Best results in [MP04]	Our method
Only structure cue	87.8 (with $LBP_{8,1}$ in RGB)	88.0
Only pure color cue	95.4 (with 3D histograms in HSV, $B = 16$ )	94.5
Structure + Pure color	94.6 (with $Gabor_{3,4}$ and 3D histograms in RGB, $B = 16$ )	89.0

Table 4.15: Comparison of best average percentage classification results for  $DS_3$  with state of the art results presented in [MP04].

obtained by 3D histograms in HSV color space with  $B = 16$  and the best results presented for structure information are computed through  $LBP_{8,1}$  in RGB color space. Then the best results by fusing both the feature cues are presented for 3D histograms in RGB with  $B = 16$  used as color feature cue and  $Gabor_{3,4}$  as structure feature cues. The decision rule used for fusion is the maximum dissimilarity.

As we use the same color and texture features for all the data sets along with the same fusion method, therefore the comparison of the results through our approach for the different data sets is more judicious. It can be noted that for the two

test data sets  $DS_1$  and  $DS_2$ , our method and the best results reported so far *i.e.* as in [MP04] are approximately of the same order when individual color and texture feature cues are considered. For  $DS_2$ , the best results with our approach and the ones in [MP04] are approximately the same even when the two feature cues are fused. For  $DS_3$ , authors in [MP04] report an average percentage classification of 94.6%. The corresponding percentage computed with our approach is 88.97%. It is to note here that in [MP04], main objective was to produce maximum percentage classification using different combinations of color and texture features and different fusion methods. Contrary in our work, the main goal is to analyse the effect of luminance chrominance spectral decorrelation in the perceptual color spaces and its implications on the color texture classification. Even under this consideration, the presented approach outperforms the state of art in certain cases while compete well in other cases in terms of average percentage classification results.

#### 4.4.4 Pixel Classification

The luminance and chrominance spatial structure feature cues used for color texture classification can also be used for color texture segmentation. To show their pertinence, we conducted a few color texture pixel classification experiments using these feature cues in the three used color spaces. The ground truth data associated with complex natural images is difficult to estimate and its extraction is highly influenced by the subjectivity of the human operator. Thus, the proposed pixel classification algorithm was used to perform pixel classification of natural as well as synthetic color textures which possess unambiguous ground truth data. Test images were taken from the color image database used in [IW08]. The database was constructed using color images from Vistex and Photoshop databases.

In the proposed supervised pixel classification method, a small sub image was used as the training image for each class. Image observation model parameters and multichannel complex prediction error were computed for this sub image. Then these parameters are used to compute the multichannel complex prediction error of the complete image, for each of the four test color images shown in Figure 4.9. A normal practice for such parametric texture models, is to model the prediction error through a parametric probability distribution [BS94]. Thus, the distribution of this multichannel complex linear prediction error can be modeled as a single multidimensional complex Gaussian distribution. However in real world problems, this error sequence does not follow a Gaussian distribution in a perfect manner *i.e.* it can follow some different distributions. In this case it is difficult to have good classification results with a Gaussian hypothesis over multichannel linear prediction error sequence. In this work we have chosen different

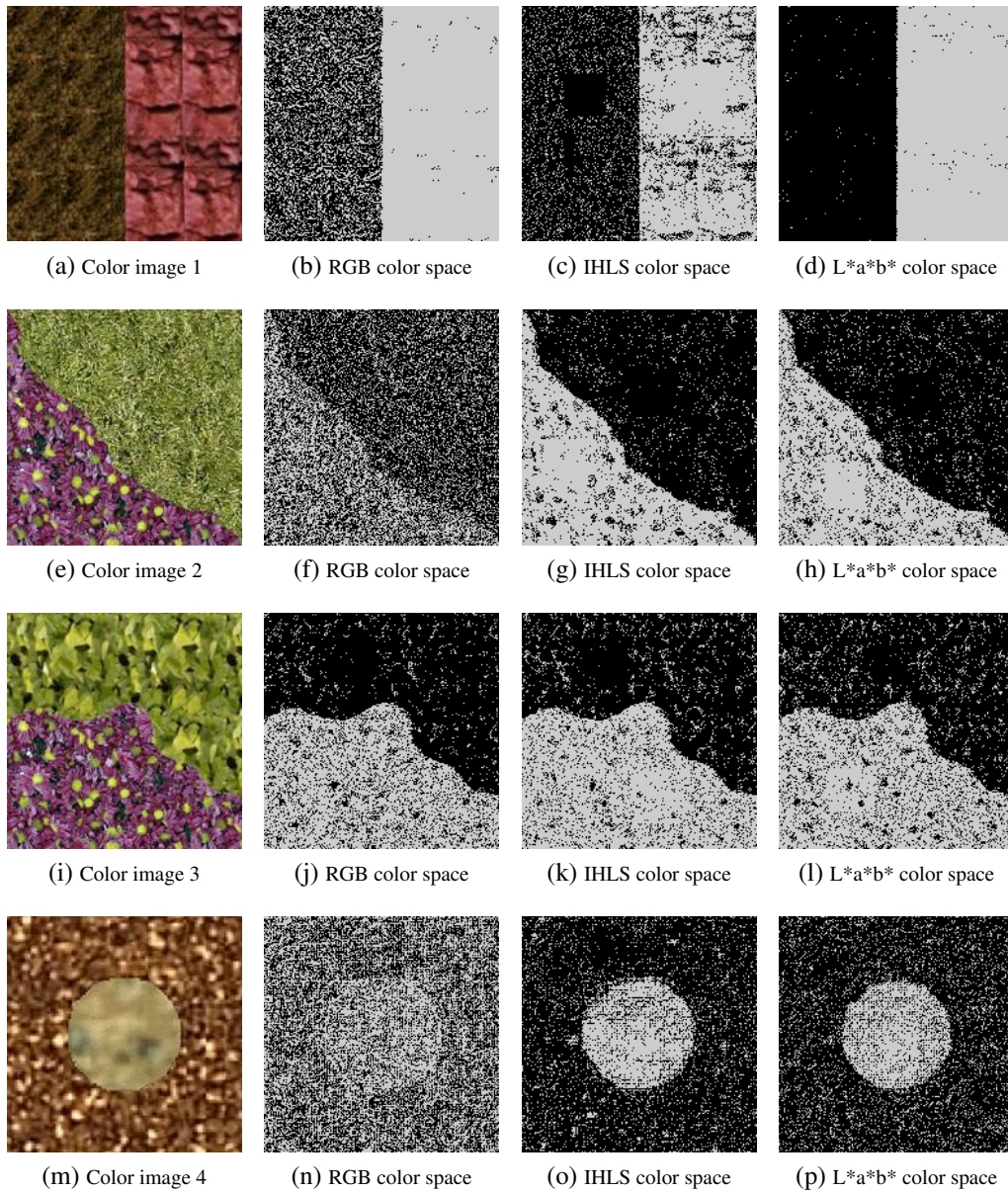


Figure 4.9: Test color textured images and their pixel classification results in the three discussed color spaces.

parametric (cf. chapter 5) and non-parametric approaches to estimate the distribution function of this multichannel complex linear prediction error sequence. Here, in this experiment, we present the non-parametric approach used to have a final pixel level classification, which is the multidimensional version of classical kNN algorithm presented in [PZLB93]. This algorithm is used here as a logical

continuation of the color texture classification approach presented earlier in this chapter.

When implementing the basic NN classifier, experiments have shown that the results can be fairly improved if the pixels are assigned one by one to the clusters in a specific order depending on their distances to the prototypes. Therefore in [PZLB93], at each step authors consider the distances between all the unassigned pixels and all the prototypes. The smallest among these distances indicates the specific pixel that must be considered. This pixel is assigned to the cluster attached to its NN and is integrated within the set of prototypes defining this cluster. This updating rule is iterated until all the pixels are classified [MSP08]. Here we use the multichannel complex error sequences computed for the small training sub images for each color texture class as the prototypes. These prototypes are used to classify the multichannel complex prediction error for each pixel of the complete image.

		RGB	IHLS	L*a*b*
<b>Color image 1</b>	Class 1	36.0	13.4	0.4
	Class 2	0.8	16.1	0.9
	<b>Total</b>	<b>18.4</b>	<b>14.7</b>	<b>0.6</b>
<b>Color image 2</b>	Class 1	27.9	6.1	7.7
	Class 2	44.4	12.9	15.7
	<b>Total</b>	<b>34.4</b>	<b>8.8</b>	<b>10.8</b>
<b>Color image 3</b>	Class 1	7.3	10.1	11.1
	Class 2	22.2	14.7	18.5
	<b>Total</b>	<b>14.3</b>	<b>12.3</b>	<b>14.6</b>
<b>Color image 4</b>	Class 1	50.6	13.1	15.7
	Class 2	31.5	23.1	26.7
	<b>Total</b>	<b>47.1</b>	<b>14.9</b>	<b>17.8</b>
<b>Average</b>		<b>28.5</b>	<b>12.7</b>	<b>10.0</b>

Table 4.16: Percentage classification error for pixel classification experiments, for each class in each test color image. Average percentage error value for the 4 color textures in each color space is given in the bold faces.

Our main goal in these experiments too, was to compare the considered color spaces. The spatial regularization techniques like Potts model [Guy95] are known to change these initial pixel label fields based on the neighborhood energies and are often used as the final step of segmentation algorithms. Here, it is to note that

		RGB	IHLS	L*a*b*
<b>Color image 1</b>	Class 1	0.9	0.8	0.9
	Class 2	0.7	0.8	0.9
	Total	0.8	0.8	0.9
<b>Color image 2</b>	Class 1	0.7	0.9	0.9
	Class 2	0.5	0.9	0.8
	Total	0.7	0.9	0.9
<b>Color image 3</b>	Class 1	0.8	0.9	0.8
	Class 2	0.9	0.8	0.8
	Total	0.8	0.9	0.8
<b>Color image 4</b>	Class 1	0.8	0.9	0.9
	Class 2	0.2	0.6	0.5
	Total	0.5	0.8	0.8
<b>Average</b>		<b>0.7</b>	<b>0.8</b>	<b>0.9</b>

Table 4.17: Average PPV for pixel classification experiments, for each class in each test color image. Average percentage PPV value for the 4 color textures in each color space is given in the bold faces.

the results presented in Figure 4.9 are the direct output of KNN algorithm and no spatial regularization technique has been applied to these results.

The pixel classification results on the used four color images, in Figure 4.9, Table 4.16 and 4.17 depict the advantage of using perceptual color spaces instead of RGB color space for this type of computations. However for certain cases, RGB competes well with the perceptual color spaces. For color image 1, L\*a\*b\* gives better results as compared to the other considered color spaces. For the other color texture images, IHLS and L\*a\*b\* perform approximately the same. However in terms of average percentage error and average PPV values, L\*a\*b\* perform slightly better than the other color spaces.

## 4.5 Conclusion

In this chapter we have discussed and analyzed a new color texture classification methodology based upon the multichannel complex versions of the causal and non-causal linear prediction models discussed in the previous chapter. The main conclusions of this chapter can be summarized as follows:

- A useful information of pure chrominance structure, considering a zero mean case is computed and is combined with pure luminance structure information to get better color texture classification results than state of the art methods, like [PFJ06]. These results very effectively emphasizes the pertinence of using the chromatic spatial variations into account, while characterizing the color textures. This chrominance spatial structure adds significantly to the performance of the color texture analysis algorithms based on only gray level texture information. This enforces the hypothesis inferred from the results of the experiments conducted in chapter 3 *i.e.* the use of perceptual color spaces over RGB for color texture characterization is found pertinent as already presented in [Pas01].
- From the experiments conducted on the comparison of different models, it can be concluded that the causal models particularly 2D multichannel QP AR model via HM method performed better in terms of average percentage classification results than that of the non-causal ones with the used parameter estimation method and data sets.
- If we analyze the percentage classification results based on chrominance spatial structure cue,  $L^*a^*b^*$  is a better choice for chrominance structure feature cues, for all three data sets.  $L^*a^*b^*$  also shows the best results for the characterization of the overall spatial structure information for all three test data bases which is one of the very major and important findings of this part of the thesis.
- For pure color feature cues, RGB and IHLS color spaces show slightly better results than  $L^*a^*b^*$  color space. The bins considered for 3D histograms are of regular cubical shape. The color spaces with regular shaped color gamut *i.e.* RGB and IHLS are more appropriate for this kind of bin shape and therefore perform better in this case.
- The overall average percentage classification results if compared, when all the three feature cues are combined, the  $L^*a^*b^*$  color space is a better choice for  $DS_1$  and  $DS_2$ . It is to note that we have used the same set of structure and color attributes with same number of model parameters for all the three data sets. While in [MP04], the results computed with the best performing attributes from a given set of attributes are presented. This certainly shows the robustness of the approach developed in this thesis.
- In the results of pixel classification experiments, we see that the two perceptual color spaces perform better than RGB color space in terms of percentage pixel classification error and PPV for the chosen four color images

while using the proposed approach. Considering the over all average values of these two indicators,  $L^*a^*b^*$  gives an advantage over the other two color spaces.



---

## CHAPTER 5

---

# COLOR TEXTURE SEGMENTATION

---

Texture segmentation is the process of splitting an observed image into finite number of homogeneous textures. In the case of multichannel textures like color, multispectral or hyperspectral satellite images the problem becomes complex because of the underlying interactions between the different channels of a textured image. In supervised multichannel texture segmentation, a known texture sample is used to identify and/or extract the regions having the same texture in a given multichannel scene or image. A large number of algorithms have been proposed to characterize the color textures for classification and/or segmentation, during recent years making use of techniques JSEG [DM01], integrative co-occurrence matrices [Pal04], fusion of different approaches [DW01], Quaternion representation of color images [SF07] and multidimensional random field models [PFJ06], [KP06].

In this chapter we will discuss the model based texture segmentation of color and satellite images. A contextual introduction of the approach is illustrated in the section 5.1. An illustration of our model based segmentation approach with an emphasis on the different parametric approximations of the multichannel linear prediction error is given in the section 5.2. Experiments and results on the synthetic color texture images as well as on the high resolution satellite images are presented and discussed in the sections 5.3 and 5.4 respectively. Finally section 5.5 concludes the chapter.

## 5.1 Model Based Texture Segmentation

Significance of model based color texture descriptors for color texture characterization problem was discussed in chapter 2. Here we would discuss main model based approaches presented in the past for the segmentation of color textures.

In [CTB<sup>+</sup>99], the authors proposed an implementation of model based algorithm for color texture segmentation which was termed as Blobworld. The focus of this technique is the inclusion of anisotropy, polarity and contrast features in a multi-scale texture model. First, the image is filtered with a Gaussian filter and then pure color features are extracted in CIE Lab color space. For the joint probability distribution estimation of color, texture and position features, the authors propose to use GMMs. The authors demonstrated the utility of the algorithm in the context of CBIR problem. In [TZ02], data driven Markov chain Monte Carlo method is illustrated for color image segmentation. In this work the authors did not focus on the texture characterization in the color images yet have analyzed and discussed the pertinence of using model based techniques for color image analysis. The authors have formulated the problem in a Bayesian framework and analyzed various prior and likelihood models.

In [KP06], an MRF image segmentation model, which combines the color and texture features is proposed. The theoretical approach is based on Bayesian estimation. This Bayesian estimation involves simulated annealing. The image pixels are classified in different classes to obtain the final segmented image. These classes are represented by multi-variate Gaussian distributions over image features (basically an additive Gaussian noise model). Here, the authors use the perceptually uniform  $L^*u^*v^*$  color values as color features and a set of Gabor filters as texture features on gray level images. It is to note that authors did not use any optimal color texture features and state that the nature of the texture features is not crucial to the algorithm from the segmentation point of view. In the model presented here, they have primarily focused on the pertinence of Gaussian models for describing the texture feature distributions. In this work, both supervised and unsupervised frameworks for color texture segmentation are discussed. Gaussian parameters are either computed using a training data set (supervised) or estimated from the input image (unsupervised). The authors used the EM algorithm for the Gaussian parameter estimation. The authors have presented the results over synthetic and real images. They found that segmentation based purely on texture gives fuzzy boundaries but usually homogeneous regions, whereas segmentation based on color is more sensitive to local variations but provides sharp boundaries. As for the combined features, they obtained sharp boundaries and homogeneous regions.

Linear prediction models have also been extensively used to characterize the textures. In [BS94], authors used the 2D single channel real valued linear pre-

diction models for the multiple resolution segmentation of gray level textured images. The initial class label field of the image was estimated by approximating the distribution of linear prediction error (*LPE*) with a Gaussian probability distribution. Once the initial class label field of the image is estimated, this field is modeled as a Markov random field. In this work, the authors did not discuss the modeling and subsequently the segmentation of the color images using these models. Another work [AR05] presented an improved version of the approach discussed in [BS94], addressing the problem of model selection for texture segmentation. This work also addresses the gray level textures and approximates the *LPE* distribution with a Gaussian probability distribution. In [MJ92], the authors introduced first time the concept of SAR models. These concepts were later studied and extended to MSAR models in [KH03, HCG<sup>+</sup>04, KBH06]. However, in these SAR and MSAR extensions of classical 2D AR texture models, the label field function is defined over the feature space defined by the model parameters. As this parameter space has reduced dimensions and hence is not considered well adopted to describe the underlying texture function comprehensively, it needs to be analyzed with a more generic and robust method.

Generally in model based texture segmentation, the formulation of the segmentation leads to a hierarchical model. Given a 2D multichannel random field  $X$  with an observation field (a given multichannel image)  $x = \{x_n\}$ ,  $x_n \in E_x$  defined on a rectangular lattice  $\Lambda$  with size  $|\Lambda|$ , where  $n$  is a pixel location  $n = [n_1, n_2]^T \in \Lambda \subset \mathbb{Z}^2$ , then the labels  $\omega$  may also be defined on the identical lattice. Thus for each  $n$ , there is a label  $\omega_n \in E_c$  specifying to which class the observed pixel  $x_n$  belongs, with  $E_c = \{1, \dots, C\}$  is the set of all possible class/texture labels and  $C$  is the total number of texture classes in the image. It is to note that in this work  $E_x = \mathbb{R} \times \mathbb{C}$  for the images defined through the Equation (3.10) and  $E_x = \mathbb{R}^3$  for images in RGB color space. The relation between the observation field  $x$  and the label field  $\omega = \{\omega_n\}_{n \in \Lambda}$  can be described using Bayes theorem as:

$$p(\omega|x) = \frac{p(x|\omega) p(\omega)}{p(x)} \quad (5.1)$$

where  $p(x|\omega)$  is the likelihood term,  $p(\omega)$  is the regularization term and  $p(x)$  is the constant of the problem. Thus if a single texture class is denoted by  $c$  comprising of the label set  $\{n : \omega_n = c\}$ , then its likelihood function would be defined by the probability distribution,  $p(\{x_n, n : \omega_n = c\} | \theta_c^{(X)})$ , where  $\theta_c^{(X)}$  are the model parameters describing that texture class.

Now if we represent the different texture classes in an image with a model of parameter set  $\theta^{(X)}$ , then the problem of the texture segmentation can be expressed as an optimization problem over the labels of the entire image as:

$$\hat{\omega}_{MAP} = \operatorname{argmax}_{\omega \in F_c} p(\omega|x, \theta^{(X)}) \quad (5.2)$$

with  $F_c = E_c^\Lambda$ , is the set of all possible configurations of the labels over the lattice  $\Lambda$ . Using equations (5.1) and (5.2), we can state:

$$p(\omega|x, \theta^{(X)}) \propto \prod_{c \in E_c} p(\{x_n, n : \omega_n = c\} | \theta_c^{(X)}) p(\omega) \quad (5.3)$$

where  $\theta^{(X)} = \left\{ \theta_c^{(X)} \right\}_{c \in E_c}$ .

The attribution of the pixel labels with the Equation 5.2, can be formulated as supervised texture segmentation, if the number of textures and the underlying texture model parameters are known *a priori*.

In the next section we will use this general definition of the problem to define our problem of multichannel texture segmentation using the proposed parametric framework. A more detailed overview of the model based texture segmentation approaches is given in [Bar98].

## 5.2 Multichannel Texture Segmentation Model

In this section we will develop a 2D multichannel both real and complex valued model based, parametric framework for the solution of the supervised texture segmentation described by the Equation 5.2. For this, we will present the image observation model, different parametric priors for the distribution of multichannel LPE and the underlying class label field model used in this framework.

### 5.2.1 Image Observation Model

Our adopted image observation model to characterize the color textures is the 2D multichannel complex linear prediction model described by the Equations 3.11 and 3.12. Since as we have seen in the chapter 3, the multichannel complex LPE sequence is given by:

$$E_n = (X_n - \mu) - \hat{X}_n. \quad (5.4)$$

where  $\hat{X}_n = - \sum_{m \in D} A_m (X_{n-m} - \mu)$  (cf. section 3.3),  $n = (n_1, n_2) \in \Lambda \subset \mathbb{Z}^2$

in which  $\Lambda$  is the finite 2-D lattice region of size  $|\Lambda|$ .  $\hat{X}_n$  is the linear prediction of the 2D multichannel complex image estimated through either of the discussed causal and non-causal models in the two used perceptual color spaces. While in the RGB color space, the three color planes are real and hence these models as

well as the computed multichannel LPE are both real. In the developed supervised color texture segmentation approach, initial observation model parameters are computed on small training sub images of each class. A generalized block diagram for the estimation of image observation model parameters  $\theta_M$  from the training sub image is shown in Figure 5.1. Once we have the observation model parameters, we use these parameters to estimate the test color image and subsequently compute the multichannel LPE sequence  $e$  for this test image.

Classically, the distribution of this multichannel LPE sequence  $E$  can be approximated using a multivariate Gaussian approximation [AR05, BS94]. Once these approximations are estimated, initial class label field is computed with the help of these approximations.

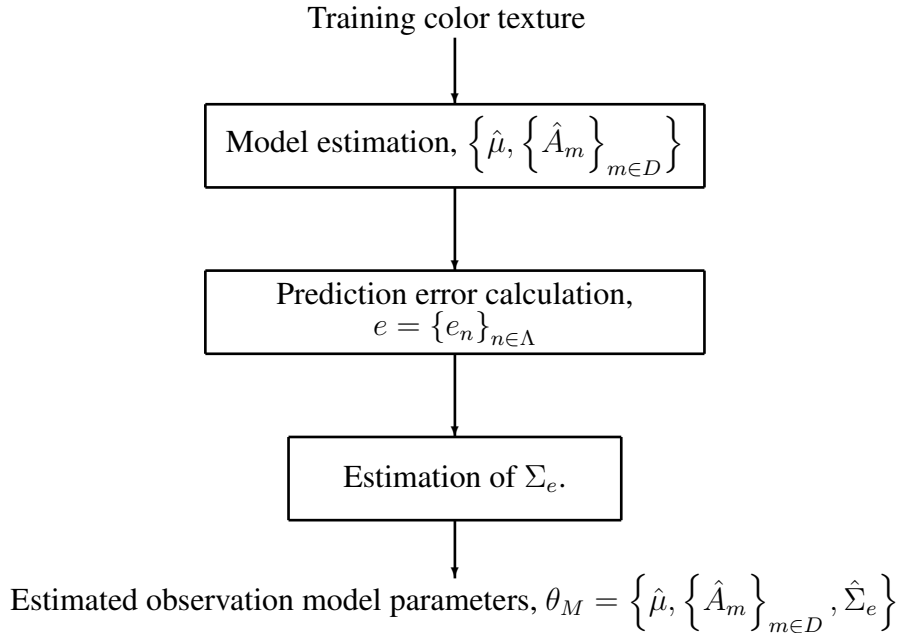


Figure 5.1: A generalized block diagram of the image observation model parameter estimation from the training sub image.

### 5.2.2 Multivariate Gaussian probability distribution

For this approximation of the multichannel LPE distribution, we assume that the multichannel LPE sequence follows a multivariate Gaussian distribution. This

multivariate Gaussian approximation for the multichannel error sequence (cf. Equations 3.11 and 3.12) may be written as :

$$p\left(e_n|\theta_c^{(X)}\right) = \frac{(2\pi)^{-p/2}}{\sqrt{\det(\Sigma_e)}} \exp\left[-\frac{e_n^T (\Sigma_e)^{-1} e_n}{2}\right] \quad (5.5)$$

where  $\Sigma_e$  is the  $p \times p$  covariance matrix. Thus the complete set of texture parameters in this case is  $\theta_c^{(X)} = \theta_M = \left\{ \hat{\mu}, \left\{ \hat{A}_m \right\}_{m \in D}, \hat{\Sigma}_e \right\}$ . Although this approximation is simple and mostly used, but it has two disadvantages:

- Segmentation results are not robust and stable.
- These results are not optimal.

To address these two problems of sub-optimal and unstable results, we propose two other parametric models for approximation of the distribution of multichannel LPE sequence  $E$ :

1. Wishart probability distribution.
2. MGMM probability distribution.

In the next subsections we will discuss both these approximations in detail.

### 5.2.3 Wishart distribution

The Wishart distribution is a generalization to multiple dimensions of the chi-square distribution. To achieve robustness and stability of approximation, this model takes into account multiple observations to define the probability of a given observation instead of using a single observation ( $e_n$  in our case). Therefore, the LPE vectors of a finite neighborhood are used along with the LPE vector of a given pixel to define the probability of LPE for that pixel.

Given  $J$ , a matrix of  $\epsilon$  LPE column vectors of dimension  $d$  taken into account for the definition of  $p(e_n)$  with  $\epsilon \geq d$ , the Wishart distribution can be characterized by its probability density function as in the following equation:

$$p\left(e_n|\theta_c^{(X)}\right) = \frac{|M|^{\epsilon-d-1} \exp\left(-\frac{1}{2}\text{Tr}(\Sigma_e^{-1}M)\right)}{2^{\epsilon(d/2)} \pi^{d(d-1)/4} |\Sigma_e|^{\epsilon/2} \prod_{i=1}^d \Gamma\left(\frac{1}{2}(\epsilon+i-1)\right)} \quad (5.6)$$

where  $M = J^T J$  is a positive semidefinite matrix of size  $d \times d$ . Here we have considered the first order horizontal and vertical neighboring LPE vectors. Therefore in our case  $\epsilon = 5$  and  $J$  is given as:

$$J = [e_{n-1_v}, e_{n-1_h}, e_n, e_{n+1_v}, e_{n+1_h}]^T \quad (5.7)$$

with  $1_h = [1, \emptyset]$  and  $1_v = [\emptyset, 1]$ . In the case of three channel complex LPE in RGB color space  $d = 3$  as  $P = 3$ . In the case of two channel complex LPE for the images defined by the Equation (3.10) in IHLS and L\*a\*b\* color spaces, we have a zero imaginary component for the first (luminance) channel. Hence, in this case too we have  $d = 3$  although  $P = 2$ .  $\Gamma$  is the gamma function. The complete set of texture parameters in this case too, is  $\theta_c^{(X)} = \theta_M$ .

### 5.2.4 Multivariate Gaussian Mixture Model

In this section we present an MGMM model for the distribution of multichannel LPE sequence  $E$ . The Gaussian mixture model for the multichannel error sequence  $E$  is defined as:

$$p(e_n | \theta_c^{(X)}) = \sum_{k=1}^K \alpha_k p(e_n | \theta_k) \quad (5.8)$$

where  $\alpha_1, \dots, \alpha_K$  are the prior probabilities of each Gaussian component of the mixture, and  $K > 1$  is the number of components of MGMM. Each  $\theta_k = \{\mu_{k,e}, \Sigma_{k,e}\}$ ,  $k = 1, \dots, K$ , is the set of model parameters defining the  $k$ th component of the mixture model, with  $\mu_{k,e}$  is the mean and  $\Sigma_{k,e}$  is the covariance matrix of  $k$ th component of the mixture. The prior probability values must satisfy following conditions:

$$\alpha_k > 0, k = 1, \dots, K \quad (5.9)$$

and

$$\sum_{k=1}^K \alpha_k = 1 \quad (5.10)$$

For the 2D complex error sequence  $E$ , MGMM can be conceived by considering the real and imaginary parts of the complex error sequence as two variates of the mixture model. For MGMM, each component density  $p(e_n | \theta_k)$  is a normal probability distribution with  $d = 3$  in our case as we do not consider the imaginary component of the luminance channel (cf. section 5.2.3):

$$p(e_n | \theta_k) = \frac{(2\pi)^{-p/2}}{\sqrt{\det(\Sigma_{k,e})}} \exp \left[ -\frac{1}{2} (e_n - \mu_{k,e})^T (\Sigma_{k,e})^{-1} (e_n - \mu_{k,e}) \right] \quad (5.11)$$

Thus the complete set of texture parameters is  $\theta_c^{(X)} = \{\theta_K, \theta_M\}$  with mixture model parameter set denoted by  $\theta_K$  is given as  $\theta_K = \{\theta_1, \dots, \theta_K, \alpha_1, \dots, \alpha_K\}$ . It is important to note that in this case the observation model parameter set computed through the training sub image is  $\theta_M = \{\hat{A}_m\}_{m \in D, \hat{\mu}}$ .

The mixture model parameter set  $\theta_K$  is also estimated from the training sub image along with the training model parameter set  $\theta_M$ . The most widely used approach for the estimation of the MGMM parameter set  $\theta_K$ , from a given dataset is to use MLE:

$$\hat{\theta}_K = \operatorname{argmax}_{\theta} p(e|\theta) \quad (5.12)$$

where  $f(\theta) = p(e|\theta)$  is the likelihood function. The EM algorithm is a general iterative technique for computing MLE when observed data can be considered as incomplete. The algorithm consists of two steps: An E-step and an M-step. The EM algorithm produces a sequence of estimates  $\theta_K^{(t)}$ ,  $t = 0, 1, 2, \dots$  by repeating these two steps. If  $\theta_K^{(t)}$  denotes the estimated mixture model parameter set at iteration  $t$ , then at iteration  $(t + 1)$  the E-step computes the expected complete data log-likelihood function:

$$Q(\theta_K, \theta_K^{(t)}) = \sum_{n \in \Lambda} \sum_{k=1}^K \{\log \alpha_k p(e_n | \theta_k)\} P(k | e_n; \theta_K^{(t)}) \quad (5.13)$$

where  $P(k | e_n; \theta_K^{(t)})$  is the *a posteriori* probability and is computed as:

$$P(k | e_n; \theta_K^{(t)}) = \frac{\alpha_k^{(t)} p(e_n | \theta_k^{(t)})}{\sum_{l=1}^K \alpha_l^{(t)} p(e_n | \theta_l^{(t)})} \quad (5.14)$$

The M-step finds the estimate of  $\theta_K$  at iteration  $(t + 1)$ , by maximizing the hidden variable  $Q(\theta_K, \theta_K^{(t)})$ :

$$\alpha_k^{(t+1)} = \frac{1}{|\Lambda|} \sum_{n \in \Lambda} P(k | e_n; \theta_K^{(t)}) \quad (5.15)$$

$$\mu_{k,e}^{(t+1)} = \frac{\sum_{n \in \Lambda} e_n P(k | e_n; \theta_K^{(t)})}{\sum_{n \in \Lambda} P(k | e_n; \theta_K^{(t)})} \quad (5.16)$$

$$\Sigma_{k,e}^{(t+1)} = \frac{\sum_{n \in \Lambda} P(k | e_n; \theta_K^{(t)}) (e_n - \mu_{k,e}^{(t+1)}) (e_n - \mu_{k,e}^{(t+1)})^T}{\sum_{n \in \Lambda} P(k | e_n; \theta_K^{(t)})} \quad (5.17)$$

EM algorithm is strongly dependent on initialization of parameter values. One way is to start with a number of random starts and then assigning the final value which gives the maximum-likelihood. This will increase the computation time, as evident. In our approach we have used well known K-means algorithm to compute the initial values of mixture model parameter set  $\theta_K$ .

### 5.2.5 Label Field Estimation

In this section we present the maximum *a posteriori* (MAP) estimation of the final class label field as in [BS94, AR05]. As discussed in the section 5.1, the likelihood method defines the *a posteriori* law  $p(\omega|x)$  as the probability of getting one specific realization of the label field knowing the observation field.  $p(\omega|x)$  can be written in a general form according to the Gibbs distribution [Guy95]:

$$p(\omega|x) \propto \exp(-U_D(x, \omega) - U_i(\omega)) \quad (5.18)$$

in which  $U_D$  is an “energy function” depending on the given observation field  $x$  and the label field  $\omega$ , while  $U_i$  is the energy function depending only on the label field and which will allow the regularization of the label field. Let’s now define  $U_x(\omega) = U_D(x, \omega) + U_i(\omega)$ . Following the Equation (5.18), the MAP estimation of  $\omega$  can then be written in the terms of this energy function:

$$\hat{\omega}_{MAP} = \arg \max_{\omega \in F_c} [p(\omega|x)] = \arg \min_{\omega \in F_c} [U_x(\omega)] \quad (5.19)$$

Therefore, we have to optimize  $U_x : F_c \rightarrow \mathbb{R}$  to find  $\hat{\omega}_{MAP}$ , the segmentation of the textured image. We can write:

$$U_D(x, \omega) = \sum_n \left( -\log \left( p \left( e_n | \theta_{\omega_n}^{(X)} \right) \right) \right) \quad (5.20)$$

where  $p \left( e_n | \theta_{\omega_n}^{(X)} \right)$  is the corresponding conditional probability of the LPE given the respective model parameters of our parametric models of LPE (cf. Equations (5.5), (5.6) and (5.8)).

Now we have to model the label field in order to obtain  $U_i(\omega)$ . Our choice consists of two terms of energies associated to the label field,  $U_i(\omega) = U_{i,1}(\omega) + U_{i,2}(\omega)$ . This definition of  $U_i$  makes it different from the classical Potts model. The term  $U_{i,1}(\omega)$  represents the Gibbs energy term associated to the Potts model [BS94]:

$$U_{i,1}(\omega) = \beta \left( \sum_{\langle n_1, n_2 \rangle_1} (1 - \delta(\omega_{n_1}, \omega_{n_2})) + \sum_{\langle n_1, n_2 \rangle_2} (1 - \delta(\omega_{n_1}, \omega_{n_2})) \right) \quad (5.21)$$

with  $\delta$  the Kronecker symbol,  $\beta$  the weight term or hyperparameter of the Potts model and  $\langle n_1, n_2 \rangle_p$ ,  $p = 1, 2$ , signifying  $\|n_1 - n_2\|_2 = \sqrt{p}$ ,  $(n_1, n_2) \in \Lambda^2$ ,  $n_1 \neq n_2$ . It is to note that the classical definition of the Potts model [BS94] contains a factor of  $\frac{1}{\sqrt{2}}$  with the second term. this factor is omitted here as this new definition does not affect the final results significantly. Potts model assumption corresponds to a general hypothesis about the label field: the classes can be permuted without any influence on the probability law. The hyperparameter  $\beta$  represents the global cost function of region boundaries. As we increase the value of  $\beta$ , the total length of the region boundaries in the estimated label field decreases.

As in [TZ02], we added an energy term  $U_{i,2}(\omega)$ , which depends on the size of the region. The size of a region  $R$ ,  $A = |R|$  in label fields follows a probability distribution which encourages the large regions to form. This prior is defined as

$$p(A) \propto \exp(-\gamma A^{-\phi}) \quad (5.22)$$

where  $\phi$  is taken as a constant in [TZ02]. In this work we have studied the influence of this coefficient on the segmentation results.  $\gamma$  is a scale factor which controls the scale of segmentation. Therefore  $U_{i,2}(\omega)$  may be defined as

$$U_{i,2}(\omega) = \gamma \left( \sum_{i=1}^{n_R} |R_i|^{-\phi} \right) \quad (5.23)$$

$\gamma$  is proposed to be taken as a constant in [TZ02]. Herein, we also varied the values of  $\gamma$  to study the effects of varying scale factor on the final results.  $n_R$  is the total number of regions in  $\omega$  such that  $\Lambda = \bigcup_{i=1}^{n_R} R_i$ ,  $R_i \cap R_j = \emptyset$ ,  $(i, j) \in \llbracket 1, n_R \rrbracket^2$ .

To validate the theoretical approach developed in this section, different sets of experiments were carried out. These used synthetic color textures as well as high resolution satellite images. The experimental procedures, test conditions and results of these experiments are presented in the next sections.

### 5.3 Synthetic Color Textures

As we discussed in the pixel classification experiments (cf. section 4.4.4), the ground truth data associated with complex natural images is difficult to estimate and its extraction is highly influenced by the subjectivity of the human operator. Thus, the evaluation of the proposed parametric texture segmentation framework was performed on natural as well as synthetic color textures which possess unambiguous ground truth data. Like in pixel classification experiments, for these tests

too, the test images were taken from the color texture database used in [IW08]. The database in [IW08] was constructed using color textures from Vistex and Photoshop databases.

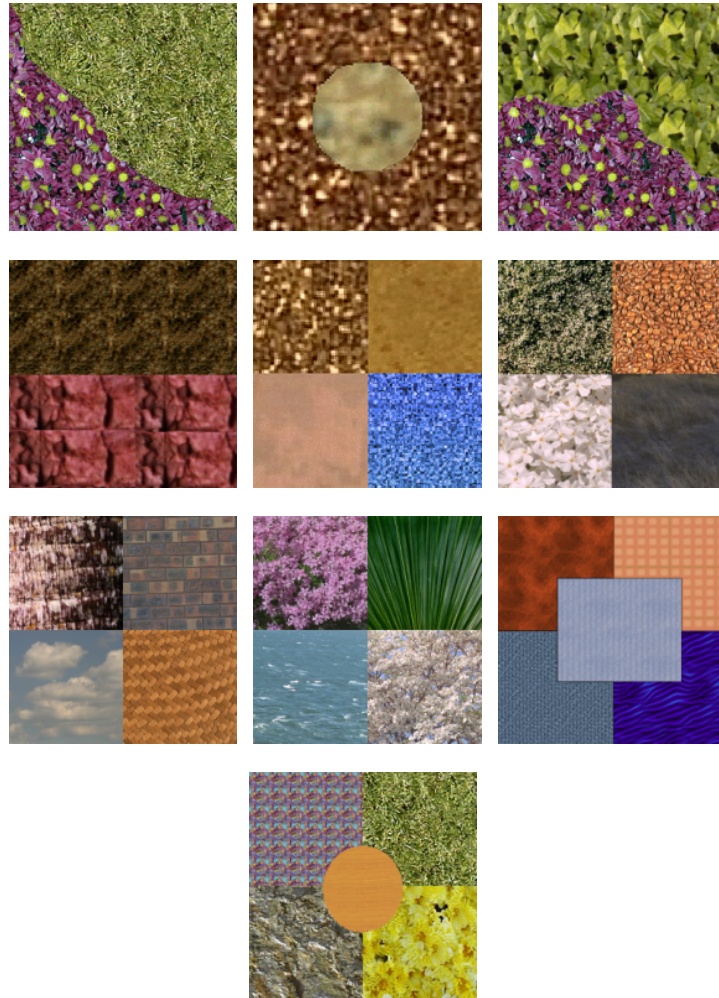


Figure 5.2: Data base of ten color images used for simulations.

In the first phase of the proposed supervised color texture segmentation algorithm (cf. section 5.2), a single sub image of size  $32 \times 32$  was used as the training image for each class. Image observation model parameters and multichannel prediction error were computed for this sub image. Then, using this image observation model and the multichannel LPE sequence, parameter sets for the used parametric approximations were calculated. Now these parameters were used to compute the initial class label field for each of the ten test textured color images shown in Figure 5.2. In the second phase of the algorithm, this coarse

class label field is spatially regularized. For this second phase of the algorithm, we conducted two sets of experiments.

### 5.3.1 Classical Potts Model

In the first set of experiments, we did not use the region size energy term  $U_{i,2}$  discussed in Equation 5.23, therefore for this set of experiments we just had  $U_i(l) = U_{i,1}(l)$ . We applied an iterative solution to the Potts model and it was computed through conventional Iterative Condition Mode (ICM). The hyperparameter,  $\beta$  was varied from 0.25 to 5.85 with a linear interval of 0.2. This resulted in 29 different segmentations of each image for a given observation model, a given color space and a given parametric model of the LPE distribution. Experiments were conducted using all three (causal and non-causal) 2D multichannel real and complex linear prediction models. The model orders for 2D QP AR model and 2D NSHP AR model were kept (2, 2), while for 2D GMRF model the order was 5. These model orders were chosen to establish a consistency with the choices made in the chapter 4. These results can be analyzed to evaluate the performance of the used multichannel real and complex image observation models, parametric approximations of the LPE distribution and the used color spaces.

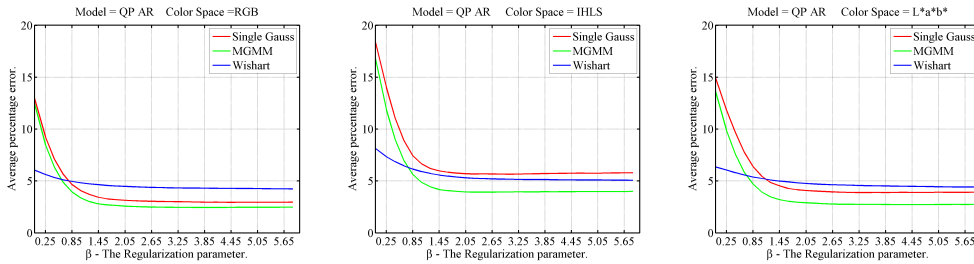


Figure 5.3: Comparison of the average percentage error of the segmentation results obtained using three different parametric models of the LPE in RGB, IHLS and  $L^*a^*b^*$  color spaces (from left to right respectively). The observation model used is 2D multichannel QP AR model.

If we analyze these results, it is clear that the MGMM approximation of the multichannel LPE distribution shows better results than the other two approaches in the terms of mean percentage error for the ten color images used in these experiments. This enforces the hypothesis that multichannel LPE may not be best approximated using a simple Gaussian distribution.

These results may also be analyzed with reference to the comparison of the used causal and non-causal multichannel image observation models, we see that the causal models i.e. 2D multichannel NSHP AR model and 2D multichannel

	RGB (%/ $\beta$ )	IHLS (%/ $\beta$ )	L*a*b* (%/ $\beta$ )
GMRF	10.44/2.05	12.95/2.25	7.65/2.45
NSHP AR	3.45/4.05	5.90/2.85	3.98/3.85
QP AR	<b>2.94/4.45</b>	5.65/3.05	3.88/3.45

Table 5.1: Average percentage pixel classification error of 10 color textures with corresponding values of  $\beta$ . The parametric model of the LPE used is the classical multivariate Gaussian distribution. The best result is indicated in bold faces.

	RGB (%/ $\beta$ )	IHLS (%/ $\beta$ )	L*a*b* (%/ $\beta$ )
GMRF	10.36/1.85	12.58/2.05	5.86/2.65
NSHP AR	2.93/4.05	4.21/2.85	2.91/5.25
QP AR	<b>2.44/3.65</b>	3.92/2.25	2.72/4.05

Table 5.2: Average percentage pixel classification error of 10 color textures with corresponding values of  $\beta$ . The parametric model of the LPE distribution used is MGMM. The best result is indicated in bold faces.

	RGB (%/ $\beta$ )	IHLS (%/ $\beta$ )	L*a*b* (%/ $\beta$ )
GMRF	9.52/5.85	10.97/5.85	6.67/5.85
NSHP AR	4.47/5.85	5.43/5.85	4.57/5.85
QP AR	<b>4.23/5.85</b>	5.07/5.85	4.41/5.85

Table 5.3: Average percentage pixel classification error of 10 color textures with corresponding values of  $\beta$ . The parametric model of the LPE distribution used is the Wishart distribution. The best result is indicated in bold faces.

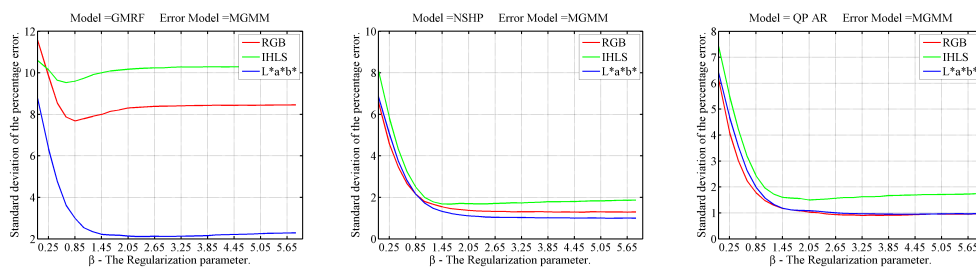


Figure 5.4: Comparison of the standard deviation of the average segmentation error in three different color spaces using 2D multichannel GMRF, NSHP AR and QP AR models (from left to right respectively). The parametric model used for LPE approximation is MGMM.

QP AR model perform better than the non-causal model i.e. 2D multichannel

GMRF model. This better performance of causal models for characterizing color textures, has already been observed and studied in detail in chapters 3 and 4. The best results presented in this set of experiments are all in the cases when 2D multichannel QP AR model is used as the image observation model. The percentage error scores obtained through 2D multichannel NSHP AR model are also very closed to those obtained through 2D multichannel QP AR model. As the 2D multichannel QP AR model gives the best scores, graphical representation of the results obtained using this image observation model are shown in Figure 5.3. In these figures, average percentage pixel classification error of ten color images using different parametric models of the LPE distribution against varying values of  $\beta$ , the regularization parameter of the Potts model is plotted.

The initial value of the average percentage error in these plots is given for  $\beta = 0$ , i.e. the percentage error value that is computed over the initial class label field estimated through the parametric approximations of the LPE distribution without using any spatial regularization (cf. Equation 5.21). Analyzing these plotted results (cf. Figure 5.3), two significant observations are made. First, the overall performance of the MGMM approximation after the spatial regularization is better than the other two approximations for all the three color spaces. Secondly, the Wishart distribution does not show the global minimum values of the average percentage error, yet the initial value of the percentage error in this case is much lower than the other two error models. This is attributed to the robust and stable prior term computed in the case of Wishart distribution as it considers multiple observations i.e. LPE vectors to compute the probability of a given observation (LPE vector). This observation makes the Wishart distribution a strong candidate as an approximation for the LPE distributions in the applications where no spatial regularization is needed.

Out of these segmentation results with different models, the ones which showed the minimum average percentage pixel classification error of 10 color textures are presented in Tables 5.1, 5.2 and 5.3.

For the comparison of results in different color spaces, only average percentage error values are not sufficient. Therefore we computed the standard deviation values of these results for the color space comparison. The MGMM approximation of the multichannel LPE distribution has shown the stable and best results. Therefore for the color space comparison, we used the results obtained through this model. These results are presented in Figure 5.4. These are the plots of the variance of percentage error results for the ten textures plotted against the different values of  $\beta$ , the regularization parameter.

These results clearly indicate better and stable results in the case of RGB and L\*a\*b\* color spaces. However, L\*a\*b\* color space shows an edge over RGB color spaces in certain cases, for example in Figure 5.4. In the case of MGMM

approximation, the results obtained in all the used color spaces are equally stable and robust which makes it really very hard to pick one up as the better candidate than the other.

### 5.3.2 Region Size Penalty

In this second set of experiments, we used the region size energy term  $U_{i,2}$  discussed in Equation 5.23, therefore for this set of experiments we had  $U_i(l) = U_{i,1}(l) + U_{i,2}(l)$ . In these experiments we again applied an iterative solution computed through the conventional ICM. In these experiments we used  $\beta$  i.e. the hyperparameter of the Potts model, as a *progressively varying parameter*. We used the regularized segmentation result obtained through one value of  $\beta$  as an initial class label field for the next value of  $\beta$ . The value of the hyperparameter  $\beta$  was varied from 0.1 to 5.0 with an exponential interval. For the region energy term, we fixed the hyperparameter  $\gamma = 2$  and the coefficient  $c = 0.9$ . Experiments were conducted using only 2D multichannel QP AR model, as it performed best in the first experiment set. The model order for 2D QP AR model was kept  $(2, 2)$ .

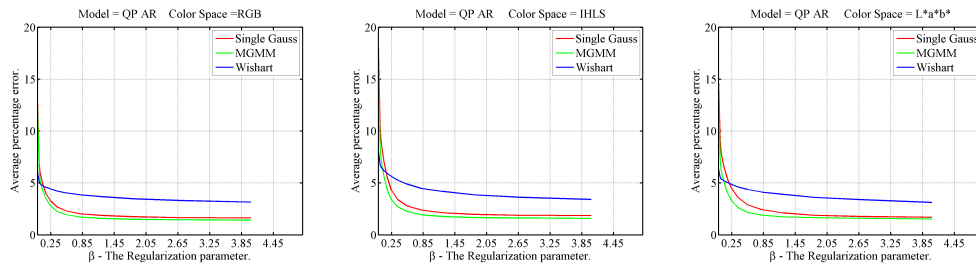


Figure 5.5: Comparison of the average percentage error of the segmentation results obtained with region penalty term, using three different parametric models of the LPE in RGB, IHLS and  $L^*a^*b^*$  color spaces (from left to right respectively). The observation model used is 2D multichannel QP AR model.

This resulted in 13 different segmentations of each image for a given color space and a given parametric model of the LPE distribution. Out of these segmentations, the ones which showed the minimum average percentage pixel classification error of 10 color textures are presented in Table 5.4. These results can be analyzed in the exact same manner as the results presented in the previous sub section. These are analyzed to evaluate the performance of the used parametric approximations of the LPE distribution and the used color spaces. These results show approximately the same observations and they reinforce the results and observations made at the end of the previous experiment. In addition to these

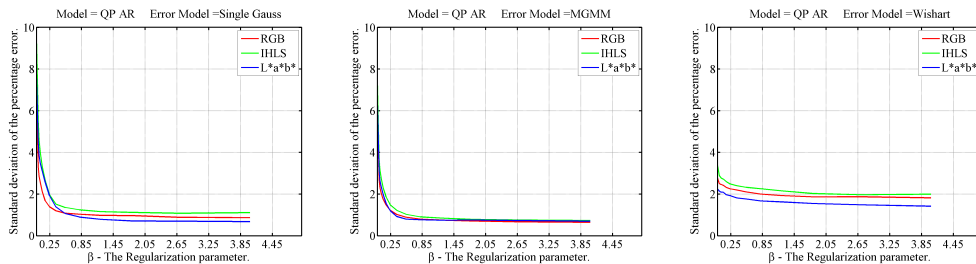


Figure 5.6: Comparison of the standard deviation of the average segmentation error in three different color spaces with region penalty term, using 2D multichannel multivariate Gaussian, MGMM and Wishart distribution models (from left to right respectively). The observation model used is 2D multichannel QP AR model.

observations, these results (presented in Figure 5.5) depict another important observation on the spatial regularization step of the algorithm about the region size penalty term used. It is evident from these results that penalizing very small region sizes (of around 5 to 10 pixels in our case) for disappearance and favoring the large regions to form in the test images give us much improved segmentation results. Using this region size penalty term in the spatial regularization step of the proposed algorithm has not only improved the segmentation results in the terms of percentage mean error. The algorithm also reaches to a fine and stable level of segmentation at lower values of hyperparameter  $\beta$ .

	RGB	IHLS	L*a*b*
Single Gauss	1.62	1.85	1.68
MGMM	<b>1.40</b>	1.58	1.52
Wishart	3.14	3.37	3.09

Table 5.4: Average percentage pixel classification error of 10 color textures. The image observation model is 2D multichannel QP AR model. The best results are indicated in bold faces.

In this experiment set, for the comparison of results in different color spaces, same procedure as in previous one has been adopted. The 2D multichannel QP AR model has shown the stable and best results. Therefore for the color space comparison, we used the results obtained through this model. These results are presented in Figure 5.6. These are the plots of the standard deviation of the percentage error results for the ten textures plotted against the different values of  $\beta$ , the regularization parameter.

These results clearly indicate better and more stable results in the case of RGB and L\*a\*b\* color spaces. However, L\*a\*b\* color space shows an edge in the stability of results over the RGB color space in the cases when classical Gaussian approximation or Wishart approximation is used (cf. Figure 5.6). In the case of MGMM approximation of the LPE distribution, the results obtained in all the used color spaces are equally stable and hence it is really very hard to pick one up as the better candidate.

For the test images 3, and 10, the final segmented results computed in RGB and L\*a\*b\* color spaces using different approximations are presented in Figures 5.7, 5.8, 5.9 and 5.10 respectively. These segmentation results are obtained using 2D multichannel QP AR model. In each figure, the first, second and the third row present the segmentation results computed using classical single Gaussian approximation, MGMM approximation and the Wishart distribution respectively. The first column in these figures, show the segmented images without any spatial regularization *i.e.* with  $\beta = 0$ . The second column presents the segmented images using ICM with Potts model for spatial regularization. Finally the third column shows the final segmented images using ICM with Potts model (with variable  $\beta$ ) and the added region size penalty term for the spatial regularization. The similar image organization has been adopted in all these figures. These results reinforce the observations made earlier in this section.

### 5.3.3 Comparative Analysis

The color texture segmentation performance of the color texture descriptor discussed in this chapter can be compared to the similar state of the art approaches presented in the recent years. One such work is presented in [KP06]. The authors represented the different classes in the image by Multivariate Gaussian Mixture Model (*MGMM*). They used Gabor filters as texture features whereas pixel values in CIE L\*u\*v\* color space are considered as color feature cue. In [KP06], authors have used 4 color texture images prepared from Vistex color texture database. First one of these 4 color texture images is of size  $256 \times 256$ , while the other three are of size  $128 \times 128$ . These four images are presented in Figure 5.11 (row 1). In [KP06], authors have discussed both supervised and non-supervised frameworks of color texture segmentation. Here we discuss only the supervised color texture segmentation results computed through ICM.

To compare the results obtained through our method with the ones presented in [KP06], we conducted experiments on these four images also. 2D QP AR model was used as the image observation model, and MGMM was used as the approximation method for LPE distribution. Final segmented images in RGB and L\*a\*b\* color spaces are presented in Figure 5.11 (row 2 and row 3 respectively).

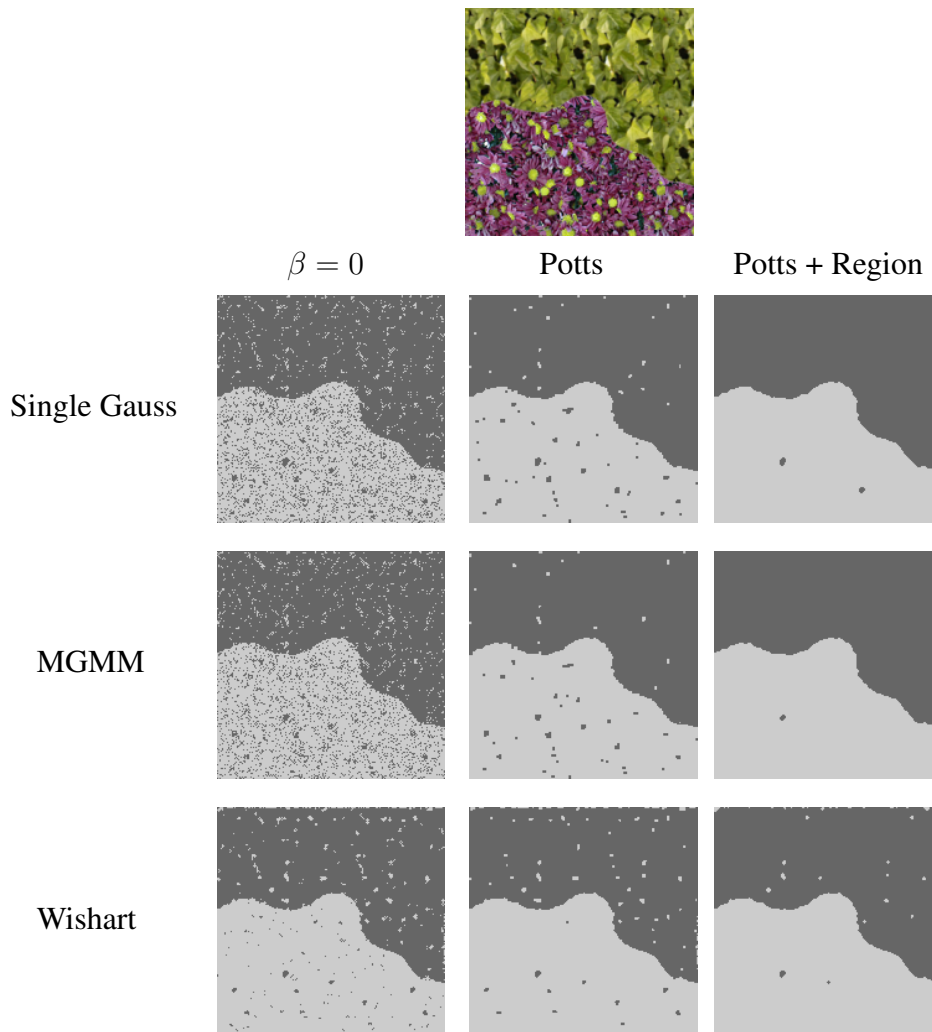


Figure 5.7: Segmentation results without spatial regularization (column  $\beta = 0$ ), with spatial regularization using only Potts model (column **Potts**) and with spatial regularization using Potts model with varying  $\beta$  and region size penalty (column **Potts + Region**) for the color texture 3 using single Gaussian (row 2), MGMM (row 3) and Wishart approximation (row 4) in RGB color space.

A quantitative comparison of the individual as well as average percentage error results is presented in the Table 4.5.

In [KP06], color and texture are characterized using different descriptors. In this work we have presented a pure texture descriptor which also characterizes the chromatic spatial variations of the image (in the case of IHLS and L\*a\*b\* color spaces) and approximates the spatial distribution of the pure color content of the image. Taking this consideration into account, it is clear that for three out

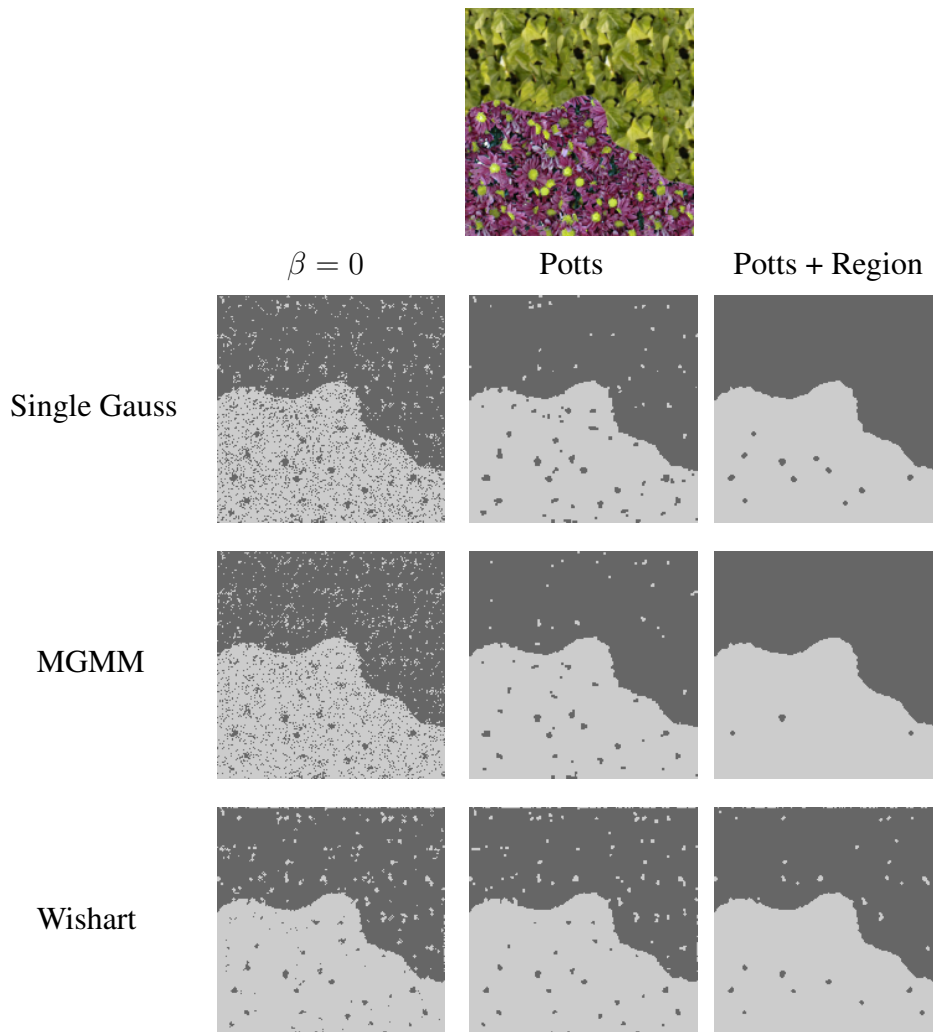


Figure 5.8: Segmentation results without spatial regularization (column  $\beta = 0$ ), with spatial regularization using only Potts model (column **Potts**) and with spatial regularization using Potts model with varying  $\beta$  and region size penalty (column **Potts + Region**) for the color texture 3 using single Gaussian (row 2), MGMM (row 3) and Wishart approximation (row 4) in L\*a\*b\* color space.

of four images, our method gives better results than the ones presented (using the texture descriptor) in [KP06]. For these images, our method with only a texture descriptor gives results which are approximately of the same order as the best ones in [KP06] (using both color and texture descriptors).

For the first image, as stated in [KP06], three regions contain a wooden texture with nearly matching colors and a small difference in the direction (left and lower part) or scale (middle part) in texture. The two other regions have similar

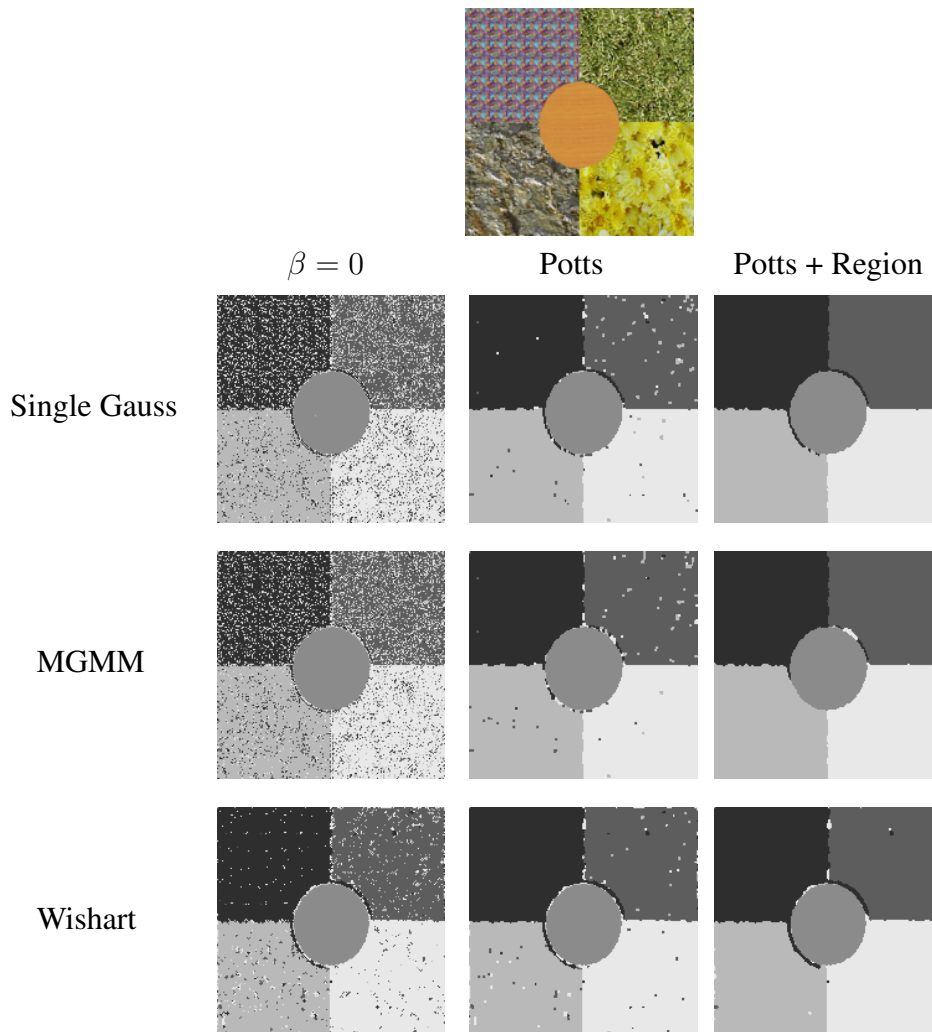


Figure 5.9: Segmentation results without spatial regularization (column  $\beta = 0$ ), with spatial regularization using only Potts model (column **Potts**) and with spatial regularization using Potts model with varying  $\beta$  and region size penalty (column **Potts + Region**) for the color texture 10 using single Gaussian (row 2), MGMM (row 3) and Wishart approximation (row 4) in RGB color space.

texture but completely different color. This makes the segmentation of this image an ill-posed problem demanding rotation and scale invariance from the texture descriptor which is out of the scope of this work. For this image, our method performs lower than that of the one presented in [KP06]. Comparison of the overall average percentage error also shows that the presented method gives quite satisfactory results.

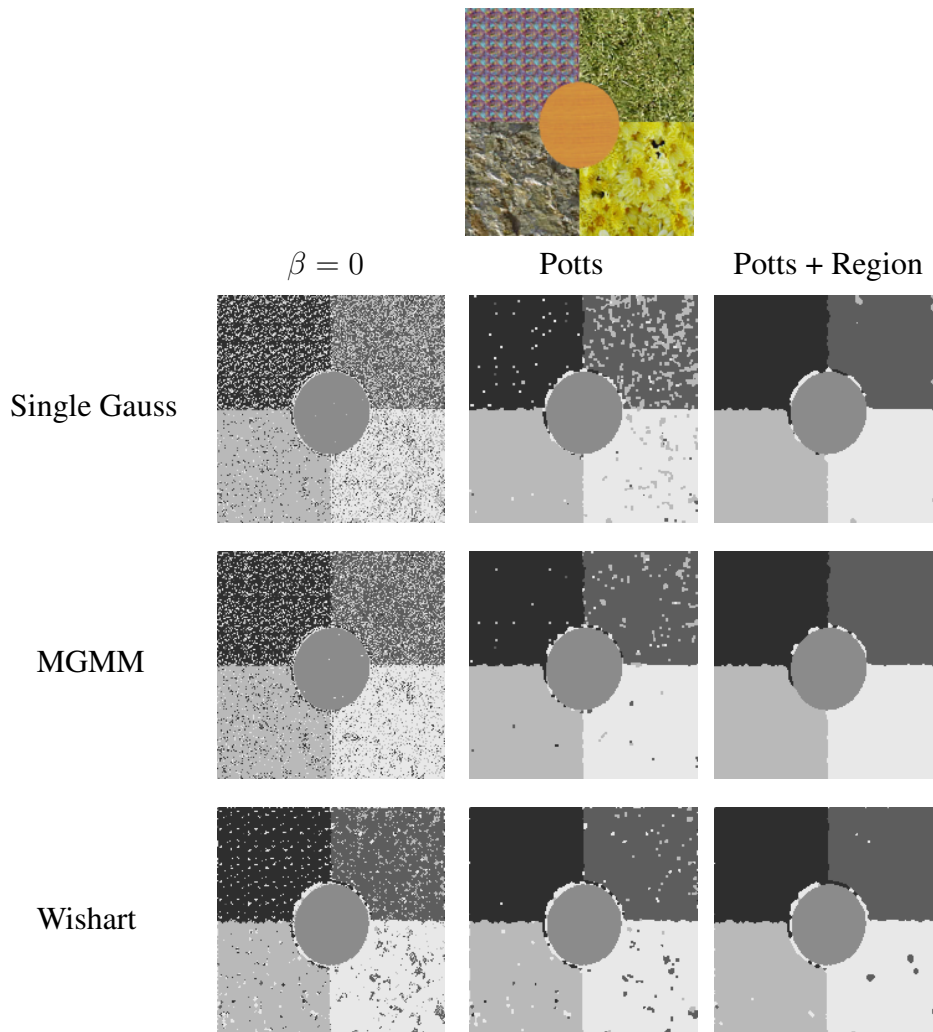


Figure 5.10: Segmentation results without spatial regularization (column  $\beta = 0$ ), with spatial regularization using only Potts model (column **Potts**) and with spatial regularization using Potts model with varying  $\beta$  and region size penalty (column **Potts + Region**) for the color texture 10 using single Gaussian (row 2), MGMM (row 3) and Wishart approximation (row 4) in  $L^*a^*b^*$  color space.

## 5.4 High Resolution Satellite Images

Segmentation in high resolution satellite images has been a point of interest for researchers over the past few years. Several approaches based on parametric and/or non-parametric features of these images have been proposed [LW07, GTYH07]. A parametric approach to address the classification of aerial images presented in [DJG00], discusses the fusion of color and texture features for aerial image

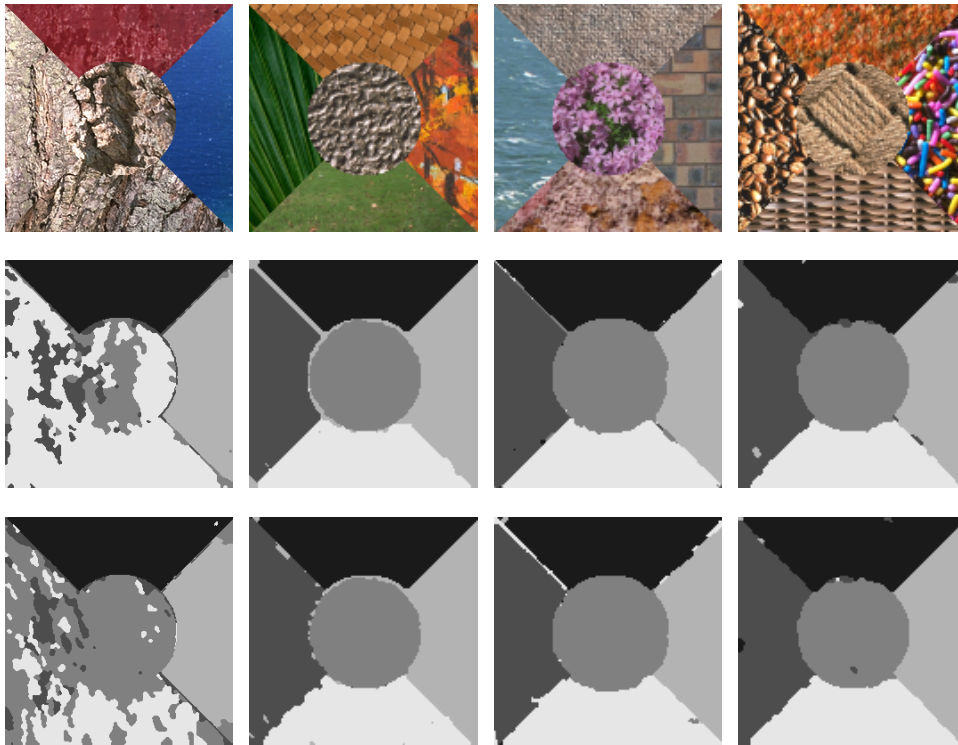


Figure 5.11: The original images (row 1) and the final segmentation results using our method in RGB (row 2) and ( $L^*a^*b^*$ ) color spaces for a comparative analysis with [KP06].

	Method in [KP06]			Our Method	
	Texture only	Color only	Combined	RGB	$L^*a^*b^*$
Color Texture 1	20.6	23.1	11.4	29.3	27.1
Color Texture 2	23.3	1.8	0.45	3.2	3.2
Color Texture 3	18.3	2.0	1.0	3.0	3.5
Color Texture 4	25.6	7.5	3.9	2.4	2.4
Average	22.9	17.2	4.2	9.5	9.0

Table 5.5: Comparative analysis of the approach with the results presented in [KP06] with respect to the percentage error.

segmentation application. In this approach, maximum likelihood segmentation is applied to the image in each feature space (color and gray level texture) separately. A final segmentation is obtained by combining the likelihoods in the two spaces using a certainty function. For texture feature computation in the intensity

information of the image, the authors have made use of the SAR model discussed in [MJ92]. In this work authors have assumed a classical multivariate Gaussian probability distribution for the data and gave a hypothesis that the reported results could be improved using multimodal probability distributions.

Most of these approaches appear to give suboptimal results for high resolution satellite images. This happens so, as:

- These do not have control over the fusion process of low resolution multispectral images with high resolution monospectral images.
- The details in these images are difficult to model through conventional color and texture descriptors and their utilization methodologies.

We developed a framework for the land cover classification in high resolution satellite images in which the fusion of these images can be addressed along with the segmentation process while ensuring the coherence between the two. It consists of two steps. In the first step we merge the multispectral images of low spatial resolution with a monospectral image of higher spatial resolution in order to improve the resolution of multispectral images. This image fusion is based on the search of an optimal 3D hybrid color space (cf. section - The Fusion Approach). In the second step we apply our parametric segmentation discussed in this chapter to obtain a land cover classification map of these high resolution satellite images. We conducted the experiments on high resolution satellite images using the proposed texture segmentation framework. These images are acquired through **IKONOS** and **QuickBird** observation satellites.

### 5.4.1 The Fusion Approach

As presented in [Pet01], IKONOS acquires a panchromatic image (*Pan*) with a resolution of 1m/pixel and a multispectral image comprising of  $B_1$ ,  $B_2$ ,  $B_3$  and near Infra Red *i.e.* NIR ( $B_4$ ) bands with a resolution of 4m/pixel. Whereas, QuickBird acquires a panchromatic image (*Pan*) with a resolution of 0.7m/pixel and a multispectral image comprising of  $B_1$ ,  $B_2$ ,  $B_3$  and near Infra Red *i.e.* NIR ( $B_4$ ) bands with a resolution of 2.8m/pixel. For the images from both these satellites, the spectral bands  $B_1$ ,  $B_2$  and  $B_3$  correspond to the Blue, Green and Red channels of a color image [Pet01]. As an example, the relative spectral response of IKONOS imagery is shown in Figure 5.12, taken from [web].

The high resolution Pan images are highly textured and contain large amount of useful data for land cover classification. In order to make use of this high resolution information of the panchromatic image in a multispectral context, various approaches for the fusion of high resolution Pan images with low resolution images in  $B_1$ ,  $B_2$  and  $B_3$  bands have been proposed. These techniques use the high

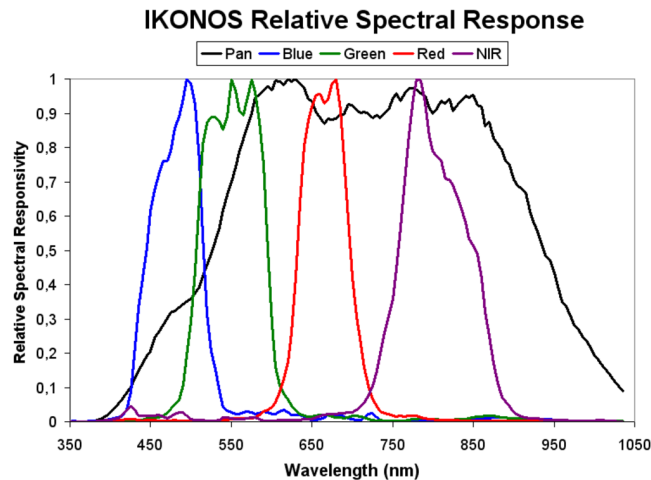


Figure 5.12: The relative spectral response of IKONOS imagery [web].

resolution Pan images along with the low resolution  $B_1$ ,  $B_2$  and  $B_3$  to produce high resolution versions of multispectral *i.e.*  $B_1$ ,  $B_2$ ,  $B_3$  images.

The approach of image fusion at different spatial and spectral resolutions, used in this thesis generalizes the different nonlinear color space transformations based on supervised training [AGK09]. This allows to consider the specificities and the particularities of the satellite images, to generalize the existing methods and to improve the fusion product. The approach employs hybrid color space construction method [Aba08]. After application of this method, the appropriate hybrid components denoted by  $I^*$ ,  $S^*$  and  $H^*$  are estimated with  $I^*$  component containing the most spatial information and thus the closest to the high resolution monospectral image. This allows to verify the identification constraint between the high and the low frequencies and hence the detailed information is preserved.

The rest of the fusion procedure does not differ much from the classic procedure stated in [WJCK90]. The core advantage of the added step is to extract the best combination of the three color variables from the multispectral images. For further details on this approach, [AGK09, Aba08] can be consulted. The resulting high resolution, real valued  $B_1$ ,  $B_2$ ,  $B_3$  images (represented by an RGB vector) can be converted to our two channel complex image representation using the discussed color spaces (cf. chapter 3).

We used a total of twenty (20) high resolution satellite images in these experiments. The content of these high resolution images is very rich and different classes are very similar. A brief description of these images is given in the Table 5.6. The area of study is the Island of Guadeloupe.

Image	Size (pixels)	Nr. classes	Land cover
Sat image $QB_1$	$512 \times 512$	4	Forest, agricultural and herbaceous land
Sat image $QB_2$	$512 \times 512$	5	-do-
Sat image $QB_3$	$512 \times 512$	2	Forest and herbaceous land
Sat image $IK_4$	$468 \times 468$	6	Forest and agricultural land
Sat image $IK_5$	$1008 \times 488$	5	-do-
Sat image $IK_6$	$960 \times 640$	4	Forest, agricultural land and sea
Sat image $QB_7$	$512 \times 512$	2	Forest and herbaceous land
Sat image $QB_8$	$512 \times 512$	2	-do-
Sat image $QB_9$	$512 \times 512$	2	-do-
Sat image $QB_{10}$	$512 \times 512$	2	-do-
Sat image $QB_{11}$	$512 \times 512$	3	Forest, agricultural and herbaceous land
Sat image $QB_{12}$	$512 \times 512$	3	-do-
Sat image $QB_{13}$	$512 \times 512$	3	-do-
Sat image $QB_{14}$	$512 \times 512$	4	Forest, agricultural, herbaceous land, empty field
Sat image $QB_{15}$	$512 \times 512$	3	Forest, agricultural land and empty field
Sat image $QB_{16}$	$512 \times 512$	3	Forest, herbaceous land and empty field
Sat image $QB_{17}$	$512 \times 512$	2	Forest and agricultural land
Sat image $QB_{18}$	$512 \times 512$	3	Forest, herbaceous land and empty field
Sat image $QB_{19}$	$512 \times 512$	3	Forest, agricultural and herbaceous land
Sat image $QB_{20}$	$512 \times 512$	3	-do-

Table 5.6: Brief description of the twenty high resolution satellite images.

	Classification (%)		Sensitivity (%)		Global error (%)	
	Single Gauss	MGMM	Single Gauss	MGMM	Single Gauss	MGMM
Sat image $QB_1$	84.1	82.4	80.3	79.5	8.6	9.4
Sat image $QB_2$	85.8	85.6	75.9	75.0	7.4	7.4
Sat image $QB_3$	93.9	89.5	93.7	91.0	7.1	11.5
Sat image $IK_3$	80.9	77.2	74.7	70.8	7.6	8.9
Average	86.2	83.7	81.2	79.1	7.7	9.3

Table 5.7: Land cover classification results in terms of classification, sensitivity and global error in RGB color space.

Out of these twenty images, four high resolution satellite images (Figure 5.13), one of the size  $468 \times 468$  pixels from IKONOS (Figure 5.13d) and three of the size  $512 \times 512$  from QuickBird (Figures 5.13a, 5.13b and 5.13c) were used in the initial set of experiments. A brief overview of the underlying land cover details for these four images are given as follows:

- Sat image  $QB_1$  contains a total of four classes in which there are two different classes representing agricultural land, one representing a forest region

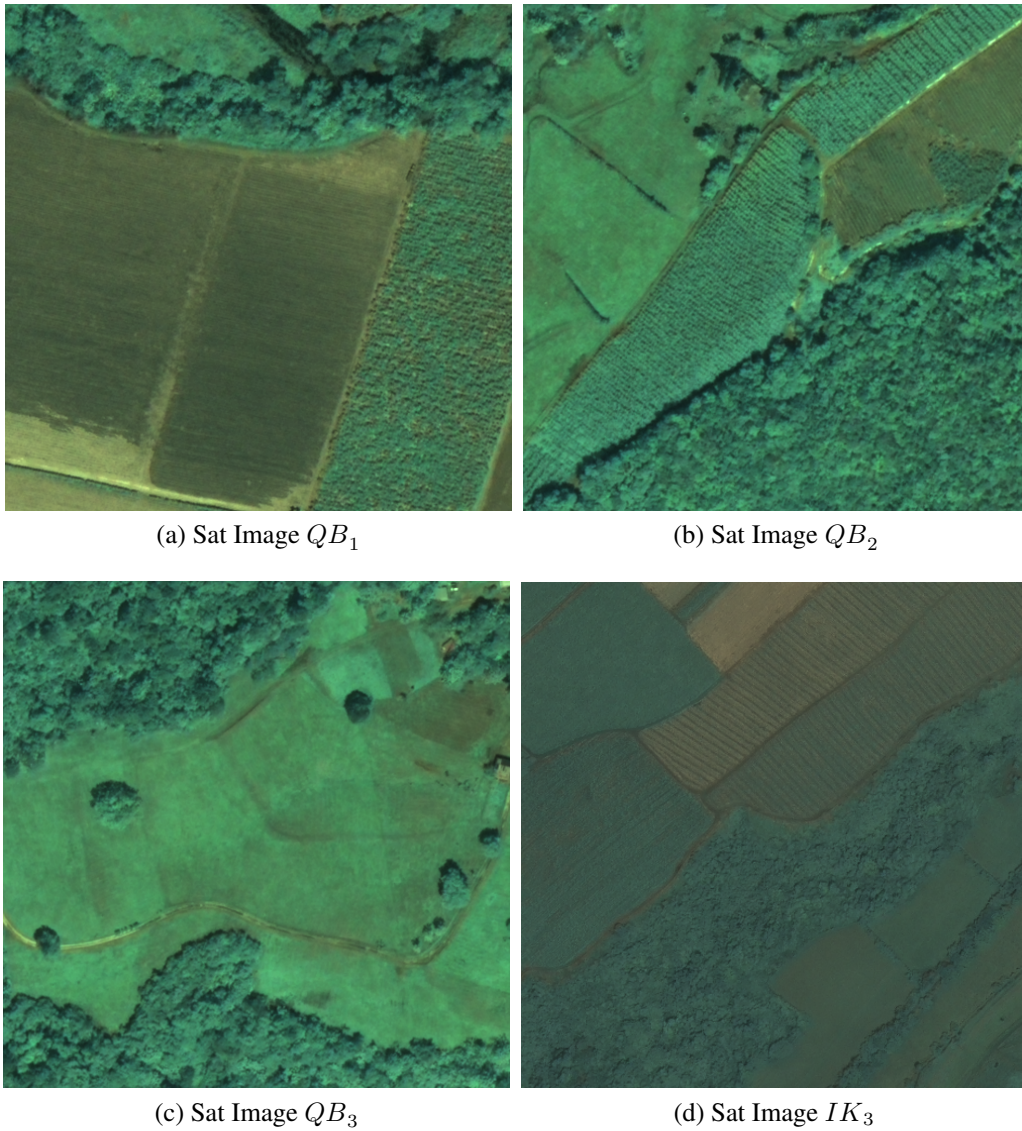


Figure 5.13: Four multichannel Satellite images used for initial simulations.

and another of the herbaceous land (see mask in the row 1 of the Figures 5.14 and 5.15).

- *Sat image  $QB_2$*  contains five classes representing forest, herbaceous land and three different classes of the agricultural fields (see mask in the row 2 of the Figures 5.14 and 5.15).

	Classification (%)		Sensitivity (%)		Global error (%)	
	Single Gauss	MGMM	Single Gauss	MGMM	Single Gauss	MGMM
Sat image $QB_1$	87.7	90.4	81.2	82.6	6.7	5.4
Sat image $QB_2$	87.1	87.1	75.7	75.9	6.8	6.8
Sat image $QB_3$	97.5	97.4	96.2	96.1	3.5	3.6
Sat image $IK_3$	85.6	87.8	83.6	85.4	36.3	5.3
Average	89.5	<b>90.7</b>	84.2	<b>85.0</b>	6.0	<b>5.3</b>

Table 5.8: Land cover classification results in terms of classification, sensitivity and global error in L\*a\*b\* color space.

- Sat image  $QB_3$  contains only two classes representing forest and herba-ceous regions (see mask in the row 3 of the Figures 5.14 and 5.15).
- Sat image  $IK_3$  contains six classes among which one is a representative of a forest region while other five classes represent different agricultural fields (see mask in the row 4 of the Figures 5.14 and 5.15).

For synthetic color texture segmentation experiments, MGMM approximation produced the optimal and stable overall performance when used in L\*a\*b\* color space along with the region size penalty term for the spatial regularization. Hence, we used the same configuration for these experiments too and also compared the results for these images using the classical Gaussian approximation for the distribution of the multichannel LPE in both RGB and L\*a\*b\* color spaces. In this set of experiments, the values of the hyper parameter  $\beta$  and the region size parameters  $\gamma$  and  $\phi$  are fixed as  $\beta = 2$ ,  $\gamma = 5$  and  $\phi = 0.9$ . (cf. section 5.2.5).

The respective class masks of the land cover created by experts for these four images and the segmentation results using 2D multichannel QP AR model of order (3, 3) with both the approximations of the multichannel LPE in RGB and L\*a\*b\* color spaces are also shown in Figures 5.14 and 5.15 (columns 2 and 3 respectively). The results for the land cover classification experiments, in RGB and L\*a\*b\* color spaces are presented in Tables 5.7 and 5.8 respectively. From these tables, the results in these two color spaces can be compared in terms of the percentage classification, percentage sensitivity and the percentage global error [Aba08]. The overall best results are indicated in boldfaces. It can be noticed that both the approximations of the multichannel LPE distribution have shown competitive results. However, the results are optimal and show increased stability through MGMM approximation when used in the L\*a\*b\* color space along with the region size penalty term for the spatial regularization. It can also be observed clearly from these results that the L\*a\*b\* color space presents the better over all results than RGB.

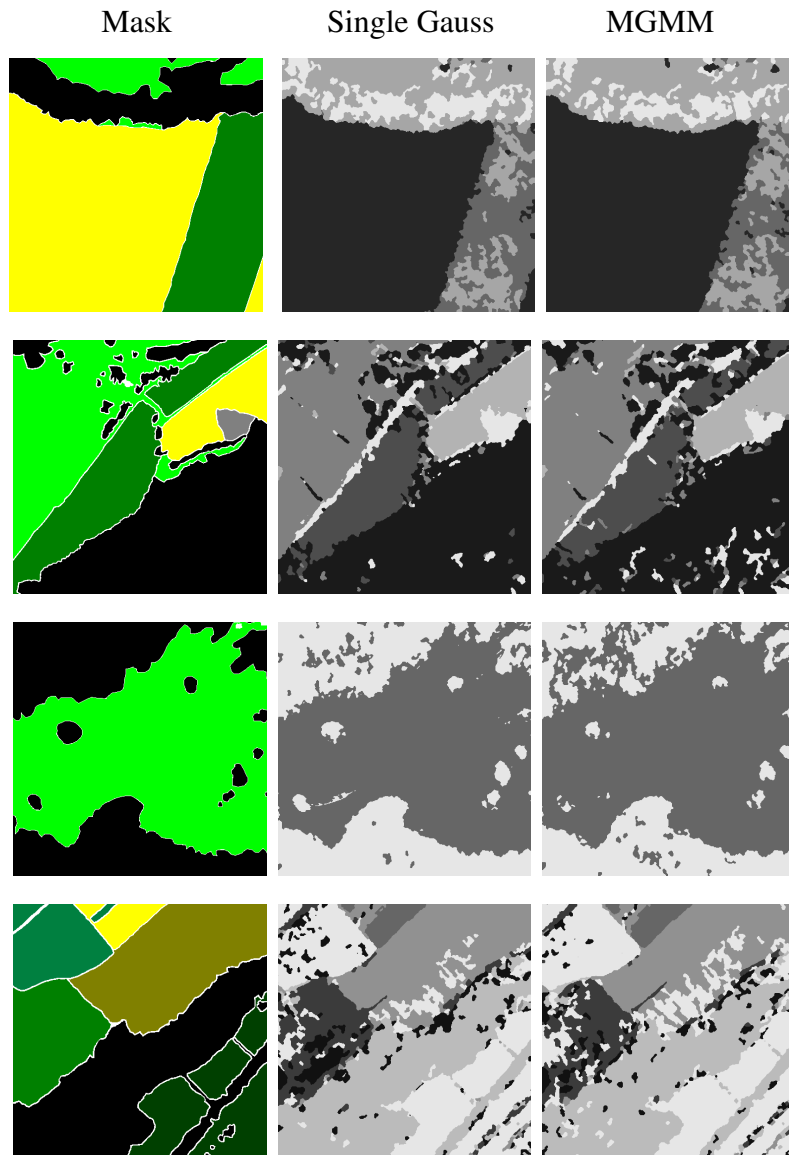


Figure 5.14: Segmentation results of the four used satellite images in RGB color space.

From these results we can see that the final segmentation results of the high resolution satellite images could be improved by a further fine tuning of the region size parameters *i.e.*  $\gamma$  and  $\phi$ . The effects of these parameters on the final results are studied in the following subsection.

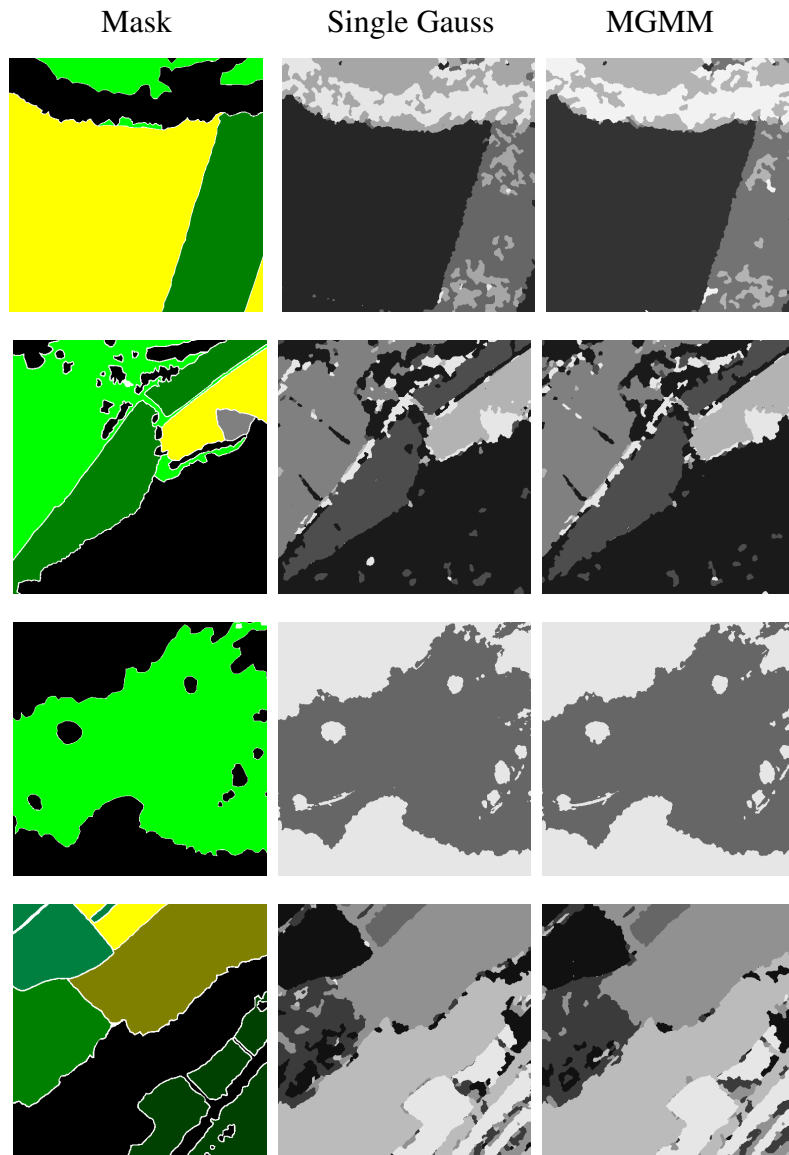


Figure 5.15: Segmentation results of the four used satellite images in  $L^*a^*b^*$  color space.

### 5.4.2 Effects of Varying Region Parameters

To improve the land area classification results of the chosen high resolution satellite images (cf. Figure 5.13), we carried out another set of experiments. In this set of experiments we varied the region size energy parameters *i.e.* the region size coefficient  $\phi$  and the segmentation scale factor  $\gamma$ , to study the effects of these parameters on the final segmentation results. The region size coefficient  $\phi$  was

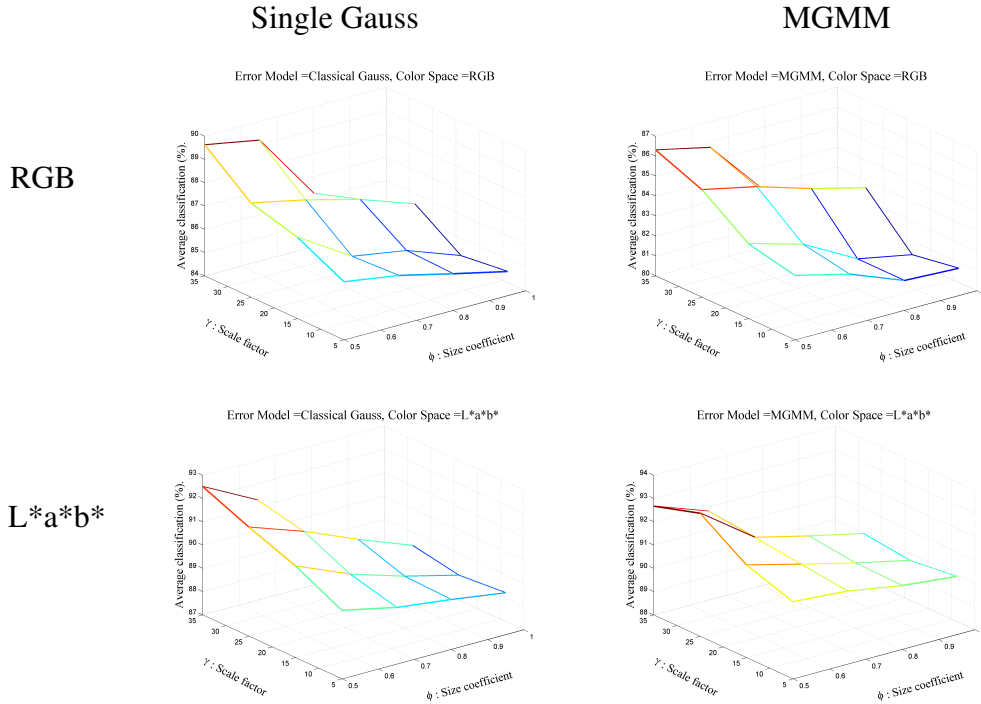


Figure 5.16: Average percentage pixel classification of four satellite images in RGB (row 1) and  $L^*a^*b^*$  (row 2) color space using classical Gaussian (left) and MGMM (right) approximations for the distribution of multichannel LPE.

varied from 0.5 to 0.95 with a linear interval of 0.15 and the segmentation scale factor was varied from 5 to 35 with a linear interval of 10. these experiments were (again like previous set of experiments on the four satellite images) conducted in RGB and  $L^*a^*b^*$  color spaces using classical Gaussian and MGMM approximations of the multichannel LPE distribution.

These results computed in the terms of average percentage values of pixel classification and sensitivity along with the global error are presented in Figures 5.16, 5.17 and 5.18. These results show that the overall effects of the region size parameters can be viewed as a physical description of the Equation 5.22. From these figures following important observations can be made:

- For the lower values of the region size coefficient  $\phi$ , the small region formation in the final label field is discouraged and hence better segmentation results are observed at lower values of  $\phi$ .
- If we analyze the effects of  $\gamma$ , in certain cases (e.g. when MGMM approximation is used in  $L^*a^*b^*$  color space), after a certain threshold value, the increase in  $\gamma$  makes the region size penalty term significant as compared to

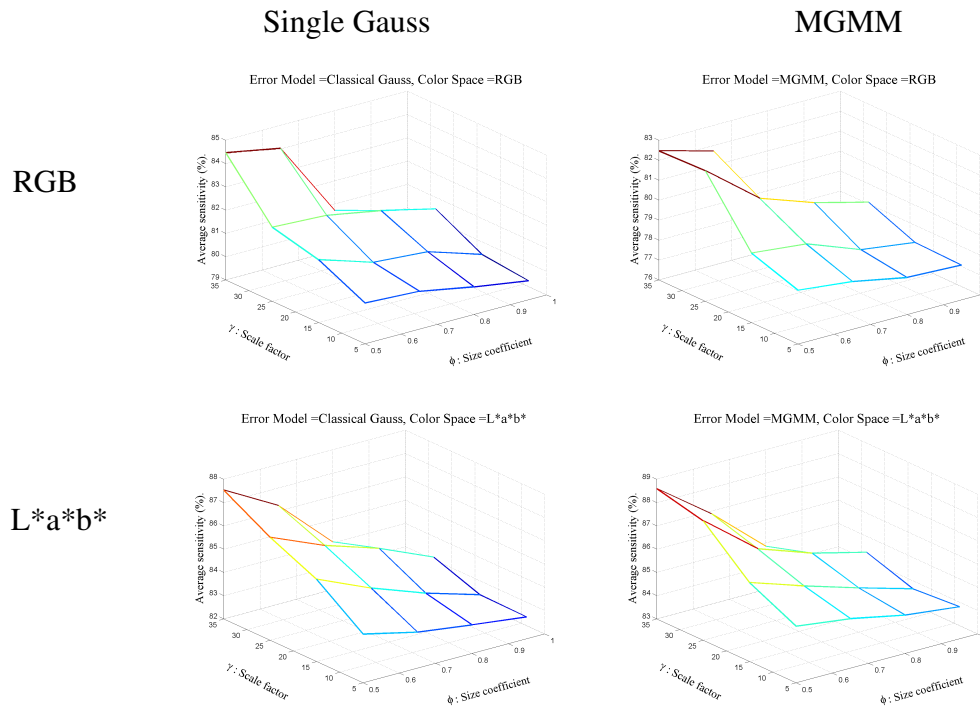


Figure 5.17: Average percentage sensitivity of four satellite images in RGB (row 1) and  $L^*a^*b^*$  (row 2) color space using classical Gaussian (left) and MGMM (right) approximations for the distribution of multichannel LPE.

the Potts energy term which leads to an over segmentation and the overall results deteriorate.

The best results computed in terms of individual as well as average percentage values of classification error and sensitivity along with the global error for these four images are shown in the Tables 5.9 and 5.10 respectively. The best overall results obtained in the two used color spaces are presented in bold faces.

These tables indicate that the segmentation results obtained for highly textured, high resolution satellite images, using MGMM approximation in  $L^*a^*b^*$  color space are better. It is also important to note that the variation of the region size parameters have given an overall 3% increase in the average percentage classification and sensitivity results of the previous experiment on high resolution satellite images (cf. Tables 5.7 and 5.8).

The final segmentation results for this first set of experiments, using both these approximations in RGB and  $L^*a^*b^*$  color spaces along with the respective class masks of the land cover created by experts for these four images are shown in Figures 5.19 and 5.20 (columns 2 and 3 respectively).

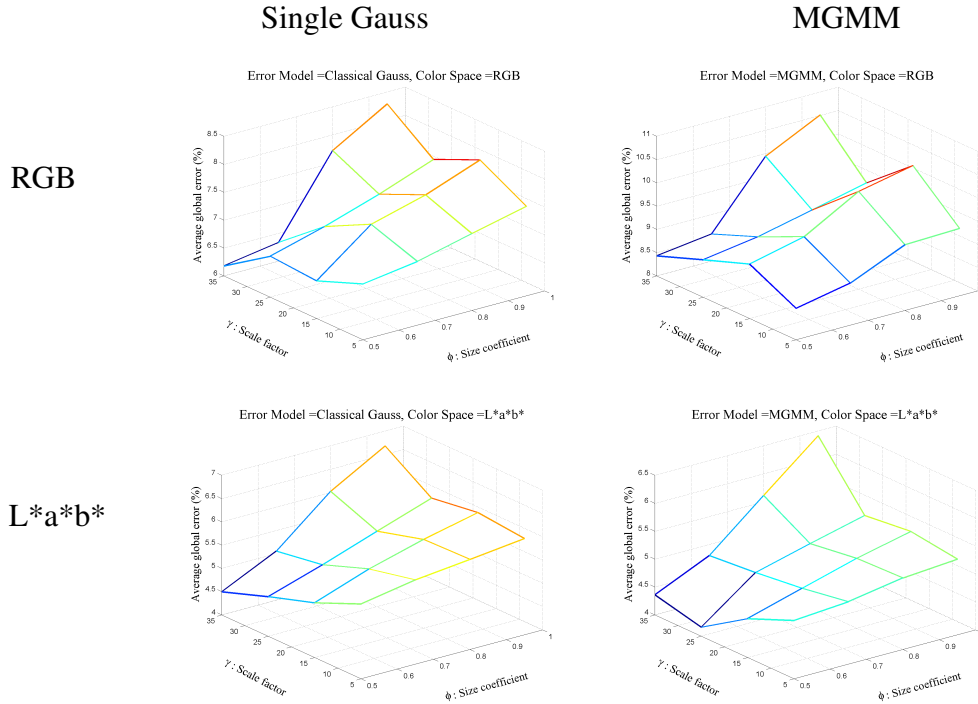


Figure 5.18: Average percentage global error of four satellite images in RGB (row 1) and  $L^*a^*b^*$  (row 2) color space using classical Gaussian (left) and MGMM (right) approximations for the distribution of multichannel LPE.

	Classification (%)		Sensitivity (%)		Global error (%)	
	Single Gauss	MGMM	Single Gauss	MGMM	Single Gauss	MGMM
Sat image $QB_1$	84.3	82.7	81.3	81.3	8.4	9.2
Sat image $QB_2$	89.5	88.5	79.1	79.4	5.9	6.2
Sat image $QB_3$	95.3	88.7	95.0	90.8	5.6	12.3
Sat image $IK_3$	82.9	81.4	73.2	78.6	6.9	7.4
Average	89.6	86.3	84.5	82.5	6.7	8.8

Table 5.9: Land cover classification results in terms of percentage values of pixel classification and sensitivity along with global error in RGB color space.

The optimal values of the region size parameters  $\gamma$  and  $\phi$  (computed from the first set of experiments on four images) are used to segment the remaining sixteen satellite images, in the second set of experiments. These images are shown in Figures 5.21 and 5.22. The segmentation results for these images are again computed using 2D multichannel QP AR model of order (3, 3), with classical single Gaussian and MGMM approximations of the multichannel LPE in both the

	Classification (%)		Sensitivity (%)		Global error (%)	
	Single Gauss	MGMM	Single Gauss	MGMM	Single Gauss	MGMM
Sat image $QB_1$	90.5	94.5	83.5	87.2	5.3	3.3
Sat image $QB_2$	90.0	89.9	79.8	80.0	5.6	5.7
Sat image $QB_3$	97.8	97.8	96.5	96.5	3.2	3.2
Sat image $IK_3$	88.4	91.0	85.8	88.8	5.1	4.2
Average	92.5	<b>93.3</b>	87.5	<b>88.6</b>	4.8	<b>4.1</b>

Table 5.10: Land cover classification results in terms of classification, sensitivity and global error in L\*a\*b\* color space.

color spaces *i.e.* RGB and L\*a\*b\*. For this set of experiments, values of the hyper parameter  $\beta$  and the region size parameters  $\gamma$  and  $\phi$  are fixed as  $\beta = 2$ ,  $\gamma = 25$  and  $\phi = 0.5$ .

The final segmented images for this set of experiments are presented in the Appendix C. The segmentation results in terms of percentage values of the classification error and sensitivity along with the global error, for these sixteen images in RGB and L\*a\*b\* color spaces are shown in the Tables 5.11 and 5.12 respectively. The best overall results obtained in the two used color spaces are again highlighted through bold faces.

	Classification (%)		Sensitivity (%)		Global error (%)	
	Single Gauss	MGMM	Single Gauss	MGMM	Single Gauss	MGMM
Sat image $IK_5$	49.1	44.3	75.4	75.3	22.9	24.9
Sat image $IK_6$	93.4	91.1	86.8	82.5	4.1	5.2
Sat image $QB_7$	97.7	97.7	97.2	97.2	2.8	2.8
Sat image $QB_8$	99.4	99.2	97.6	96.9	0.8	1.0
Sat image $QB_9$	97.5	97.3	95.7	95.9	3.2	3.4
Sat image $QB_{10}$	96.6	96.3	95.6	95.2	4.2	4.4
Sat image $QB_{11}$	89.4	84.1	89.6	86.8	8.7	12.3
Sat image $QB_{12}$	88.2	83.8	84.8	79.0	9.8	12.8
Sat image $QB_{13}$	94.7	92.1	93.9	92.1	5.0	6.7
Sat image $QB_{14}$	95.8	96.0	91.1	91.0	4.1	3.9
Sat image $QB_{15}$	98.4	98.0	93.5	94.1	1.4	1.7
Sat image $QB_{16}$	94.2	93.6	86.7	84.9	5.8	6.2
Sat image $QB_{17}$	98.4	98.6	95.1	95.2	5.5	5.3
Sat image $QB_{18}$	93.9	93.1	90.6	90.1	7.2	7.7
Sat image $QB_{19}$	96.8	96.1	93.3	93.1	5.4	5.8
Sat image $QB_{20}$	98.0	98.1	95.0	95.1	2.4	2.3
Average	92.6	91.2	91.4	90.3	5.8	6.7

Table 5.11: Land cover classification results in terms of classification, sensitivity and global error in the RGB color space.

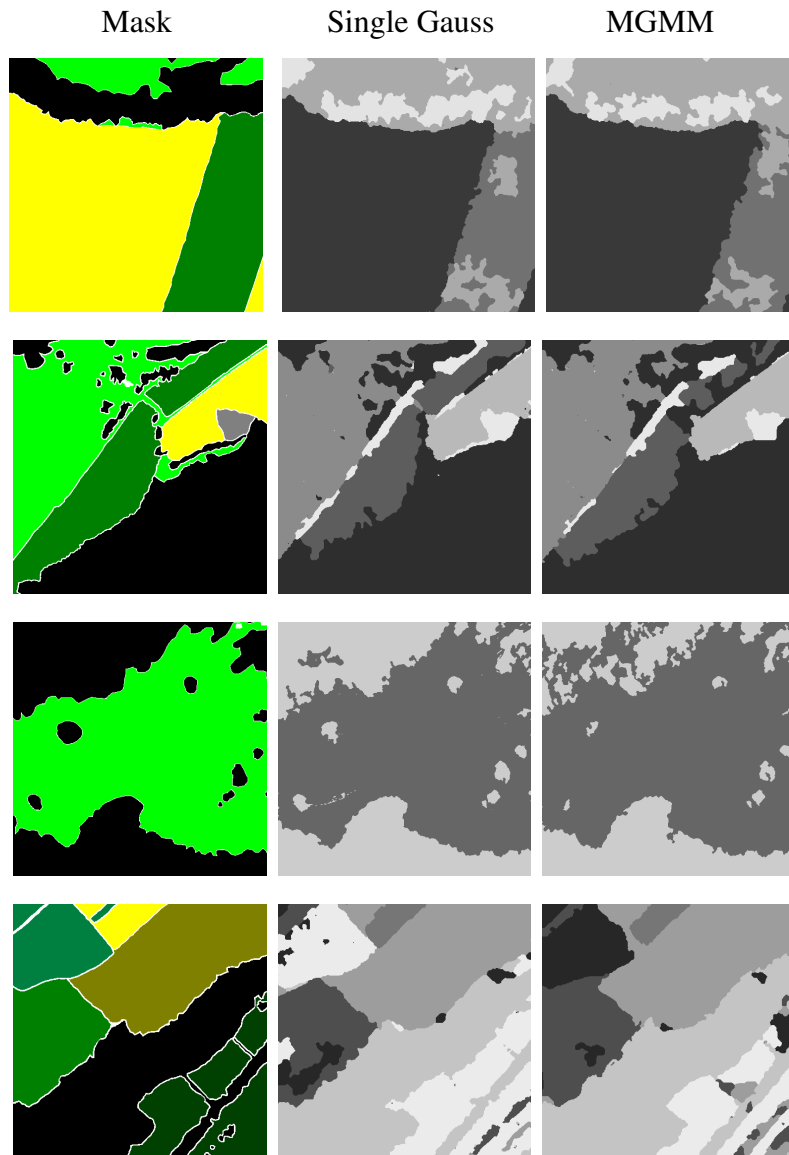


Figure 5.19: Segmentation results of the four used satellite images in RGB color space.

From these results it can be stated that both the approximations of the multichannel LPE distribution have shown good overall segmentation results. However, the results are optimal and show increased stability through MGMM approximation when used in the  $L^*a^*b^*$  color space along with the region size penalty term for the spatial regularization. It can also be observed clearly from these results that the  $L^*a^*b^*$  color space presents the better overall results than RGB.

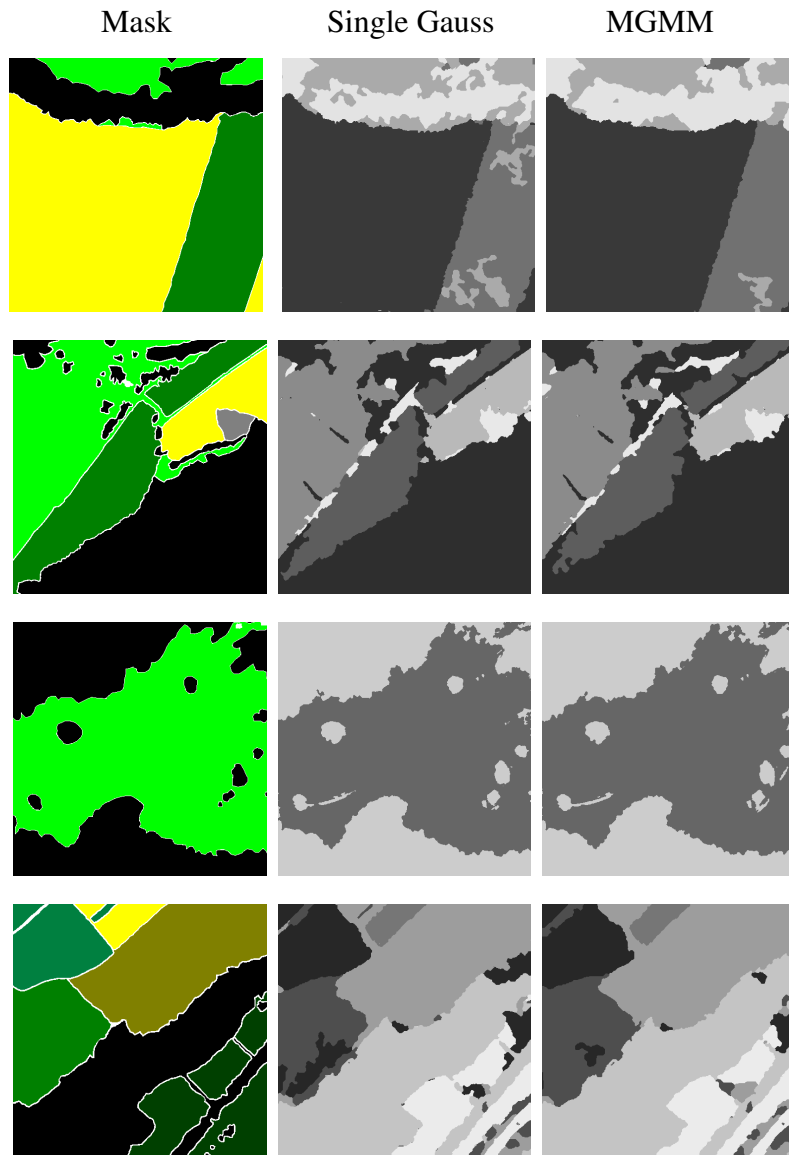


Figure 5.20: Segmentation results of the four used satellite images in  $L^*a^*b^*$  color space.

## 5.5 Conclusion

In this chapter we have proposed and analyzed a parametric model based framework of color texture segmentation based on different parametric approximations for the real and/or complex valued LPE distribution. The main conclusions drawn from this study could be stated as follows:

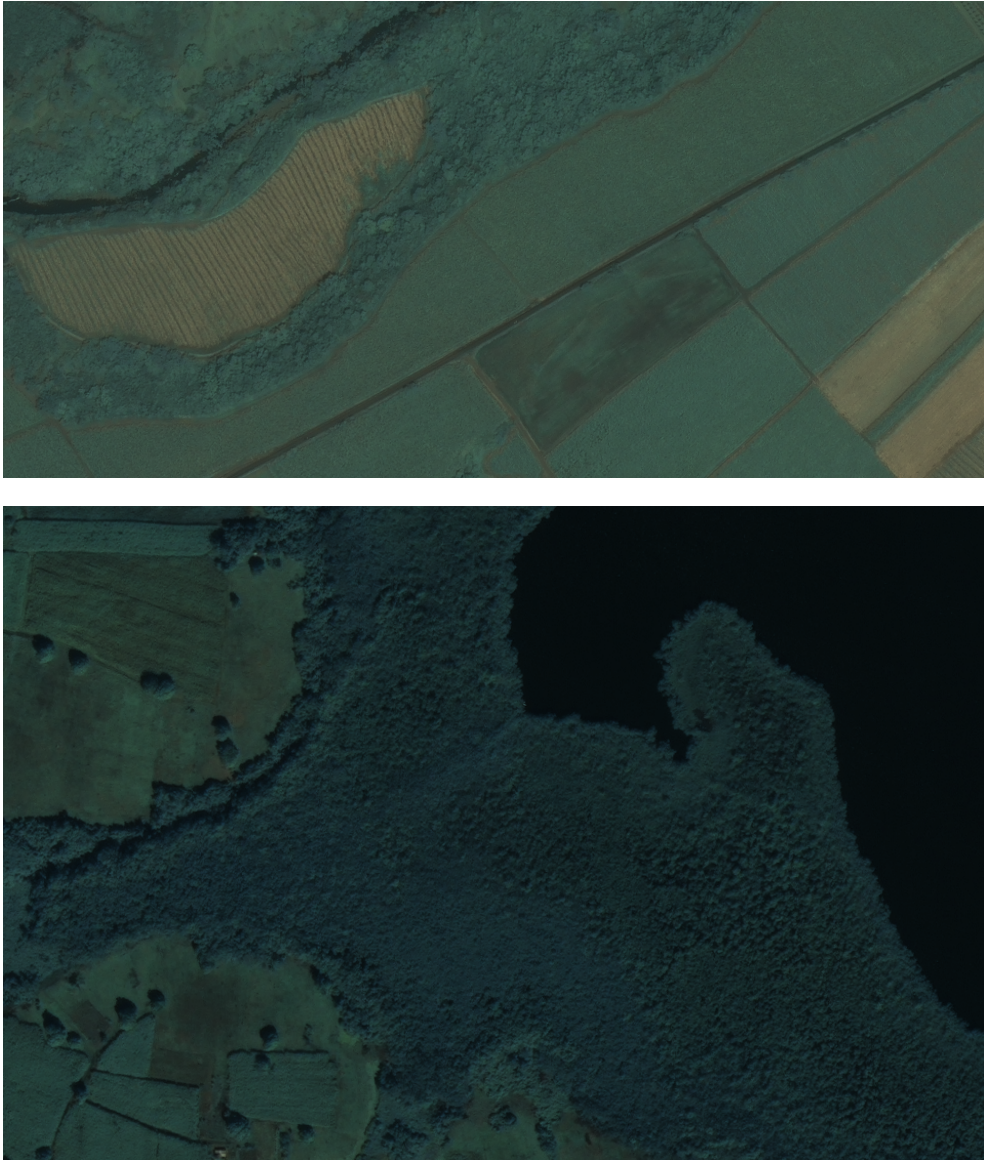


Figure 5.21: High resolution IKONOS satellite images (Sat image  $IK_5$  (row 1) and Sat image  $IK_6$  (row 2)) used in the second set of experiments.

- Among the three multichannel linear prediction models used as image observation models, 2D QP AR model has shown the best results, for both real (in RGB color space) and complex valued images (in perceptual color spaces). This is consistent with our previous findings for color texture characterization and classification (cf. chapter 4).

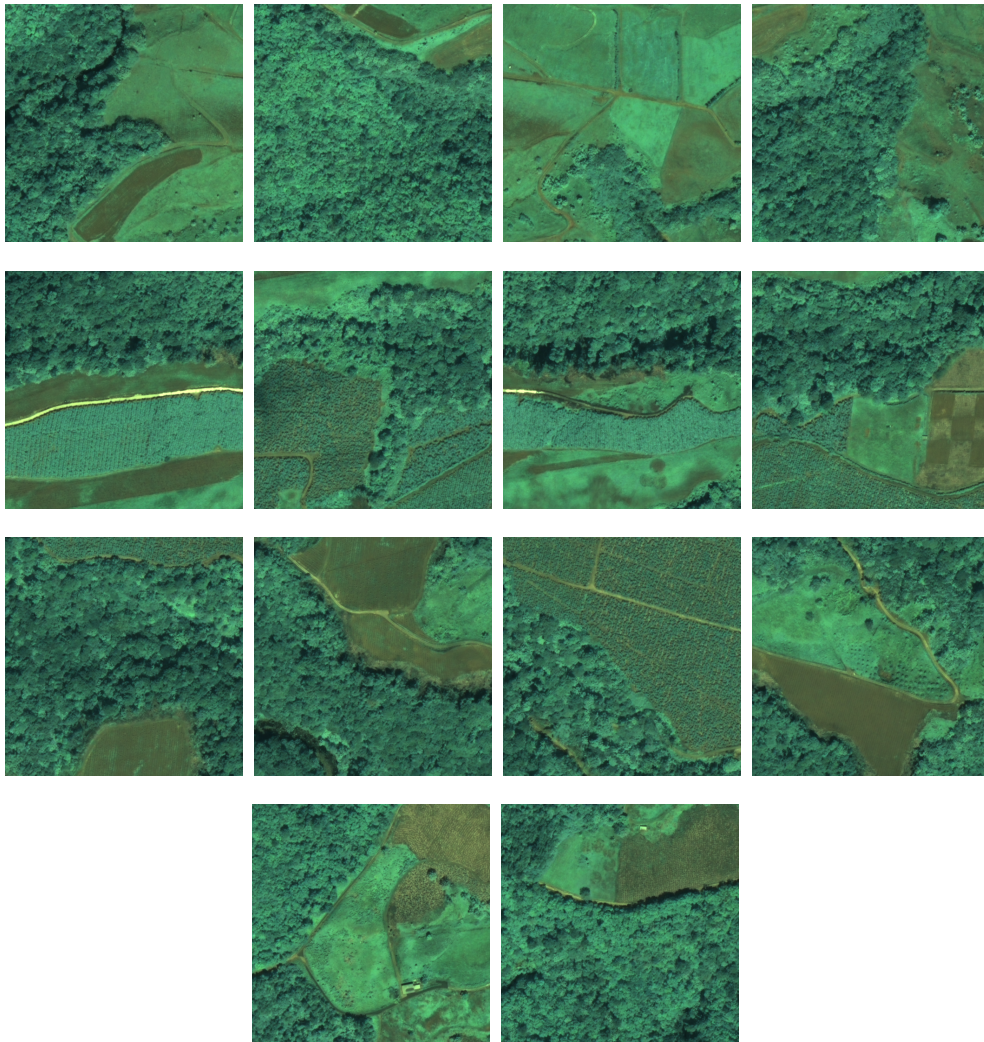


Figure 5.22: High resolution QuickBird satellite images (Sat image  $QB_7$  to Sat image  $QB_{20}$  in raster scan manner) used in the second set of experiments.

- Three different parametric models were used to approximate the probability distribution of the multichannel LPE. These included classically used multivariate Gaussian distribution, multivariate Gaussian mixture models and the Wishart distribution. A comparison of these three approaches have shown an overall advantage of using MGMM approximation for this approximation instead of a multivariate Gaussian distribution for synthetic color textures as well as high resolution satellite images. It exhibited better multichannel texture segmentation results in terms of mean percentage

	Classification (%)		Sensitivity (%)		Global error (%)	
	Single Gauss	MGMM	Single Gauss	MGMM	Single Gauss	MGMM
Sat image $IK_5$	84.8	82.8	76.5	74.8	8.7	9.5
Sat image $IK_6$	96.7	96.9	94.8	95.8	2.4	2.3
Sat image $QB_7$	97.1	97.1	96.7	96.6	3.4	3.5
Sat image $QB_8$	99.6	99.5	98.9	99.0	0.6	0.7
Sat image $QB_9$	97.2	97.5	94.6	95.4	3.5	3.2
Sat image $QB_{10}$	96.5	96.8	95.4	95.8	4.3	3.9
Sat image $QB_{11}$	95.6	96.1	93.1	93.7	4.6	4.2
Sat image $QB_{12}$	86.4	86.7	86.9	87.0	11.1	10.9
Sat image $QB_{13}$	94.0	94.2	93.2	93.9	5.5	5.3
Sat image $QB_{14}$	95.6	96.3	90.1	91.1	4.2	3.8
Sat image $QB_{15}$	96.8	96.8	89.7	89.7	2.4	2.5
Sat image $QB_{16}$	94.5	94.7	87.7	89.2	5.6	5.4
Sat image $QB_{17}$	97.5	97.8	94.3	94.5	6.4	6.2
Sat image $QB_{18}$	92.9	93.2	89.8	89.9	7.8	7.7
Sat image $QB_{19}$	96.2	96.2	92.0	92.1	5.8	5.8
Sat image $QB_{20}$	97.3	97.2	95.0	95.0	2.8	2.9
Average	94.9	<b>95.0</b>	91.8	<b>92.1</b>	4.9	<b>4.9</b>

Table 5.12: Land cover classification results in terms of classification, sensitivity and global error in the L\*a\*b\* color space.

errors over the used synthetic color texture database as well as the satellite images.

- The Wishart distribution also produced good initial class label fields without any spatial regularization. However during spatial regularization through Potts model, as the initially computed log likelihood term using this distribution becomes very significant, therefore it is less *affected* by the spatial regularization in general.
- The introduction of the region size based penalty term [TZ02] in the conventional Potts energy model has shown improved results in terms of percentage errors of color texture segmentation. Moreover this term has also shown an earlier optimal convergence (for lower values of the hyperparameter  $\beta$  (cf. section 5.3.2)) as compared to the spatial regularization using classical Potts model (cf. section 5.3.1).
- The comparison of results in the three used color spaces shows that the RGB and the L\*a\*b\* color spaces perform better than IHLS color space in terms of the percentage errors as well as the stability of the results. However RGB and L\*a\*b\* color spaces have the same order of percentage errors, yet L\*a\*b\* color space shows a significant improvement in terms of stability of the segmentation results in most of the presented cases.

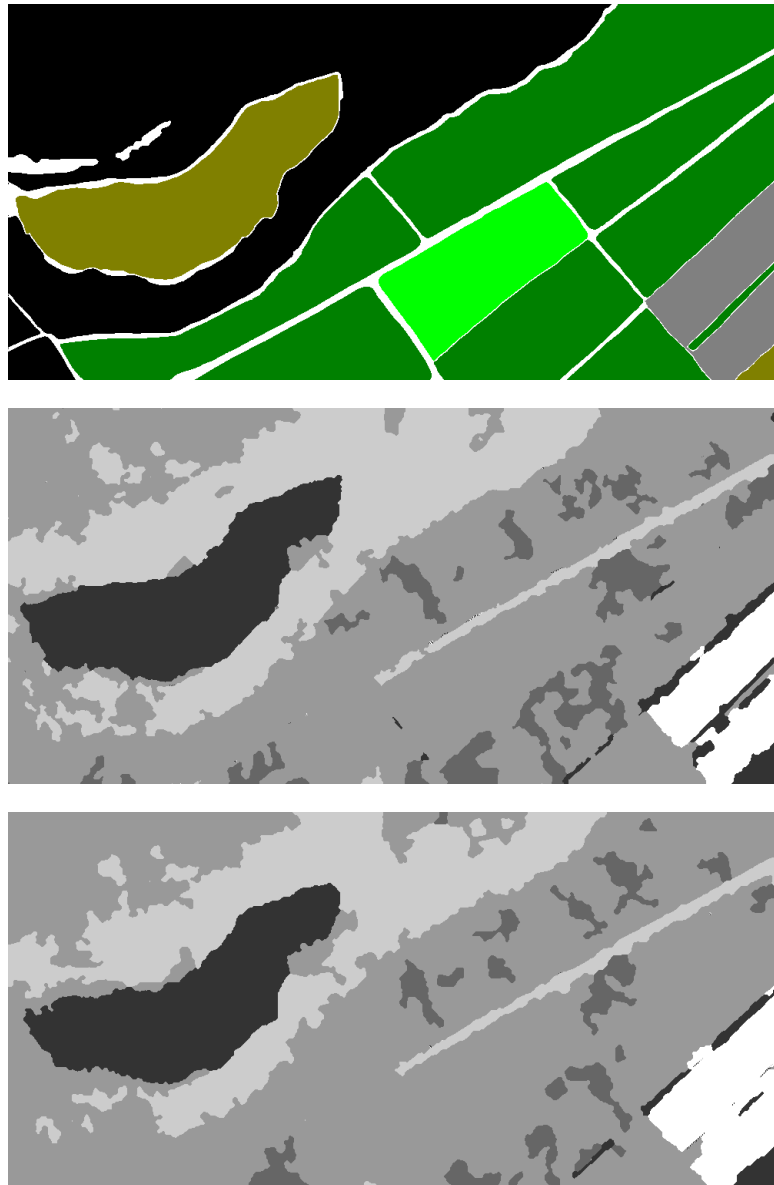


Figure 5.23: Segmentation results of the images Sat image  $IK_5$  in RGB color space using classical Gaussian (row 2) and MGMM (row 2) approximations for the multichannel LPE.

- For the segmentation experiments performed on the high resolution satellite images,  $L^*a^*b^*$  color space has shown better results than RGB color space. This difference is clear in terms of the various parameters computed over the results on these images.

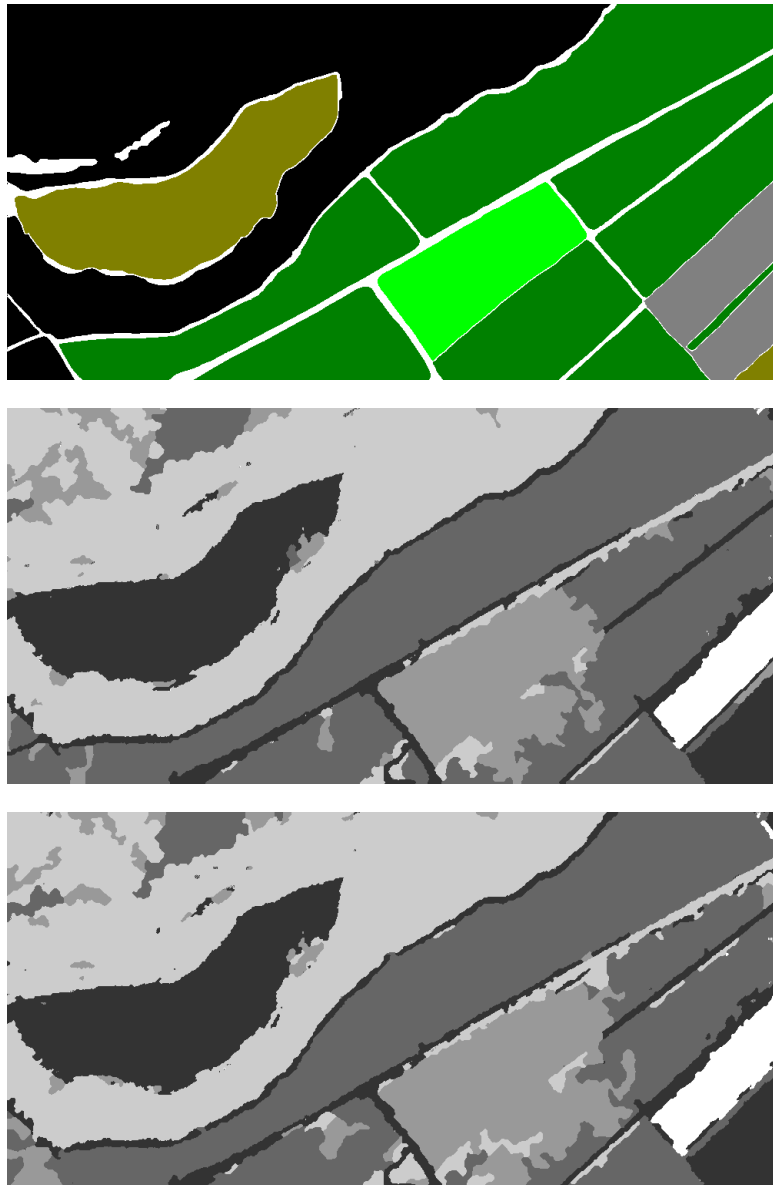


Figure 5.24: Segmentation results of the images Sat image  $IK_5$  in  $L^*a^*b^*$  color space using classical Gaussian (row 2) and MGMM (row 2) approximations for the multichannel LPE.

- The results of the experiments performed on these high resolution satellite images also prove the pertinence of the method for this application along with the desired robustness and stability.

The better performance of the RGB color space in the case of synthetic color texture images, may appear as a contradiction to our prior findings on color texture

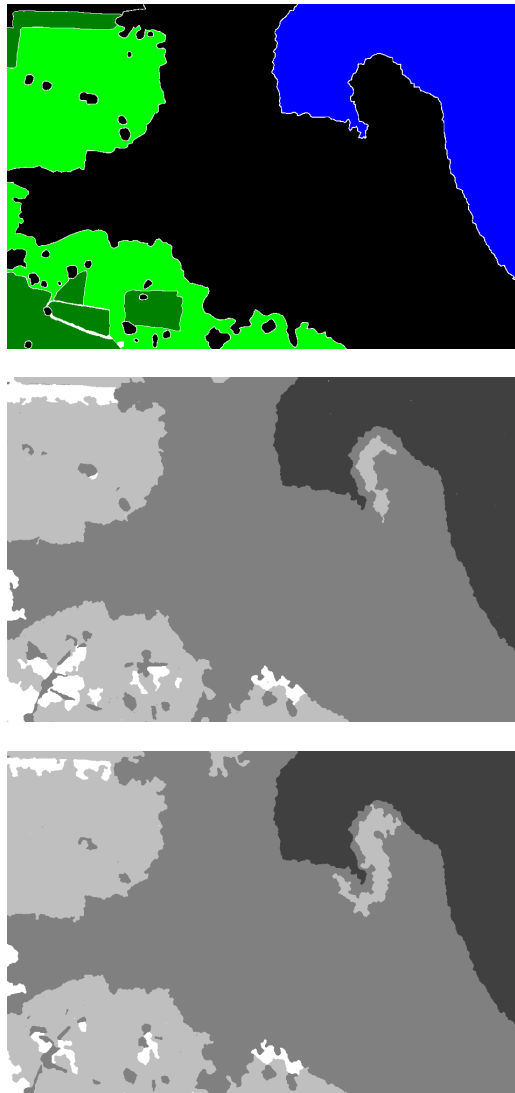


Figure 5.25: Segmentation results of the images Sat image  $IK_6$  in RGB color space using classical Gaussian (row 2) and MGMM (row 2) approximations for the multichannel LPE.

characterization in the chapter 4. However this is not the case. In the chapter 4, the mathematical models used were based on the decorrelation of the different channels in color images, therefore RGB (having a higher inter channel correlation characteristic) showed inferior results than the two perceptual color spaces. Whereas in this chapter, the parametric models used for the approximation of multichannel LPE distribution (for example MGMM) exploit the interchannel corre-

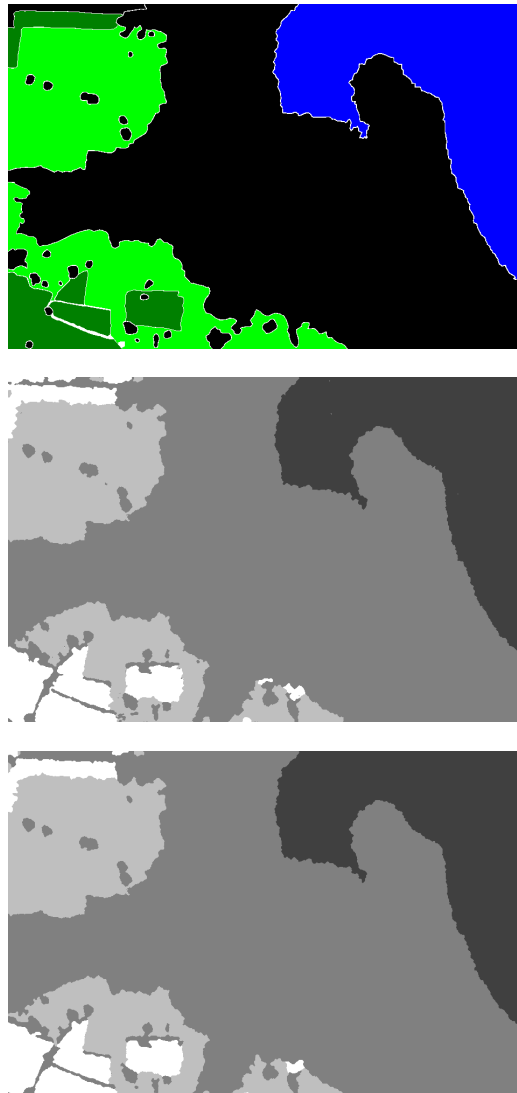


Figure 5.26: Segmentation results of the images Sat image  $IK_6$  in  $L^*a^*b^*$  color space using classical Gaussian (row 2) and MGMM (row 2) approximations for the multichannel LPE.

lation of the color planes through modeling of the joint probability distributions of the LPE.

---

## CHAPTER 6

---

# DISCUSSION

---

In this chapter we will discuss the novelties presented in this thesis and the achievement of different research objectives of this research work.

### 6.1 Conclusion

In this thesis we have presented a new model based approach for the characterization of color textures. This methodology is validated for the classification and segmentation of color textures as well as for the land cover classification in high resolution multispectral satellite images.

The approach makes use of the chrominance as well as the luminance spatial structure information in color texture images. The two channel complex color image representation has shown satisfactory results for the applications demanding independent analysis of both these information including classification and segmentation. In this study we have theoretically adapted and successfully used the two dimensional multichannel complex linear prediction models for modeling of these two channel color images in perceptual color spaces like IHLS and  $L^*a^*b^*$  which has not been used so far. We have also presented a new parametric approach for model based combined power spectrum estimation for both the channels in perceptual color spaces. A useful information of pure chrominance structure, is computed and is combined with the pure luminance structure information to achieve better color texture characterization.

In this work, a comparison of the used color spaces *i.e.* RGB, IHLS and  $L^*a^*b^*$  based on the inter plane decorrelation characteristics of these color spaces is presented. The study illustrates that the  $L^*a^*b^*$  shows the minimum correlation

between luminance and chrominance information and hence is better among the used color spaces for the color texture classification using the stated approach. This observation is supported by the outcomes of different sets of experiments conducted during this work.

For this comparison, we introduced a novel quantitative measure (the interference ratio) of the luminance-chrominance spectral interference for both the considered perceptual color spaces based on our parametric spectral estimation technique. A comparison of the considered color spaces based on this measure, under varying test conditions *i.e.* different image sizes, varied noise levels and different frequency sets proved clearly that IHLS exhibits more correlation of luminance and chrominance information than  $L^*a^*b^*$  color space. Based on this analysis, we developed the hypothesis that chrominance structure information of color textured images could get better characterized in  $L^*a^*b^*$  than in IHLS color space and hence could provide better results.

In color texture classification experiments, conducted on three different data sets, it is clearly observed that chrominance spatial structure adds significantly to the performance of color texture classification algorithms. Also, the percentage classification results based on chrominance spatial structure cue depict that  $L^*a^*b^*$  is a better choice for chrominance structure characterization in all the three data sets.  $L^*a^*b^*$  also shows the best results for the characterization of the overall spatial structure information for all three test data sets. This enforces the hypothesis inferred from the results of the spectral analysis experiments. In the results of pixel classification experiments too, we have observed that the  $L^*a^*b^*$  color space performs better than the other two color spaces in terms of the percentage pixel classification error and PPV for the chosen test color images while using the proposed approach.

We have also presented a parametric Bayesian framework of color texture segmentation based on the different parametric models. Among the three multichannel linear prediction models used, 2D QP AR model has shown the best results for color texture segmentation. This is consistent with our previous findings for parametric spectral analysis and color texture classification.

The novelty of the color texture segmentation approach lies in the multimodal approximation of the multichannel LPE distribution. In this framework, two different parametric approaches along with a classical monomodal approximation were used for this purpose. These included classically used multivariate Gaussian distribution, multivariate Gaussian mixture models and the Wishart distribution. A comparison of these three approaches have shown an overall advantage of using a multimodal distribution for this approximation instead of a multivariate Gaussian distribution for synthetic color textures as well as high resolution multispectral satellite images. The multivariate Gaussian mixture model approximation

has shown better color texture segmentation results in terms of mean percentage errors over the used color texture database.

The Wishart distribution also produced good initial class label fields without any spatial regularization. However during spatial regularization through Potts model, as the initially computed log likelihood term using this distribution becomes very significant, therefore it is less *affected* by the spatial regularization in general.

We introduced a region size based penalty term in the conventional Potts energy model. This has shown improved results in terms of percentage errors of color texture segmentation. Moreover this term has also shown an earlier optimal convergence in terms of increasing hyperparameter values as compared to the classical spatial regularization using Potts model.

These experiments were conducted in three color spaces i.e. RGB, IHLS and  $L^*a^*b^*$ . The comparison of results in these color spaces show that the RGB and the  $L^*a^*b^*$  color spaces perform better than IHLS color space in terms of the percentage errors as well as the stability of the results. However RGB and  $L^*a^*b^*$  color spaces have the same order of percentage errors, yet  $L^*a^*b^*$  color space shows a significant improvement in terms of stability of the segmentation results in most of the presented cases. The better performance of the RGB color space may appear as a contradiction to our prior findings on color texture classification. However this is not the case. In color texture classification experiments, the mathematical models used were based on the decorrelation of the different channels in color images, therefore RGB (having a higher inter channel correlation characteristic) showed inferior results than the two perceptual color spaces. Whereas in this work, the parametric models used for the approximation of multichannel LPE distribution (for example MGMM) make use of the joint probability distributions of the multichannel LPE. Hence, in these experiments decorrelation of the planes becomes less significant which is in complete accordance to our findings in classification experiments.

The segmentation experiments conducted on the high resolution satellite images also confirm the pertinence of the method for both characterization and segmentation of highly textured images. The  $L^*a^*b^*$  color space along with the MGMM approximation of the multichannel LPE sequence has shown the stable and robust results. Introduction of the region size energy term in the classical Potts model improved the final segmentation results for these images significantly.

## 6.2 Perspectives

The proposed color texture descriptor could be improved to take into account the contextual information of highly structured and non-structured regions in an image by using a Wold like decomposition method.

One of the future perspectives may include the development of a rotation and scale invariant version of the color texture descriptor proposed in this thesis. The PSD estimates computed through our approach could be used to compute the rotation invariant descriptors belonging to the Fourier-Mellin transform family [ACRN98].

The comparison of the used color spaces based on the luminance-chrominance decorrelation in this work could be extended to other color spaces of the same family. This could help the researchers to develop a final and certain choice for the best performing color space for color texture analysis.

Another important development could be to test and compare the performance of the proposed color texture segmentation framework with the non-parametric approaches like the ones presented in [MSP08, PZLB93]. An unsupervised version of the presented segmentation methodology could be developed on the basis of [AR05].

The texture classification and segmentation approaches developed in this work could also be extended to the multispectral satellite images of higher number of spectral bands.

---

---

# LIST OF PUBLICATIONS

---

## International Journals

I.-U.-H. Qazi, O. Alata, J.-C. Burie, and C. Fernandez-Maloigne, “Color spectral analysis for spatial structure characterization of textures in IHLS color space.” *Pattern Recognition*, vol. 43, pp. 663–675, March 2010.

I.-U.-H. Qazi, O. Alata, A. Moussa, J.-C. Burie, and C. Fernandez-Maloigne, “Choice of a pertinent color space for color texture characterization using parametric spectral analysis,” *Pattern Recognition*, Revision submitted.

I.-U.-H. Qazi, O. Alata, J.-C. Burie, M. Abadi, A. Moussa, and C. Fernandez-Maloigne, “Parametric models of linear prediction error distribution for color texture and satellite image segmentation,” *Computer Vision and Image Understanding*, Under review.

## International Conferences

I.-U.-H. Qazi, O. Alata, J.-C. Burie, A. Moussa and C. Fernandez-Maloigne, “Modèles paramétriques et segmentation.” in *To appear in Proceedings of Colloque Africain sur la Recherche en Informatique et en Mathématiques Appliquées (CARI)*, October 2010.

A. Moussa\*, M. Maouene, I.-U.-H. Qazi, O. Alata, J. C. Burie and A. Sbihi, “Classification d’images couleur texturées.” in *To appear in Proceedings of Colloque Africain sur la Recherche en Informatique et en Mathématiques Appliquées (CARI)*, October 2010.

I.-U.-H. Qazi, A. Moussa, O. Alata, J.-C. Burie, and C. Fernandez-Maloigne, “Parametric and non-parametric models of linear prediction error for color texture segmentation,” in *Proceedings of the International Conference on Signal-Image Technology and Internet based Systems (SITIS)*, December 2009.

I.-U.-H. Qazi, O. Alata, J.-C. Burie, and C. Fernandez-Maloigne, “Luminance chrominance spatial structure model in psychovisual colour spaces,” in *Proceedings of the 11th Congress of the International Colour Association (AIC)*, September 2009.

I.-U.-H. Qazi, F. Ghazi, O. Alata, J.-C. Burie, and C. Fernandez-Maloigne, “A multivariate Gaussian mixture model of linear prediction error for colour texture segmentation,” in *Proceedings of the European Signal Processing Conference (EUSIPCO)*, August 2009.

I.-U.-H. Qazi, O. Alata, J.-C. Burie, and C. Fernandez-Maloigne, “Spatial structure characterization of textures in IHLS colour space,” in *Proceedings of the IEEE International Conference on Acoustics, Speech, and Signal Processing (ICASSP)*, pp. 1069–1072, April 2009.

## National Conferences

O. Alata, I.-U.-H. Qazi, J.-C. Burie, and C. Fernandez-Maloigne, “Analyse de l’image couleur dans les espaces RGB,  $L^*a^*b^*$  et IHLS à l’aide des lois de mélange Gaussiennes multidimensionnelles et de la prédiction linéaire bidimensionnelle,” in *Journée GDR ”Analyse de Scènes Couleur Fixes et Dynamiques”*, January 2010.

I.-U.-H. Qazi, J.-C. Burie, O. Alata, and C. Fernandez-Maloigne, “Détermination d’un espace couleur pertinent pour la caractérisation de textures couleur,” in *Proceedings of the 22ème GRETSI, Dijon (France)*, September 2009.

O. Alata, I.-U.-H. Qazi, J.-C. Burie, and C. Fernandez-Maloigne, “Analyse spectrale paramétrique dans les espaces couleur permettant la séparation intensité lumineuse et chromaticité,” in *Journée GDR ”Modèle stochastique multivarié en traitement des images”*, March 2009.

O. Alata, I.-U.-H. Qazi, J.-C. Burie, and C. Fernandez-Maloigne, “Analyse spectrale paramétrique pour la caractérisation de textures couleurs,” in *Proceedings of the Ecole d’Hiver sur l’Image Numérique Couleur (EHINC)*, January 2009.

## **Invited Papers**

C. Fernandez-Maloigne, O. Alata, J.-C. Burie, and I.-U.-H. Qazi, "Structure characterization of textures in IHLS colour space.," in *Annual Meeting of TTLA*, December 2008. ITRI, Taiwan.



# APPENDIX A

---

## COLOR SPACE TRANSFORMATIONS

---

### RGB to IHLS Transformation

A color image defined by the RGB vector defined in the section 3.2.1 can be converted to IHLS color space by following set of equations:

$$Y^1 = 0.2126R + 0.7152G + 0.0722B \quad (\text{A.1})$$

$$S = \max(R, G, B) - \min(R, G, B) \quad (\text{A.2})$$

$$H = \begin{cases} 360^\circ - H' & \text{if } B > G \\ H' & \text{otherwise} \end{cases} \quad (\text{A.3})$$

where  $H'$  is given as:

$$H' = \arccos \left[ \frac{R - \frac{1}{2}G - \frac{1}{2}B}{(R^2 + G^2 + B^2 - RG - RB - BG)^{\frac{1}{2}}} \right] \quad (\text{A.4})$$

It gives very small values of saturation which are also independent of Luminance values. This makes feature extraction simpler for the achromatic images. The inverse transform from IHLS to RGB is given as:

$$\begin{bmatrix} R \\ G \\ B \end{bmatrix} = \begin{bmatrix} 1.0000 & 0.7875 & 0.3714 \\ 1.0000 & -0.2125 & -0.2059 \\ 1.0000 & -0.2125 & 0.9488 \end{bmatrix} \begin{bmatrix} Y \\ C_1 \\ C_2 \end{bmatrix} \quad (\text{A.5})$$

---

<sup>1</sup>Luminance term, it could also be denoted by  $L$ .

where  $C_1$  and  $C_2$  are given as:

$$C_1 = K \times \cos(H) \quad (\text{A.6})$$

$$C_2 = -K \times \sin(H) \quad (\text{A.7})$$

and

$$K = \frac{\sqrt{3}S}{2 \sin(120^\circ - H^*)} \quad (\text{A.8})$$

where  $H^* = H - l \times 60^\circ$  for which  $l \in \{0, 1, 2, 3, 4, 5\}$  so that  $0^\circ \leq H^* \leq 60^\circ$ .

## RGB to L\*a\*b\* Transformation

For an RGB color image defined as in the section 3.2.1, the transformation from the RGB to the L\*a\*b\* color space is based on an intermediate system, known as the CIE XYZ space (ITU-Rec BT.709). The formulae for RGB to CIE XYZ transformation are [WS00]:

$$\begin{aligned} X &= 0.412453R + 0.357580G + 0.180423B \\ Y &= 0.212671R + 0.715160G + 0.072169B \\ Z &= 0.019334R + 0.119193G + 0.950227B \end{aligned} \quad (\text{A.9})$$

L\*a\*b\* color space is then defined on the CIE XYZ space based on  $X_W$ ,  $Y_W$  and  $Z_W$  representing a reference white which is a CIE standard illuminant,  $D_{65}$  in our case. Mathematical relations defining L\*a\*b\* color space on CIE XYZ are also given in [WS00].

$$\begin{aligned} L^* &= 116 \times \left(\frac{Y}{Y_W}\right)^{\frac{1}{3}} - 16 \text{ for } \frac{Y}{Y_W} > 0.008856 \\ L^* &= 903.3 \times \frac{Y}{Y_W} \text{ for } \frac{Y}{Y_W} \leq 0.008856 \\ a^* &= 500 \times \left( f\left(\frac{X}{X_W}\right) - f\left(\frac{Y}{Y_W}\right) \right) \\ b^* &= 200 \times \left( f\left(\frac{Y}{Y_W}\right) - f\left(\frac{Z}{Z_W}\right) \right) \\ &\text{with } f(\mu) = \mu^{\left(\frac{1}{3}\right)} \text{ for } \mu > 0.008856 \\ &f(\mu) = 7.787 \times \mu + \frac{16}{116} \text{ for } \mu \leq 0.008856 \end{aligned} \quad (\text{A.10})$$

where  $X_W$ ,  $Y_W$  and  $Z_W$  are the CIE XYZ tristimulus values of the reference white point  $D_{65}$ .

---

## APPENDIX B

---

# PERFORMANCE MEASURES

---

Percentage color texture classification for each color texture is related to the fraction of test textures or pixels (in the case of segmentation) correctly labeled:

$$Per_{classification} = \frac{TP}{n} \times 100 \quad (\text{B.1})$$

where  $TP$  (*True Positive*) is the number of correctly classified test textures or pixels (in the case of segmentation) and  $n$  is the number of total test textures or pixels for that class.

PPV, defined in the following equation indicates the ability of a classifier to detect true class membership.

$$PPV = \frac{TP}{TP + FP} \quad (\text{B.2})$$

where  $FP$ , (*False Positive*) for a given class membership, is the number of test textures or pixels which are classified as class members while in fact they do not belong to the given class i.e. the number of test subimages wrongly classified as class members out of all the test textures or pixels for all other classes.

Sensitivity (in percent) of a classifier can be defined as:

$$Per_{sensitivity} = \frac{TP}{TP + FN} \times 100 \quad (\text{B.3})$$

where  $FN$  (*False Negative*) is the number of test textures or pixels which were not correctly classified.



---

## APPENDIX C

---

# SEGMENTATION RESULTS

---

In this appendix we present the segmentation results of the satellite images Sat image  $QB_7$  to Sat image  $QB_{20}$  in RGB and L\*a\*b\* color spaces using classical single Gaussian and MGMM approximations for the multichannel LPE in the Figures C.1 to C.7.

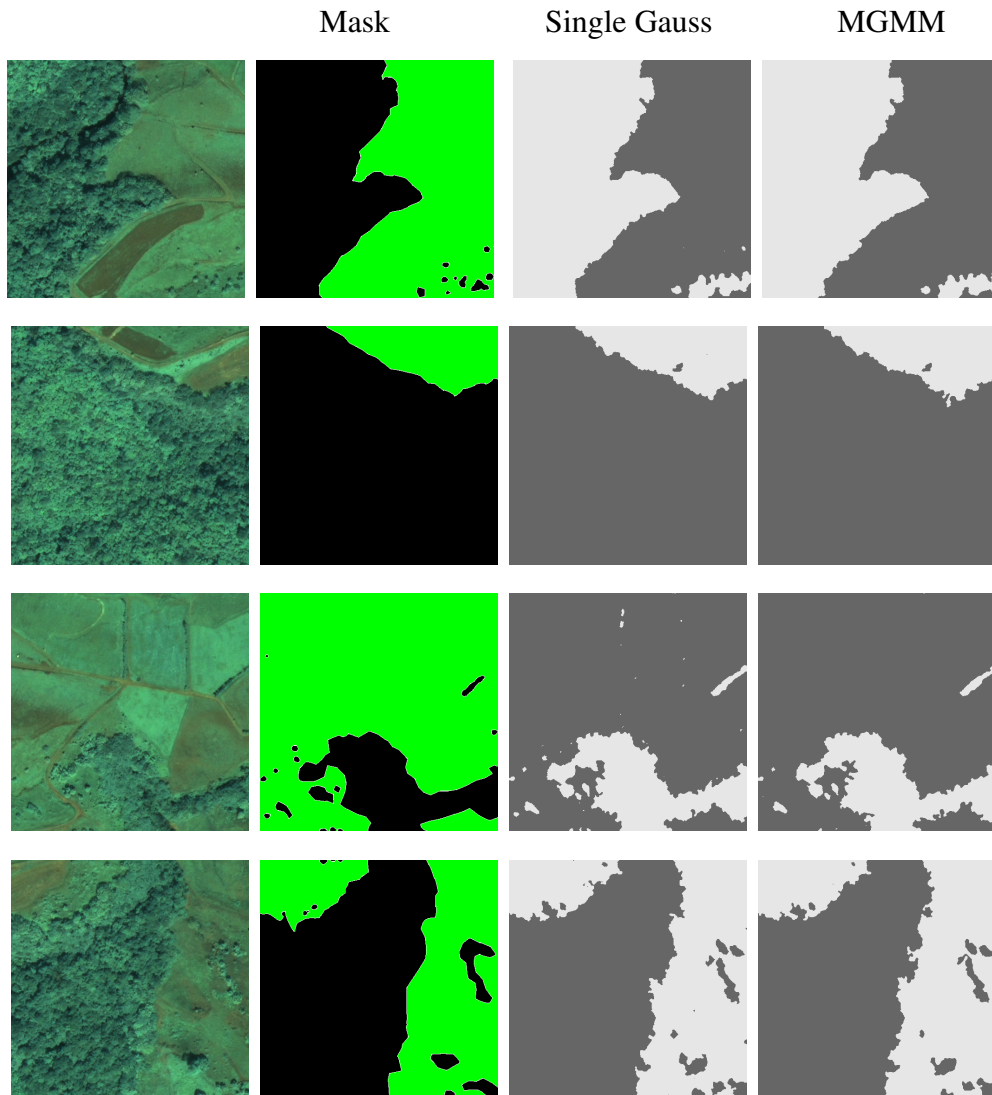


Figure C.1: Segmentation results of the satellite images Sat image  $QB_7$  to Sat image  $QB_{10}$  (rows 1 to 4 respectively) in RGB color space.

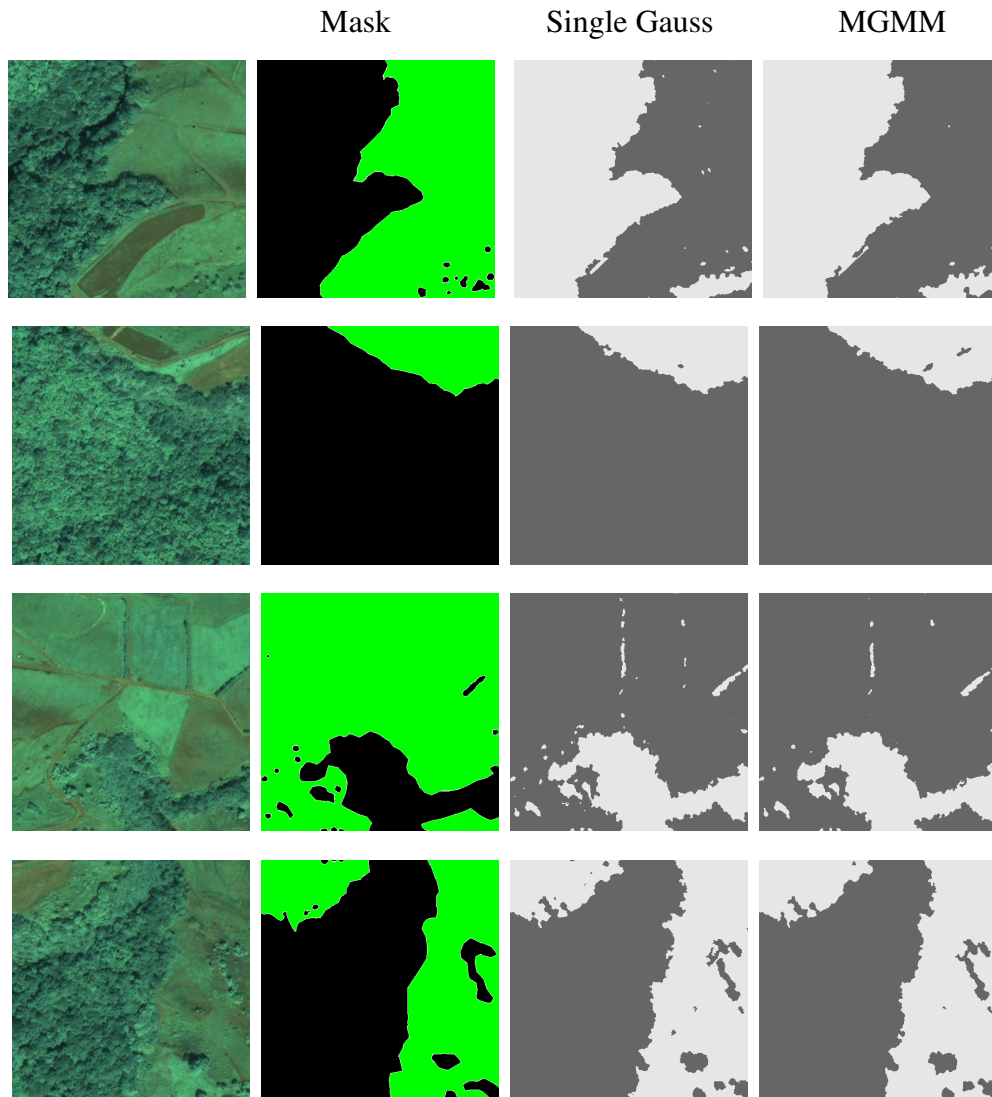


Figure C.2: Segmentation results of the satellite images Sat image  $QB_7$  to Sat image  $QB_{10}$  (rows 1 to 4 respectively) in  $L^*a^*b^*$  color space.

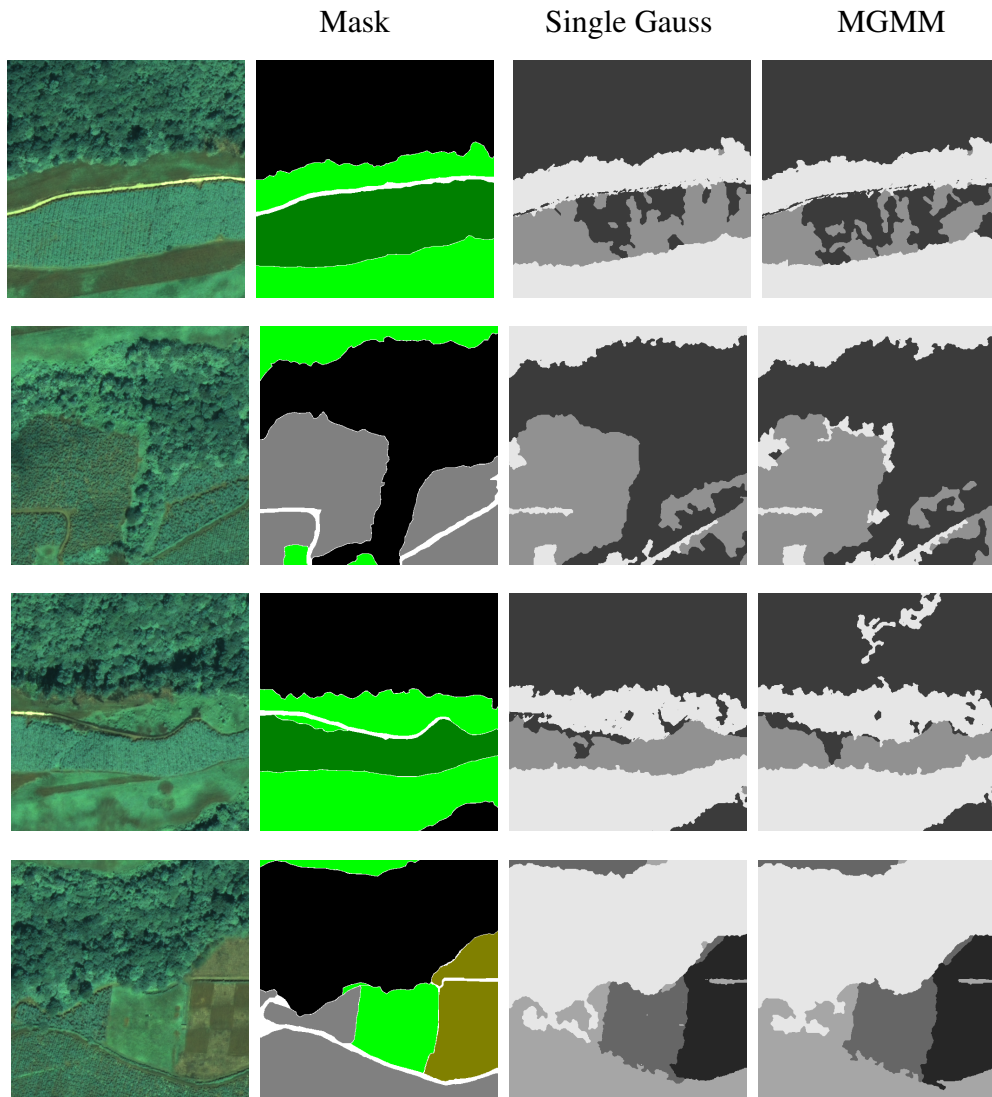


Figure C.3: Segmentation results of the satellite images Sat image  $QB_{11}$  to Sat image  $QB_{14}$  (rows 1 to 4 respectively) in RGB color space.

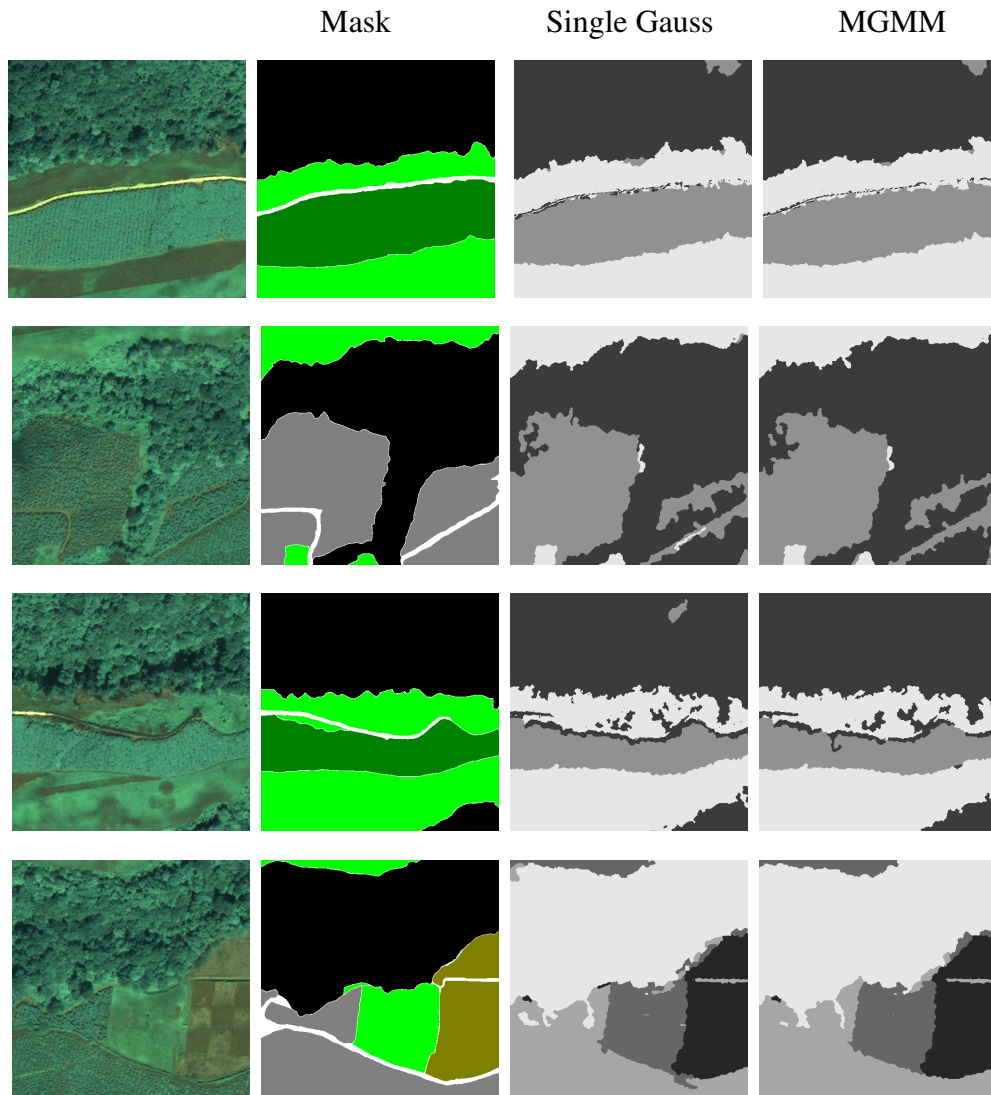


Figure C.4: Segmentation results of the satellite images Sat image  $QB_{11}$  to Sat image  $QB_{14}$  (rows 1 to 4 respectively) in  $L^*a^*b^*$  color space.

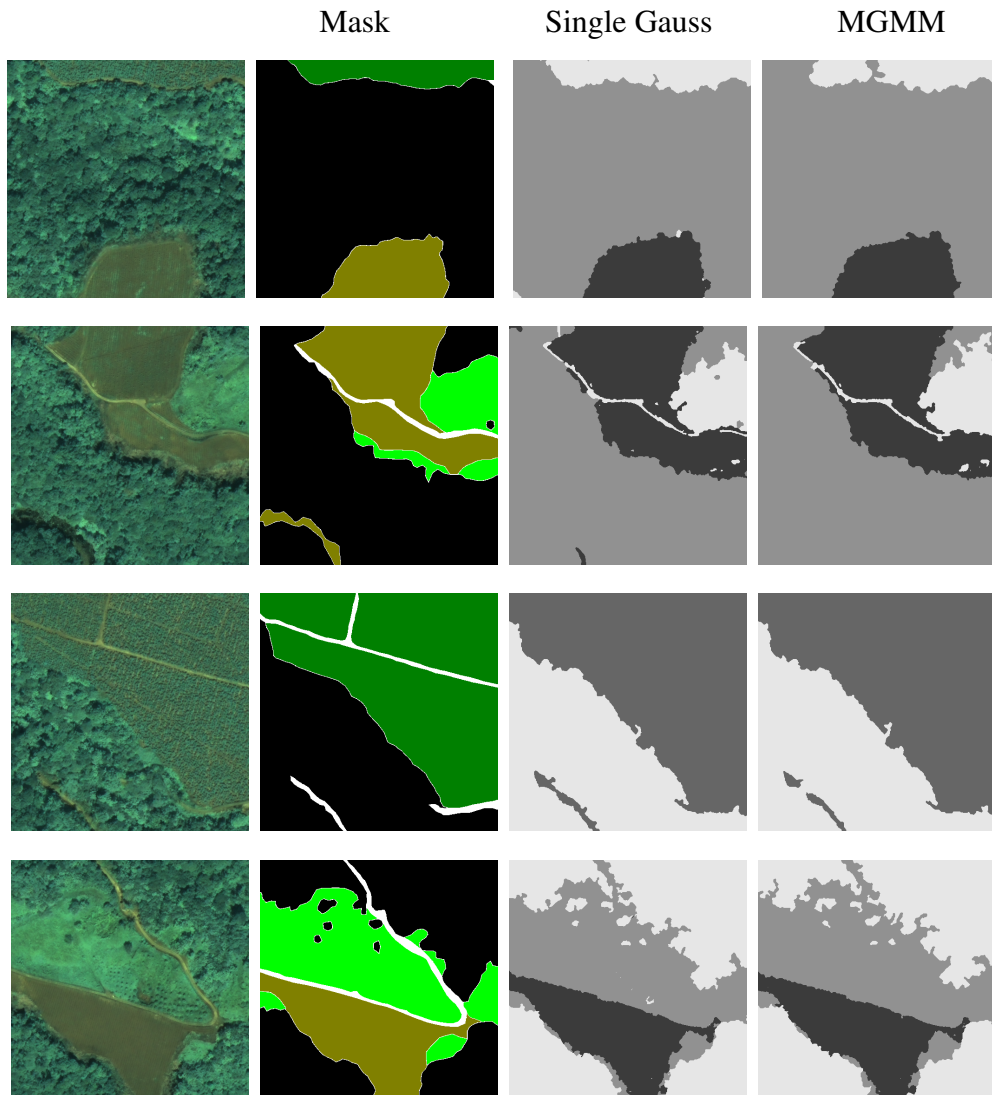


Figure C.5: Segmentation results of the satellite images Sat image  $QB_{15}$  to Sat image  $QB_{18}$  (rows 1 to 4 respectively) RGB color space.

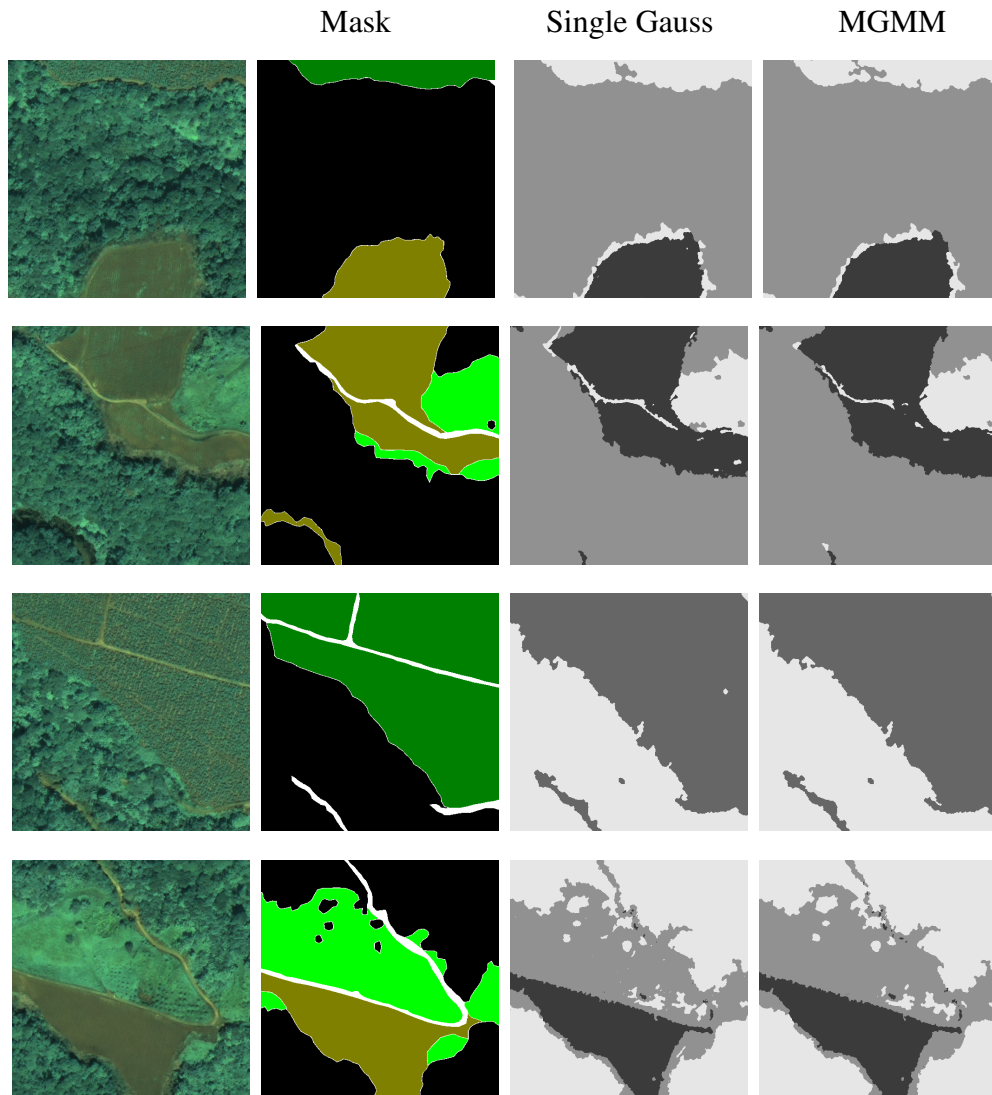


Figure C.6: Segmentation results of the satellite images Sat image  $QB_{15}$  to Sat image  $QB_{18}$  (rows 1 to 4 respectively) in  $L^*a^*b^*$  color space.

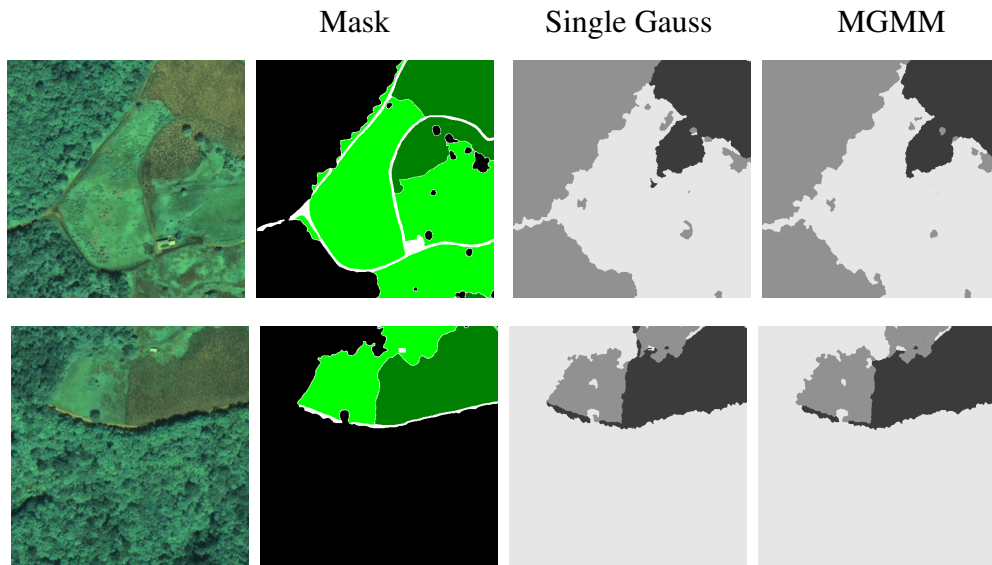


Figure C.7: Segmentation results of the satellite images Sat image  $QB_{19}$  and Sat image  $QB_{20}$  (rows 1 and 2 respectively) in RGB color space.

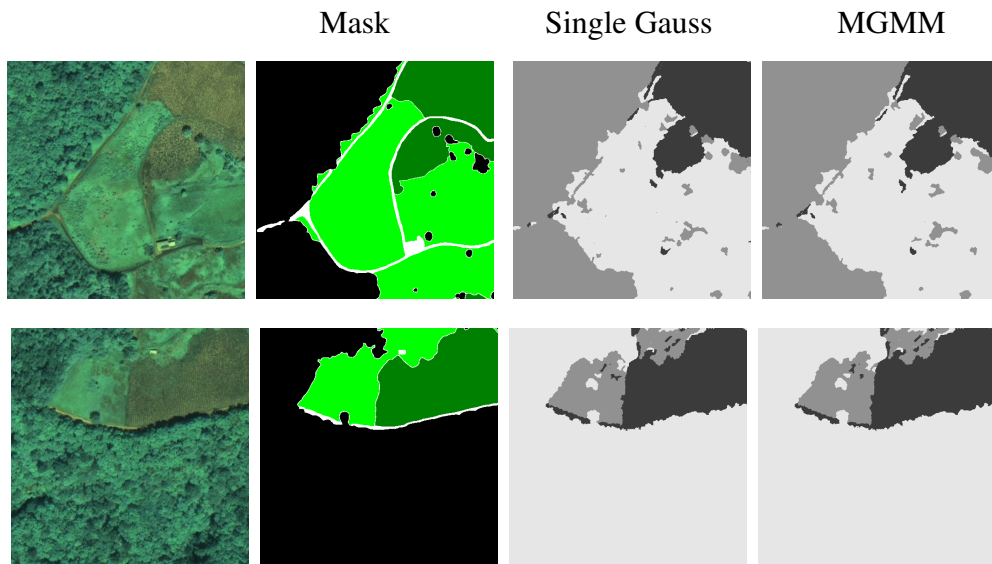


Figure C.8: Segmentation results of the satellite images Sat image  $QB_{19}$  and Sat image  $QB_{20}$  (rows 1 and 2 respectively) in  $L^*a^*b^*$  color space.

---

---

## BIBLIOGRAPHY

---

- [Aba08] M. Abadi. *Couleur et texture pour la représentation et la classification d'images multi-résolutions*. PhD thesis, Université des Antilles et de la Guyane, laboratoire GRIMAAG, Guadeloupe, 2008.
- [ABN97] O. Alata, P. Baylou, and M. Najim. A new 2-D spectrum estimate using multichannel AR approach of 2-D fast RLS algorithms. In *proceedings of IEEE International Conference on Image Processing*, pages II: 442–445, Washington, DC, USA, 1997.
- [ACRN98] O. Alata, C. Cariou, C. Ramananjarasoa, and M. Najim. Classification of rotated and scaled textures using HMHV spectrum estimation and the fourier-mellin transform. In *Proceedings of the IEEE International Conference on Image Processing*, pages 53–56, Chicago, Illinois, USA, 1998.
- [ADB04] Vincent Arvis, Christophe Debain, and Michel Berducat ; Albert Benassi. Generalization of the cooccurrence matrix for colour images: application to colour texture classification. *Image Analysis and Stereology*, 23:63–72, 2004.
- [AGK09] M. Abadi, E. Grandchamp, and M. Khoudeir. Improving spatial and spectral resolution of satellite images. In Joo Manuel R. S. Tavares & R.M. Natal Jorge, editor, *Computational Vision and Medical Image Processing, Porto Portugal*, pages 115–119, Porto, Portugal, October 2009. Taylor & Francis Groupe.
- [AH03] N. Angelo and V. Haertel. On the application of gabor filtering in supervised image classification. *International Journal of Remote Sensing*, 24(10):2167–2189, 2003.

- [AML08] Moulay A. Akhloufi, Xavier Maldague, and Wael Ben Larbi. A new color-texture approach for industrial products inspection. *Journal of Multimedia*, 3(3):44–50, 2008.
- [AMT<sup>+</sup>09] Dawit Assefa, Lalu Mansinha, Kristy F. Tiampo, Henning Rasmussen, and Kenzu Abdella. Local quaternion fourier transform and color image texture analysis. *Signal Processing*, In Press, Corrected Proof:–, 2009.
- [AQ09] O. Alata and L. Quintard. Is there a best color space for color image characterization or representation based on multivariate gaussian mixture model ?. *Computer Vision and Image Understanding*, 113(8):867–877, August 2009.
- [AR05] O. Alata and C. Ramananjarasoa. Unsupervised textured image segmentation using 2-D quarter plane autoregressive model with four prediction supports. *Pattern Recognition Letters*, 26(8):1069 – 1081, 2005.
- [AZ07] Mohand Saïd Allili and Djemel Ziou. Globally adaptive region information for automatic color-texture image segmentation. *Pattern Recognition Letters*, 28(15):1946–1956, 2007.
- [Bar98] S.A. Barker. *Image Segmentation using Markov Random Field Models*. PhD thesis, Signal Processing and Communications Laboratory, University of Cambridge, United Kingdom, 1998.
- [Bas89] M. Basseville. Distance measures for signal processing and pattern recognition. *Signal Process.*, 18(4):349–369, 1989.
- [BJC95] D.A. Bader, J. JaJa, and R. Chellappa. Scalable data-parallel algorithms for texture synthesis using gibbs random-fields. *IEEE Transactions on Image Processing*, 4(10):1456–1460, 1995.
- [BK98] J.W. Bennett and A. Khotanzad. Multispectral random field models for synthesis and analysis of color images. *IEEE Transactions on Pattern Analysis and Machine Intelligence*, 20(3):327–332, March 1998.
- [BK99] J.W. Bennett and A. Khotanzad. Maximum likelihood estimation methods for multispectral random field image models. *IEEE Transactions on Pattern Analysis and Machine Intelligence*, 21(6):537–543, June 1999.

- [BS94] Charles A. Bouman and Michael Shapiro. A multiscale random field model for bayesian image segmentation. *IEEE Transactions on Image Processing*, 3:162–177, 1994.
- [BT59] R. B. Blackman and J. W. Tukey. *The measurement of power spectra, from the point of view of communications engineering*. Dover Publications, 1959.
- [Cas06] F. Castanie, editor. *Spectral Analysis*. ISTE Ltd, London, 2006.
- [CC85] R. Chellappa and S. Chatterjee. Classification of textures using gaussian markov random fields. *IEEE Transactions on Acoustics, Speech and Signal Processing*, 33:959–963, August 1985.
- [CCF07] P. Christophe, P. Couteron, and F. Fromard. Predicting and mapping mangrove biomass from canopy grain analysis using fourier-based textural ordination of ikonos images. *Remote Sensing Environment*, 109(3):37–392, 2007.
- [CFP91] Fernand S. Cohen, Zhigang Fan, and Maqbool A. Patel. Classification of rotated and scaled textured images using gaussian markov random field models. *IEEE Transactions on Pattern Analysis and Machine Intelligence*, 13(2):192–202, 1991.
- [CHK83] R. Chellappa, Yu-Hen Hu, and Sun-Yuan Kung. On two-dimensional markov spectral estimation. *IEEE Transactions on Acoustics, Speech and Signal Processing*, 31:836–841, 1983.
- [CIE86] Colorimetry. Technical Report CIE 15.2, International Commission on Illumination, 1986.
- [CJ83] G.R. Cross and A.K. Jain. Markov random field texture models. *IEEE Transactions on Pattern Analysis and Machine Intelligence*, 5(1):25–39, January 1983.
- [CPW98] C. H. Chen, L. F. Pau, and P. S. P. Wang, editors. *Texture Analysis, The Handbook of Pattern Recognition and Computer Vision (2nd Edition)*, chapter 2.1, pages 207–248. World Scientific Publishing Coompany, 1998.
- [CSF05] Samuel Chindaro, Konstantinos Sirlantzis, and Michael C. Fairhurst. *Analysis and Modelling of Diversity Contribution to Ensemble-Based Texture Recognition Performance*, pages 387–396. 2005.

- [CTB<sup>+</sup>99] Chad Carson, Megan Thomas, Serge Belongie, Joseph M. Hellerstein, and Jitendra Malik. Blobworld: A system for region-based image indexing and retrieval. In *Proceedings of Third International Conference on Visual Information and Information Systems*, pages 509–516, Amsterdam, Holland, 1999.
- [DCFM07] Patrice Denis, Philippe Carre, and Christine Fernandez-Maloigne. Spatial and spectral quaternionic approaches for colour images. *Computer Vision and Image Understanding*, 107(1-2):74 – 87, 2007. Special issue on color image processing.
- [DJG00] M. P. Dubuisson-Jolly and A. Gupta. Color and texture fusion: application to aerial image segmentation and GIS updating. *Image and Vision Computing*, 18(10):823 – 832, 2000.
- [dLGDAL08] Rodrigo de Luis-García, Rachid Deriche, and Carlos Alberola-López. Texture and color segmentation based on the combined use of the structure tensor and the image components. *Signal Processing*, 88(4):776–795, 2008.
- [DM01] Y. Deng and B.S. Manjunath. Unsupervised segmentation of color-texture regions in images and video. *IEEE Transactions on Pattern Analysis and Machine Intelligence*, 23(8):800–810, August 2001.
- [DW01] A. Drimbarean and P. F. Whelan. Experiments in colour texture analysis. *Pattern Recognition Letters*, 22(10):1161–1167, 2001.
- [DZ86] Silvano Di Zenzo. A note on the gradient of a multi-image. *Computer Vision, Graphics and Image Processing*, 33(1):116–125, 1986.
- [ES00] C. Evans and S.J. Sangwine. Hypercomplex color-sensitive smoothing filters. In *Proceedings of IEEE International Conference on Image Processing*, pages Vol I: 541–544, Vancouver, BC, Canada, 2000.
- [ES07] T.A. Ell and S.J. Sangwine. Hypercomplex fourier transforms of color images. *IEEE Transactions on Image Processing*, 16(1):22–35, January 2007.

- [FAA00] Burks T. F., Shearer S. A., and Payne F. A. Classification of weed species using color texture features and discriminant analysis. *Transactions of the American Society of Agricultural Engineers*, 43(2):441–448, 2000.
- [Gar08] René Garello, editor. *Two-Dimensional Signal Analysis*. Wiley-ISTE, 2008.
- [GTYH07] J. Grazzini, A. Turiel, H. Yahia, and I. Herlin. A multifractal approach for extracting relevant textural areas in satellite meteorological images. *Environmental Modelling and Software*, 22(3):323–334, 2007.
- [Guy95] X. Guyon, editor. *Random fields on a network - modeling, statistics and application*. Springer-Verlag, 1995.
- [GW07] P. Ganarski and C. Wemmert. Collaborative multi-step mono-level multi-strategy classification. *Journal on Multimedia Tools and Applications*, 35(1):1–27, october 2007.
- [Har79] R. M. Haralick. Statistical and structural approaches to texture. *Proceedings of the IEEE*, 67(5):786–804, 1979.
- [HCG<sup>+</sup>04] O J. Hern, John Cook, Michael Griffin, Cynthia De Rama, and Michael MCGovern. Color image segmentation using multispectral random field texture model and color content features. *Journal of Computer Science and Technology*, 4(3), 2004.
- [HCG<sup>+</sup>05] O J. Hernandez, John Cook, Michael Griffin, Cynthia De Rama, and Michael MCGovern. Classification of color textures with random field models and neural networks. *Journal of Computer Science and Technology*, 5(3), 2005.
- [HGS05] Minh A. Hoang, Jan-Mark Geusebroek, and Arnold W.M. Smeulders. Color texture measurement and segmentation. *Signal Processing*, 85(2):265 – 275, 2005. Special issue on Content Based Image and Video Retrieval.
- [HM04] Michal Haindl and Stanislav Mikeš. Model-based texture segmentation. *Lecture Notes in Computer Science*, 3212:306–313, 2004.

- [HM06] M. Haindl and S. Mikes. Unsupervised texture segmentation using multispectral modelling approach. In *proceedings of International Conference on Pattern Recognition*, pages II: 203–206, Hong Kong, 2006.
- [HMP09] Michal Haindl, Stanislav Mikeš, and Pavel Pudil. Unsupervised hierarchical weighted multi-segmenter. In *Proceedings of 8th International Workshop on Multiple Classifier Systems*, pages 272–282, Reykjavik, Iceland, 2009.
- [HS80] M. Hassner and J. Sklansky. The use of markov random fields as models of texture. *Computer Graphics and Image Processing*, 12(4):357–370, April 1980.
- [HS03] Allan Hanbury and Jean Serra. A 3D-polar coordinate colour representation suitable for image analysis. Technical Report PRIP-TR-77, Institute of Computer Aided Automation, Vienna University of Technology, Vienna, Austria, 2003.
- [HSD73] Robert M. Haralick, K. Shanmugam, and Its'hak Dinstein. Textural features for image classification. *IEEE Transactions on Systems, Man and Cybernetics*, 3(6):610–621, 1973.
- [IMK<sup>+</sup>04] D. K. Iakovidis, D. E. Maroulis, S. A. Karkanis, P. Papageorgas, and M. Tzivras. Texture multichannel measurements for cancer precursors' identification using support vector machines. *Measurement*, 36:297 – 313, 2004.
- [IW08] D.E. Ilea and P.F. Whelan. CTexAn adaptive unsupervised segmentation algorithm based on Color-Texture coherence. *IEEE Transactions on Image Processing*, 17(10):1926–1939, 2008.
- [JC79] L. Jackson and H. Chien. Frequency and bearing estimation by two-dimensional linear prediction. In *Proceedings of IEEE International conference on Accoustics, Speach and Signal Processing*, pages 665–668, Washington DC, USA, 1979.
- [JCR05] A. Mojsilovic J. Chen, T. N. Pappas and B. E. Rogowitz. Adaptive perceptual color-texture image segmentation. *IEEE Transactions on Image Processing*, 14(10):1524–1536, 2005.
- [JJS01] Don Johnson, Don H. Johnson, and Sinan Sinanovic'. Symmetrizing the kullback-leibler distance. Technical report, IEEE Transactions on Information Theory, 2001.

- [Jus77] J.H. Justice. A levinson-type algorithm for two-dimensional wiener filtering using bivariate szeg polynomials. *Transactions of the IEEE*, 65(6):882 – 886, 1977.
- [KBH06] Alireza Khotanzad, Jesse W. Bennett, and Orlando J. Hernandez. A classification methodology for color textures using multispectral random field mathematical models. *Mathematical and Computational Applications*, 11(2), 2006.
- [KC83] R.L. Kashyap and R. Chellappa. Estimation and choice of neighbors in spatial-interaction models of images. *Information Theory, IEEE Transactions on*, 29(1):60 – 72, 1983.
- [KCK82] R.L. Kashyap, R. Chellappa, and A. Khotanzad. Texture classification using features derived from random field models. *Pattern Recognition Letters*, 1(1):43 – 50, 1982.
- [KH03] Alireza Khotanzad and Orlando J. Hernandez. Color image retrieval using multispectral random field texture model and color content features. *Pattern Recognition*, 36(8):1679 – 1694, 2003.
- [KP06] Z. Kato and T.-C. Pong. A Markov random field image segmentation model for color textured images. *Image and Vision Computing*, 24(10):1103–1114, 2006.
- [KPQ03] Z. Kato, T.C. Pong, and S.G. Qiang. Unsupervised segmentation of color textured images using a multi-layer mrf model. In *proceedings of IEEE International Conference on Image Processing*, pages I: 961–964, Barcelona, Spain, 2003.
- [KT81] R. Kumaresan and D.W. Tufts. A two-dimensional technique for frequency-wavenumber estimation. *Transactions of the IEEE*, 69(11):1515–1517, 1981.
- [KTB04] D. Kalenova, P.J. Toivanen, and V. Botchko. Color differences in a spectral space. In *International Conference on Computer Graphic, Imaging and Visualization*, pages 368–371, Penang, Malaysia, 2004.
- [Law85] W. M. Lawton. A complete spectral characterization of quarter-plane autoregressive models. *IEEE Transactions on Acoustics, Speech and Signal Processing*, 33:1617–1619, 1985.

- [LM98] J.G. Liu and J.M. Moore. Pixel block mixing modulation: adding spatial detail to tm band 6 thermal imagery. *International Journal of Remote Sensing*, 19(13):2477–2491, 1998.
- [LMVMPF08] Fernando López, José Miguel Valiente, José Manuel Prats, and Alberto Ferrer. Performance evaluation of soft color texture descriptors for surface grading using experimental design and logistic regression. *Pattern Recognition*, 41(5):1744–1755, 2008.
- [LRWW98] Jeffrey C. Lagarias, James A. Reeds, Margaret H. Wright, and Paul E. Wright. Convergence properties of the nelder–mead simplex method in low dimensions. *SIAM J. on Optimization*, 9(1):112–147, 1998.
- [LTR99] B.L. Steward L. Tang, L.F. Tian and J.F. Reid. Texture-based weed classification using gabor wavelets and neural network for real-time selective herbicide applications. *Transactions of the American Society of Agricultural Engineers*, 1999.
- [LW07] D. Lu and Q. Weng. A survey of image classification methods and techniques for improving classification performance. *Int. J. Remote Sens.*, 28(5):823–870, 2007.
- [MALDTB05] J. Martinez-Alajarin, J.D. Luis-Delgado, and L.M. Tomas-Balibrea. Automatic system for quality-based classification of marble textures. *IEEE Transactions on Systems, Man and Cybernetics*, 35:488–497, 2005.
- [Mar80] T. Marzetta. Two-dimensional linear prediction: Autocorrelation arrays, minimum-phase prediction error filters, and reflection coefficient arrays. *IEEE Transactions on Acoustics, Speech and Signal Processing*, 28(6):725 – 733, 1980.
- [MJ92] Jianchang Mao and Anil K. Jain. Texture classification and segmentation using multiresolution simultaneous autoregressive models. *Pattern Recognition*, 25(2):173 – 188, 1992.
- [MKC88] Welch R. M., Sengupta S. K., and D. W. Chen. Cloud field classification based upon high spatial resolution textural features part i : Gray level co-occurrence matrix approach. *Journal of Geophysical Research. Part D, Atmospheres*, 93(10):663–681, 1988.

- [MP04] T. Maenpaa and M. Pietikainen. Classification with color and texture: jointly or separately? *Pattern Recognition*, 37(8):1629–1640, August 2004.
- [MS98] Andrzej Materka and Michal Strzelecki. Texture analysis methods A review. Technical report, Institute of Electronics, Technical University of Lodz, Poland., 1998.
- [MSP08] Ahmed Moussa, Abderrahmane Sbihi, and Jack-G erard Postaire. A markov random field model for mode detection in cluster analysis. *Pattern Recognition Letters*, 29(9):1197–1207, 2008.
- [MTJ02] Pietik inen M., M enp   T., and Viertola J. Color texture classification with color histograms and local binary patterns. In *Proceedings of 2nd International Workshop on Texture Analysis and Synthesis*, pages 109–112, Copenhagen, 2002.
- [MVK<sup>+</sup>02] Christian M nzenmayer, Heiko Volk, Christian K ublbeck, Klaus Spinnler, and Thomas Wittenberg. Multispectral texture analysis using interplane sum- and difference-histograms. In *Proceedings of the 24th DAGM Symposium on Pattern Recognition*, pages 42–49, London, UK, 2002. Springer-Verlag.
- [NTA02] Ndi A. Nyoungui, E. Tonye, and A. Akono. Evaluation of speckle filtering and texture analysis methods for land cover classification from sar images. *International Journal of Remote Sensing*, 23(9), 2002.
- [OMP<sup>+</sup>02] Timo Ojala, Topi M enp  , Matti Pietik inen, Jaakko Viertola, Juha Kyll nen, and Sami Huovinen. Outex - new framework for empirical evaluation of texture analysis algorithms. In *Proceedings of 16th International Conference on Pattern Recognition*, page 10701, Quebec, Canada, 2002.
- [OMTM02] Alireza Osareh, Majid Mirmehdi, Barry Thomas, and Richard Markham. Comparison of colour spaces for optic disc localisation in retinal images. In *Proceedings of 16th International Conference on Pattern Recognition*, page 10743, Quebec City, Canada, 2002.
- [OPH96] Timo Ojala, Matti Pietikinen, and David Harwood. A comparative study of texture measures with classification based on featured distributions. *Pattern Recognition*, 29(1):51–59, 1996.

- [OPM02a] Timo Ojala, Matti Pietikäinen, and Topi Mäenpää. Multiresolution gray-scale and rotation invariant texture classification with local binary patterns. *IEEE Transactions on Pattern Analysis and Machine Intelligence*, 24(7):971–987, 2002.
- [OPM02b] Timo Ojala, Matti Pietikinen, and Topi Menp. Multiresolution gray-scale and rotation invariant texture classification with local binary patterns. *IEEE Transactions On Pattern Analysis And Machine Intelligence*, 24(7):971–987, 2002.
- [Out] <http://www.outex.oulu.fi/>.
- [Pal04] C. Palm. Color texture classification by integrative co-occurrence matrices. *Pattern Recognition*, 37(5):965–976, May 2004.
- [Pas98] George Paschos. Chromatic correlation features for texture recognition. *Pattern Recognition Letters*, 19(8):643–650, 1998.
- [Pas01] G. Paschos. Perceptually uniform color spaces for color texture analysis: An empirical evaluation. *IEEE Transactions on Image Processing*, 10(6):932–937, June 2001.
- [Pet01] B. Peterson. Ikonos relative spectral response and radiometric calibration coefficients, se-ref-016, rev. a. Technical report, Space Imaging, Inc., April 2001.
- [PFJ06] Haim Permuter, Joseph Francos, and Ian Jermyn. A study of gaussian mixture models of color and texture features for image classification and segmentation. *Pattern Recognition*, 39(4):695–706, 2006.
- [PGGS<sup>+</sup>09] Filiberto Pla, Gema Gracia, Pedro García-Sevilla, Majid Mirme-hdi, and Xianghua Xie. Multi-spectral texture characterisation for remote sensing image segmentation. In *Proceedings of the 4th Iberian Conference on Pattern Recognition and Image Analysis*, pages 257–264, Póvoa de Varzim, Portugal, 2009.
- [PGM<sup>+</sup>] R. Picard, C. Graczyk, S. Mann, J. Wachman, L. Picard, and L. Campbell. Vision texture. <http://vismod.media.mit.edu/pub/VisTex/VisTex.tar.gz>.
- [PH95] D. K. Panjwani and G. Healey. Markov random field models for unsupervised segmentation of textured color images. *IEEE Transactions on Pattern Analysis and Machine Intelligence*, 17(10):939–954, 1995.

- [PKLS00] Christoph Palm, Daniel Keysers, Thomas Lehmann, and Klaus Spitzer. Gabor filtering of complex hue/saturation images for color texture classification. In *Proceedings of International Conference on Computer Vision, Pattern Recognition, and Image Processing*, pages 45–49, Atlantic City, USA, 2000.
- [PL02] Christoph Palm and Thomas M. Lehmann. Classification of color textures by gabor filtering. *International Journal of Machine Graphics & Vision. SI: Latest results in color image processing and applications*, 11(2/3):195–219, 2002.
- [PMV02] Matti Pietikäinen, Topi Mäenpää, and J. Viertola. Color texture classification with color histograms and local binary patterns. In *Proceedings of 2nd International Workshop on Texture Analysis and Synthesis*, pages 109–112, Copenhagen, 2002.
- [PP03] George Paschos and Maria Petrou. Histogram ratio features for color texture classification. *Pattern Recognition Letters*, 24(1-3):309–314, 2003.
- [PP06] S. Shivashankar P.S.Hiremath and Jagadeesh Pujari. Wavelet based features for color texture classification with application to cbir. *International Journal of Computer Science and Network Security*, 6(9A):124 – 133, 2006.
- [PVM08a] Alice Porebski, Nicolas Vandenbroucke, and Ludovic Macaire. Haralick feature extraction from lbp images for color texture classification. In *Proceedings of International Workshops on Image Processing Theory, Tools and Applications*, pages 1–8, Sousse, Tunisia, November 2008.
- [PVM08b] Alice Porebski, Nicolas Vandenbroucke, and Ludovic Macaire. Neighborhood and haralick feature extraction for color texture analysis. In *Proceedings of European Conference on Colour in Graphics, Image and Vision*, pages 316–321, Terrassa, Spain, June 2008.
- [PZLB93] J.-G. Postaire, R. D. Zhang, and C. Lecocq-Botte. Cluster analysis by binary morphology. *IEEE Transactions on Pattern Analysis and Machine Intelligence*, 15(2):170–180, 1993.
- [QABFM09] I.-U.-H. Qazi, O. Alata, J.-C. Burie, and C. Fernandez-Maloigne. Spatial structure characterization of textures in ihls colour space.

- In *IEEE International Conference on Acoustics, Speech and Signal Processing*, pages 1069–1072, Taipei, Taiwan, Avril 2009.
- [QABFM10] I.-U.-H. Qazi, O. Alata, J.-C. Burie, and C. Fernandez-Maloigne. Color spectral analysis for spatial structure characterization of textures in IHLS color space. *Pattern Recognition*, 43(3):663 – 675, 2010.
- [RSS<sup>+</sup>02] P.V.N. Rao, M.V.R.S. Sai, K. Sreenivas, M.V.K. Rao, B.R.M. Rao, R.S. Dwivedi, and L. Venkataratnam. Textural analysis of irs-1d panchromatic data for land cover classification. *International Journal of Remote Sensing*, 23(17):3327–3345, September 2002.
- [RVAB06] B. Dorizzi R. V. Andreao and J. Boudy. ECG signal analysis through hidden Markov models. *IEEE Transactions on Biomedical Engineering*, 53(8):1541–1549, 2006.
- [SBS99] Sabine Susstrunk, Robert Buckley, and Steve Swen. Standard RGB Color Spaces. In *IS T/SID 7th Color Imaging Conference*, volume 7, Scottsdale Arizona, 1999.
- [SD98] Michael Schroder and Alex Dimai. Texture information in remote sensing images: A case study, 1998.
- [SE01] S.J. Sangwine and T.A. Ell. Hypercomplex fourier transforms of color images. In *Proceedings of IEEE International Conference on Image Processing*, pages I: 137–140, Thessaloniki, Greece, 2001.
- [Sen08] Abdulkadir Sengur. Wavelet transform and adaptive neuro-fuzzy inference system for color texture classification. *Expert Systems with Applications*, 34(3):2120–2128, 2008.
- [Ser83] Jean Serra. *Image Analysis and Mathematical Morphology*. Academic Press, Inc., Orlando, FL, USA, 1983.
- [SF07] Lilong Shi and Brian Funt. Quaternion color texture segmentation. *Computer Vision and Image Understanding*, 107(1-2):88–96, 2007.
- [SHZ07] G. Scarpa, M. Haindl, and J. Zerubia. A hierarchical finite-state model for texture segmentation. In *proceedings of IEEE International Conference on Acoustics, Speech and Signal Processing*, pages I: 1209–1212, Honolulu, Hawaii, USA, 2007.

- [SRSD98] M. Schroder, H. Rehrauer, K. Seidel, and M. Datcu. Spatial information retrieval from remote-sensing images—part II: Gibbs-Markov random fields. *IEEE Transactions on Geoscience and Remote Sensing*, 36(5):1446, September 1998.
- [SZ06] M. Scarpa, G. Haindl and J. Zerubia. Hierarchical finite state modeling for texture segmentation with application to forest classification. Research Report 6066, INRIA, France, 2006.
- [TES99] C. W. Therrien and H. T. El-Shaer. Multichannel 2-D AR spectrum estimation. *IEEE Transactions on Acoustics, Speech, and Signal Processing*, 37:1798 – 1800, 1999.
- [TZ02] Z. Tu and S.-C. Zhu. Image segmentation by Data-Driven Markov Chain Monte Carlo. *IEEE Transactions on Pattern Analysis and Machine Intelligence*, 24:657–673, 2002.
- [VMP03] Nicolas Vandenbroucke, Ludovic Macaire, and Jack-G erard Postaire. Color image segmentation by pixel classification in an adapted hybrid color space: application to soccer image analysis. *Computer Vision and Image Understanding*, 90(2):190–216, 2003.
- [web] [http://www.geoeye.com/CorpSite/assets/docs/technical-papers/2008/IKONOS\\_Relative\\_Spectral\\_Response.xls](http://www.geoeye.com/CorpSite/assets/docs/technical-papers/2008/IKONOS_Relative_Spectral_Response.xls).
- [WJCK90] T. M. Lillesand W. J. Carper and R. W. Kiefer. The use of intensity-hue-saturation transformation for merging spot panchromatic and multispectral image data. *Photogrammetric Engineering & Remote Sensing*, 56(4):459-467, 1990.
- [WS00] G. W. Wyszecki and S. W. Stiles. *Color science: Concepts and methods, Quantitative data and formulae*. Wiley, New York, 2000.
- [WSLD99] G. Van De Wouwer, P. Scheunders, S. Livens, and D. Van Dyck. Wavelet correlation signatures for color texture characterization. *Pattern Recognition*, 32:443–451, 1999.
- [XM07] Xianghua Xie and Majid Mirmehdi. Texems: Texture exemplars for defect detection on random textured surfaces. *IEEE Trans. Pattern Anal. Mach. Intell.*, 29(8):1454–1464, 2007.

- [ZL88] L. Zou and B. Liu. On resolving two-dimensional sinusoids in white noise using different spectral estimates. *IEEE Transactions on Acoustics, Speech and Signal Processing*, 36(8):1338 – 1350, 1988.

## Résumé

Cette thèse détaille la conception, le développement et l'analyse d'un nouvel outil de caractérisation des textures exploitant les modèles de prédiction linéaire complexe sur les espaces couleur perceptuels séparant l'intensité lumineuse de la partie chromatique. Des modèles multicanaux 2-d causaux et non-causaux ont été utilisés pour l'estimation simultanée des densités spectrales de puissance d'une image "bi-canal", le premier contenant les valeurs réelles de l'intensité et le deuxième les valeurs complexes de la partie chromatique. Les bonnes performances en terme de biais et de variance de ces estimations ainsi que l'usage d'une distance appropriée entre deux spectres assurent la robustesse et la pertinence de l'approche pour la classification de textures. Une mesure de l'interférence existante entre l'intensité et la partie chromatique à partir de l'analyse spectrale est introduite afin de comparer les transformations associées aux espaces couleur. Des résultats expérimentaux en classification de textures sur différents ensembles de tests, dans différents espaces couleur (RGB, IHLS et  $L^*a^*b^*$ ) sont présentés et discutés. Ces résultats montrent que la structure spatiale associée à la partie chromatique d'une texture couleur est mieux caractérisée à l'aide de l'espace  $L^*a^*b^*$  et de ce fait, cet espace permet d'obtenir les meilleurs résultats pour classifier les textures à l'aide de leur structure spatiale et des modèles de prédiction linéaire.

Une méthode bayésienne de segmentation d'images texturées couleur a aussi été développée à partir de l'erreur de prédiction linéaire multicanale. La contribution principale de la méthode réside dans la proposition d'approximations paramétriques robustes pour la distribution de l'erreur de prédiction linéaire multicanale : la distribution de Wishart et une approximation multimodale exploitant les lois de mélanges gaussiennes multivariées. Un autre aspect original de l'approche consiste en la fusion d'un terme d'énergie sur la taille des régions avec l'énergie du modèle de Potts afin de modéliser le champ des labels de classe à l'aide d'un modèle de champ aléatoire possédant une distribution de Gibbs. Ce modèle de champ aléatoire est ainsi utilisé pour régulariser spatialement un champ de labels initial obtenu à partir des différentes approximations de la distribution de l'erreur de prédiction. Des résultats expérimentaux en segmentation d'images texturées couleur synthétiques et d'images satellites hautes résolutions QuickBird et IKONOS ont permis de valider l'application de la méthode aux images fortement texturées. De plus les résultats montrent l'intérêt d'utiliser les approximations de la distribution de l'erreur de prédiction proposées ainsi que le modèle de champ de labels amélioré par le terme d'énergie qui pénalise les petites régions. Les segmentations réalisées dans l'espace  $L^*a^*b^*$  sont meilleures que celles obtenues dans les autres espaces couleur (RGB et IHLS) montrant à nouveau la pertinence de caractériser les textures couleur par la prédiction linéaire multicanale complexe à l'aide de cet espace couleur.

### Mots clés:

Modèles de prédiction linéaire 2-d multicanale complexe, Estimation paramétrique de spectres, Classification de textures couleur, Segmentation d'images texturées couleur, Images satellites hautes résolutions, IKONOS, QuickBird.

## Abstract

This thesis details the conception, development and analysis of a novel color texture descriptor based on the luminance-chrominance complex linear prediction models for perceptual color spaces. In this approach, two dimensional complex multichannel versions of both causal and non-causal models are developed and used to perform the simultaneous parametric power spectrum estimation of the luminance and the *combined chrominance* channels of the proposed two channel complex color image. The accuracy and precision of these spectral estimates along with the spectral distance measures ensure the robustness and pertinence of the approach for color texture classification. A luminance-chrominance spectral interference based quantitative measure for the color space comparison is also introduced. The experimental results for different test data sets, in IHLS and L\*a\*b\* color spaces are presented and discussed. These results have shown that the chrominance structure information of the color textured images could get better characterized in L\*a\*b\* color space and hence could provide the better color texture classification results.

A Bayesian framework based on the multichannel linear prediction error is also developed for the segmentation of textured color images. The main contribution of this segmentation methodology resides in the robust parametric approximations proposed for the multichannel linear prediction error distribution. These comprised of a unimodal approximation based on the Wishart distribution and a multimodal approximation based on the multivariate Gaussian mixture models. Another novelty of this approach is the fusion of a region size energy term with the conventional Potts model energy to develop a Gibbs random field model of the class label field. This improved label field model is used for the spatial regularization of the initial class label estimates computed through the proposed parametric priors. Experimental results for the segmentation of synthetic color textures as well as high resolution QuickBird and IKONOS satellite images validate the application of this approach for highly textured images. Advantages of using these priors instead of classical Gaussian approximation and improved label field model are evident from these results. They also verify that the L\*a\*b\* color space exhibits better performance among the used color spaces, indicating its significance for the characterization of complex textures through this approach.

### Keywords:

Multichannel complex linear prediction models, Parametric spectrum estimation, Color texture classification, Color texture segmentation, High resolution satellite images, IKONOS, QuickBird.